

Phenomenology of the Higgs and Flavour Physics in the Standard Model and Beyond

DISSERTATION

zur Erlangung des akademischen Grades

doctor rerum naturalium
(Dr. rer. nat.)
im Fach Physik

eingereicht an der
Mathematisch-Wissenschaftlichen Fakultät
Humboldt-Universität zu Berlin

von
M.Sc. Lina Alasfar
geboren am 27. 09. 1994 in Riad

Präsident der Humboldt-Universität zu Berlin:
Prof. Dr. Peter Frensch

Dekan der Mathematisch-Wissenschaftlichen Fakultät:
Prof. Dr. Elmar Kulke

Gutachter:

Abstract

This thesis investigates some future aspects of Higgs measurements a decade after its discovery, focusing on the potential for future runs of the Large Hadron Collider (LHC). In particular, it aims to probe challenging couplings of the Higgs like its self-coupling and interaction with light quarks.

The first part provides an overview of Higgs theory and measurements, with some meta-analysis of most recent results focusing on the Standard Model Effective Field theory (SMEFT). The second part is about single-Higgs production, starting with a two-loop calculation of the gluon fusion component of Zh to reduce its theoretical uncertainties. Then, the potential for constraining the Higgs trilinear self-coupling from single Higgs rates is revisited; by including equally weakly-constrained four-heavy-quark operators entering at the next-to-leading order in single Higgs rates. These operators highly correlate with the trilinear self-coupling, thus affecting the fits made on this coupling from single Higgs data.

The third part focuses on the Higgs pair production, an essential process for measuring Higgs-self coupling, employing multivariate analysis to study its potential for probing light Yukawa couplings. Thereby exploring the sensitivity of Higgs pair production for the light-quark Yukawa interactions.

Finally, the fourth part showcases some models aiming to explain the recent flavour anomalies in the light of a global SMEFT Bayesian analysis combining flavour and electroweak precision measurements.

Keywords: Higgs Physics, Standard Model Effective Field Theory, Flavour observables, Statistical data analysis.

Zusammenfassung

fuer spaeter

Schlagwörter: Higgs Physik, Standardmodell-Effektivfeld-Theorie, Flavour Anomalies, Statistische Datenanalyse

Contents

1	Introduction	1
I	Higgs Physics	7
2	The Standard Model Higgs boson	9
2.1	Spontaneous symmetry breaking	9
2.1.1	Nambu-Goldstone theorem	12
2.2	The Braut-Englert-Higgs mechanism	13
2.3	Yukawa interaction	16
2.4	The Higgs and EW precision observables	18
2.4.1	Custodial symmetry	19
2.5	Theoretical constraints on the Higgs	23
2.5.1	Electroweak precision data fits	23
2.5.2	Partial-wave unitarity	23
2.5.3	Other bounds	27
3	Experimental measurements of the Higgs boson	31
3.1	Overview of the Large Hadron Collider	31
3.2	Higgs properties	33
3.2.1	Higgs boson mass measurements	33
3.2.2	Higgs full width	34
3.2.3	Higgs spin and parity	36
3.3	Measurements of Higgs rates and couplings	36
3.3.1	Higgs cross-sections	36
3.3.2	Constraints on Higgs couplings	39
3.4	Challenges and outlook	40
4	Higgs and effective field theories	43
4.1	The Standard Model effective field theory	44
4.1.1	Single Higgs processes in SMEFT	47
4.1.2	Higgs pair production and SMEFT	49
4.2	The chiral Lagrangian	50
4.2.1	Translation between SMEFT and HEFT	52
4.2.2	EFT and κ -formalism	52
4.3	Conclusions	53

II Single Higgs Processes at the LHC	55
5 Overview of Higgs production at colliders	57
5.1 Current status of the Higgs production channels	58
5.1.1 Gluon fusion process	58
5.1.2 Vector boson fusion	59
5.1.3 Associated production with EW bosons	60
5.1.4 Associated production with top quarks	61
5.2 Concluding remarks	62
6 Virtual two-loop calculation of Zh production via gluon fusion	63
6.1 General notation	64
6.1.1 The transverse momentum expansion	65
6.2 Born cross-section in the p_T -expansion	67
6.3 NLO calculation	70
6.3.1 Renormalisation	70
6.3.2 Calculation of the exact virtual corrections	72
6.3.3 Calculation of the p_T -expanded virtual corrections	74
6.4 Results and conclusions	74
7 Four top operators in Higgs production and decay	79
7.1 Contribution of four-fermion operators to Higgs rates at NLO	80
7.1.1 Analytic calculations	81
7.1.2 SMEFT-NLO calculation of $t\bar{t}h$	86
7.1.3 Results	88
7.2 Fit to Higgs observables	89
7.2.1 Fit results	93
7.2.2 Prospects for HL-LHC	99
7.3 Conclusion	99
III Higgs Pair Production	103
8 Overview of Higgs pair production at colliders	105
8.1 Higgs pair production by gluon fusion	105
8.1.1 Theoretical uncertainties	107
8.2 Other processes	108
8.2.1 VBF hh	108
8.2.2 Di-Higgsstrahlung	109
8.2.3 Associated Higgs pair production with t -quarks	109
8.3 Experimental overview for Higgs pair production	109
8.3.1 Prospects for the HL-LHC	112
8.4 Summary	112

9 Higgs pair as a probe for light Yukawa couplings	113
9.1 SMEFT and light Yukawa couplings	114
9.2 Higgs pair production and Higgs decays with modified light Yukawa couplings	117
9.2.1 Higgs pair production via quark anti-quark annihilation	117
9.2.2 Higgs decays	120
9.3 Event generation for the final state $hh \rightarrow b\bar{b}\gamma\gamma$	121
9.4 Cut-based analysis	123
9.4.1 Analysis strategy	124
9.4.2 Statistical analysis	125
9.5 Optimised search for Higgs pair via Interpretable machine learning	125
9.5.1 Constructing features	126
9.5.2 Exploratory network analysis	126
9.5.3 Classification analysis	129
9.6 Fit results	132
9.7 Overview of Light Yukawa searches	136
9.8 Discussion and conclusion	139
IV Flavour physics	143
10 Data-inspired models for $b \rightarrow s\ell\ell$ anomalies	145
10.1 Flavour anomalies in SMEFT	147
10.1.1 Theoretical preamble	147
10.1.2 SMEFT fit	150
10.1.3 Fit results	151
10.2 Z' with vector-like partners	155
10.2.1 SMEFT matching and constraints	160
10.2.2 Expanding the model	162
10.3 Leptoquark scenarios	163
10.4 Conclusion	164
11 Conclusion	167
A Details of Zh calculation	171
A.1 Orthogonal Projectors in $gg \rightarrow ZH$	171
A.2 Two-loop Results	172
B Two-parameter fits of four-fermion operators and C_ϕ for HL-LHC	175
C Prospects for Higgs pair production at the FCC	177

List of abbreviations

Colliders and working groups .

CERN	Conseil européen pour la recherche nucléaire.
LHC	Large Hadron Collider
HL-LHC	High-Luminosity LHC
CMS	Compact Muon Solenoid
ATLAS	A Toroidal LHC ApparatuS
LEP	Large Electron-Positron Collider
ALEPH	Apparatus for LEp PHysics
SLC	Stanford Linear Collider
FCC	Future circular collider
HXSWG	Higgs cross-section working group
PDG	Particle data group

Higgs and Standard Model physics.

SM	Standard Model
QCD	Quantum chromodynamics
QED	Quantum electrodynamics
EFT	Effective field theory
SMEFT	Standard Model effective field theory
HEFT	Higgs effective field theory
EW	Electroweak
VEV/ vev	Vacuum expectation value
EWSB	Electroweak symmetry breaking
EWPO	Electroweak precision observables
EWChL	Electroweak chiral Lagrangian
SSB	Spontaneous symmetry breaking

$SU(N)$	Special unitary (group) of dimension N
ggF	Gluon fusion (processes)
$q\bar{q}A$	Quark anti-quark annihilation (processes)
PDF	Parton distribution functions
BR	Branching ratio
STXS	Simplified template cross-sections

Higher order computations.

RGE	Renormalisation group equation or evolution
LO, NLO ...	Leading order, Next to leading order etc.
HTL	Heavy top limit
HPL	Harmonic polylogarithms
GPL	Generalised polylogarithms
HE	High energy expansion

Flavour.

CKM	Cabibbo-Kobayashi-Maskawa-Matrix
\mathcal{CP}	Charge conjugation and parity
MFV	Minimal flavour violation
AFV	Aligned flavour violation
SFV	Spontaneous flavour violation
PDD	Phenomenological data-driven
PMD	Phenomenological model-driven
FCNC	Flavour-changing neutral currents
LUV	Lepton universality violation

Data analysis/statistics.

MC	Monte Carlo (simulation)
ML	Machine learning
BDT	Boosted decision tree

XGBoost	EXtreme gradient boosted decision tree
DNN	Deep Neural Networks
MCMC	Markov chain Monte Carlo (Bayesian analysis)
PCo	Principle component
FDR	False discovery rate
ANOVA	Analysis of variation
HDPI	Highest density posterior interval
CI	Credible interval (Bayesian statistics)
CL	Confidence interval (Frequentist statistics)
New Physics.	
4F	Four-fermion
NP	New physics
BSM	Beyond the Standard Model
VLQ	Vector-like quarks
LQ	Leptoquarks
2HDM	Two-Higgs-doublet model
CHM	Composite Higgs model
MSSM	Minimal supersymmetric Standard Model
SILH	Strongly interacting light Higgs

1 Introduction

The discovery of the Higgs boson in 2012 by ATLAS [1] and CMS [2] experiments at the Large Hadron Collider (LHC) marks the completion of the Standard Model of particle physics (SM) [3–5]; as it was a direct prediction of the spontaneous symmetry breaking mechanism observed in the SM [6–10]. However, this discovery has brought more questions than answers, and even after a decade of its discovery, there is a lot to know about this particle and its potential connections with physics beyond the SM. Understanding the properties and couplings of the Higgs boson has become the preeminent goal of the LHC. Higgs measurements are getting progressively accurate, and our understanding of this particle is approaching a few per cent-level. The future runs of the LHC will open the doors to the Higgs-precision era. However, increased luminosity, i.e. data acquisition from the LHC, without improving the theoretical prediction of Higgs processes is futile. Therefore, to ensure the experimental efforts’ success in probing Higgs couplings and properties at the required precision, it is imperative to include higher-order calculations for Higgs production cross-sections.

An example of such processes is the associated production of Higgs with Z bosons, which suffers from higher theoretical uncertainties than its sister process, the Wh production, because it contains a gluon fusion sub-process $gg \rightarrow Zh$. Furthermore, the gluon fusion channel generally tends to have large higher-order corrections compared to the quark-initiated one. Thereby, prompting the need to compute its Next-to-leading order corrections , in order to improve the theoretical prediction of the Zh production. Such computations can be carried out efficiently using state-of-the-art analytic technique based on the expansion in small transverse momentum proposed in ref. [11].

After a decade of *Higgs physics*, and over ten-thousand Higgs-related publications, we still have a lot to learn about the Higgs boson. In particular, its potential structure is yet to be probed experimentally, and its couplings to the light quarks and leptons are. Measurements of Higgs self-coupling will reveal if there are, for instance, new scalars beyond the Higgs boson that we have not yet directly observed. Furthermore, studying Higgs coupling to light fermions is essential in understanding the source of their masses’ origin and explaining the significant hierarchy between these across the three generations of matter.

The conclusion of the SM-related discoveries did not leave any specific hints to the nature and scale of new physics (NP). Moreover, many experimental searches have excluded NP at scale close to the electroweak symmetry breaking, for most recent searches cf. [12–23]. Although NP is needed to explain the shortcomings of the SM, for example, the neutrino masses, dark matter and so on. This motivated parametrising NP effects in a model-independent manner, with the ansatz that the it has a scale higher than the LHC reach. This formalism is known as the Standard Model Effective Field Theory (SMEFT)

framework [24–28]. In SMEFT, all NP interactions are summarised in a numerable set of mass dimension six operators, that makes minimal assumptions about the nature of NP, guaranteeing a model-independent approach to collider searches.

The use of SMEFT in higher-order calculations of Higgs rates has revealed insights into the Higgs potential by the appearance of Higgs trilinear self-coupling within electroweak loop corrections of single-Higgs processes. So that the measurements of single-Higgs rates at the LHC can be used to constrain this coupling [29–36]. Nevertheless, more SMEFT observables can also enter in single-Higgs loops that alter these measurements’ constraining power. The interconnectivity between the Higgs and top-quark sectors is further emphasised within the SMEFT framework, as recent global fits have established strong correlations between observables from both sectors as well as the electroweak precision observables (EWPO) [37]. Strong correlations between the top sector and EWPO are also seen at loop-level [38] thus; one expects to see similar correlations emerging from loop effects of top operators on Higgs processes.

The observation of Higgs pairs is slated for the High-Luminosity (HL) LHC operating phase. This rare process will be –if observed– the *pièce de résistance* of the LHC Higgs physics programme [39], directly measuring the Higgs self-interaction, also untangling Higgs potential measurements from the top-sector interactions. Furthermore, this process could be of great utility in probing Higgs coupling to light quarks, from the enhancement of the quark-initiated Higgs pair production *not sure what to cite here*. The full potential of Higgs pair production can be exploited when it is treated as a multivariate problem by implementing an interpretable machine learning analysis technique [40]. In this manner, it is possible to have a simultaneous measurement of the two most elusive Higgs interactions, light-quark Yukawa and the trilinear couplings.

Recent measurements, by Belle and Babar, in addition to the LHCb experiment at CERN, of B -mesons semi-leptonic decays showed some tension with the SM predictions of lepton flavour universality of electroweak couplings [41–45], with up to $\sim 3\sigma$ deviation from the SM [46–49]. These anomalies require models with some flavour violation that makes model-building for explaining these anomalies a tree-level and Augean task [50–59]. Additionally, to complicate things further, these anomalies are in tension with EWPO. Hence, promoting a more careful treatment of these anomalies, by introducing them at the loop level in SMEFT and performing a global fit combining both flavour and EWPO data. The fit result would allow for a SMEFT guided UV-model building for these anomalies, with extended Higgs and top sectors.

This thesis is structured as follows: I start with an introduction to Higgs physics and its role in the SM in chapter 2, followed by theoretical constraints on the Higgs. In chapter 3, I review of state-of-the-art Higgs measurements and the constraints on Higgs couplings derived from the latest LHC data. After that, I present the basics of Effective Fields Theories relevant to Higgs physics at the LHC in chapter 4.

The second part of the thesis focuses on the production of –single– Higgs at the LHC, starting with an overview in chapter 5, followed by a discussion on the use of the p_T –

expansion technique for obtaining an analytic expression for the virtual correction of the gluon fusion Zh production in [chapter 6](#). Next, [chapter 7](#) showcases the potential of single-Higgs processes to probe four-fermion operators from the top sector of SMEFT by performing higher-order computations of these processes in SMEFT. The potential for constraining these operators for the considered single-Higgs production processes alongside the trilinear Higgs self-coupling is investigated by means of a Bayesian fit. The third part of the thesis focuses on the production of Higgs boson in pairs at the HL-LHC ([chapter 8](#)). Afterwards, in [chapter 9](#), I show the potential for employing Higgs pair production to probe light quark couplings to the Higgs boson. In addition, I show a multivariate analysis method, that maximises the efficiency of extracting the Higgs pair signal using interpretable machine learning. The last part of the thesis, [chapter 10](#), describes the potential UV models for the B anomalies, inspired by a global SMEFT fit and minimal flavour violation (MFV).

List of publications

1. **L. Alasfar**, J. de Blas and R. Gröber,
Higgs probes of top quark contact interactions and their interplay with the Higgs self-coupling,
arXiv:2202.02333 [hep-ph] (Submitted to JHEP).
2. **L. Alasfar**, G. Degrassi, P. P. Giardino, R. Gröber and M. Vitti,
Virtual corrections to $gg \rightarrow ZH$ via a transverse momentum expansion,
JHEP **05** (2021), 168
arXiv:2103.06225 [hep-ph].
3. **L. Alasfar**, A. Azatov, J. de Blas, A. Paul and M. Valli,
B anomalies under the lens of electroweak precision,
JHEP **12** (2020), 016
arXiv:2007.04400 [hep-ph].
4. **L. Alasfar**, R. Corral Lopez and R. Gröber,
Probing Higgs couplings to light quarks via Higgs pair production,
JHEP **11** (2019), 088
arXiv:1909.05279 [hep-ph].

Part I

Higgs Physics

2 The Standard Model Higgs boson

2.1 Spontaneous symmetry breaking

Before talking about symmetry breaking, we need to discuss the concept of symmetry in physics. Symmetry is a crucial part of studying physical systems. It manifests not only as a geometric feature of physical objects but also in the dynamics of physical systems. For example, one can find symmetries in the equations of motion, Lagrangians/Hamiltonians and actions. The magnetisation of materials is a good example of symmetry's role in describing physical behaviour. For instance, paramagnetic materials have a positive magnetic susceptibility χ_B due to the random arrangement of their electrons' spins. The paramagnetic material spins arrangement will therefore possess rotational symmetry. The material has no *preferred direction* in space [60]. *Au contraire*, ferromagnetic materials with the electrons' spins aligned in a certain direction will not have such symmetry as there will be a preferred direction, see Figure 2.1.

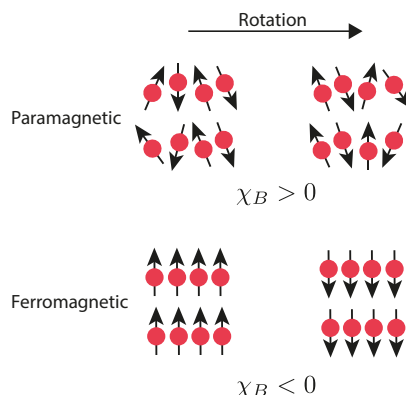


Figure 2.1. In paramagnetic materials, the spins are randomly distributed such that a rotation performed on the system will keep the spin distribution invariant. However, the symmetry is broken for ferromagnetic materials, where the spins are aligned in a single direction, and the system has a preferred direction.

In particle physics and quantum field theory, symmetry plays an essential role in the taxonomy and dynamics of elementary particles and their bound states, i.e. hadrons, cf. [61, 62]. There are two types of symmetries considered when studying elementary particles and their quantum fields: external and internal symmetries. The first is the symmetry of the spacetime background. Typically, this is a four-dimensional Poincaré symmetry. Higher spacetime dimensions or non-flat geometries are considered in some models. However, there is no current evidence of higher dimensions or indications of

non-flat spacetime from colliders and cosmological observations [63]. The second class of symmetries is internal symmetries stemming from the quantum nature of these particles/fields. Because their state is described by a ray in complex Hilbert/Fock spaces, internal symmetries are simply symmetries of rotations in these spaces that keep the action variation unchanged. Internal symmetries are usually described in terms of simple or product of simple Lie groups, e.g. $SU(N)$ ¹. Particles/fields will be arranged as multiplets in some representation of the groups. If the rotations of the states could be parametrised by constants, the symmetry is called global. Alternatively, if these transformations are themselves functions of the spacetime, the symmetry is then called local or **gauged**.

Gauge symmetries describe rotations in the state of space that depends on spacetime. The generator of the gauge transformations could propagate between two spacetime points. This is the way particle interactions are described in quantum field theory. The generators of these gauge transformations are called gauge bosons, and they mediate the interactions between the particles and hence transform under the adjoint representation of the gauge group. Gauge symmetries are the basis of describing the fundamental interactions of nature, called gauge theories.

An example of a gauge theory that is realised in nature is the **Standard Model** (SM), which is a gauge theory based on the group $G_{\text{SM}} := SU(3)_C \otimes SU(2)_L \otimes U(1)_Y$. The first simple group is for the *strong* interaction described by quantum chromodynamics (QCD). The product of the two remaining groups $SU(2)_L \otimes U(1)_Y$ forms the Weinberg-Salam *electroweak* (EW) model [3–5], where $SU(2)_L$ describes the weak interaction which only couples to *left handed* fermions and $U(1)_Y$ is the weak hypercharge Y gauge group, defined by the formula

$$Y = 2(Q - T_3). \quad (2.1)$$

Where Q is the electric charge and T_3 is the third component of the weak isospin. A description of the matter content of the SM and their multiplicities with respect to G_{SM} is shown in Table 2.1

The SM has been very successful at describing particle interactions even when challenged by numerous precision tests at LEP and SLD [67–70]. Later at DØ [71] and the LHC [72, 73] Nevertheless, it fails to describe the ground state if only the fermion and gauge sectors are considered. This shortcoming is that the W^\pm and Z bosons are massive. This violates the EW gauge symmetry. This can be easily seen by looking at the mass term of a spin one field B_μ^A

$$\mathcal{L} = m_B B^{A,\mu} B_\mu^A, \quad (2.2)$$

and performing an $SU(N)$ gauge transformation

$$B_\mu^A \rightarrow B_\mu^A + \partial_\mu \Lambda^A + g \varepsilon_{BC}^A B_\mu^B \Lambda^C. \quad (2.3)$$

¹Gauge theories based on finite groups have been proposed in the literature, but their phenomenological significance is yet to be further investigated [64, 65]

Particle/Field	G_{SM} multiplicity	mass [GeV]
Quarks		
$Q = (u_L), (d_L), (c_L), (s_L), (t_L), (b_L)$	$(\mathbf{3}, \mathbf{2})_{\frac{1}{6}}$	$m_u = 2.16 \cdot 10^{-3}, m_d = 2.67 \cdot 10^{-3}$
$U = u_R, c_R, t_R$	$(\mathbf{3}, \mathbf{1})_{\frac{2}{3}}$	$m_c = 0.93 \cdot 10^{-2}, m_s = 1.27$
$D = d_R, s_R, b_R$	$(\mathbf{3}, \mathbf{1})_{-\frac{1}{3}}$	$m_t = 172.4, m_b = 4.18$
Leptons		
$L = (\nu_{e,L}), (\nu_{\mu,L}), (\nu_{\tau,L})$	$(\mathbf{1}, \mathbf{2})_{-\frac{1}{2}}$	$m_e = 0.511 \cdot 10^{-3}, m_\mu = 1.05 \cdot 10^{-2}$
$E = e_R, \mu_R, \tau_R$	$(\mathbf{1}, \mathbf{1})_{-1}$	$m_\tau = 1.77, m_\nu = ??$
Gauge bosons		
$g/G_\mu^A, A = 1 \dots 8$	$(\mathbf{8}, \mathbf{1})_0$	0.0
γ/A_μ	$(\mathbf{1}, \mathbf{1})_0$	0.0
W_μ^\pm	$(\mathbf{1}, \mathbf{3})_0$	80.379
Z_μ	$(\mathbf{1}, \mathbf{3})_0$	91.1876
The Higgs boson		
h	$(\mathbf{1}, \mathbf{2})_{\frac{1}{2}}$	125.10

Table 2.1. The SM constituents, their multiplicities with respect to the SM gauge group $G_{\text{SM}} := SU(3)_C \otimes SU(2)_L \otimes U(1)_Y$ and masses. The mass of the neutrinos ν is zero according to the SM prediction, but observations suggest that they are massive, and only the difference between the three masses is known [66]. The values of the masses are taken from the Particle Data Group (PDG) [63], and used throughout this thesis.

We see that the mass term does not preserve gauge symmetry. Secondly, because the SM is a chiral theory, only left-handed fermions are doublets under $SU(2)_L$. Thus, the Dirac mass term

$$\mathcal{L}_D = m_D \bar{\psi}_L \psi_R + \text{h.c.}, \quad (2.4)$$

cannot be a singlet under $SU(2)_L$, this again violates the EW symmetry. Despite quark and lepton masses being forbidden by the EW symmetry, we have already measured them, and since they also carry charges, this mass has to come from a Dirac mass term.

For the EW model to be consistent in the ground state like it is in the interaction states. A mechanism for spontaneous symmetry breaking (SSB) needed to be introduced.

2.1.1 Nambu-Goldstone theorem

Coming back to the example of the paramagnetic-ferromagnetic materials, when a ferromagnetic metal is heated above a certain temperature, known as the Curie Temperature T_C , it will undergo a phase transition and become paramagnetic. In the mean-field theory approximation, the magnetic susceptibility is related to the temperature of the metal via the relation

$$\chi_B \sim (T - T_C)^{-\gamma}, \quad (2.5)$$

where γ is called a critical exponent. We see that if the metal temperature is $T > T_C$; the metal is in an *disordered phase* and when it is $T < T_C$, the metals becomes in the *ordered phase*, i.e. χ_B is the order parameter of this system. At the Curie temperature, the system will be at the *critical point*, and the susceptibility is divergent. The exponent γ cannot be used to describe the system at the critical point.

There is a “pictorial” description of the metal at the critical point, which helps understand the Nambu-Goldstone theorem. Starting at $T > T_C$, the metal would be in a paramagnetic phase, where the spins are randomly arranged. As the temperature becomes lower and lower, thermal fluctuations start to lessen. In some regions of the metal, the spins will start to get aligned. With continued cooling, nearing T_C , these turned spins will affect their neighbours by flipping their direction. At the critical point $T = T_C$, the system behaves peculiarly when one would see regions of spins in “up” and others in “down” directions. The system will resemble a fractal of these regions, becoming scale-invariant. Additionally, waves of oscillating local magnetisation will propagate. These waves, or spinless quasiparticles (called Magnons), are Goldstone bosons emerging from SSB that manifests at $T < T_C$ as the spins will be arranged in a certain single direction and the metal becomes ferromagnetic.

The Nambu-Goldstone theorem

When a continuous symmetry has a conserved current but broken in the ground state (vacuum) is called to be spontaneously broken. A scalar boson is associated with each broken generator of this spontaneously broken symmetry. The modes of these bosons are fluctuations of the order parameter.

This theorem first emerged from condensed matter physics, particularly superconduc-

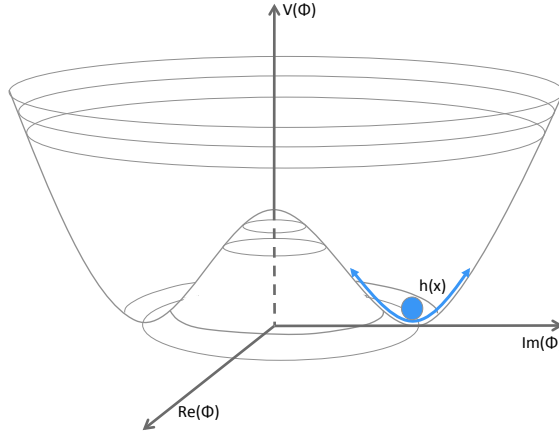


Figure 2.2. The characteristic shape of the Higgs potential showing a non-zero vacuum. The physical Higgs boson is an oscillation within the energy well illustrated in the diagram with blue arrows., this illustration is taken from [78].

tors [74, 75]. However, it soon got applied to relativistic quantum field theories [76].

2.2 The Braut-Englert-Higgs mechanism

To solve the aforementioned shortcomings of the Weinberg-Salam model, the Nambu-Goldstone theorem has been first proposed by P. W. Anderson [77]. However, the way that Anderson formulated his theory was unfamiliar to particle physicists and used a non-relativistic picture to illustrate how photons could gain mass in an electron plasma with a plasma frequency ω_p

$$m_\gamma^{\text{plasma}} = \frac{\hbar\omega_p}{c^2} \quad (2.6)$$

Later on, a theory that explains the mass generation of the EW gauge bosons was published in an almost simultaneous manner by R. Braut and F. Englert [6], P. Higgs [7, 8] and G. Guralnik, C. R. Hagen, and T. Kibble [9, 10]². The Higgs mechanism starts by considering the SSB of the electroweak sector of the SM via the pattern

$$SU(2)_L \otimes U(1)_Y \longrightarrow U(1)_Q \quad (2.7)$$

This is achieved by the vacuum expectation value (vev) of a complex scalar field $\phi \sim$

²All of these authors have contributed to the theory of SM (SSB). By calling it the “Braut-Englert-Higgs” mechanism or the “Higgs” boson. I, by no means, have intended to ignore the role played by the rest; rather, I wanted to stick to the most widely-used terminology in the field.

$(\mathbf{1}, \mathbf{2}, +1/2)$, with the Lagrangian

$$\mathcal{L} = D_\mu \phi^* D^\mu \phi - V[\phi], \quad V[\phi] := \mu^2 \phi^* \phi + \lambda (\phi^* \phi)^2, \quad (2.8)$$

with $V[\phi]$ denoting the Higgs potential, illustrated in Figure 2.2, and generating a non-vanishing vacuum for $\mu^2 < 0$. The field ϕ is given explicitly by

$$\phi = \begin{pmatrix} \phi^1 + i\phi^2 \\ \frac{1}{\sqrt{2}}(h + v) - i\phi^3 \end{pmatrix} \quad (2.9)$$

The covariant derivative

$$D_\mu = \partial_\mu - ig_2 \frac{\sigma_a}{2} W_\mu^a - ig_1 \frac{1}{2} B_\mu, \quad (2.10)$$

dictates the coupling between the Higgs field and the EW gauge bosons and g_3 , g_2 and g_1 are, respectively, the coupling constants of $SU(3)_C$, $SU(2)_L$ and $U(1)_Y$. The minimum of the scalar potential is obtained by

$$\frac{\partial V}{\partial \phi} |_{\phi \rightarrow v} = 0, \quad (2.11)$$

which for a tachyonic mass $\mu^2 < 0$ will have a real non-vanishing values v corresponding to the vev of this field $\langle \phi \rangle = \begin{pmatrix} 0 \\ \frac{v}{\sqrt{2}} \end{pmatrix}$.

According to the Nambu-Goldstone theorem, the three broken generators of $SU(2)_L \otimes U(1)_Y$ will become massive, and they are the W^\pm and Z bosons, while the photon will remain massless. We will have three massless Goldstone bosons $G^\pm = \frac{1}{2}(\phi^1 \pm i\phi^2)$ and $G^0 = \phi^3$ that are “eaten” by those as mentioned earlier massive W^\pm and Z bosons, where these Goldstone bosons become the longitudinal polarisations of W^\pm and Z . To see this more concretely, we start by looking at the terms of the EW Lagrangian, where the field ϕ couples to the gauge bosons in the unbroken phase

$$D_\mu \phi^* D^\mu \phi = \frac{1}{2} |\partial_\mu \phi|^2 + \frac{1}{8} g_2^2 |\phi|^2 |W_\mu^1 + iW_\mu^2|^2 + \frac{1}{8} |\phi|^2 |g_2 W_\mu^3 - g_1 B_\mu|^2. \quad (2.12)$$

After SSB, we have the gauge bosons in the mass basis

$$\begin{aligned} W_\mu^\pm &= \frac{1}{\sqrt{2}}(W_\mu^1 \pm iW_\mu^2), \\ Z_\mu &= \frac{1}{\sqrt{g_1^2 + g_2^2}} (g_2 W_\mu^3 - g_1 B_\mu), \\ A_\mu &= \frac{1}{\sqrt{g_1^2 + g_2^2}} (g_2 W_\mu^3 + g_1 B_\mu). \end{aligned} \quad (2.13)$$

From this, the electric charge is identified as the coupling constant to the photon A_μ

$$e = \frac{g_1}{\sqrt{g_1^2 + g_2^2}}. \quad (2.14)$$

It is useful to define the Weinberg angle θ_W , an important EW parameter relating the electric charge to the weak coupling g_2

$$\sin \theta_W = \frac{e}{g_2} \approx 0.231214, \quad (2.15)$$

typically the sin and cos of the Weinberg angle are denoted by s_W and c_W , respectively. We use the unitary gauge, to absorb the Goldstone bosons into the W^\pm and Z longitudinal polarisations. In this gauge the Higgs doublet can be written as

$$\phi \rightarrow \begin{pmatrix} 0 \\ \frac{1}{\sqrt{2}}(h + v). \end{pmatrix}, \quad v = 246 \text{ GeV}. \quad (2.16)$$

With these substitutions, one can read off the masses of the gauge bosons from their bilinear terms in (2.12)

$$m_W = \frac{v g_2}{2} \quad m_Z = \frac{v}{2} \sqrt{g_1^2 + g_2^2} \quad m_A = 0. \quad (2.17)$$

Since ϕ is a complex scalar doublet, it has four components, three of which correspond to the Goldstone bosons; one remains as a physical field $h(x)$, which is identified as the “Higgs boson” discovered in the Summer of 2012 [1, 2]. The couplings between the Higgs boson and the electroweak bosons are related to their mass via the vev

$$g_{hVV} = \frac{2m_V^2}{v}, \quad g_{hhVV} = \frac{2m_V^2}{v^2}. \quad (2.18)$$

By substituting (2.16), into the Higgs potential (2.8) one can also write the mass of the physical Higgs boson in terms of the vev

$$m_h = \sqrt{2\lambda}v. \quad (2.19)$$

The Higgs boson mass is related to the μ parameter via the relation

$$m_h^2 = -2\mu^2, \quad (2.20)$$

One can see that the mass term after SSB changes its sign, characterising the order parameter for this system, analogous to the magnetic susceptibility for the magnetisation of materials example. One could also identify the self-couplings of h , the trilinear and

quartic couplings

$$g_{hhh} = 3\lambda v = 3\frac{m_h^2}{v}, \quad g_{hhhh} = 3\lambda = 3\frac{m_h^2}{v^2}. \quad (2.21)$$

2.3 Yukawa interaction

It is possible to also use the Higgs vev to give fermions their masses by introducing Yukawa-interaction terms, first introduced by S. Weinberg [5]

$$\mathcal{L}_{\text{Yuk}} = -y_e \bar{L} \phi E - y_d \bar{Q} \phi D - y_u \bar{Q} \tilde{\phi} U + \text{h.c.}, \quad (2.22)$$

with $\tilde{\phi} = i\sigma_2\phi$ and y_e, y_d, y_u are 3×3 matrices. These matrices are free parameters in the SM. As the Higgs boson acquires a vev, the fermions will acquire a mass $m_f = vy'_f$ and the Higgs boson coupling to the fermions is given by

$$g_{h\bar{f}f} = \frac{m_f}{v}, \quad (2.23)$$

and the Yukawa matrices will be fixed in the mass basis y'_f by measurements of the fermion masses.

Leptonic Yukawa matrix is diagonal, with a degeneracy between the flavour and mass basis, this manifests as lepton family number conservation. That is, the lepton family operator commutes with the Hamiltonian. However, for the quarks, the situation is more complicated. One can rotate these matrices to the mass basis via a bi-unitary transformation via the unitary matrices $\mathcal{V}_q, \mathcal{U}_q$ for $q = u, d$

$$y_q \longrightarrow y'_q = \mathcal{V}_q^\dagger y_q \mathcal{U}_q = \text{diag}(m_{q1}, m_{q2}, m_{q3}). \quad (2.24)$$

The is no degeneracy here as the Hamiltonian does not commute with the quark flavour operator. The transformation matrices for the up and down-type quarks are not the same. The charged EW quark currents contain flavour mixing described by the Cabibbo-Kobayashi-Maskawa (CKM) matrix [79, 80]. Figure 2.3 shows all the SM couplings' strengths, with the thickness of the chord is proportional to the strength of the coupling; the Higgs couplings are highlighted in orange. In this figure, one cannot easily see Higgs coupling to the fermions, except for its couplings to the third generation. Strictly speaking, if we further examined the Yukawa coupling using a logarithmic scale and focused on the quark sector as Figure 2.4 illustrates. These Yukawa couplings span about six orders of magnitude with a marked hierarchy. These couplings are, in fact, free parameters in the SM and only determined by the experimental measurements of the quark masses. This hierarchy of quark masses, therefore, cannot be explained by the SM Braut-Englert-Higgs mechanism and is sometimes known as the “old” flavour puzzle. In later chapters, we will examine the experimental effort to measure these couplings better and how Higgs pair production can be used to probe them in chapter 9. Even the potential of using techniques from *interpretable machine learning* to further improve

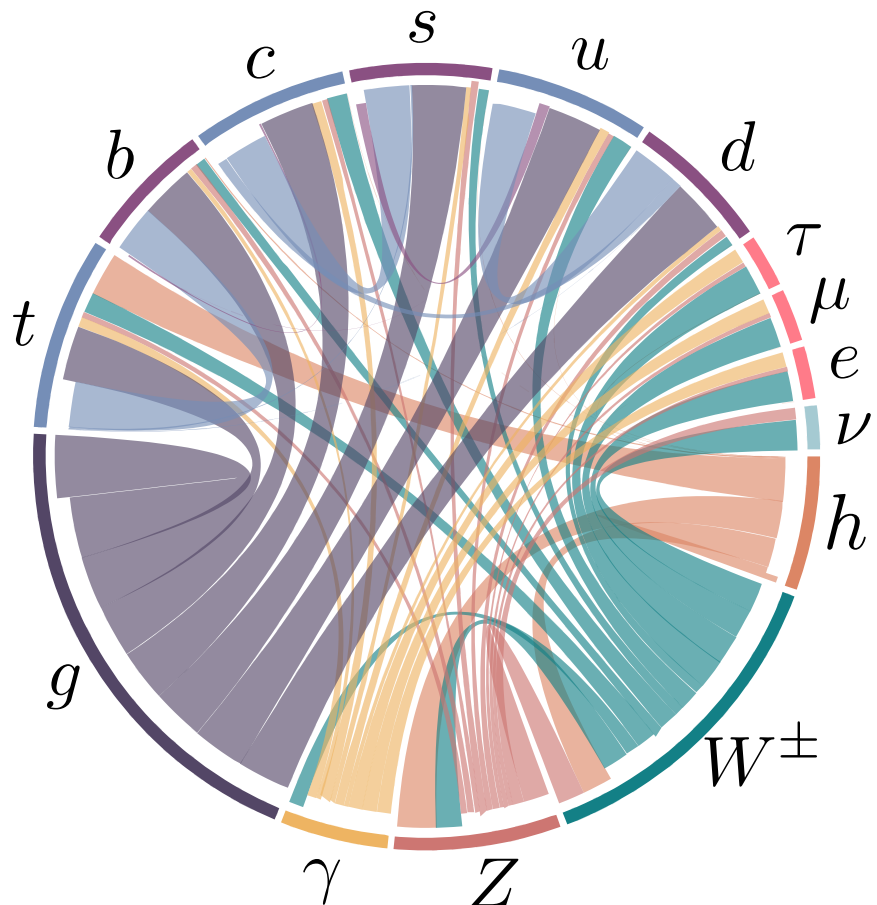


Figure 2.3. A chord diagram showing the SM couplings, with the coupling strength illustrated by the chord thickness. Higgs couplings are coloured in orange.

Higgs pair sensitivity to probing light quarks Yukawa couplings.

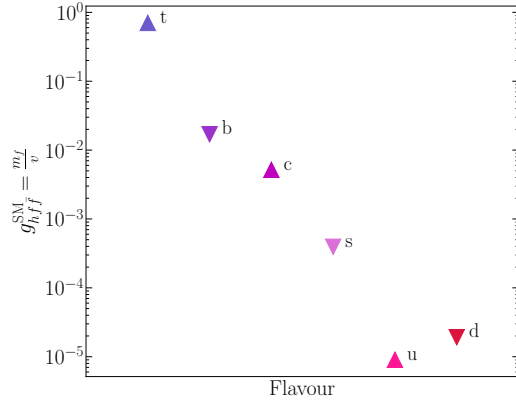


Figure 2.4. The SM Yukawa couplings are proportional to the quark masses because the Higgs Yukawa couplings span about 6 orders of magnitude, as seen in the case of quarks here. The SM cannot explain this large hierarchy.

2.4 The Higgs and EW precision observables

One of the most valuable sources for studying new physics (NP) above the EW scale is provided by indirect tests of the SM via the so-called EW precision observables (EWPO). These include, in particular, the very precise measurements at the Z pole performed at the Large Electron-Positron collider (LEP) and the Stanford Linear Collider (SLC). In corroboration with the Higgs boson discovery and the experimental information collected at LHC and Tevatron, they provide strong constraints on theories beyond the SM (BSM) that lead to significant deformations of the standard EW sector [38, 78, 81–88].

Higgs physics is deeply intertwined with the EW sector as many of the Higgs parameters are linked to EWPO. For instance, the Higgs vev is determined from Fermi's constant $v = (\sqrt{2}G_F)^{-1/2}$, which is in turn fixed by the muon lifetime τ_μ measurements [89–92]. This can be seen when we examine the theoretical prediction for τ_μ

$$\tau_\mu^{-1} = \frac{G_F^2 m_\mu^5}{192\pi^3} \left(1 - \frac{8m_e^2}{m_\mu}\right) \left[1 - 1.810 \frac{\alpha}{\pi} + (6.701 \pm 0.002) \left(\frac{\alpha}{\pi}\right)^2\right], \quad (2.25)$$

then comparing this formula with the experimental measurements of τ_μ . This confrontation leads to a very precise measurement on G_F [63]

$$G_F = 1.1663787(6) \cdot 10^{-5} \text{ GeV}^{-2}, \quad (2.26)$$

given the value of the fine structure constant $\alpha^{-1} = 137.03599976(50)$.

Another important EWPO is the ratio between the W and Z masses

$$\rho = \frac{m_W^2}{c_W^2 m_Z^2}. \quad (2.27)$$

At leading order (LO), this parameter is equal to unity in the SM. The ρ parameter depends on the representation of the scalar sector of the EW model. If one supplements the SM EW sector with ϕ_i scalars having T_i weak isospin and $T_{3,i}$ being its third component; each of these scalars acquires a vev v_i . Then the ρ parameters can be estimated based on these properties via the relation [93, 94]

$$\rho = \frac{\sum_i [T_i(T_i + 1) - T_{3,i}^2] v_i^2}{2 \sum_i T_{3,i}^2 v_i^2}. \quad (2.28)$$

From (2.28) one can see that a real triplet scalar, for instance, would not fit the experimental EW measurement of ρ . Rather, a complex doublet is the simplest scalar possible for the EW symmetry breaking.

Radiative corrections to the EW gauge bosons mass from vacuum polarisation diagrams could potentially cause ρ to deviate significantly from unity. This is not the case, as the experimentally measured value of ρ [63] of:

$$\rho_{\text{exp}} = 1.00038 \pm 0.00020 \quad (2.29)$$

Additionally, it is possible to think of an extended Higgs sector, where there are multiple scalars with different $SU(2)_L$ multiplicities. Or a composite Higgs sector, in which the Higgs boson is a pseudo-Nambu-Goldstone boson, cf. [95, 96]. How can such models be built assuring the ρ parameter is protected from change? The answer to this question lies in a symmetry of the Higgs Lagrangian known as custodial symmetry.

2.4.1 Custodial symmetry

After SSB, a residual global symmetry known as the custodial symmetry protects the ρ parameter from obtaining large radiative corrections at higher orders in perturbation theory. This symmetry must be kept in extended or composite Higgs models, in order to “survive” the current experimental constraints. This symmetry can be seen by rewriting the Higgs potential as

$$V = \frac{\lambda}{4} \left(\phi_1^2 + \phi_2^2 + \phi_3^2 + \phi_4^2 - 2\mu^2 \right)^2. \quad (2.30)$$

This potential is invariant under $SO(4) \simeq SU(2)_L \otimes SU(2)_R$ rotations. However, when the Higgs field acquires a non-vanishing vev, $\phi_4 \rightarrow h + v$, the potential becomes

$$V = \frac{\lambda}{4} \left(\phi_1^2 + \phi_2^2 + \phi_3^2 + h^2 + 2vh + v^2 - 2\mu^2 \right)^2, \quad (2.31)$$

which is only invariant under $SO(3) \simeq SU(2)_V$ transformations, i.e. the diagonal part of the original group. This global SSB pattern comes alongside the EW-SSB of the gauge group $SU(2)_L \otimes U(1)_Y$ as global $SU(2)_L$ is itself the gauged $SU(2)_L$ group. Additionally, the T_3 component of the $SU(2)_R$ global group is the gauged $U(1)_Y$, and the T^3 component of the custodial group $SU(2)_V$ is gauged as well and identified to be the electric charge operator, i.e. the generator of $U(1)_Q$.

$$\underbrace{SU(2)_R}_{\supset U(1)_Y} \otimes \overbrace{SU(2)_L}^{\text{gauged}} \longrightarrow \underbrace{SU(2)_V}_{\supset U(1)_Q}. \quad (2.32)$$

This pattern indicates that the symmetry is already broken by the gauging of the diagonal part of $SU(2)_R$ (the hypercharge). The custodial symmetry is only *approximate* in the limit of $g_1 \rightarrow 0$, and $\rho = 1$ is a consequence of $g_1 \neq 0$. The symmetry breaking pattern $\mathbf{2} \otimes \mathbf{2} = \mathbf{3} \oplus \mathbf{1}$ also allows us to identify the Goldstone bosons as the custodial triplet and the physical Higgs h as the custodial singlet, explaining the electric charge pattern they have.

We could use the isomorphism between the special orthogonal and special unitary groups to parametrise the Higgs doublet as an $SU(2)_L \otimes SU(2)_R$ bidoublet

$$\mathcal{H} = (\tilde{\phi} \ \phi) = \frac{1}{\sqrt{2}} \begin{pmatrix} \phi_4 - i\phi_3 & \phi_1 + i\phi_2 \\ \phi_1 - i\phi_2 & \phi_4 + i\phi_3 \end{pmatrix}, \quad (2.33)$$

with the bi-unitary transformations

$$\mathcal{H} \longrightarrow \mathcal{U}_L \mathcal{H} \mathcal{U}_R^\dagger, \quad (2.34)$$

which leaves any traces of the form $\text{Tr}(\mathcal{H}^\dagger \mathcal{H})$, invariant. The Higgs potential could be rewritten in terms of the bidoublet

$$V = -\frac{\mu^2}{2} \text{Tr}(\mathcal{H}^\dagger \mathcal{H} + \frac{\lambda}{4} (\text{Tr}(\mathcal{H}^\dagger \mathcal{H}))^2) \quad (2.35)$$

The vev is hence written in this representation as

$$\langle \mathcal{H} \rangle = \frac{v}{\sqrt{2}} \mathbb{1}_{2 \times 2}. \quad (2.36)$$

We can also look at the Yukawa sector, and observe that in the case where $y_u = y_d = y$, we can also write the left-handed and right-handed quarks as $SU(2)_L \otimes SU(2)_R$ bidoublets and $SU(2)_R$ doublets, respectively. Hence, the quark part of the Yukawa Lagrangian in (2.22) becomes

$$\mathcal{L}_{yuk} \supset \frac{y}{\sqrt{2}} (\bar{u}_L \ \bar{d}_L) \begin{pmatrix} \phi_4 - i\phi_3 & \phi_1 + i\phi_2 \\ \phi_1 - i\phi_2 & \phi_4 + i\phi_3 \end{pmatrix} \begin{pmatrix} u_R \\ d_R \end{pmatrix}, \quad (2.37)$$

which is invariant under custodial transformations, but when $y_u \neq y_d$, this Lagrangian term breaks custodial symmetry. Thus, the differences between the up-type and down-type quark masses $m_u - m_d$ are considered **spurions** of the custodial symmetry and one expects to see radiative corrections to ρ being proportional to these spurions.

This can be shown concretely by examining the radiative corrections that could lead to a deviation of ρ from unity ($\Delta\rho$). These corrections are known as the **oblique correction** that come from electroweak vacuum polarisations $\Pi_{VV}(p^2)$, as shown in Figure 2.5, for more details on these corrections and their calculation see refs.. [97, 98]

The one-loop correction to the ρ parameter is given in terms of the Π_{VV} by

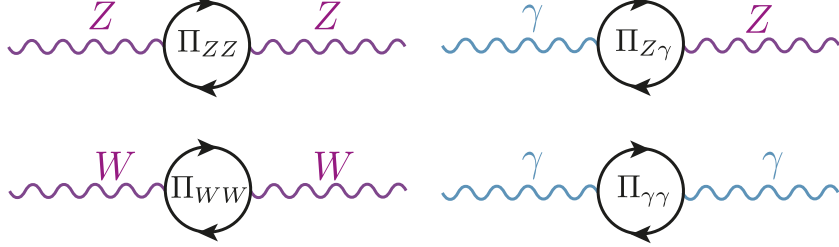


Figure 2.5. The oblique corrections, are radiative correction with electroweak gauge bosons propagators. Namely, the vacuum polarisations of the Z , W^\pm and γ bosons.

$$\Delta\rho = \frac{\Pi_{WW}(0)}{m_W^2} - \frac{\Pi_{ZZ}(0)}{m_Z^2}. \quad (2.38)$$

The dominant contributions are given by [99]

$$\Delta\rho = \frac{3G_F}{8\sqrt{2}\pi^2} \left((m_t^2 - m_b^2) - \frac{2m_t^2 m_b^2}{m_t^2 - m_b^2} \ln \frac{m_t^2}{m_b^2} \right) + \dots . \quad (2.39)$$

Since $m_b \ll m_t$, the correction is non-vanishing, and (2.39) shows clearly how the radiative corrections are proportional to the spurions of the custodial symmetry. However, this radiative correction is absorbed into the SM definition of ρ , i.e. the $\overline{\text{MS}}$ definition of the ρ -parameter $\rho^{\overline{\text{MS}}}$.

One can study NP effects violating the custodial symmetry by looking at deviations from $\rho = 1$ coming from the NP degrees of freedom. Given the experimentally measured value of ρ (2.29), many NP models violating this symmetry can already be excluded. Nevertheless, ρ alone does not capture the full story of EWPO. For instance, adding a new quark doublet would not necessarily violate the custodial symmetry though it still can be excluded by EWPO. It is hence useful to introduce new parameters known as the **oblique parameters** [98, 100–103] ³

³The are also called the Peskin–Takeuchi parameters, however, W. Marciano and J. Rosner also D. Kennedy and P. Langacker published the same parametrisation proposals almost simultaneously. Therefore, I preferred not to use this eponym instead of calling them the oblique parameters, as they stem from the oblique corrections.

The oblique parameters

$$\begin{aligned}
 S &:= \frac{4c_W^2 s_W^2}{\alpha} \left[\frac{\Pi_{ZZ}^{\text{NP}}(m_Z^2) - \Pi_{ZZ}^{\text{NP}}(0)}{m_Z^2} - \frac{c_W^2 - s_W^2}{c_W s_W} \frac{\Pi_{Z\gamma}^{\text{NP}}(m_Z^2)}{m_Z^2} - \frac{\Pi_{\gamma\gamma}^{\text{NP}}(m_Z^2)}{m_Z^2} \right], \\
 T &:= \frac{\rho^{\overline{\text{MS}}} - 1}{\alpha} = \frac{1}{\alpha} \left[\frac{\Pi_{WW}^{\text{NP}}(0)}{m_W^2} - \frac{\Pi_{ZZ}^{\text{NP}}(0)}{m_Z^2} \right], \\
 U &:= \frac{4s_W^2}{\alpha} \left[\frac{\Pi_{WW}^{\text{NP}}(m_W^2) - \Pi_{WW}^{\text{NP}}(0)}{m_W^2} - \frac{c_W}{s_W} \frac{\Pi_{Z\gamma}^{\text{NP}}(m_Z^2)}{m_Z^2} - \frac{\Pi_{\gamma\gamma}^{\text{NP}}(m_Z^2)}{m_Z^2} \right] - S.
 \end{aligned} \tag{2.40}$$

The NP contributions to the EW vacuum polarisations $\Pi_{VV}^{\text{NP}}(p^2)$ could either come from loop or tree-level effects. Typically both T and U are related to custodial symmetry violation. However, U has an extra suppression factor of m_{NP}^2/m_Z^2 compared to T and S . The most recent fit result for these parameters is [63]

$$\begin{aligned}
 S &= -0.01 \pm 0.10, \\
 T &= 0.03 \pm 0.13, \\
 U &:= 0.02 \pm 0.11.
 \end{aligned} \tag{2.41}$$

But since T and S tend to give stronger constraint on NP, as they do not suffer from the suppression that U has. One can perform a two-parameter fit of S and T setting $U = 0$; the most recent fit is shown in Figure 2.6, with the best fit values [63],

$$\begin{aligned}
 S &= 0.00 \pm 0.07, \\
 T &= 0.05 \pm 0.06.
 \end{aligned} \tag{2.42}$$

The oblique parameters are important in constraining effective operators in the Higgs sector, namely

$$\begin{aligned}
 \mathcal{O}_S &= \phi^\dagger \sigma_i \phi W_{\mu\nu}^i B^{\mu\nu}, \\
 \mathcal{O}_T &= |\phi^\dagger D_\mu \phi|^2.
 \end{aligned} \tag{2.43}$$

For example, \mathcal{O}_S appears in Technicolour models causing large deviations of S [101, 104–106]. Moreover, constraints on the T parameter are important for top mass generation as well as modifications to $Zb\bar{b}$ coupling in such models [107, 108]. We will revisit these operators when we discuss the Higgs and effective field theories in chapter 4.

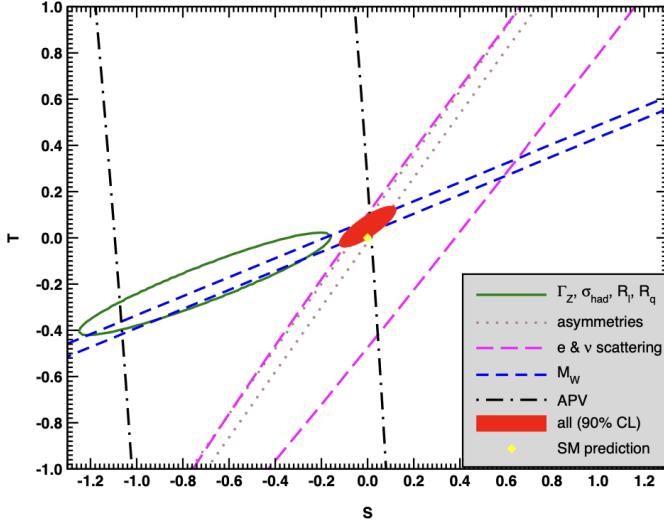


Figure 2.6. Fit results from various EWPO's for T and S setting $U = .$ The contours show 1σ contours (39.35% for closed contours and 68% for the rest). This plot is obtained from the PDG [63].

2.5 Theoretical constraints on the Higgs

2.5.1 Electroweak precision data fits

Even prior to the Higgs boson discovery at LHC, many theoretical aspects of the Higgs sector provided relatively strong bounds on the Higgs properties, particularly its mass. For instance, using the EWPO measurements at LEP provided input for a fit based on radiative effects coming from the Higgs boson to such observables [67] as in diagram (a) of Figure 2.7, the bounds improved with the improvements of EWPO measurements, these bounds were known as the “blue band” plots seen with their progression in Figure 2.8.

2.5.2 Partial-wave unitarity

Another bound on Higgs mass emerged from studying the longitudinally polarised elastic scattering amplitudes of the EW vector bosons $V_L V_L \rightarrow V_L V_L$ at high energies $E \gg m_W$, where the Goldstone equivalence theorem holds [109], see diagrams (b) in Figure 2.7. This bound comes from applying the partial wave perturbative unitarity on the EW boson scattering amplitude. I will derive here this bound starting from the **Optical theorem**, which is a direct result from the unitarity of the **S** matrix.

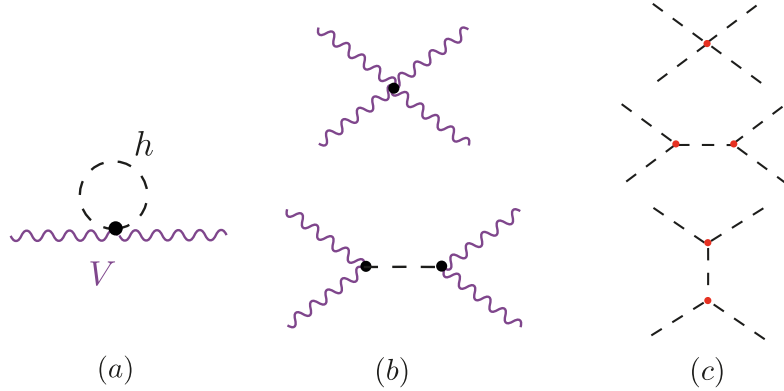


Figure 2.7. Diagrams contributing to theoretical bounds on the Higgs, (a) shows an example of radiative corrections to EWPO from the Higgs boson. The diagrams in (b) show an elastic scattering of EW vector bosons leading to a bound on the Higgs mass from perturbative unitarity, similarly in (c) diagrams for $hh \rightarrow hh$ scattering leading to constraints on Higgs self-coupling.

The optical theorem

Let \mathcal{M}_{aa} be a covariant matrix element for an elastic scattering process for a particle a : $a \rightarrow a$, then the following relation applies

$$\sum_f \int d\Phi_n(p_a, p_i^f) |\mathcal{M}_{af}|^2 = 2\Im(\mathcal{M}_{aa}), \quad (2.44)$$

where the sum is over all intermediate n -particle states f with momenta p_i^f and $d\Phi_n(p_a, p_i^f)$ is the n -particle phase space.

If we only consider a $2 \rightarrow 2$ process with momentum states. $| p_1, p_2 \rangle \rightarrow | k_1, k_2 \rangle$, then

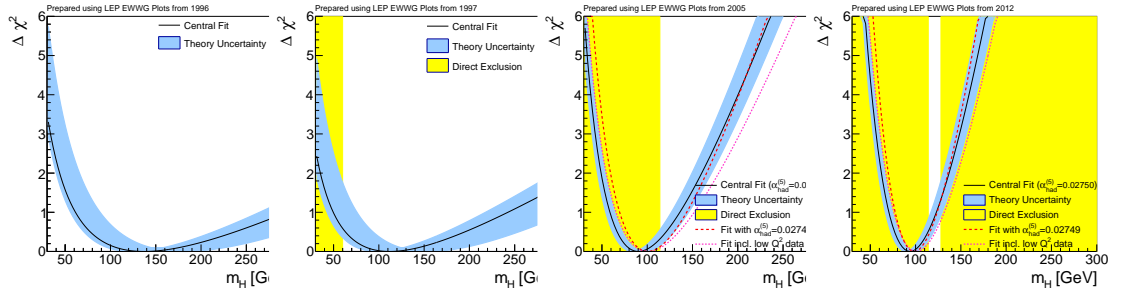


Figure 2.8. Progression of the “blue band” plots with LEP data from 1996 up to 2012 prior to the announcement of the Higgs boson discovery. These plots were taken from [78], based on data from LEP [67].

the LHS of (2.44), after expanding the two-particle phase space, simplifies to

$$\begin{aligned} & \int \frac{d^3 k_1}{(2\pi)^3 2E_1} \int \frac{d^3 k_2}{(2\pi)^3 2E_2} (2\pi)^4 \delta^4(p_1 + p_2 - k_1 - k_2) |\mathcal{M}(s, t)|^2, \\ &= \frac{1}{16\pi} \int_{-1}^1 d(\cos \theta) |\mathcal{M}(s, t)|^2, \end{aligned} \quad (2.45)$$

with the Mandelstam variables

$$\begin{aligned} s &= k_1 + k_2, \\ t &= k_1 - p_1, \\ u &= k_1 - p_2, \\ s + t + u &= 4m^2. \end{aligned} \quad (2.46)$$

Using the relation between the Mandelstam variable t , and the scattering angle θ :

$$t = \frac{1}{2}(s - 4m^2)(\cos \theta - 1), \quad (2.47)$$

we could expand the matrix element $\mathcal{M}(s, t)$ in terms of *partial waves*, isolating s from the scattering angle dependence

$$\mathcal{M}(s, t) = 16\pi \sum_j (2j+1) a_j P_j(\cos \theta). \quad (2.48)$$

For each a_j is the j th partial wave amplitude, and $P_j(\cos \theta)$ is the corresponding Legendre polynomial:

$$P_j(z) = \frac{1}{j!} \frac{1}{2^j} \frac{d^j}{dz^j} (z^2 - 1)^j, \quad (2.49)$$

which satisfies the following conditions

$$\int_{-1}^1 dz P_j(z) P_k(z) = \frac{1}{2j+1} \delta_{jk}, \quad (2.50a)$$

$$P_j(1) = 1 \quad \forall j. \quad (2.50b)$$

Applying the aforementioned relations , one gets for the LHS of (2.44)

$$\begin{aligned}
 & \int \frac{d^3 k_1}{(2\pi)^3 2E_1} \int \frac{d^3 k_2}{(2\pi)^3 2E_2} (2\pi)^4 \delta^4(p_1 + p_2 - k_1 - k_2) |\mathcal{M}(s, t)|^2, \\
 &= \frac{1}{16\pi} \int_{-1}^1 d(\cos \theta) \left[16\pi \sum_j (2j+1) a_j(s) P_j(\cos \theta) \right] \times \\
 & \quad \left[16\pi \sum_k (2k+1) a_k^*(s) P_k(\cos \theta) \right], \\
 &= 32\pi \sum_j (2j+1) |a_j(s)|^2. \tag{2.51}
 \end{aligned}$$

Moreover, for the RHS of (2.44)

$$2\Im(\mathcal{M}_{aa}) = \underbrace{2\Im(\mathcal{M}(s, 0))}_{t \text{ is integrated out.}} = 32\pi \sum_j (2j+1) \Im(a_j(s)). \tag{2.52}$$

The partial-wave amplitudes $a_j(s)$ are hierachal, otherwise large cancellations are needed. Thus, we can compare the partial wave amplitudes term-by-term

$$|a_j(s)|^2 \leq \Im(a_j(s)) \Rightarrow \Re(a_j(s))^2 + \Im(a_j(s))^2 \leq \Im(a_j(s)). \tag{2.53}$$

Rearranging terms, we have

$$\Re(a_j(s)) + \left(\Im(a_j(s)) - \frac{1}{2} \right)^2 \leq \frac{1}{4}. \tag{2.54}$$

The partial wave amplitude must remain within the unitarity circle for the perturbation theory to be valid, i.e.

$$\Re(a_j(s)) \leq \frac{1}{2}. \tag{2.55}$$

This is known as the perturbative partial wave unitarity constraint.

When (2.55) is applied for $V_L V_L \rightarrow V_L V_L$ in the Goldstone boson equivalence theorem regime, in particular for $V = W$ boson, we get for the S -wave ($j = 0$) partial amplitude

$$a_0 \sim \frac{m_h^2}{16\pi v^2} \left(2 + \mathcal{O}\left(m_h^2/s\right) \right). \tag{2.56}$$

Looking at the asymptotic behaviour as $s \rightarrow \infty$, the following upper bound on the Higgs mass is obtained

$$\frac{m_h^2}{8\pi v^2} < \frac{1}{2} \Leftrightarrow m_h \leq 870 \text{ GeV}. \tag{2.57}$$

Indeed this bound is obsolete after the direct Higgs mass detection. However, it is very important to demonstrate the power of this technique in constraining the Higgs boson's parameters. This method can be applied to any elastic scattering with the Higgs being

the mediator, e.g. $ZZ \rightarrow ZZ$ and $WW \rightarrow ff$. Such processes can be used to constrain their corresponding couplings, i.e. g_{ZZh} , $g_{f\bar{f}h}$ and so on. An important bound can be derived by examining the Higgs elastic scattering $hh \rightarrow hh$ shown in (c) of Figure 2.7, in order to set bounds on Higgs self-interactions g_{hhh} and g_{hhhh} . This is what exactly has been done in ref. [110], where the authors have found that the S -wave partial amplitude for this process is given by

$$a_0 = -\frac{1}{2} \frac{\sqrt{s(s-4m_h^2)}}{16\pi s} \left[g_{hhh}^2 \left(\frac{1}{s-m_h^2} - 2 \frac{\log \frac{s-3m_h^2}{m_h^2}}{s-4m_h^2} \right) + g_{hhhh} \right], \quad (2.58)$$

which leads to unitarity bounds on the trilinear g_{hhh} and the quartic g_{hhhh} couplings of:

$$\left| g_{hhh}/g_{hhh}^{\text{SM}} \right| \lesssim 6.5, \quad \text{and} \quad \left| g_{hhhh}/g_{hhhh}^{\text{SM}} \right| \lesssim 65. \quad (2.59)$$

A more stringent constraint can be obtained by looking at the one-loop correction to the $hh \rightarrow hh$ scattering amplitude within the full kinematic range. The unitarity bound here is obtained by looking at the one-loop amplitude at the threshold, and is given by

$$\left| g_{hhhh}/g_{hhhh}^{\text{SM}} \right| \lesssim 6. \quad (2.60)$$

It should be noted that the unitarity bound on the trilinear coupling depends on the ansatz that was used for estimating the size of the NP contributions to the scattering amplitudes. These bounds are, hitherto, the strongest on these two couplings, even when compared to the ones coming from current experimental searches.

2.5.3 Other bounds

Further theoretical bounds can be obtained by studying quantum effects on the Higgs potential. For example, if we looked at the solution of the renormalisation group equation (RGE) for the Higgs self-coupling λ with the boundary condition $\lambda(v) = \lambda_0$ and ignoring other SM particle-contributions:

$$\lambda(Q^2) = \frac{\lambda_0}{1 - \frac{3}{4\pi^2} \log \frac{Q^2}{v^2}}. \quad (2.61)$$

We see that the running of λ will encounter a pole, known as Landau pole when the denominator vanishes. This will happen at the scale

$$Q_c = v e^{4\pi^2/3\lambda_0} = v e^{4\pi^2 v^2 / 3m_h^2}. \quad (2.62)$$

This indicates that the theory will break down at scales larger or equal to Q_c . Since the “critical scale” is a function of the Higgs mass, this allows to set an upper limit on the Higgs mass, assuming the SM will be valid up to a certain scale Q_c . This is known as **quantum triviality** constraint [111]. The reasoning behind such constraint stems

from the low energy behaviour of (2.61) leading to a vanishing interaction. If we want the Higgs Lagrangian to be perturbative for all scales, then λ has to be vanishing, and the theory becomes non-interacting or *trivial*.

Another bound coming from the RGE of λ is the **stability bound** that considers the stability of the Higgs potential given the running of λ ; requiring that the Higgs potential is an operator bounded from below. This bound is obtained by approximating the solution of the RGE at small λ

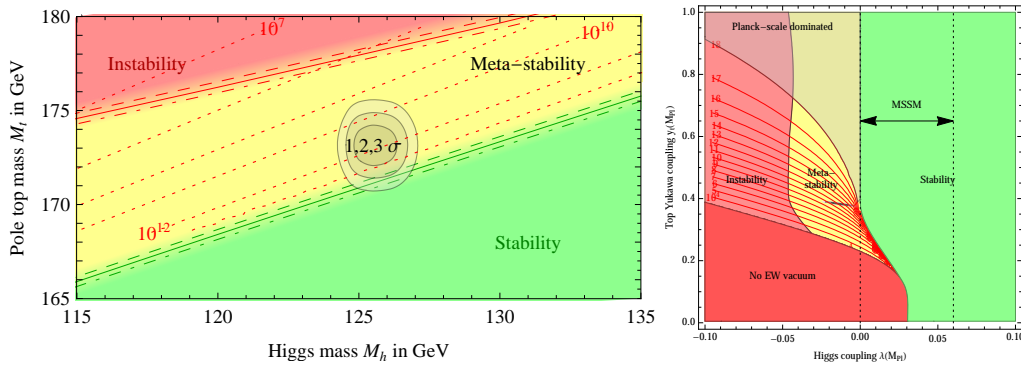
$$\lambda(Q^2) \sim \lambda_0 + \frac{1}{16\pi^2} \left[-\frac{12m_t^4}{v^4} + \frac{3}{16} (2g_2^4 + (g_2^2 + g_1^2)^2) \right] \log \frac{Q^2}{v^2}. \quad (2.63)$$

For the Higgs potential to be bounded from below, $\lambda(Q^2)$ ought to be positive, i.e. $\lambda(Q^2) > 0$. Since λ_0 can be expressed in terms of the mass, we get a bound on m_h from this condition

$$m_h^2 > \frac{v^2}{8\pi^2} \left[-\frac{12m_t^4}{v^4} + \frac{3}{16} (2g_2^4 + (g_2^2 + g_1^2)^2) \right] \log \frac{Q^2}{v^2}. \quad (2.64)$$

Leading to $m_h \approx 130$ GeV, assuming that the SM is valid up to the Grand Unified Theory (GUT) scale of $\sim 10^{16}$ GeV. Alternatively, the bound becomes $m_h \approx 180$ GeV for Q being at the Planck scale $\sim 10^{19}$ GeV.

More sophisticated calculations and discussion for the Higgs potential and vacuum stability has been a subject of great interest in pre- and post-Higgs discovery eras cf. [111–114]. The state-of-the-art calculation for the vacuum stability at two-loop level has been performed in ref. [115], in which, the authors have also included finite temperature effects to construct a phase diagram in the $m_t - m_h$ and $m_t - \lambda(M_{pl})$ planes as shown in Figure 2.9. It indicates that the measured Higgs mass is likely compatible with a metastable vacuum rather than absolute stability. This shows a finite probability for the Higgs vacuum (false vacuum) to decay into a lower energy state (true vacuum) via quantum tunnelling.



3 Experimental measurements of the Higgs boson

The observation of the Higgs boson, followed by the extensive measurement of its properties and couplings, has been on the top of the LHC programme priorities [116]. When this thesis was written, the particle physics community was celebrating a decade since the Higgs boson's discovery. Looking back ten years from now, when I have witnessed the discovery of the Higgs boson via a news press conference in the Summer of 2012 and decided to be a part of this enormous step that humanity has taken. I feel astonished by the progress made in understanding the last piece of the SM to be unravelled!

In this chapter, I will start with an overview of the extraordinary LHC and its experiments in section 3.1. Then, I will provide a state-of-the-art status review of the experimental measurements of the Higgs boson properties in section 3.2 and its cross-sections and couplings in section 3.3. An the end, I will discuss the challenges and outlook for the future runs of the LHC ???. The rest of the thesis will address a small part of these challenges.

3.1 Overview of the Large Hadron Collider

The Large Hadron Collider (LHC) is the largest particle accelerator in the CERN accelerators complex, with a circumference of about 26 km and over 9590 superconducting magnets that are cooled to 1.9 K. It was built as an upgrade the Large electron-positron collider (LEP), which ended its operation in the year 2000. The LHC contains four main experiments situated at the four beam crossing points: ATLAS, CMS, LHCb and ALICE. There are also smaller experiments such as LHCf, MilliQan, TOTEM and others. For more details about the LHC cf. [117, 118], or the LHC technical design report [119] for an in-depth review.

The LHC started operation in September 2008, with low energy proton beams, then gradually increased to an energy of 3.5 TeV per proton to reach a centre of mass energy of \sqrt{s} of 7 TeV. The data-taking period started in 2011. By 2012, its energy had increased to $\sqrt{s} = 8$ TeV and operated at this energy for about a year and a half, followed by a stopping its operation in mid-2013, concluding what is known as **Run-I**. In 2015, **Run-II** has started with almost double the energy $\sqrt{s} = 13$ TeV, and lasted for ca. 3 years. As this thesis is written, preparations are being made to get **Run-III** started and it will last until 2024. During these runs, heavier nuclei such as ^{207}Pb and ^{131}Xe have been collided either with protons or with themselves [120].

From, 2025 and beyond, the **High-Luminosity LHC** (HL-LHC) era will commence,

see Figure 3.2. The LHC will be shut down for extensive upgrades [121] to potentially increase its energy up to $\sqrt{s} = 14$ TeV and increase its collision rate; hence the name *high luminosity* is given for this operation period. This leads us to an important notion in particle physics phenomenology *integrated luminosity*.

The performance of a particle collider depends on many factors, but for phenomenological studies, like this thesis, the most important of which are the centre-of-mass energy \sqrt{s} and the integrated luminosity \mathcal{L} . This is mainly because particle-collider experiments are basically “counting experiments”. All of the discoveries or bounds on physical observables are obtained from the number of signal versus background events. In a collider, the number of expected events $N_{\text{exp}}^{\text{spec}}$ for a given resonance R and a subsequent decay final state X at any collider experiments is given by

$$N_{\text{exp}}^{\text{spec}} = \sigma(pp \rightarrow R) \text{BR}(R \rightarrow X) \mathcal{L} \epsilon_{\text{SEL}}. \quad (3.1)$$

Where ϵ_{SEL} is the selection efficiency, which depends on many factors like the detector geometry and particle identification performance etc., as well as the nature of signal at hand; it can be improved by better detected or selection cuts. The production cross-section increases typically quadratically with \sqrt{s} , hence comes the need for higher energies, but this can only be achieved by building new colliders from scratch. On the other hand, the integrated luminosity can be increased by running the experiment for a longer period of time without the need for a new collider. This is because the integrated luminosity is the time integral of the collider’s luminosity $L(t)$ over its operation time T

$$\mathcal{L} = \int^T L(t). \quad (3.2)$$

Therefore, we see that the integrated luminosity for the LHC experiments will increase over time as more collisions take place. Figure 3.1 shows the integrated luminosity for ATLAS and CMS experiments as it increases with each operation period of the LHC. Protons travel in the LHC in **bunches**, when these bunches cross, the protons inside of them collide at a certain frequency f . When two bunches with N_1 and N_2 protons per bunch, respectively collide, each bunch will have an effective cross-section $4\pi\sigma_i$ corresponding to their physical sizes $\sigma \sim 16 \mu\text{m}$, the luminosity is therefore given - approximately- by

$$L = \frac{f N_1 N_2}{4\pi\sigma_1\sigma_2}, \quad (3.3)$$

which is for the LHC averages to $\sim 10^{34}$ collisions $\text{cm}^{-2} \text{s}^{-1}$ [122, 123].

The total physics-viable pp -collisions integrated luminosity for Run-I was 4.57 fb^{-1} for 7 TeV and 20.3 fb^{-1} for 8 TeV (ATLAS [124]) and 5.55 fb^{-1} at 7 TeV and 21.8 fb^{-1} at 8 TeV (CMS [125]). As for Run-II the integrated luminosity is 139 fb^{-1} at 13 TeV (ATLAS [126]) and 137 fb^{-1} at 13 TeV (CMS [125]). The expected integrated luminosity by the end of Run-III is 300 fb^{-1} [127] and 3000 fb^{-1} by the end of the HL-LHC at energy of 14 TeV [121].

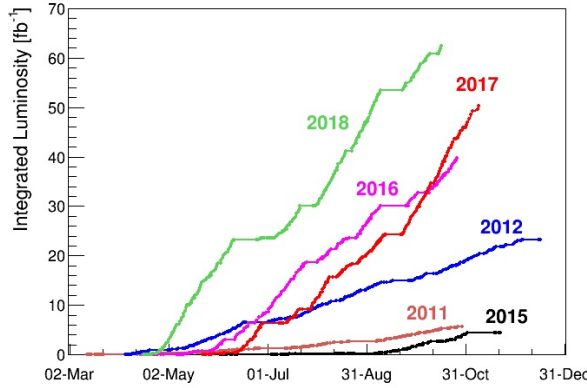


Figure 3.1. The integrated luminosity of the CMS and ATLAS experiments combined over the operation period from 2011–2018, source [122].

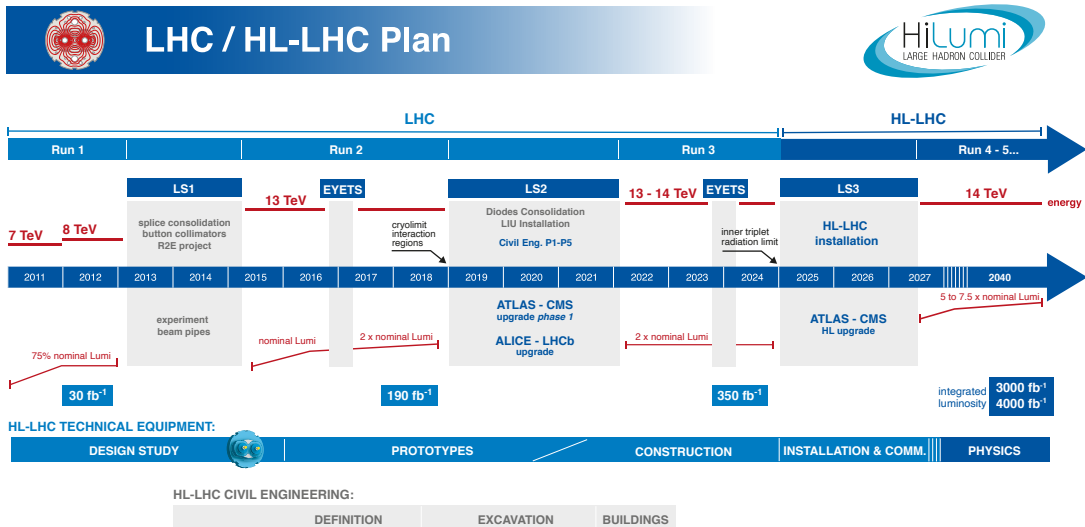


Figure 3.2. A timeline of the LHC operation showing Run-I, Run-II and future planned runs of the LHC, including the HL-LHC, source [120].

3.2 Higgs properties

3.2.1 Higgs boson mass measurements

To measure the mass of the Higgs boson with high precision, one needs to consider final states that can be reconstructed with high momentum and mass resolutions. This is typically achieved when no hadronic constituents in the decays are involved, such as

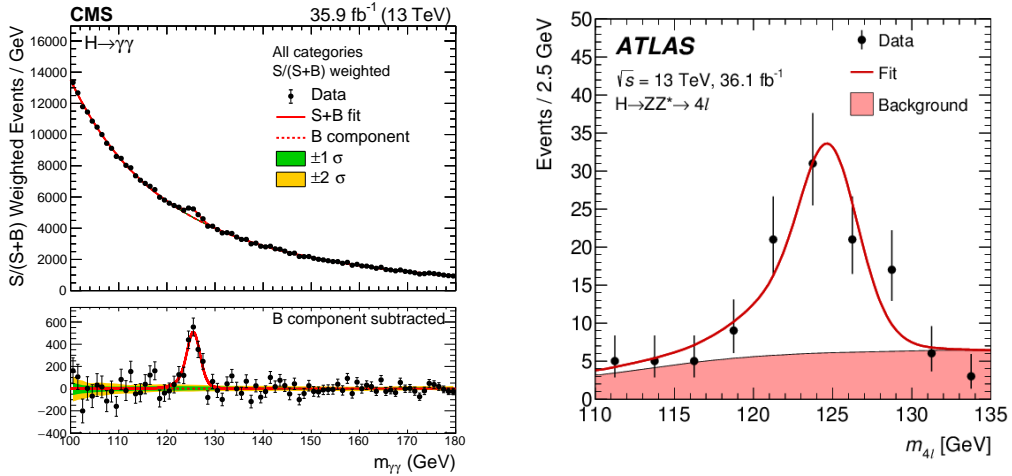


Figure 3.3. The invariant mass distributions of diphoton $m_{\gamma\gamma}$ (CMS [128]) and four lepton $m_{4\ell}$ (ATLAS [129]) final states showing a clear peak at the Higgs mass, with smooth background. These final states are ideal for Higgs mass measurements. The figures are taken from their respective references.

$h \rightarrow \gamma\gamma$ and $h \rightarrow ZZ^* \rightarrow 4\ell$. Reconstructing the invariant mass distributions $m_{\gamma\gamma}$ and $m_{4\ell}$ one observes that the Higgs peak is narrow over a relatively smooth background, see Figure 3.3; this is ideal for the measurement of the Higgs mass. It should be noted that the width of the resonance is due to the detector resolution and does not correspond to the actual Higgs width.

There have been consistent improvements of the Higgs mass measurements since its discovery. In Figure 3.4, I have performed a meta-analysis on ATLAS and CMS measurements of the Higgs mass in Run-I and Run-II of the LHC for both diphoton and ZZ^* final states based on the data from the studies [128–131] using a random effects model [132], the random effect variable is the study itself. The pooling of the studies yielded a mass measurement of $m_h = 125.21 \pm 0.10$ that translates to a 0.11% accuracy. The heterogeneity of the studies is found to be $I^2 = 49\%$ ($p = 0.05$). Different measurements combination techniques were used in [128] and [63] yielded a slightly different central values but all of the results agree within the uncertainties.

3.2.2 Higgs full width

The SM values of the Higgs boson full width is $\Gamma_h = 4.1$ GeV and it can be accessed in the LHC by looking at the ratio of on-shell vs off-shell Higgs production and decay to the $ZZ^{(*)}$ state, and $ZZ^{(*)} \rightarrow 4\ell, 2\ell 2\nu$, namely

$$\frac{\sigma(gg \rightarrow h \rightarrow ZZ^*)}{\sigma(gg \rightarrow h^* \rightarrow ZZ)} = \kappa_g^2 \kappa_Z^2 \frac{4m_Z^2}{m_h \Gamma_h}, \quad (3.4)$$

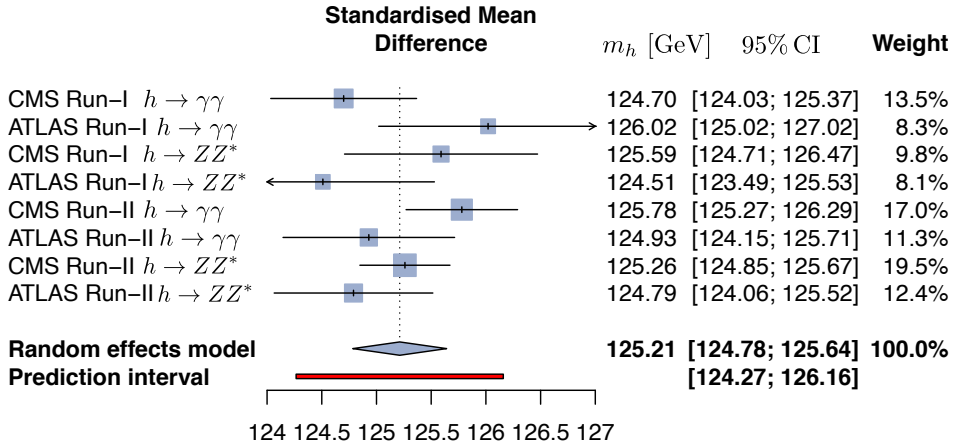


Figure 3.4. A meta analysis preformed to combine all the measurements of the Higgs mass from Run-I and Run-II, the combined result was obtained from pooling all of the studies using the random effects model method.

where the κ here denotes the ratio between the measured or modified coupling with the Higgs and the SM prediction, i.e.

$$\kappa_X := \frac{g_{XXh}}{g_{X}^{SM}}. \quad (3.5)$$

The κ -formalism is commonly used in reporting experimental constraints/ of the Higgs couplings; it will be discussed in more detail in chapter 4.

Unfortunately, it is not possible to directly measure the Higgs full width at the LHC, as this requires full reconstruction of the collision event and study the recoil mass, and this is only possible at lepton colliders [133, 134]. Alas, it is still possible to extract bounds on Γ_h using (3.4). ATLAS used this method to constrain the full width of the Higgs using Run-II data [135], while CMS has performed the same analysis using Run-I and Run-II data combined [136], the results are 95% CL bounds of Γ_h

$$\Gamma_h < 14.4 \text{ GeV} \quad (\text{ATLAS}) \quad 0.08 \text{ GeV} < \Gamma_h < 9.16 \text{ GeV} \quad (\text{CMS}), \quad (3.6)$$

with the combined bound approaching $\sim 3\Gamma_h^{\text{SM}}$.

3.2.3 Higgs spin and parity

According to the SM predictions, the Higgs boson is a scalar and \mathcal{CP} even ($J^p = 0^+$). However, the discovery of a peak in the $m_{\gamma\gamma}$ distribution on its own would not automatically imply that the particle discovered is scalar; it could be a spin-2 boson or a pseudoscalar ($J^p = 0^-$). To study the J^p properties of the Higgs, one needs to examine the differential distributions of angular variables such as the rapidity y or transverse momentum p_T . Both ATLAS and CMS collaborations studied the angular distributions of the Higgs decays $h \rightarrow ZZ^*$, $h \rightarrow WW^*$ and $h \rightarrow \gamma$, then tested the alternative hypothesis for J^p against the SM [137, 138]. The analysis results showed that the SM 0^+ hypothesis is favoured at $> 99.9\%$ CL.

3.3 Measurements of Higgs rates and couplings

3.3.1 Higgs cross-sections

The total inclusive Higgs boson cross-section has been measured using the final states $h \rightarrow \gamma\gamma$ and $h \rightarrow ZZ^* \rightarrow 4\ell$, and their combinations. The measurements have been done at the three energies of the LHC : 7 TeV, 8 TeV [139] and 13 TeV [140? , 141]. As shown in Figure 3.5, the measured inclusive cross-section is in agreement with the SM prediction across all of the LHC operation energies.

In addition to the inclusive cross-section measurements, differential cross-sections of the Higgs have been measured for p_T and y as we have seen in subsection 3.2.3 for Higgs's J^p determination. Additionally, the differential cross-sections for other variables have been studied including N_{jets} , p_T^{jet} , m_{jj} , $\delta\phi_{jj}$ and others. The channels $h \rightarrow ZZ^*$, $h \rightarrow WW^*$ and $h \rightarrow \gamma$ were used for these studies. The most recent results using the full Run-II data can be found in [141–144].

A collection of measurements of Higgs production and decay rates has been carried out by both ATLAS and CMS. These measurements are also carried out in what is known as the “Standard Template Cross-Sections” (STXS) framework. The STXS is fiducial cross-sections in exclusive phase-space regions or bins stratified by the Higgs boson production channels. They have the advantage of standardisation of cuts and final results such that measurements could be easily combined across analyses. More details about the STXS framework can be found in the reports of LHC Higgs cross-sections working group (HXSWG) [145]. Table 3.1 presents a summary of the state-of-art measurements of the Higgs rates separated into production and decay channels using the total LHC Run-II data from ATLAS and CMS experiments. The HL-LHC projections from the CMS experiment are given as a comparison. The results in this table are written in terms of the signal strength, which is directly extracted from measuring the number of

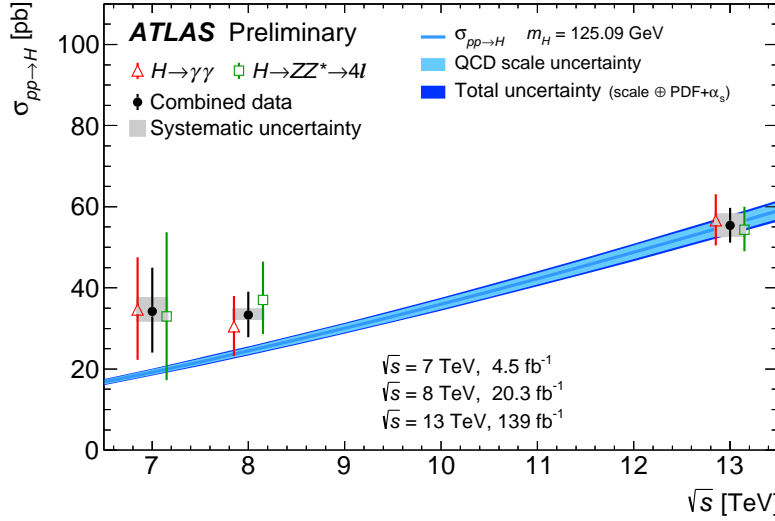


Figure 3.5. The total inclusive cross-section measurements by ATLAS collaboration [142] for 7, 8 and 13 TeV using $h \rightarrow \gamma\gamma$ and $h \rightarrow ZZ^* \rightarrow 4\ell$. channels and their combination (black points) compared to the SM prediction with the uncertainties shown as blue line with light and dark blue bands for QCD scale uncertainties and total uncertainties, respectively. This plot is taken from the quoted results.

events dividing them by the SM prediction

$$\mu_{\text{Exp}} := \frac{\sigma \cdot \text{BR}}{\sigma^{\text{SM}} \cdot \text{BR}^{\text{SM}}}. \quad (3.7)$$

Production	Decay	$\mu_{\text{Exp}} \pm \delta\mu_{\text{Exp}}$ (symmetrised)		Ref.	
		LHC Run-II			
		CMS 137 fb^{-1} ATLAS 139 fb^{-1}	CMS 3 ab^{-1}		
ggF	$h \rightarrow \gamma\gamma$	0.99 ± 0.12 1.030 ± 0.110	1.000 ± 0.042	[146–148]	
	$h \rightarrow ZZ^*$	0.985 ± 0.115 0.945 ± 0.105	1.000 ± 0.040		
	$h \rightarrow WW^*$	1.285 ± 0.195 1.085 ± 0.185	1.000 ± 0.037	[146, 148, 149]	
	$h \rightarrow \tau^+\tau^-$	0.385 ± 0.385 1.045 ± 0.575	1.000 ± 0.055		
	$h \rightarrow b\bar{b}$	2.54 ± 2.44 —	1.000 ± 0.247	[148, 149]	
	$h \rightarrow \mu^+\mu^-$	0.315 ± 1.815 —	1.000 ± 0.138	[148, 149]	
VBF	$h \rightarrow \gamma\gamma$	1.175 ± 0.335 1.325 ± 0.245	1.000 ± 0.128	[146–148]	
	$h \rightarrow ZZ^*$	0.62 ± 0.41 1.295 ± 0.455	1.000 ± 0.134		
	$h \rightarrow WW^*$	0.65 ± 0.63 0.61 ± 0.35	1.000 ± 0.073	[146, 148, 149]	
	$h \rightarrow \tau^+\tau^-$	1.055 ± 0.295 1.17 ± 0.55	1.000 ± 0.044		
	$h \rightarrow b\bar{b}$	— 3.055 ± 1.645	—	[146]	
	$h \rightarrow \mu^+\mu^-$	3.325 ± 8.075 —	1.000 ± 0.540	[148]	
$t\bar{t}h$	$h \rightarrow \gamma\gamma$	1.43 ± 0.30 0.915 ± 0.255	1.000 ± 0.094	[146–148]	
	$h \rightarrow VV^*$	$0.64 \pm 0.64 (ZZ^*)$ $0.945 \pm 0.465 (WW^*)$ 1.735 ± 0.545	$1.000 \pm 0.246 (ZZ^*)$ $1.000 \pm 0.097 (WW^*)$ —		
	$h \rightarrow \tau^+\tau^-$	0.845 ± 0.705 1.27 ± 1.0	1.000 ± 0.149	[146, 148, 149]	
	$h \rightarrow b\bar{b}$	1.145 ± 0.315 0.795 ± 0.595	1.000 ± 0.116		
	$h \rightarrow \gamma\gamma$	0.725 ± 0.295 1.335 ± 0.315	$1.000 \pm 0.233 (Zh)$ $1.000 \pm 0.139 (W^\pm h)$	[146–148]	
Vh	$h \rightarrow ZZ^*$	1.21 ± 0.85 1.635 ± 1.025	$1.000 \pm 0.786 (Zh)$ $1.000 \pm 0.478 (W^\pm h)$	[146, 148, 149]	
	$h \rightarrow WW^*$	1.850 ± 0.438 —	$1.000 \pm 0.184 (Zh)$ $1.000 \pm 0.138 (W^\pm h)$	[148, 150]	
	$h \rightarrow b\bar{b}$	— 1.025 ± 0.175	$1.000 \pm 0.065 (Zh)$ $1.000 \pm 0.094 (W^\pm h)$	[146, 148]	
	Zh CMS	$h \rightarrow \tau^+\tau^-$ $h \rightarrow b\bar{b}$	1.645 ± 1.485 0.94 ± 0.32	—	
$W^\pm h$ CMS	$h \rightarrow \tau^+\tau^-$ $h \rightarrow b\bar{b}$	3.08 ± 1.58 1.28 ± 0.41		[149]	

Table 3.1. The experimental single Higgs production and decay rates measurements from the complete data of LHC Run II and projections for the HL-LHC. The uncertainties were symmetrised here. The table is published in [151].

3.3.2 Constraints on Higgs couplings

The measurements of the Higgs rates and their combination have been used to set bounds on the Higgs couplings. The most recent bounds have been reported by ATLAS using the Higgs inclusive rates and STXS for the full Run-II data [152], and by CMS using Higgs rates shown in Table 3.1 [149]. In Figure 3.6, I present the aggregation of the ATLAS and CMS bounds on the Higgs coupling modifiers in the κ formalism defined in eq. (3.5). The aggregation of these bounds was performed taking into account the experiment effects, as described in [153] assuming there is no correlation between ATLAS and CMS measurements.

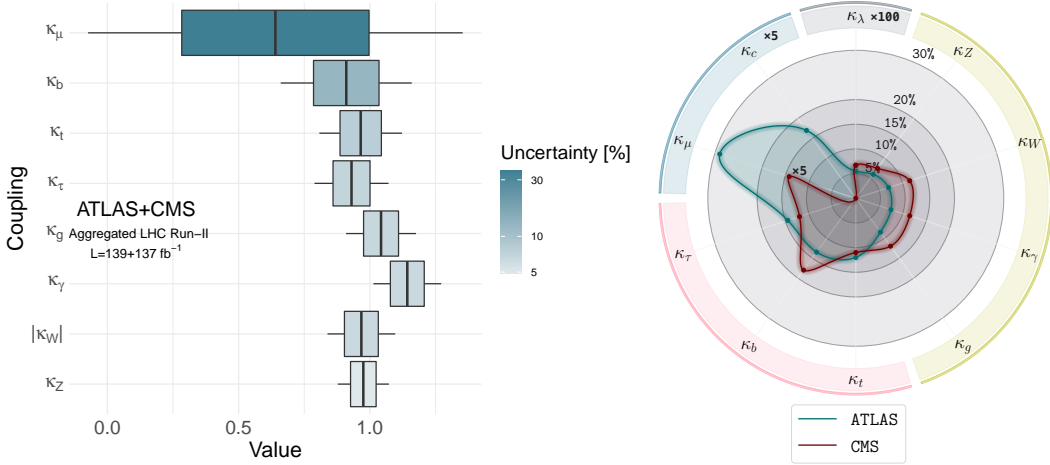


Figure 3.6. (left) Meta-analysis aggregation of the most recent bounds from ATLAS [152] and CMS [149] on the Higgs coupling modifiers κ . (right) The individual 68% CI uncertainties on the coupling modifiers from ATLAS and CMS.

The measured bounds on the Higgs coupling to the gauge bosons, including the effective couplings to γ and g , as well as the couplings to the third-generation fermions are within few percent of the SM prediction. The bounds on the coupling to the W boson seems to favour a negative value in CMS fits, due to the channel used to constraint it $h \rightarrow WW$ depending on κ_W^2 , thus making the best fit value of ~ -1 within the SM prediction. An independent analysis on the relative signs of κ_W and κ_t was preformed using $t\bar{t}/t\bar{t}h$ processes in ref. [154]. Only the absolute value of κ_W is reported in my combination of the analyses results. Additionally, the observation of the decays $h \rightarrow b\bar{b}$ [155–157] and $h \rightarrow \tau\tau$ [158, 159] leads to direct measurements of the beauty and τ Yukawa couplings. This has made their bounds comparable to the gauge bosons and top couplings with the Higgs, with less than 10% uncertainty. *Au contraire*, bounds on the Yukawa couplings of second and first generation fermions remain very weak.

Recently, ATLAS and CMS have preformed searches for the decay $h \rightarrow \mu\mu$ [160, 161] using the Run-II data. These searched have shown evidence o (3σ) for this decay. Consequently improving the constraints on κ_μ , though as seen in Figure 3.6, the uncertainty

remains high $\sim 36\%$. Studies on the Higgs decaying to charm pairs are significantly more challenging, and they have only permitted to set upper 95% CL bounds on $|\kappa_c|$ of 8.5 for ATLAS [162, 163] and 70 for CMS [164]. There are no planned direct searches for the first generation Yukawa couplings (*direct*) measurements planned for the LHC. It is not possible to directly access decays of the Higgs to up or down quarks at the LHC. Other methods for probing these couplings will be extensively discussed in chapter 9.

By the end of the HL-LHC, it is projected that the couplings of the Higgs, including the ones with gauge bosons, third-generation fermions, and the muon Yukawa, will be measured at a few per cent level [39]. This is highlighted by Figure 3.7, in this figure I show the improvement in the κ measurement uncertainty expected by the HL-LHC compared to Run-II.

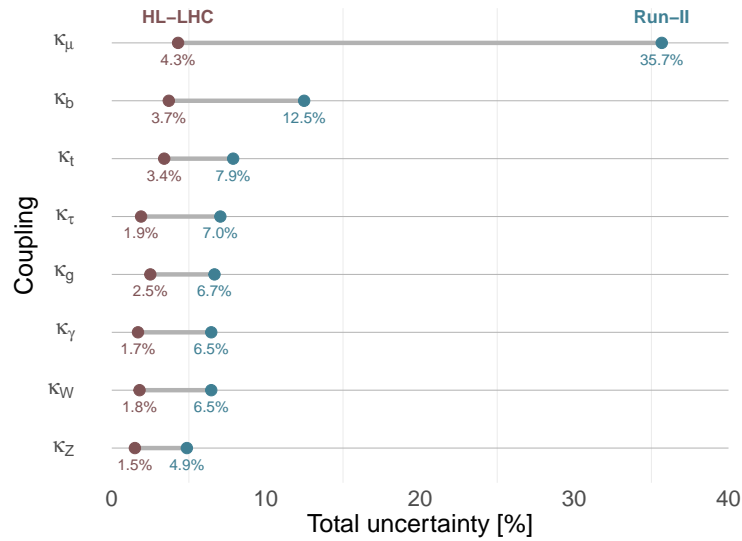


Figure 3.7. Dumbbell plot illustrating the improvement of the uncertainties on the Higgs coupling's measurement projected for the HL-LHC compared to the current combined CMS and ATLAS measurements from Run-II data.

3.4 Challenges and outlook

The future runs of the LHC hold a lot of potential for further understanding the properties of our 10-year old Higgs boson. Although, for some processes and couplings there will still be a lot of challenges ahead. For instance, the observation of $h \rightarrow c\bar{c}$ will require highly efficient charm-tagging, which is expected to improve at the HL-LHC by a factor of 2.5 [165]. The signal strength of the rare decay $h \rightarrow Z\gamma$ currently is only constrained to 3.6 times the SM values at 95% CL [166] and it is expected to be measured at the HL-LHC with $\sim 10\%$ uncertainty.

Other Higgs boson couplings that we did not discuss above are the Higgs self-interactions

(trilinear and quartic), as I have shown in subsection 2.5.2 that the perturbative unitarity bound derived in ref. [110] is the strongest on these couplings so far. To experimentally measure Higgs self-couplings, it is imperative to observe multiple Higgs production. Namely, to access the trilinear self-coupling, Higgs pair production must be observed. Similarly, the quartic Higgs coupling measurement needs triple Higgs production observation. Woefully, these processes are experimentally arduous to detect, due to their low inclusive cross-section ~ 30 fb for hh [167] and < 0.1 fb for hhh at LHC maximum expected operational energy of 14 TeV. The triple Higgs production will remain challenging even for future colliders, e.g. for the FCC-hh at 100 TeV. This process has a cross-section of only ~ 5 fb [168]. To put these numbers in the context of single Higgs production, recall the inclusive single-Higgs production cross-section of ~ 70 pb at the current LHC operation energy. The triple Higgs production thus, will not be accessible at the LHC, and consequently, the quartic self-coupling will not be measured. However, the HL-LHC has a promising outlook to measure the trilinear self-coupling.

In chapter 7, I will discuss the potential for using single-Higgs processes to indirectly probe the trilinear coupling, as proposed by several studies [29–36] and the challenges accompanying it. Later in chapter 8, the Higgs pair production at the LHC will be overviewed along with the current and future searches for this process and the bounds from them on the trilinear Higgs self-coupling.

Light quark Yukawa couplings are another example of formidable couplings to probe at the LHC. chapter 9 will be dedicated to overviewing the potential for Higgs pair production in the measurement of these elusive couplings. The focal point of that chapter will be multi-variate analysis in signal vs background separation.

4 Higgs and effective field theories

The study of the Higgs properties, couplings and rates aims to shed light on the structure of its potential and how it is responsible for the EW symmetry breaking. Explaining the vacuum expectation value and the mass of the Higgs has been the aim of many theoreticians and phenomenologists. This is because the SM offers no insights into the nature of the Higgs potential, as its parameters are unconstrained by the SM gauge structure, for the most part. Rather, these input parameters need to be supplied from experimental observations. The Higgs potential shown in eq. (2.8) is the minimal one that could explain the EW symmetry breaking, but nature may not have taken the minimalist approach.

In order to test whether the Higgs potential is in the minimalist SM form or there are other more complex structures involved, one can start by measuring Higgs rates and confronting them against the SM prediction as overviewed in the previous chapter, using the κ formalism. Nonetheless, this approach does not help understand what new physics structures caused a deviation, if observed. Conversely, we are interested in knowing what are the allowed NP structures given the current (or future) measurements of the Higgs rates. Of course, by looking at concrete models, one would get insight into the aforementioned questions by confronting them with Higgs data. However, this is a tedious task, as there are numerous ways NP might manifest .

In order to make the search for NP more accessible and model-agnostic, we revert to **effective field theories** (EFT), one of the most perspicacious concepts of quantum field theory. In the EFT framework, the interactions mediated by NP at the small scale of arbitrary complexity can be systematically simplified by approximating these interactions via integrating the UV degrees of freedom, leaving only numerable operators added to the SM. The premise of EFTs can be simply illustrated in Figure 4.1. For example, the LHC might not be able to resolve the UV degrees of freedom at their scale Λ ; rather, one can only observe the effective interactions they mediate. These new interactions depend on a set of free parameters known as **Wilson coefficients**, which would be constrained or set from experiments. These “phenomenological Lagrangians”, as called by Weinberg [169], are not necessarily renormalisable but still allow for robust predictions that can be tested at colliders, including higher-order effects.

This chapter is organised as follows: In section 4.1, the Higgs sector of Standard Model effective field theory (SMEFT) is presented along with the parametrisation of single and di-Higgs rates in terms of the SMEFT Wilson coefficients. In contrast to the SMEFT formalism, section 4.2 will present a non-linear EFT formalism known as the EW Chiral Lagrangian (EWChL) or (Higgs)EFT. Finally, I will conclude this chapter in section 4.3.

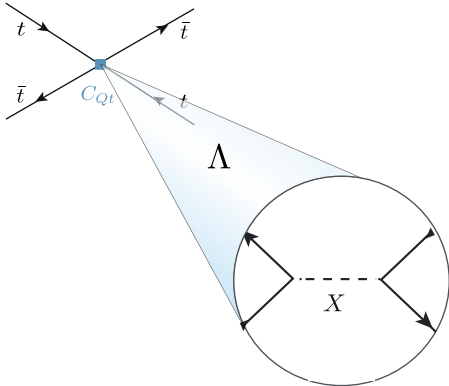


Figure 4.1. The premise of EFT stems from observing interactions at collider energy reach without being able to resolve the details of the NP mediating them, as the NP degrees of freedom have an energy scale Λ higher than the collider's reach.

4.1 The Standard Model effective field theory

There is no unique way of defining an EFT for the Higgs boson h . One could consider the field h as an EW singlet or as a part of the doublet ϕ like the SM itself. The first ansatz is more compatible with a heavier Higgs, and the effective coupling based on it could be derived from the EWChL as we shall see in section 4.2. However, after discovering the Higgs has a mass close to m_Z , the second option for an EFT seemed more fitting, albeit more restrictive. Assuming that the NP resonances would occur at masses $\Lambda \gg m_Z$, one can integrate them out, yielding a set of effective operators of mass dimension > 4 . Hence, one can think of the SM Lagrangian of mass dimensions 2 and 4 as a part of a more general EFT that contains the same fields and symmetries, known as the Standard Model Effective field theory (SMEFT).

From simple dimensional analysis, we know that the Higher dimensional operators need to contain an inverse mass with some power $p = 4 - d$ in the couplings, there is a clear power counting in the SMEFT Lagrangian, such that it is possible to collect all operators of the same mass dimension d into a d -mass-dimensional Lagrangians taking the form

$$\mathcal{L}^{(d)} = \frac{1}{\Lambda^{d-4}} \sum_i C_i \mathcal{O}_i. \quad (4.1)$$

For any $d > 4$, the Lagrangian in eq. (4.1) is not renormalisable, yet it is still predictive via fitting the Wilson coefficients C_i order-by-order to experimental measurements. This power-counting property allows for predictability even when having, in principle, an infinite number of free Wilson coefficients. All of these operators are suppressed by the NP scale (irrelevant operators with respect to the renormalisation group). To illustrate this, if the NP scale is set to $\Lambda = 1$, then the effects of dimension-six operators will be at the per cent level. At the same time, dimension-eight operators will have effects of order $\sim 10^{-4}$, allowing to ignore the dimension-eight and higher operators in the

majority of the LHC studies. Regarding dimension-five, there is only one operator called the Weinberg operator [170]

$$\mathcal{O}_{\nu\nu} = (\tilde{\phi}L_p)^T \mathcal{C}(\tilde{\phi}^\dagger L_q), \quad (4.2)$$

where \mathcal{C} is the charge conjugation operator. The Weinberg operator violates leptonic number and generates neutrino masses after EW symmetry breaking; similar effects are generated from dimension-seven operators [171]. These effects do not yield considerable collider phenomenology. Hence, I shall be discussing SMEFT with dimension-six operators only, for studies on Higher-dimensional SMEFT operators cf. [171–174].

The SMEFT Lagrangian up to dimension-six operators is given by

$$\mathcal{L}_{\text{SMEFT}}^{d=6} = \mathcal{L}_{\text{SM}} + \frac{1}{\Lambda^2} \sum_i C_i \mathcal{O}_i. \quad (4.3)$$

The study of dimension-six effective operators in characterising NP indirect collider signatures has been first proposed in [175, 176]. Nowadays, phenomenological studies of EFTs with dimension-six operators primarily focus on using a set of complete and non-redundant “basis”. This is since different effective operators will correspond to the same observables, e.g. same scattering amplitudes of SM particles. This is the case if the operators can be related using equations of motion, Fierz transformations, integration by parts or field redefinitions. Thus leading to non-trivial and counter-intuitive relations between operators. Consequently, the construction of basis for the dimension-six SMEFT Lagrangian of eq. (4.3) is a cumbersome task. Such task has been accomplished by [25] recently forming what is known as the **Warsaw Basis**. Another set of basis is the strongly-interacting light Higgs basis (SILH), initially proposed by [24], before the Warsaw basis and completed in refs. [26, 27]. A more recent set of basis has been published in [28] using a subset of couplings characterising the interactions of mass eigenstates in the effective Lagrangian.

The complete $d = 6$ SMEFT is described by 2499 independent parameters [177–179]. However, if one suppresses the flavour indices, assuming SMEFT is flavour universal, their inventory is significantly reduced. In the Warsaw basis, for example, assuming Baryon number conservation and dropping the flavour indices, one has only 59 operators, listed in Table 4.1. It should be noted that all of the SMEFT basis will produce the same phenomenology, though the choice of basis is sometimes helpful in simplifying the analysis. In this thesis, I will focus on Warsaw basis.

The SMEFT operators can either modify SM parameters (couplings, masses) or introduce new vertices that do not exist in the SM, like four-fermion operators, or both like $\mathcal{O}_{\phi e}$. An example of operators modifying SM parameters is $\mathcal{O}_{\phi D}$, which leads to modification of the Z boson mass after EW symmetry breaking

$$\frac{C_{\phi D}}{\Lambda^2} |\phi^\dagger D_\mu \phi|^2 \rightarrow \frac{C_{\phi D} v^4}{16 \Lambda^2} (g_2^2 + g_1^2) Z^\mu Z_\mu. \quad (4.4)$$

Additionally, from field redefinitions, we get indirect contributions to the W mass from

X^3		Pure Higgs		$\psi^2\phi^3 + \text{h.c.}$	
\mathcal{O}_G	$f^{ABC}G_\mu^{A\nu}G_\nu^{B\rho}G_\rho^{C\mu}$	$\mathcal{O}_{\phi\square}$	$(\phi^\dagger\phi)\square(\phi^\dagger\phi)$	$\mathcal{O}_{e\phi}$	$(\phi^\dagger\phi)(\bar{l}_p e_r \phi)$
$\mathcal{O}_{\widetilde{G}}$	$f^{ABC}\widetilde{G}_\mu^{A\nu}G_\nu^{B\rho}G_\rho^{C\mu}$	$\mathcal{O}_{\phi D}$	$(\phi^\dagger D_\mu\phi)^*(\phi^\dagger D_\mu\phi)$	$\mathcal{O}_{u\phi}$	$(\phi^\dagger\phi)(\bar{q}_p u_r \widetilde{\phi})$
\mathcal{O}_W	$\epsilon^{IJK}W_\mu^{I\nu}W_\nu^{J\rho}W_\rho^{K\mu}$	\mathcal{O}_ϕ	$(\phi^\dagger\phi)^3$	$\mathcal{O}_{d\phi}$	$(\phi^\dagger\phi)(\bar{q}_p d_r \phi)$
$\mathcal{O}_{\widetilde{W}}$	$\epsilon^{IJK}\widetilde{W}_\mu^{I\nu}W_\nu^{J\rho}W_\rho^{K\mu}$				
$X^2\phi^2$		$\psi^2 X\phi + \text{h.c.}$		$\psi^2\phi^2 D$	
$\mathcal{O}_{\phi G}$	$\phi^\dagger\phi G_{\mu\nu}^A G^{A\mu\nu}$	\mathcal{O}_{eW}	$(\bar{l}_p\sigma^{\mu\nu}e_r)\tau^I\phi W_{\mu\nu}^I$	$\mathcal{O}_{\phi l}^{(1)}$	$(\phi^\dagger i\overleftrightarrow{D}_\mu\phi)(\bar{l}_p\gamma^\mu l_r)$
$\mathcal{O}_{\phi\widetilde{G}}$	$\phi^\dagger\phi\widetilde{G}_{\mu\nu}^A G^{A\mu\nu}$	\mathcal{O}_{eB}	$(\bar{l}_p\sigma^{\mu\nu}e_r)\phi B_{\mu\nu}$	$\mathcal{O}_{\phi l}^{(3)}$	$(\phi^\dagger i\overleftrightarrow{D}_\mu^I\phi)(\bar{l}_p\tau^I\gamma^\mu l_r)$
$\mathcal{O}_{\phi W}$	$\phi^\dagger\phi W_{\mu\nu}^I W^{I\mu\nu}$	\mathcal{O}_{uG}	$(\bar{q}_p\sigma^{\mu\nu}T^A u_r)\widetilde{\phi} G_{\mu\nu}^A$	$\mathcal{O}_{\phi e}$	$(\phi^\dagger i\overleftrightarrow{D}_\mu\phi)(\bar{e}_p\gamma^\mu e_r)$
$\mathcal{O}_{\phi\widetilde{W}}$	$\phi^\dagger\phi\widetilde{W}_{\mu\nu}^I W^{I\mu\nu}$	\mathcal{O}_{uW}	$(\bar{q}_p\sigma^{\mu\nu}u_r)\tau^I\widetilde{\phi} W_{\mu\nu}^I$	$\mathcal{O}_{\phi q}^{(1)}$	$(\phi^\dagger i\overleftrightarrow{D}_\mu\phi)(\bar{q}_p\gamma^\mu q_r)$
$\mathcal{O}_{\phi B}$	$\phi^\dagger\phi B_{\mu\nu}B^{\mu\nu}$	\mathcal{O}_{uB}	$(\bar{q}_p\sigma^{\mu\nu}u_r)\widetilde{\phi} B_{\mu\nu}$	$\mathcal{O}_{\phi q}^{(3)}$	$(\phi^\dagger i\overleftrightarrow{D}_\mu^I\phi)(\bar{q}_p\tau^I\gamma^\mu q_r)$
$\mathcal{O}_{\phi\widetilde{B}}$	$\phi^\dagger\phi\widetilde{B}_{\mu\nu}B^{\mu\nu}$	\mathcal{O}_{dG}	$(\bar{q}_p\sigma^{\mu\nu}T^A d_r)\phi G_{\mu\nu}^A$	$\mathcal{O}_{\phi u}$	$(\phi^\dagger i\overleftrightarrow{D}_\mu\phi)(\bar{u}_p\gamma^\mu u_r)$
$\mathcal{O}_{\phi WB}$	$\phi^\dagger\tau^I\phi W_{\mu\nu}^I B^{\mu\nu}$	\mathcal{O}_{dW}	$(\bar{q}_p\sigma^{\mu\nu}d_r)\tau^I\phi W_{\mu\nu}^I$	$\mathcal{O}_{\phi d}$	$(\phi^\dagger i\overleftrightarrow{D}_\mu\phi)(\bar{d}_p\gamma^\mu d_r)$
$\mathcal{O}_{\phi\widetilde{WB}}$	$\phi^\dagger\tau^I\phi\widetilde{W}_{\mu\nu}^I B^{\mu\nu}$	\mathcal{O}_{dB}	$(\bar{q}_p\sigma^{\mu\nu}d_r)\phi B_{\mu\nu}$	$\mathcal{O}_{\phi ud} + \text{h.c.}$	$i(\widetilde{\phi}^\dagger D_\mu\phi)(\bar{u}_p\gamma^\mu d_r)$
$(\bar{L}L)(\bar{L}L)$			$(\bar{R}R)(\bar{R}R)$		
\mathcal{O}_{ll}	$(\bar{l}_p\gamma_\mu l_r)(\bar{l}_s\gamma^\mu l_t)$		\mathcal{O}_{ee}	$(\bar{e}_p\gamma_\mu e_r)(\bar{e}_s\gamma^\mu e_t)$	
$\mathcal{O}_{qq}^{(1)}$	$(\bar{q}_p\gamma_\mu q_r)(\bar{q}_s\gamma^\mu q_t)$		\mathcal{O}_{uu}	$(\bar{u}_p\gamma_\mu u_r)(\bar{u}_s\gamma^\mu u_t)$	
$\mathcal{O}_{qq}^{(3)}$	$(\bar{q}_p\gamma_\mu\tau^I q_r)(\bar{q}_s\gamma^\mu\tau^I q_t)$		\mathcal{O}_{dd}	$(\bar{d}_p\gamma_\mu d_r)(\bar{d}_s\gamma^\mu d_t)$	
$\mathcal{O}_{lq}^{(1)}$	$(\bar{l}_p\gamma_\mu l_r)(\bar{q}_s\gamma^\mu q_t)$		\mathcal{O}_{eu}	$(\bar{e}_p\gamma_\mu e_r)(\bar{u}_s\gamma^\mu u_t)$	
$\mathcal{O}_{lq}^{(3)}$	$(\bar{l}_p\gamma_\mu\tau^I l_r)(\bar{q}_s\gamma^\mu\tau^I q_t)$		\mathcal{O}_{ed}	$(\bar{e}_p\gamma_\mu e_r)(\bar{d}_s\gamma^\mu d_t)$	
			$\mathcal{O}_{ud}^{(1)}$	$(\bar{u}_p\gamma_\mu u_r)(\bar{d}_s\gamma^\mu d_t)$	
			$\mathcal{O}_{ud}^{(8)}$	$(\bar{u}_p\gamma_\mu T^A u_r)(\bar{d}_s\gamma^\mu T^A d_t)$	
$(\bar{L}L)(\bar{R}R)$			$(\bar{L}R)(\bar{L}R) + \text{h.c.}$		
\mathcal{O}_{le}	$(\bar{l}_p\gamma_\mu l_r)(\bar{e}_s\gamma^\mu e_t)$		$\mathcal{O}_{quqd}^{(1)}$	$(\bar{q}_p^j u_r)\epsilon_{jk}(\bar{d}_s^k d_t)$	
\mathcal{O}_{lu}	$(\bar{l}_p\gamma_\mu l_r)(\bar{u}_s\gamma^\mu u_t)$		$\mathcal{O}_{quqd}^{(8)}$	$(\bar{q}_p^j T^A u_r)\epsilon_{jk}(\bar{q}_s^k T^A d_t)$	
\mathcal{O}_{ld}	$(\bar{l}_p\gamma_\mu l_r)(\bar{d}_s\gamma^\mu d_t)$		$\mathcal{O}_{lequ}^{(1)}$	$(\bar{l}_p^j e_r)\epsilon_{jk}(\bar{q}_s^k u_t)$	
\mathcal{O}_{qe}	$(\bar{q}_p\gamma_\mu q_r)(\bar{e}_s\gamma^\mu e_t)$		$\mathcal{O}_{lequ}^{(3)}$	$(\bar{l}_p^j \sigma_{\mu\nu} e_r)\epsilon_{jk}(\bar{q}_s^k \sigma^{\mu\nu} u_t)$	
$\mathcal{O}_{qu}^{(1)}$	$(\bar{q}_p\gamma_\mu q_r)(\bar{u}_s\gamma^\mu u_t)$		\mathcal{O}_{ledq}	$(\bar{l}_p^j e_r)(\bar{d}_s q_{tj})$	
$\mathcal{O}_{qu}^{(8)}$	$(\bar{q}_p\gamma_\mu T^A q_r)(\bar{u}_s\gamma^\mu T^A u_t)$				
$\mathcal{O}_{qd}^{(1)}$	$(\bar{q}_p\gamma_\mu q_r)(\bar{d}_s\gamma^\mu d_t)$				
$\mathcal{O}_{qd}^{(8)}$	$(\bar{q}_p\gamma_\mu T^A q_r)(\bar{d}_s\gamma^\mu T^A d_t)$				

Table 4.1. Complete list of the dimension-six SMEFT operators in the Warsaw basis [25]. The \mathcal{CP} violating operators contains the dual fields \tilde{X} . The flavour labels of the form p, r, s, t on the \mathcal{O} operators are suppressed on the left hand side of the tables.

$C_{\phi D}$, combining both effects as a deviation in the ρ parameter, we get

$$\delta\rho = \frac{v^2}{2\Lambda^2} C_{\phi D}. \quad (4.5)$$

Allowing to constrain $C_{\phi D}$ from the T parameter

$$T = \frac{-2\pi v^2}{\Lambda^2} \frac{(g_1^2 + g_2^2)}{g_1^2 g_2^2} C_{\phi D}. \quad (4.6)$$

Another operator that affects the oblique parameters directly is $\mathcal{O}_{\phi WB}$, as it modifies the S parameter in the following way

$$S = \frac{16\pi v^2}{g_1 g_2 \Lambda^2} C_{\phi WB}. \quad (4.7)$$

SM coupling modifications by SMEFT operators related to EWPOs are investigated in chapter 10. Additionally, the contributions of the SMEFT Wilson coefficients to SM parameters are not only from tree-level effects like in eq. (4.4) but could also come at loop-level, either from finite or RGE contributions.

SMEFT is suitable as a low energy limit for supersymmetric models [180] or some classes of composite Higgs models [181, 182]

4.1.1 Single Higgs processes in SMEFT

Single Higgs production and decay processes are modified at LO by a relatively long list of operators summarised in eqs. (4.8), (4.9) and (4.10). Explicit formulae for the Higgs rates dependence on the Wilson coefficients of these operators can be found in [183]

SMEFT operators modifying Higgs rates at LO

Higgs operators

$$\begin{aligned} &C_{\phi D}, \mathcal{O}_{\phi\square}, \mathcal{O}_{\phi G}, \mathcal{O}_{\phi W}, \mathcal{O}_{\phi B}, \mathcal{O}_{\phi WB}, \mathcal{O}_{\phi l}^{(1)}, \\ &\mathcal{O}_{\phi l}^{(3)}, \mathcal{O}_{\phi e}, \mathcal{O}_{\phi q}^{(1)}, \mathcal{O}_{\phi q}^{(3)}, \mathcal{O}_{\phi u}, \mathcal{O}_{\phi d}, \mathcal{O}_{\tau\phi}, \mathcal{O}_{t\phi}, \mathcal{O}_{b\phi}, \mathcal{O}_{tb\phi}. \end{aligned} \quad (4.8)$$

Top-quark operators

$$\mathcal{O}_{tG}, \mathcal{O}_{tW}, \mathcal{O}_{tB}, \quad (4.9)$$

other

$$\mathcal{O}_G, \mathcal{O}_{ll}^{(1)}, \mathcal{O}_{Qq}^{(1),(3)}, \mathcal{O}_{tu}, \mathcal{O}_{td}^{(1),(8)}, \mathcal{O}_{Qu}^{(1),(8)}, \mathcal{O}_{Qd}^{(1),(8)}. \quad (4.10)$$

The third-generation quarks are denoted by Q while the first and second-generation quarks are assumed to have the same coupling and are denoted by q, u, d .

Some of these operators are strongly constrained from EWPO data such as $\mathcal{O}_{\phi D}$ and

$\mathcal{O}_{\phi WB}$, while others still have weak bounds from current measurements and are insensitive to EWPOs. Most recent fits on SMEFT Wilson coefficients can be found in ref. [38], where Higgs and EW data were used to fit a subset of the SMEFT Wilson coefficients of the operators listed above. The fit also includes the effects of RGE and NLO (even NNLO for m_W). While in [184], a global fit for a larger set of operators, but only with LO effects, including EW, Higgs and top-quark data. A study published in ref. [185] has utilised EWPO data to constrain the four-fermion operators appearing in Higgs rates at LO and operators with four heavy quarks, using their NLO effects on EW bosons pole masses. We shall see in chapter 7 that the latter operators also contribute to Higgs rates at NLO. A wider scope analysis including a wide range of Higgs, top-quark, di-boson and EWPO data has been performed in [37].

The dependence of single Higgs rates on the SMEFT Wilson coefficients gets more complicated once higher-order effects are taken into account. In the fit results reported from [38], the RGE of these Wilson coefficients introduces mixing with operators that do not appear at LO, also loop corrections to the rates and masses of the EW and Higgs bosons.

A prominent example of an operator appearing only at NLO in single Higgs processes is \mathcal{O}_ϕ , which modifies the Higgs self-interactions, namely the trilinear coupling. Typically, one needs to observe Higgs pair production to directly probe the Higgs trilinear self-coupling. However, due to the appearance of Higgs self-interaction and its modifiers, i.e. C_ϕ in SMEFT context, in higher-order EW corrections [186, 187] and Higgs observables [29–36], one can extract bounds on the Higgs trilinear coupling from single Higgs and EWPO data. Figure 4.2 illustrates example Feynman diagrams of single Higgs processes of which the trilinear Higgs self-coupling enters via NLO corrections. Using the

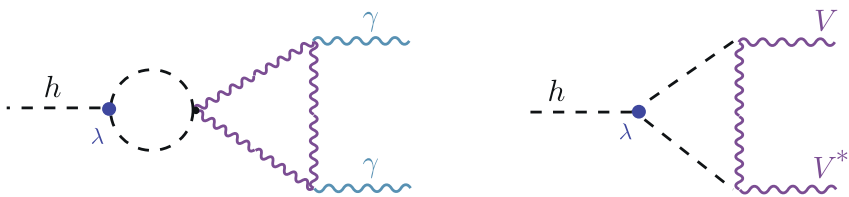


Figure 4.2. NLO EW corrections of single Higgs processes, were the Higgs trilinear self-coupling (the red circle) enters. Here the Higgs decay to two photons is shown as an example.

results from the aforementioned references, a global fit with all operators that enter at tree-level in addition to the loop effects from the Higgs self-coupling has been preformed in refs. [38, 188]. Additionally, experimental searches for Higgs trilinear self-coupling have been presented by ATLAS [189] and CMS [149].¹

¹I present references here to the most recent results.

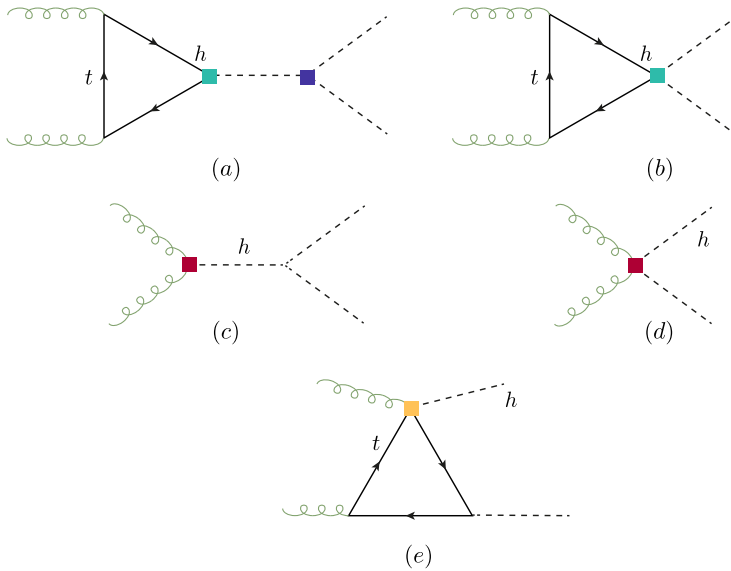


Figure 4.3. Example of diagrams illustrating how the dimension-six SMEFT operators enter in Higgs pair production at hadron colliders.

4.1.2 Higgs pair production and SMEFT

Higgs pair production in hadron colliders is sensitive to six \mathcal{CP} even SMEFT operators², under the assumption of Minimal Flavour violation (MFV).³ These operators are

$$\mathcal{O}_{\phi D}, \mathcal{O}_{\phi \square}, \mathcal{O}_\phi, \mathcal{O}_{t\phi}, \mathcal{O}_{\phi G}, \mathcal{O}_{tG}, \quad (4.11)$$

and their effects, with the corresponding colours are demonstrated in Figure 4.3, except for $\mathcal{O}_{\phi D}$ and $\mathcal{O}_{\phi \square}$, as they modify all SM Higgs vertices. However, MFV is not the only way to approach SMEFT, there exist more complex flavour structures that allow for significant enhancements of the first and second generation Yukawa couplings without being excluded by flavour observables. Such formalisms will be discussed in chapter 9. The primary operator to constrain from Higgs pair as mentioned before is \mathcal{O}_ϕ , for two reasons; a) the rest of the operators appearing in di-Higgs can be strongly constrained from single Higgs and top quark processes. b) The effect of \mathcal{O}_ϕ on Higgs pair production is significantly higher than in single Higgs or EW observables. This is illustrated in Figure 4.4 by comparing the relative change of the gluon fusion cross-sections at NLO QCD for single and di-Higgs production. This is not surprising since C_ϕ appears at LO in Higgs pair production. Another advantage for Higgs pair production searches is the sensitivity of this process to non-linear couplings, for example, diagrams (b) and (d) of Figure 4.3. Although in SMEFT, these diagrams correspond to the same operators in

²For or Higgs pair production with \mathcal{CP} violating operators, see ref. [190].

³MFV assumes that new physics operators will follow the same flavour hierarchies as the SM.

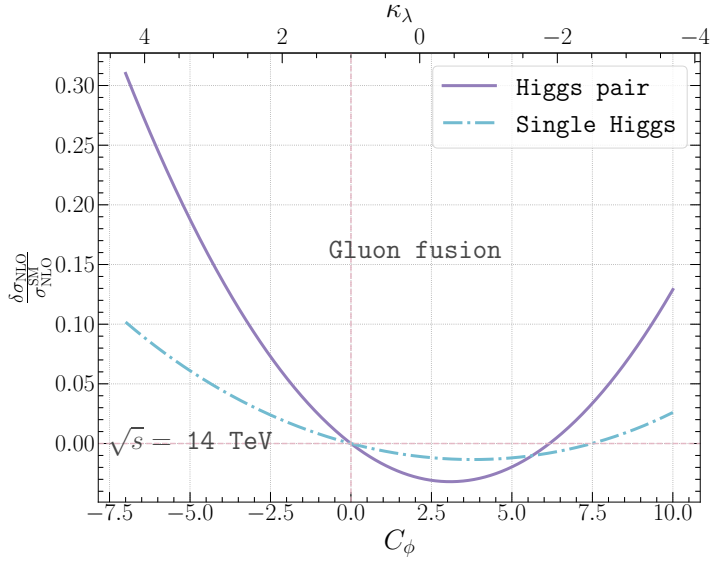


Figure 4.4. The relative change of the NLO QCD cross-section of gluon fusion production of single Higgs (dashed line) and Higgs pair (solid line) at a pp collider with $\sqrt{s} = 14$ TeV as a function of C_ϕ or the corresponding κ_λ .

(a) and (c), respectively, in another EFT, this is not necessarily the case.

4.2 The chiral Lagrangian

Given the strong bonds on the ρ parameter, it would be plausible to assume that the NP maintains the custodial symmetry $SU(2)_V$ and treats the chiral symmetry breaking pattern $SU(2)_L \otimes SU(2)_R \rightarrow SU(2)_V$ the same way the QCD chiral symmetry breaking is treated. Considering the pions as pseudo-Nambu Goldstone bosons to describe their properties and couplings. In the pion case, this is known as **chiral perturbation theory** [191, 192]. The same mathematical description could be applied to the case of EW symmetry breaking by constructing the EW chiral Lagrangian (EWChL). In this formalism, the Goldstone bosons $\pi^a(x)$ of the SM are considered the generators of $SU(2)_L$ unitary transformation.

$$\mathcal{U}(x) = e^{i\pi^a(x)\sigma_a/v}, \quad (4.12)$$

which implies that the Goldstone fields transform non-linearly under $SU(2)_L \otimes SU(2)_R$. As for the Higgs boson $h(x)$, it is added as an $SU(2)_L \otimes U(1)_Y$ singlet, and can appear in the EWChL at any power. Contrary to the SMEFT power counting in the NP scale Λ , in the EWChL, terms are ordered according to their *chiral dimension* χ , defined for

spacetime derivatives ∂_μ , bosonic ϕ, X_μ and ψ fermionic generic fields as [193, 194]

$$[\phi]_\chi = 0, [X]_\chi = 0, [\partial_\mu]_\chi = 1, [\psi]_\chi = 2. \quad (4.13)$$

The zeroth-order term of the EWChL possesses a chiral dimension of $\chi = 2$, while higher-order terms could be considered terms generated perturbatively from L loop interactions, an having a chiral dimension $\chi = 2L + 2$. The expansion of the EWChL is in the chiral order in addition to the powers of $h(x)/v$. This power-counting causes some SMEFT dimension-six operators to be considered of a higher order in EWChL. A prominent example of this is the chromomagnetic operator \mathcal{O}_{tG} being of chiral dimension five. The relevant terms for single- and di-Higgs production of the EWChL are given in the Unitary gauge by [188, 195]

$$\begin{aligned} \mathcal{L}_{\text{HEFT}} = & \frac{h}{v} \left[\left(\delta c_W m_W^2 W_\mu^+ W^{-\mu} + \delta c_Z \frac{m_Z^2}{2} Z_\mu Z^\mu \right) \right. \\ & + c_{ww} \frac{g_2^2}{2} W_{\mu\nu}^+ W^{-\mu\nu} + c_{w\square} g_2^2 \left(W_\mu^- \partial_\nu W^{+\mu\nu} + \text{h.c.} \right) + c_{\gamma\gamma} \frac{\alpha}{8\pi} A_{\mu\nu} A^{\mu\nu} \\ & + c_{zz} \frac{g_2^2 + g_1^2}{4} Z_{\mu\nu} Z^{\mu\nu} + c_{z\gamma} \frac{eg_1}{16\pi^2} Z_{\mu\nu} A^{\mu\nu} + c_{z\square} g_2^2 Z_\mu \partial_\nu Z^{\mu\nu} + c_{\gamma\square} g_2 g_1 Z_\mu \partial_\nu A^{\mu\nu} \Big] \\ & + \frac{\alpha_s}{8\pi} \left(c_{gg} \frac{h}{v} + c_{gg}^{(2)} \frac{h^2}{2v^2} \right) \text{Tr}[G_{\mu\nu} G^{\mu\nu}] - \sum_f \left[m_f \left(c_f \frac{h}{v} + c_{ff} \frac{h^2}{2v^2} \right) \bar{f}_R f_L + \text{h.c.} \right] \\ & - c_{hh} \frac{m_h^2}{2v} h^3 + \dots, \end{aligned} \quad (4.14)$$

I have omitted here the kinetic and mass terms of the Higgs, \mathcal{CP} violating terms, as well as couplings not relevant to LHC phenomenology and higher chiral order operators.

In addition to NP effects, this Lagrangian also includes the LO and NLO SM vertices, for example the parameter $\delta c_V = 1$ corresponds to the tree-level coupling between the Higgs field and the EW bosons $V = W, Z$. While the coupling $c_{gg} = 4/3$ corresponds to the SM effective coupling at NLO if the heavy top limit (HTL) $m_t \rightarrow \infty$ is applied.

In contrast to the SMEFT, the couplings of one and two Higgs bosons to fermions or gluons become de-correlated. Giving this Lagrangian a richer phenomenology for Higgs pair production.

The HEFT coefficients modifying the Higgs pair production via gluon fusion are

$$c_{hh}, \textcolor{teal}{c}_t(a), \textcolor{teal}{c}_{tt}(b), \textcolor{red}{c}_{gg}(c), \textcolor{red}{c}_{gg}^{(2)}(d), \quad (4.15)$$

with the same colours highlighted in the operator insertions of Figure 4.3 and the letter next to the coefficient indicates the diagram, in which the coefficient appears. Full parametrisation of the Higgs pair cross-section at NLO (inclusive and differential) and NNLO (inclusive) can be found in refs. [196–198] and implemented at NLO in POWHEG-BOX [199].

UV-complete models that are related to the EWChL are composite Higgs models [181, 182, 200], dilaton theories [201], techni-dilaton models [202], technicolour models [203] and other models with induced EW symmetry breaking [204, 205].

4.2.1 Translation between SMEFT and HEFT

In order to facilitate the translation between SMEFT and HEFT or to the κ -formalism, one needs to put the SMEFT Lagrangian into the canonical form, that is to convert the operators with covariant derivatives acting on the Higgs to canonically normalised Higgs kinetic term. This is done done by the field redefinition.

$$\phi = \begin{pmatrix} 0 \\ h(1 + c_{h,kin}) + v \end{pmatrix}, \quad (4.16)$$

with

$$c_{h,kin} = \left(C_{\phi,\square} - \frac{1}{4} C_{\phi D} \right) \frac{v^2}{\Lambda^2}. \quad (4.17)$$

This field redefinition will generate derivative interactions of the form $h(\partial_\mu h)^2$ and $h^2(\partial_\mu h)^2$. In order to remove these terms, and for sake of simplicity, I use a gauge-dependent field redefinition⁴

$$h \rightarrow h + c_{h,kin} \left(h + \frac{h^2}{v} + \frac{h^3}{3v^2} \right). \quad (4.18)$$

This field redefinition leads to $c_{h,kin}$ modifying all Higgs couplings.

Before discussing the translation between SMEFT and HEFT, some words of caution are in order: First, HEFT is less restrictive than SMEFT; therefore, it contains more degrees of freedom. This makes some points of the HEFT parameter space unmappable to SMEFT. In addition, the power counting is different in both formalisms, as mentioned before. Some operators present in SMEFT will be absent in HEFT and vice-versa. In Table 4.2, the translation between the HEFT and SMEFT Wilson coefficients of the operators relevant to Higgs pair production at LO is shown. More general translation between SMEFT in Warsaw and SILH basis and HEFT can be done automatically using **Rosetta** package [207]

4.2.2 EFT and κ -formalism

The κ -formalism provides an experimentally accessible and well-defined QFT-wise approach to study the Higgs boson properties. The κ parameters are part of a more generalised formalism called the Higgs **Pseudo-observables** [208]. If the new physics contributions do not generate new Lorentz structures, there is a possible translation between the Wilson coefficients in the SMEFT Warsaw basis and the κ formalism. In

⁴For gauge-independent formalism cf. [206].

HEFT	SMEFT (Warsaw)
c_{hhh}	$1 - 2 \frac{v^4}{m_h^2} C_\phi + 3 c_{h,kin}$
c_f	$1 + c_{h,kin} - C_{f\phi} \frac{v^3}{\sqrt{2} m_f}$
c_{ff}	$-C_{f\phi} \frac{3v^3}{2\sqrt{2} m_f} + c_{h,kin}$
c_{gg}	$8\pi/\alpha_s v^2 C_{\phi G}$
$c_{gg}^{(2)}$	$4\pi/\alpha_s v^2 C_{\phi G}$

Table 4.2. Translation between the Wilson coefficients of HEFT and SMEFT for the operators relevant to Higgs pair production.

particular, taking the rescaling of the trilinear coupling, κ_λ , the translation is given by

$$\kappa_\lambda = 1 - \frac{2v^4}{m_h^2} \frac{C_\phi}{\Lambda^2} + 3 c_{h,kin}. \quad (4.19)$$

A similar relation exists for the rescaling of the quark Yukawa couplings κ_q

$$\kappa_q = 1 + c_{h,kin} - \frac{v^3}{\sqrt{2} m_q} \frac{C_{q\phi}}{\Lambda^2}. \quad (4.20)$$

In these two examples, one can see the similarities between κ -formalism and HEFT, but this is not always the case. Other translations could be obtained by comparing how SMEFT operators modify the Higgs couplings with the SM and matching it with the corresponding κ or other Higgs pseudo-observable.

However, one should be careful while interpreting results quoted in terms of Wilson coefficients in the SMEFT framework extracted from multi-Higgs or multi-vector bosons searches. These results include couplings that are not present in the SM. For example, the $hhq\bar{q}$ coupling, though being linearly related to the quark Yukawa coupling $hq\bar{q}$, is not a rescaling of any SM Higgs coupling. With this in mind, one can strictly remain within a linear EFT and link the rescaling of the quark Yukawa, κ_q , to the $hhq\bar{q}$ coupling through

$$g_{hhq\bar{q}}^{\text{linear-EFT}} = -\frac{3}{2} \frac{1 - \kappa_q}{v} g_{hq\bar{q}}^{\text{SM}}. \quad (4.21)$$

This relation will no longer hold once a non-linear EFT, like HEFT, is used. Hence, the κ -formalism must be applied carefully when multi-Higgs signals are considered.

4.3 Conclusions

Effective field theories provide a systematic yet simplified approach for NP searches by simplifying its complex interaction structures. This can be viewed as a dimensionality reduction approach and collapsing all the NP interactions into effective ones. They would

be observed at colliders with energy reaches below the NP scale Λ . The linear approach to EFT is called the SMEFT that preserves the SM fields and symmetries, and the Higgs boson is a part of an $SU(2)_L$ doublet ϕ like the SM. In contrast, non-linear approaches such as HEFT/EWChL treat the Higgs boson as an added singlet. The latter approach is more general and introduces independent parameters involving multiple Higgs bosons. For example, the couplings $f\bar{f}h$ and $f\bar{f}hh$ will be generated in SMEFT and HEFT. Still, in SMEFT, both are related by the Wilson coefficient $C_{\phi f}$, while in HEFT, they have independent Wilson coefficients c_f and c_{ff} , respectively.

Most of the Wilson coefficients involving Higgs interactions are strongly constrained by EWPOs and Higgs and top-quark data. However, the bounds on the Wilson coefficient modifying Higgs self-couplings C_ϕ remain dominated by theoretical constraints from perturbative unitarity [110, 209]. This can be improved by the searches for Higgs pair production at the HL-LHC, as this process is more sensitive to the trilinear Higgs self-coupling than EWPO and single-Higgs data.

Part II

Single Higgs Processes at the LHC

5 Overview of Higgs production at colliders

Four distinct processes mediate the production of the Higgs boson at the LHC: gluon fusion (ggF), vector-boson fusion (VBF), vector bosons Higgsstrahlung (Vh), and the production with top (and anti-top) pair ($t\bar{t}h$). It should be noted that sometimes the ggF category will include the quark anti-quark annihilation, but this is negligible in the SM but becomes important for significant modifications of light Yukawa couplings. These processes are illustrated in Figure 5.1, and their details were summarised in Table 5.1. These four channels have been observed at the LHC with $> 5\sigma$ significance. Since the experimental measurements of this Higgs were discussed previously in chapter 3, this chapter aims to provide an overview of the current theoretical status of these channels.

Process	Cross-section 13 TeV (pb)	Theo. accuracy	Exp. uncertainty (%)	Contribution (%)
ggF	48.51	N3LO QCD & NLO EW	6.5	88
$t\bar{t}h$ & th	0.58	NLO QCD & NLO EW	20.0	1
VBF	3.78	NNLO QCD* & NLO EW	10.0	7
Vh	2.25	NNLO QCD & NLO EW	15.0	4

Table 5.1. Summary of the Higgs production processes at the LHC.

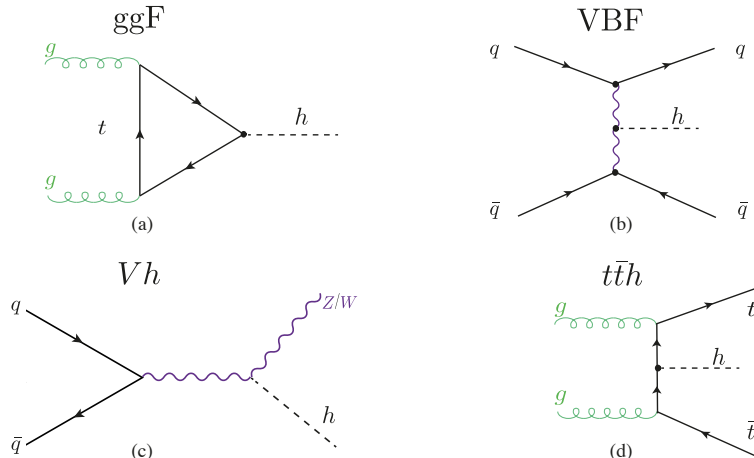


Figure 5.1. Feynman-diagram examples of the leading Higgs production processes at the LHC.

5.1 Current status of the Higgs production channels

5.1.1 Gluon fusion process

The gluon fusion (ggf) has the highest cross-section amongst all the Higgs production channels, and consequently has the lowest experimental uncertainty. This motivates continuous improvements of its theoretical prediction. The current state-of-the-art theoretical computation for the Higgs inclusive cross-section is N³LO in QCD and NLO in EW [210]. A full differential cross-section for the final state $gg \rightarrow h \rightarrow \gamma\gamma$ has been computed recently to N³LO in QCD, also for the kinematic variables y_h , y_{γ_1} , y_{γ_2} , $\Delta y_{1,2}$ using the projection-to-born method [211]. In addition to the fiducial differential cross-section in p_T with experimental cuts has been computed up to third resummed and fixed order, i.e. N³LL' N³LO dependence [212]. The theoretical computation of this fiducial cross-section with different orders compared to the experimental measurement by ATLAS [143] is shown in Figure 5.2, we can see that the resummed result has significantly smaller theoretical uncertainties. The current total theoretical uncertainty with this order calculation is 5.4%, with only 2.7% of it coming from the perturbation order cut-off of the calculation, while the rest comes from the branching fraction, PDF+ α_s , EW corrections and mass uncertainties. When compared to Table 3.1, the projected experimental uncertainty of this final states at the HL-LHC is 4.2%, we see that the uncertainties will become comparable, and if the PDF uncertainties are reduced. The

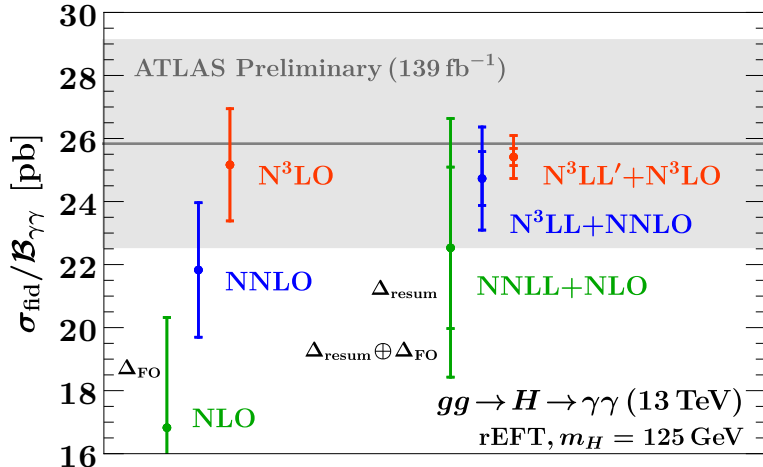


Figure 5.2. The total fiducial cross-section for the final state $gg \rightarrow h \rightarrow \gamma\gamma$ at both fixed and resummed third order compared to the experimental ATLAS measurement [143]. This figure is taken from [212].

predictions can be further improved by the computation of mixed QCD-EW effects. The virtual corrections of these effects were computed in [213], while the two-loop effects with two particle final states appearing in the real corrections of $gg \rightarrow hg$ were computed in [214] using differential equations. The computation was completed by in-

clusion of light quark initial states for the real corrections in [215] with exact quark mass dependence, reducing the EW uncertainty from 2% to $\sim 0.6\%$.

The computation of the three-loop form-factors with full top-mass dependence was carried out by [216, 217]. However, there remains an intricate interplay between the mass effects of gg , qg and qq initial states for the real matrix elements that cannot be fully controlled due to the light quark mass effects.

NLO corrections to the $h + j$ and $h + 2j$ processes were computed by [218] in the FT-approximation that uses exact born and real correction amplitudes, then approximates the two-loop virtuals by

$$|\mathcal{A}^{2\text{-loop}}(m_t, \mu_R^2)|^2 \approx |\mathcal{A}^{1\text{-loop}}(m_t \rightarrow \infty, \mu_R^2)|^2 \frac{|\mathcal{A}^{1\text{-loop}}(m_t)|^2}{A^{(0)}(m_t) \rightarrow \infty|^2}. \quad (5.1)$$

This approximation works superbly even for $p_T \gg m_t$. Later, the full top mass effects computations have been carried out in [219–221] using the high energy (HE) expansion technique.

5.1.2 Vector boson fusion

The VBF channel has a distinctive signature, making it a *bona fide* channel for Higgs signal extraction. The suppressed colour exchange between the quarks results in a little jet activity in the central rapidity region. The quarks will be scattered into two forward jets such that the decay products of the Higgs are found in the region between them. These features allow for excellent measurement of Higgs couplings, observation of challenging decays, and \mathcal{CP} properties determination. Some of these features are also shared with the Vh production channel. Both of these channels contain the VVh vertex that could be written generally as [195]

$$T^{\mu\nu}(p_1, p_2) = a_1 g^{\mu\nu} + a_2 \left(g^{\mu\nu} - 2 \frac{p_2^\mu p_2^\nu}{p_1 \cdot p_2} \right) + a_3 \frac{p_1^\alpha p_2^\beta}{p_1 \cdot p_2} \epsilon^{\mu\nu\alpha\beta}. \quad (5.2)$$

In the SM, only $a_1 \neq 0$, while the rest of the coefficients represent the anomalous coupling. For example, if $a_3 \neq 0$, then the Higgs is \mathcal{CP} odd. The study of the azimuthal angle distribution $d\sigma_{VBF}/d\Delta\phi_{jj}$ allows for the determination of these coefficients, with very little dependence on the higher-order perturbative corrections [222].

The NLO QCD inclusive cross-section is known since the 90’s [223]. Later, these corrections were made for the differential distributions cf. [224, 225]. Unlike the ggF channel, which has an NLO K-factor of 1.6 at 13 TeV [226], the VBF NLO corrections are small $\sim 10\%$. The two-loop NNLO QCD cross-section has been computed, and the most recent results of the two-loop computation were calculated via the structure-function approach [227] in addition to STXS level 1.2 bins with EW corrections [228]. These calculation are implemented in the MC event generator **HAWK** [228–231]. Although these are small corrections, they are non-negligible, and their inclusion is important for uncertainty reduction.

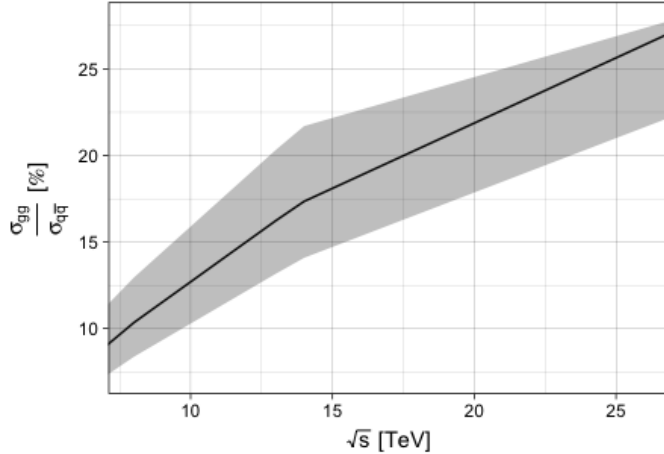


Figure 5.3. The ratio of the LO gluon fusion production cross-section $gg \rightarrow Zh$ (σ_{gg}) with respect to the NLO Drell-Yan process $q\bar{q} \rightarrow Zh$ cross-section ($\sigma_{q\bar{q}}$) at a pp collider with centre-of-mass energy \sqrt{s} . The error band captures the total theoretical uncertainties on both cross-sections dominated by σ_{gg} .

5.1.3 Associated production with EW bosons

The vector boson Higgsstrahlung channels $pp \rightarrow Wh/Zh$ are quark-initiated tree-level processes interpreted as **Drell-Yan process** [232, 233]. They have been computed up to NNLO in QCD ($\sim \alpha_s^2$), and NLO EW ($\sim \alpha^2$) [234].

Despite arising for the first time at NLO, the gluon fusion channel $gg \rightarrow Zh$ has a non-negligible contribution to the total hadronic cross-section $pp \rightarrow Zh$ that reaches up to 16% of the total cross-section contribution at 14 TeV [235], see Figure 5.3. The contribution becomes more significant when one considers the large invariant mass bins of the differential cross-section. This is due to the substantial abundance of gluonic PDFs at the LHC and the extra enhancement coming from the top quark initiated contribution near the $t\bar{t}$ threshold [236], also it has a higher scale uncertainty than the quark anti-quark annihilation $q\bar{q}A$ channel. With these points in mind, and the absence of a gluon fusion channel for the Wh channel, the Zh channel has higher theoretical uncertainties than Wh . This highlights the need to calculate the $gg \rightarrow Zh$ channel to higher orders in perturbation theory to reduce these uncertainties. The inclusion of the two-loop calculations for the ggF part would facilitate the precision measurement of the Zh channel at the future LHC runs, which in terms provides better constraints on several observables, such as sign and magnitude of the top Yukawa and ZZh couplings amongst others [237].

The leading order (LO) contribution to the $gg \rightarrow Zh$ amplitude, given by one-loop diagrams, was computed exactly in refs.[238, 239]. For the NLO computations, the virtual corrections contain multi-scale two-loop integrals, some of which are still not known analytically. The first computation of the NLO terms has been accomplished

by [240], using the HTL asymptotic expansion and setting $m_b = 0$. The HTL NLO computations pointed to a significant K -factor of about ~ 2 . Later, the computation was improved via soft gluon resummation, including NLL terms found in ref. [241]. The NLL matching the fixed-order NLO computation can be found in ref. [240]. Top quark mass effects were first implemented using a combination of HTL and Padé approximants [242]. A data-driven approach to extract the gluon fusion-dominated non-Drell-Yan part of Zh production using the known relation between Wh and Zh associated production has been investigated in ref.[243]. The differential distributions of $gg \rightarrow Zh$ at NLO were studied in ref.[244] via LO matrix element matching.

More recent studies of the NLO virtual corrections to this process were based on the high-energy (HE) expansion improved by Padé approximants with the LME, which extended the validity range of the HE expansion [245]. However, this expansion is only valid for in the invariant mass region $\sqrt{\hat{s}} \gtrsim 750 \text{ GeV}$ and $\sqrt{\hat{s}} \lesssim 350 \text{ GeV}$ that only covers $\sim 32\%$ of the hadronic cross-section. Furthermore, numerical computation of the two-loop virtual corrections, though implemented exactly in [246], are rather slow for practical use in MC simulations. This highlights the importance of an analytical method that can cover the remaining region of the cross-section and then merged with the HE expansion via Padé approximants. Fortunately, the two-loop corrections to the triangle diagrams can be computed exactly. And the loop integrals appearing in the box correction having no analytic expression can be expanded in small Z (or Higgs) transverse momentum p_T . This method was first used for Higgs pair production in [11] to compute the NLO virtual corrections to the box diagrams in the forward kinematics. In chapter 6, I discuss the calculation performed by my collaborators and myself and published in [247], which includes the full top mass dependence of the virtual two-loop correction to $gg \rightarrow Zh$ in an analytic form using the same p_T expansion technique.

5.1.4 Associated production with top quarks

The largest part of the $t\bar{t}h/th$ uncertainty budget comes from the theoretical modelling of this process's backgrounds, mainly $t\bar{t}b\bar{b}$, $t\bar{t}W$ as backgrounds for $t\bar{t}(h \rightarrow b\bar{b})$ and $t\bar{t}(h \rightarrow \text{multileptons})$, respectively. There have been several theoretical developments regarding these backgrounds. Starting with $t\bar{t}W$, the differential cross-section at NNLL+ NLO QCD calculation of this channel has been done in [248, 249] including EW corrections. In addition to the computation of the fully-decayed final state at NLO QCD [250–252] and at NLO-EW [253]. These calculations were implemented in **POWHEG-BOX** [254]. The comparison between the NLO-QCD with Parton showering vs on-shell can be found in [255]. As for $t\bar{t}b\bar{b}$, the progress in obtaining higher-order corrections is faced with challenges posed by the complexity of this channel. However, progress has been made. For instance, the off-shell effects in the fully decayed $pp \rightarrow 2\ell 2\nu 4b$ with NLO corrections were studied in [256, 257]. Further discussion of the theoretical developments of these channels is beyond the scope of this thesis.

Regarding the higher-order corrections to the $t\bar{t}h/th$ channel itself, the NLO QCD+EW effects on the off-shell multileptons final state were studied in [258]. In contrast, the NLO corrections, including SMEFT operators, were calculated in[259]. The NLO QCD+EW

with Parton showering is available in all event generators, and the SMEFT operators at NLO are available in `MadGraph5_aMC@NLO`. As of writing this thesis, there is no NNLO calculation of $t\bar{t}h/th$ available.

5.2 Concluding remarks

The precision-era of Higgs measurements requires developments on both experimental and theoretical levels. The experimental precision can be improved with higher luminosities and energies, better detectors and improved analysis techniques. Theoretical uncertainties require higher-order calculations in perturbation theory, the inclusion of mixed EW and QCD terms, the inclusion of mass effects and suitable Parton distribution functions with higher order in QCD. Much effort is being put into improving the theoretical predictions of Higgs production channels. Moreover, a plethora of computer tools have been made available to facilitate the computation of these cross-sections, for example `iHixs2` [260] or to generate full events, like `POWHEG` [261–267] and `MadGraph5_aMC@NLO` [268], and many others can be found with greater detail in the LHC-HXWG Twiki page [269].

Sometimes, to improve the measurement of the process, it is not sufficient to include Higher-order terms of the channel itself and its backgrounds that is particularly important for $t\bar{t}h$. Hence, higher-order calculations of processes like $t\bar{t}W$ with Parton-shower effects as well as improved analysis to distinguish $t\bar{t}(h \rightarrow b\bar{b})$ have a significant impact on $t\bar{t}h$ measurements. Event generator tools with SMEFT implementation for Higgs processes with patron showing interface capabilities have been implemented in a `MadGraph5_aMC@NLO` model `SMEFTatNLO` [270] that enabled loop computations with SMEFT operators and consequently fits of the SMEFT Wilson coefficients with Higgs data at NLO as we have seen in chapter 4.

There is plenty of room for future improvements in the reduction of theory uncertainty budget and providing better theoretical prediction of the Higgs processes in the SM and beyond, from the inclusion of Patron shower matching, merging and validation to the inclusion of two-loop calculations of gluon fusion Zh and EW NLO effects of $t\bar{t}he$, all in preparation for the HL-LHC Higgs precision era!

6 Virtual two-loop calculation of Zh production via gluon fusion

Higgs couplings to the weak vector bosons are approaching the precision level. For their measurements, both VBF and Vh channels are needed. The associated Higgs production with the vector bosons is crucial for measuring the VVh coupling amongst others, as discussed in subsection 5.1.3. The most notable example emphasising the importance of this channel is the measurement of the Higgs decaying to beauty quarks $h \rightarrow b\bar{b}$ by both ATLAS and CMS [271, 272]. Hence, the Vh Higgs production has significant potential for the future runs of the LHC. The statistical and systematic uncertainties coming from the experimental setup of the LHC will be eventually reduced in future runs due to higher integrated luminosity, upgraded detectors and improved analysis techniques. There is an exigency to reduce theoretical uncertainties emerging from the perturbative calculations of cross-sections; to achieve that, one should include higher-order terms. Since Wh production has no gluon fusion component, it has a better theoretical modelling compared to the Zh process. This is due to the fact that the main source of uncertainties stems from the gluon fusion sub-process present in Zh . Higher-order corrections to the $gg \rightarrow Zh$ are essential for improving this process's theoretical modelling.

It should be noted that the Zh channel can receive contributions from new particles [273], also as we shall see in chapter 10; particularly at the large invariant-mass region where the gluon fusion contribution becomes more important, and HTL approximation would typically fail. Therefore, a better understanding of the SM prediction of the Zh gluon fusion channel is crucial for the SM precision measurements of Higgs production within the SM and testing NP in this channel.

This chapter aims to demonstrate the use of the p_T -expansion technique, developed in [11] as an approach to computing the two-loop virtual corrections to $gg \rightarrow Zh$ analytically, including top quark mass effects. This method also allows for the use of Padé approximants to extend the validity range of this calculation as what has been done in ref. [274].

This chapter is structured as follows: section 6.1 contains the general notation that is used for the gluon fusion production Zh production calculation. Then in subsection 6.1.1, the transverse momentum expansion method is discussed. Calculation of the LO form-factors in the transverse momentum expansion is illustrated in section 6.2 as a proof of concept for this technique. The outline of the two-loop calculation is discussed in section 6.3. Finally, in section 6.4, the results of this calculation are shown with concluding remarks at the end. This chapter is based on the work that my collaborators and I have published in [247].

6.1 General notation

The amplitude $g_a^\mu(p_1)g_b^\nu(p_2) \rightarrow Z^\rho(p_3)h(p_4)$ can be written as

$$\mathcal{A} = i\sqrt{2}\frac{m_Z G_F \frac{\alpha_s^0}{4\pi}(\mu_R)}{\pi} \delta_{ab} \epsilon_\mu^a(p_1) \epsilon_\nu^b(p_2) \epsilon_\rho(p_3) \hat{\mathcal{A}}^{\mu\nu\rho}(p_1, p_2, p_3), \quad (6.1)$$

$$\hat{\mathcal{A}}^{\mu\nu\rho}(p_1, p_2, p_3) = \sum_{i=1}^6 \mathcal{P}_i^{\mu\nu\rho}(p_1, p_2, p_3) \mathcal{A}_i(\hat{s}, \hat{t}, \hat{u}, m_t, m_h, m_Z), \quad (6.2)$$

where μ_R is the renormalisation scale and $\epsilon_\mu^a(p_1) \epsilon_\nu^b(p_2) \epsilon_\rho(p_3)$ are the polarization vectors of the gluons and the Z boson, respectively. It is possible to decompose the amplitude into a maximum of six Lorentz structures encapsulated by the tensors $\mathcal{P}_i^{\mu\nu\rho}$. Due to the presence of the γ_5 , these projectors are proportional to the Levi-Civita total anti-symmetric tensor $\epsilon^{\alpha\beta\gamma\delta}$. One can choose to project the amplitude using a set of orthogonal basis, which is explicitly shown in [section A.1](#). The projectors should therefore satisfy the relation

$$\mathcal{P}_i^{\mu\nu\rho} \mathcal{P}_{j\mu\nu\rho} = 0, \quad \text{for } i \neq j. \quad (6.3)$$

By this choice one obtains unique form-factors corresponding to each projector

$$\mathcal{A}_i(\hat{s}, \hat{t}, \hat{u}, m_t, m_h, m_Z), \quad (6.4)$$

that are multivariate complex functions of the top quark (m_t), Higgs (m_h) and Z (m_Z) bosons masses, and of the Partonic Mandelstam variables

$$\hat{s} = (p_1 + p_2)^2, \quad \hat{t} = (p_1 + p_3)^2, \quad \hat{u} = (p_2 + p_3)^2, \quad (6.5)$$

where $\hat{s} + \hat{t} + \hat{u} = m_Z^2 + m_h^2$ and all the momenta are considered to be incoming. The form-factors \mathcal{A}_i can be perturbatively expanded in orders of α_s ,

$$\mathcal{A}_i = \sum_{k=0} \left(\frac{\alpha_s}{\pi} \right)^k \mathcal{A}_i^{(k)}. \quad (6.6)$$

Where $\mathcal{A}_i^{(0)}$ and $\mathcal{A}_i^{(1)}$ are the LO and NLO terms, respectively. Using Fermi's Golden Rule, we can write the Born Partonic cross-section as

$$\hat{\sigma}^{(0)}(\hat{s}) = \frac{m_Z^2 G_F^2 \alpha_s(\mu_R)^2}{64\hat{s}^2(2\pi)^3} \int_{\hat{t}^-}^{\hat{t}^+} d\hat{t} \sum_i |\mathcal{A}_i^{(0)}|^2, \quad (6.7)$$

where $\hat{t}^\pm = [-\hat{s} + m_h^2 + m_Z^2 \pm \sqrt{(\hat{s} - m_h^2 - m_Z^2)^2 - 4m_h^2 m_Z^2}] / 2$.

The LO ggF process has two sets of diagrams, the triangle, and the box, depicted in [Figure 6.1](#). In (a), the triangle diagram contains a neutral Goldstone boson G^0 . Instead in (b), the Z boson is mediated. The interplay between these two diagram types depends on the ξ gauge. Moreover, the Z boson is strictly off-shell, due to Furry's

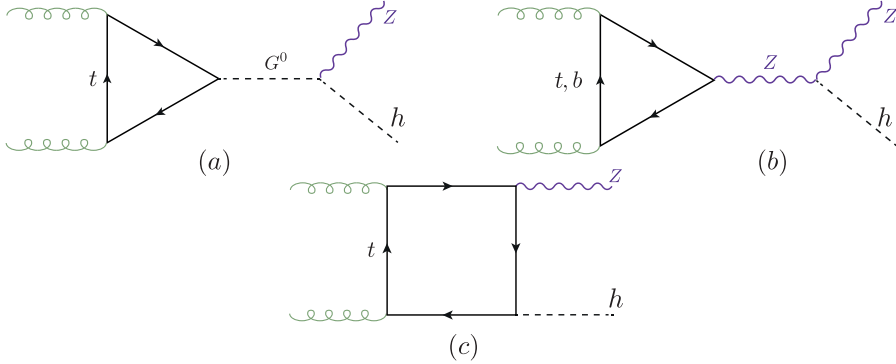


Figure 6.1. Example Feynman diagrams for the LO $gg \rightarrow Z h$ process. The triangle diagrams in a general ξ gauge involve Z and the neutral Goldstone G^0 propagators.

theorem [275]. In the Landau gauge, the Z -mediated diagrams will also vanish; this can be seen by considering the sub-amplitude ggZ^* that, in the Landau gauge, can be related to the decay of a massive vector boson with mass $\sqrt{\hat{s}}$ into two massless ones. Such process is forbidden by the Landau-Yang theorem [276, 277]. The triangle diagrams are also proportional to the mass difference between the up- and down-type quarks. In this calculation, only the top quark is considered massive. Therefore, light quarks loops do not contribute to this process. It should be noted that triangle diagrams with b -quark loops contribute to $\sim 1\%$ of the total amplitude, computed in the massless limit, i.e. $m_b \rightarrow 0$.

6.1.1 The transverse momentum expansion

Choosing to expand in small p_T of the Z boson, the first step is expressing the transverse momentum in terms of the Mandelstam variables and masses

$$p_T^2 = \frac{\hat{t}\hat{u} - m_Z^2 m_h^2}{\hat{s}}. \quad (6.8)$$

From eq.(6.8), together with the relation between the Mandelstam variables, one finds

$$p_T^2 + \frac{m_h^2 + m_Z^2}{2} \leq \frac{\hat{s}}{4} + \frac{\Delta_m^2}{\hat{s}}, \quad (6.9)$$

where $\Delta_m = (m_h^2 - m_Z^2)/2$. Eq.(6.9) implies $p_T^2/\hat{s} < 1$ that, together with the kinematical constraints $m_h^2/\hat{s} < 1$ and $m_Z^2/\hat{s} < 1$. With these relations in mind, one can expand the amplitudes in terms of small p_T^2/\hat{s} , m_h^2/\hat{s} and m_Z^2/\hat{s} , which is technically valid throughout the whole phase space, contrary to the HTL and HE limits. The caveat for this expansion is that the amplitude does not depend on p_T explicitly. Instead, one would expand in

the reduced Mandelstam variables $t'/s' \ll 1$ or $u'/s' \ll 1$, defined as

$$s' = p_1 \cdot p_2 = \frac{\hat{s}}{2}, \quad t' = p_1 \cdot p_3 = \frac{\hat{t} - m_Z^2}{2}, \quad u' = p_2 \cdot p_3 = \frac{\hat{u} - m_Z^2}{2} \quad (6.10)$$

that satisfy

$$s' + t' + u' = \Delta_m. \quad (6.11)$$

The choice of the expansion parameter t' or u' depends on whether one expands in the forward or backwards kinematics. Because the process $gg \rightarrow Zh$ has two particles in the final states with different masses, the amplitude is not symmetric under their exchange. Therefore, it is not possible to simply compute the cross-section via integrating the forward-expanded amplitude, contrary to what has been done for the Higgs pair production [11]. To overcome this issue, it is possible, via examining the projectors in section A.1 and observing that they can be split into symmetric and anti-symmetric parts with respect to the exchange $t' \leftrightarrow u'$. Then, one can expand the symmetric part in the forward kinematics, like the Higgs pair case. Regarding the anti-symmetric part, the antisymmetric factor is simply extracted by multiplying the form-factors by $1/(\hat{t} - \hat{u})$, which is written as $1/(2s' - 4t' - 2\Delta_m)$. Afterwards, the expansion in the forward kinematics can be performed then the result should be multiplied back by $(\hat{t} - \hat{u})$.

In order to implement the p_T -expansion at the Feynman-diagram level, we start by splitting the momenta into longitudinal and transverse components with respect to the beam direction. This can be done by introducing the auxiliary vector [11],

$$r^\mu = p_1^\mu + p_3^\mu, \quad (6.12)$$

that satisfies

$$r^2 = \hat{t}, \quad r \cdot p_1 = \frac{\hat{t} - m_Z^2}{2}, \quad r \cdot p_2 = -\frac{\hat{t} - m_h^2}{2}, \quad (6.13)$$

and hence can be also written as

$$r^\mu = -\frac{\hat{t} - m_h^2}{\hat{s}} p_1^\mu + \frac{\hat{t} - m_Z^2}{\hat{s}} p_2^\mu + r_\perp^\mu = \frac{t'}{s'} (p_2^\mu - p_1^\mu) - \frac{\Delta_m}{s'} p_1^\mu + r_\perp^\mu, \quad (6.14)$$

where

$$r_\perp^2 = -p_T^2. \quad (6.15)$$

substituting the definition of p_T from eq.(6.8) one obtains

$$t' = -\frac{s'}{2} \left\{ 1 - \frac{\Delta_m}{s'} \pm \sqrt{\left(1 - \frac{\Delta_m}{s'}\right)^2 - 2\frac{p_T^2 + m_Z^2}{s'}} \right\} \quad (6.16)$$

implying that the expansion in small p_T (the minus sign case in eq.(6.16)) can be realised at the level of Feynman diagrams, by expanding the propagators in terms of the vector r^μ around $r^\mu \sim 0$ or, equivalently, $p_3^\mu \sim -p_1^\mu$, see eq.(6.14).

6.2 Born cross-section in the p_T -expansion

As a baseline test for the validity and convergence behaviour of the p_T -expansion, this method is first applied to the LO amplitude, and consequently used to compute the Born Partonic cross-section. The results are then compared to the exact cross-section calculation found in [238, 239].

We start by defining the one-loop functions appearing in the similar calculation of the Born cross-section for $gg \rightarrow hh$ in the same expansion carried out in ref. [11]

$$B_0[\hat{s}, m_t^2, m_t^2] \equiv B_0^+, \quad B_0[-\hat{s}, m_t^2, m_t^2] \equiv B_0^-, \quad (6.17)$$

$$C_0[0, 0, \hat{s}, m_t^2, m_t^2, m_t^2] \equiv C_0^+, \quad C_0[0, 0, -\hat{s}, m_t^2, m_t^2, m_t^2] \equiv C_0^- \quad (6.18)$$

$$B_0[q^2, m_1^2, m_2^2] = \frac{1}{i\pi^2} \int \frac{d^n k}{\mu^{n-4}} \frac{1}{(k^2 - m_1^2)((k+q)^2 - m_2^2)}, \quad (6.19)$$

$$C_0[q_a^2, q_b^2, (q_a + q_b)^2, m_1^2, m_2^2, m_3^2] = \frac{1}{i\pi^2} \int \frac{d^d k}{\mu^{d-4}} \frac{1}{[k^2 - m_1^2][(k+q_a)^2 - m_2^2][(k-q_b)^2 - m_3^2]} \quad (6.20)$$

are the Passarino-Veltman functions [278], with d is the spacetime dimension and μ the 't Hooft mass. There are only two non-vanishing form-factors at LO, one is symmetric \mathcal{A}_2 , and the other is antisymmetric \mathcal{A}_6 , in the p_T -expansion, these form-factors are given by,

up to order $\mathcal{O}(p_T^2)$

$$\begin{aligned}
\mathcal{A}_2^{(0,\Delta)} &= -\frac{p_T}{\sqrt{2}(m_Z^2 + p_T^2)}(\hat{s} - \Delta_m)m_t^2 C_0^+, \\
\mathcal{A}_2^{(0,\square)} &= \frac{p_T}{\sqrt{2}(m_Z^2 + p_T^2)} \left\{ \right. \\
&\quad \left(m_t^2 - m_Z^2 \frac{\hat{s} - 6m_t^2}{4\hat{s}} - p_T^2 \frac{12m_t^4 - 16m_t^2\hat{s} + \hat{s}^2}{12\hat{s}^2} \right) B_0^+ \\
&- \left(m_t^2 - \Delta_m \frac{m_t^2}{(4m_t^2 + \hat{s})} + m_Z^2 \frac{24m_t^4 - 6m_t^2\hat{s} - \hat{s}^2}{4\hat{s}(4m_t^2 + \hat{s})} - \right. \\
&\quad \left. p_T^2 \frac{48m_t^6 - 68m_t^4\hat{s} - 4m_t^2\hat{s}^2 + \hat{s}^3}{12\hat{s}^2(4m_t^2 + \hat{s})} \right) B_0^- \\
&+ \left(2m_t^2 - \Delta_m + m_Z^2 \frac{3m_t^2 - \hat{s}}{\hat{s}} + p_T^2 \frac{3m_t^2\hat{s} - 2m_t^4}{\hat{s}^2} \right) m_t^2 C_0^- \\
&+ \left(\hat{s} - 2m_t^2 + m_Z^2 \frac{\hat{s} - 3m_t^2}{\hat{s}} + p_T^2 \frac{2m_t^4 - 3m_t^2\hat{s} + \hat{s}^2}{\hat{s}^2} \right) m_t^2 C_0^+ \\
&+ \log \left(\frac{m_t^2}{\mu^2} \right) \frac{m_t^2}{(4m_t^2 + \hat{s})} \left(\Delta_m + 2m_Z^2 + p_T^2 \frac{2\hat{s} - 2m_t^2}{3\hat{s}} \right) \\
&- \left. \Delta_m \frac{2m_t^2}{(4m_t^2 + \hat{s})} + m_Z^2 \frac{\hat{s} - 12m_t^2}{4(4m_t^2 + \hat{s})} + p_T^2 \frac{8m_t^4 - 2m_t^2\hat{s} + \hat{s}^2}{4\hat{s}(4m_t^2 + \hat{s})} \right\},
\end{aligned} \tag{6.22}$$

and

$$\mathcal{A}_6^{(0,\Delta)} = 0, \tag{6.23}$$

$$\begin{aligned}
\mathcal{A}_6^{(0,\square)} &= \frac{\hat{t} - \hat{u}}{\hat{s}^2} p_T \left[\frac{m_t^2}{2} \left(B_0^- - B_0^+ \right) - \frac{\hat{s}}{4} \right. \\
&- \left. \frac{2m_t^2 + \hat{s}}{2} m_t^2 C_0^- + \frac{2m_t^2 - \hat{s}}{2} m_t^2 C_0^+ \right],
\end{aligned} \tag{6.24}$$

where these form-factors are divided into triangle (Δ) and box (\square) contributions, and B_0 functions are understood as the finite part of the integrals on the right hand side of eq.(6.19).

Using several truncations of the p_T -expansion, and comparing it to the exact LO result, one can see in Figure 6.2 the exact Born partonic LO cross-section (red line) as a function of the invariant mass of the Zh system M_{Zh} , in comparison to the p_T -expansions. For the numerical evaluation of the cross-section here and in the following section, the SM

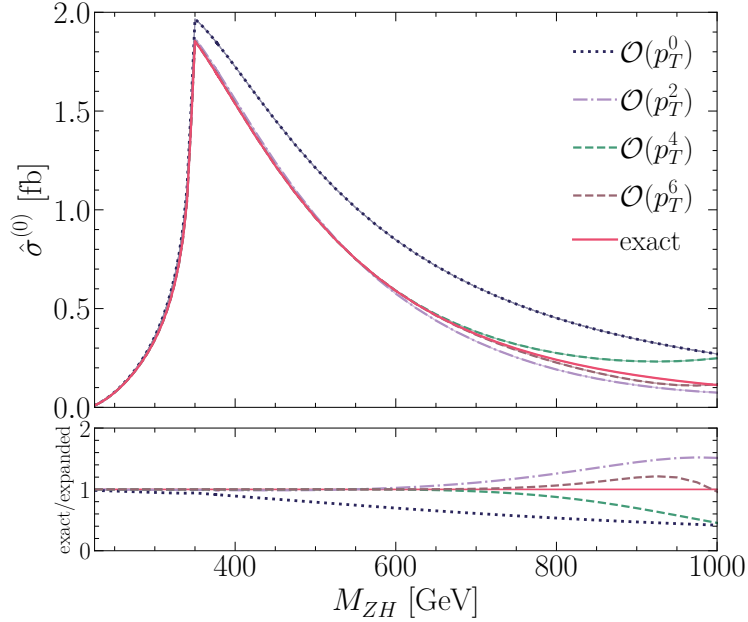


Figure 6.2. The Born Partonic cross-section as a function of the invariant mass M_{Zh} . The exact result (red line) is plotted together with expansions at different orders in p_T (dashed lines). In the bottom part, the ratios of the full result over the p_T -expanded ones at various orders are shown. This plot has been published in [247].

input parameters are used

$$m_Z = 91.1876 \text{ GeV}, \quad m_h = 125.1 \text{ GeV}, \quad m_t = 173.21 \text{ GeV}, \\ m_b = 0 \text{ GeV}, \quad G_F = 1.16637 \text{ GeV}^{-2}, \quad \alpha_s(m_Z) = 0.118.$$

From the ratio plotted in the lower panel of Figure 6.2, we observe that the $\mathcal{O}(p_T^0)$ expansion is in good agreement with the exact result when $M_{Zh} \lesssim 2m_t$. Inclusion of higher-order terms up to $\mathcal{O}(p_T^6)$ extended the validity of the expansion to reach $M_{Zh} \lesssim 750$ GeV. This is the similar behaviour seen in [11] for the Higgs pair. Therefore, one would expect the p_T -expanded two-loop virtual correction to be an accurate approximation with the exact (numerical) result for the region of the invariant mass of $M_{Zh} \sim 700 - 750$ GeV. Similar conclusions can be seen more explicitly in Table 6.1, where it is shown that the Partonic cross-section expanded to order $\mathcal{O}(p_T^4)$ agrees with the full result for $M_{ZH} \lesssim 600$ GeV on the per-mille level. The agreement further improves when $\mathcal{O}(p_T^6)$ terms are included.

M_{Zh} [GeV]	$\mathcal{O}(p_T^0)$	$\mathcal{O}(p_T^2)$	$\mathcal{O}(p_T^4)$	$\mathcal{O}(p_T^6)$	full
300	0.3547	0.3393	0.3373	0.3371	0.3371
350	1.9385	1.8413	1.8292	1.8279	1.8278
400	1.6990	1.5347	1.5161	1.5143	1.5142
600	0.8328	0.5653	0.5804	0.5792	0.5794
750	0.5129	0.2482	0.3129	0.2841	0.2919

Table 6.1. The Partonic cross-section $\hat{\sigma}^{(0)}$ at various orders in p_T and the full computation for several values of M_{Zh} . This table has been published in [247].

6.3 NLO calculation

The virtual two-loop corrections to $gg \rightarrow Zh$ are shown in Figure 6.3, which involve corrections to the triangle topology in (a) and (b). The corrections to the box topology in (c) and a new topology, denoted by the double triangle in (d). Both two-loop corrections to the triangles and the double triangle diagrams can be computed analytically. However, the virtual two-loop box diagrams contain master-integrals (MI's) that have no analytic solutions so far. The two-loop box diagrams are therefore computed in the p_T -expansion.

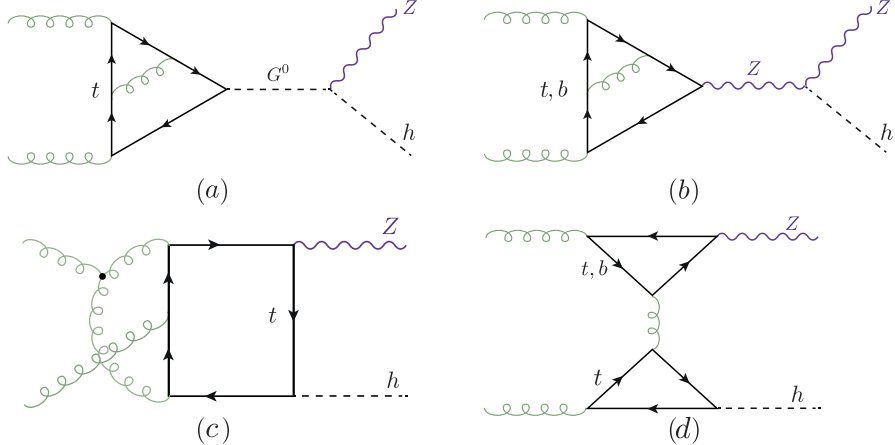


Figure 6.3. Feynman diagrams examples for the virtual NLO corrections to the $gg \rightarrow Zh$ process.

6.3.1 Renormalisation

The two-loop corrections to the triangle and box diagrams contain both UV and IR divergences. The first emerges from UV divergent sub-diagrams, such as top-quark mass renormalisation and QCD vertex correction, while the IR divergences come from

massless loops. In order to remove these divergences, it is needed to introduce adequate counter-terms. On the other hand, the double triangle topology is both UV and IR finite.

The gluon wavefunction renormalisation of the incoming gluons (external legs) is achieved by multiplying the amplitude by the renormalisation factor $Z_A^{1/2}$ for each gluon.

$$Z_A = 1 + \frac{\alpha_s^0}{4\pi} \frac{2}{3\epsilon} \left(\frac{\mu_R^2}{m_t^2} \right)^\epsilon. \quad (6.25)$$

The on-shell scheme for the top-quark mass renormalisation has been used, in which the bare mass is replaced by the renormalised one $m_0 = Z_m m$ in the propagators. This gives the $\overline{\text{MS}}$ renormalised mass.

$$Z_m = 1 + C_F \frac{3}{\epsilon}. \quad (6.26)$$

In order to convert the mass definition to the on-shell scheme, it is possible to add the finite renormalisation term

$$Z_m^{OS} = 1 - 2C_F, \quad (6.27)$$

here $C_F = (N_c^2 - 1)/2N_c$ is one of the two Casimir invariants of QCD along with $C_A = N_c$. The $q\bar{q}g$ vertex correction involves a renormalisation of the strong couplings constant α_s , which is achieved via replacing the bare constant α_s^0 with the renormalised one, hence it becomes $\alpha_s^0 = \frac{\mu_R^{2\epsilon}}{S_\epsilon} Z_{\alpha_s} \alpha_s$, where

$$Z_{\alpha_s} = 1 - \frac{\alpha_s}{4\pi} \frac{1}{\epsilon} \left(\beta_0 - \frac{2}{3} \right) \left(\frac{\mu_R^2}{m_t^2} \right)^\epsilon, \quad (6.28)$$

and the constant $\beta_0 = \frac{11}{3}C_A - \frac{2}{3}N_f$, where N_f is the number of “active” flavours. The 5-flavour scheme $N_f = 5$ is adopted here.

The loop integrals were evaluated using dimensional regularisation in $d = 4 - 2\epsilon$ dimensions. This scheme requires some caution when γ_5 is present in the amplitude. The approach followed in this calculation is letting γ_5 naively anti-commute with all d -dimensional γ_μ 's, and then correct that with the finite renormalisation constant known as **Larin counter-term** [279]

$$Z_5 = 1 - 2C_F. \quad (6.29)$$

The renormalised amplitude is written as

$$\mathcal{M}(\alpha_s, m, \mu_R) = Z_A \mathcal{M}(\alpha_s^0, m^0). \quad (6.30)$$

Putting all the above substitutions together, we get the renormalised two-loop form-

factor:

$$(\mathcal{A}^{(1)})^R = \mathcal{A}^{(1)} - \mathcal{A}_{UV}^{(0)} - \mathcal{A}_{UV,m}^{(0)} + \mathcal{A}_{\text{Larin}}^{(0)} \quad (6.31)$$

$$\mathcal{A}_{UV}^{(0)} = \frac{\alpha_s}{4\pi} \frac{\beta_0}{\epsilon} \left(\frac{\mu_R^2}{\hat{s}} \right)^{-\epsilon} \mathcal{A}^{(0)}.$$

$$\mathcal{A}_{UV,m}^{(0)} = \frac{\alpha_s}{4\pi} \left(\frac{3}{\epsilon} - 2 \right) C_F \left(\frac{\mu_R^2}{\hat{s}} \right)^{-\epsilon} m^0 \partial_m \mathcal{A}^{(0)}. \quad (6.32)$$

$$\mathcal{A}_{\text{Larin}}^{(0)} = -\frac{\alpha_s}{4\pi} C_F \mathcal{A}^{(0)}.$$

The following IR-counter-term is used in order to cancel the IR divergences

$$\mathcal{A}_{IR}^{(0)} = \frac{e^{\gamma_E \epsilon}}{\Gamma(1-\epsilon)} \frac{\alpha_s}{4\pi} \left(\frac{\beta_0}{\epsilon} + \frac{C_A}{\epsilon^2} \right) \left(\frac{\mu_R^2}{\hat{s}} \right)^{2\epsilon} \mathcal{A}^{(0)}. \quad (6.33)$$

The one-loop form-factors, need to be expanded up to order $\mathcal{O}(\epsilon^2)$, for the UV and IR counter-terms.

6.3.2 Calculation of the exact virtual corrections

The two-loop calculations of the triangle diagrams involves the diagrams with Z^* and G^0 propagators, depending on the gauge of choice. Observations found in ref. [240] shows that due to Landau-Yang theorem in the Landau gauge, all diagrams with the Z^* exchange vanish. Therefore, the part of the top triangle diagrams can be obtained from the decay amplitude of a pseudoscalar boson into two gluons that is known in the literature in the full mass dependence up to NLO terms [280, 281]. On the contrary, using the unitary gauge, the NLO calculation needs to be done with the Z^* exchange diagrams only. The calculations in these two gauges result in apparently different Lorentz structures that are linked via the Schouten identity

$$q^\alpha \epsilon^{\beta\gamma\delta\phi} + q^\beta \epsilon^{\gamma\delta\phi\alpha} + q^\gamma \epsilon^{\delta\phi\alpha\beta} + q^\gamma \epsilon^{\delta\phi\alpha\beta} + q^\delta \epsilon^{\phi\alpha\beta\gamma} + q^\phi \epsilon^{\alpha\beta\gamma\delta} = 0. \quad (6.34)$$

A cross-check has been preformed in order to ensure that the NLO calculation introduces no new Lorentz structures, and gives the same result in a general R_ξ gauge as the results in [280, 281]. The two-loop calculation has been carried out in the R_ξ gauge. The amplitudes have been automatically generated by **FeynArts** [282] and contracted with the projectors as defined in section A.1 using **FeynCalc** [283, 284] and **Package X** [285] and in-house Mathematica routines. The two-loop integrals were reduced to a set of master integrals MI, illustrated graphically in Figure 6.4 using **Kira** [286]. These MI's are either products of one-loop functions (a)-(c), (e),(f),(h) and (l) or can be found in the literature [281, 287]. Their implementation in this calculation has been validated numerically using **SecDec** [288, 289]. The virtual correction for the triangle diagrams

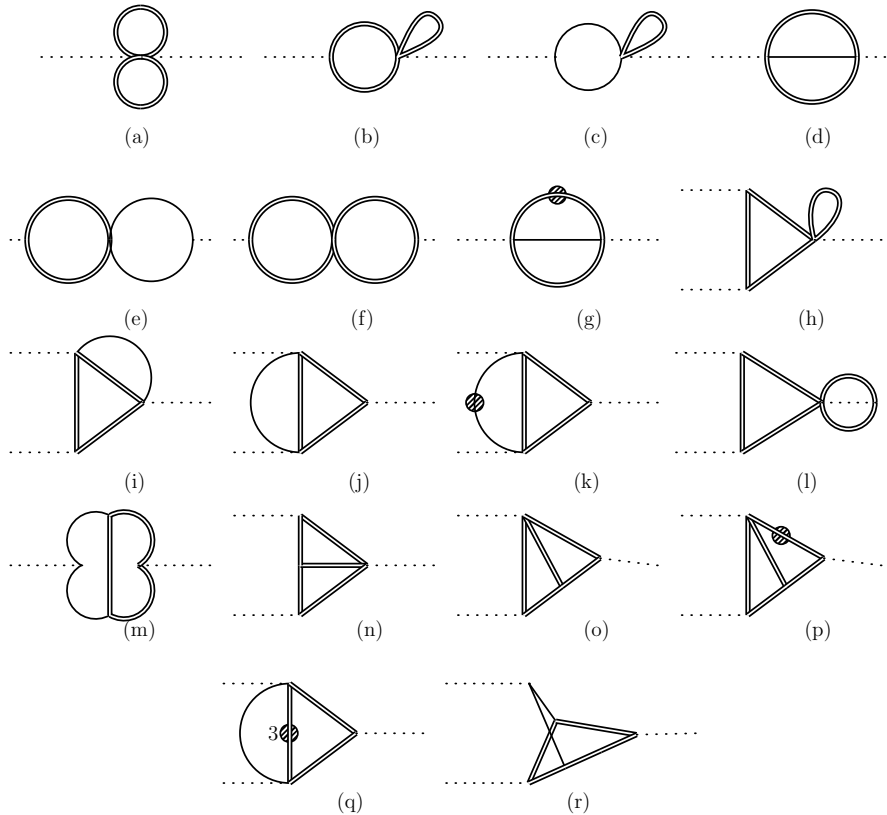


Figure 6.4. The list of two-loop master integrals (MI's) resulting from the reduction of the two-loop triangle corrections. The product of one-loop MI's appearing in this list also appear in the calculation of the double-triangle diagrams. A single line denotes a massless propagator, while a double line denotes a massive one. The dot denotes a squared propagator unless the number of the exponent is indicated.

can be separated according to their colour factors into

$$\mathcal{A}^{(1)} = C_F \mathcal{A}_{CF}^{(1)} + C_A \mathcal{A}_{CA}^{(1)}, \quad (6.35)$$

The C_A part contains a double pole $\mathcal{O}(1/\epsilon^2)$ and a single pole $\mathcal{O}(1/\epsilon)$. Whilst the C_F part only contains a UV divergent single pole, which needs to be cancelled via mass and vertex renormalisation. The poles do not have a dependence on the renormalisation scale μ_R . However, there is a dependence on that scale in the finite part, as well. No new Lorentz structures appears, and the final result in R_ξ matched the one found in [280, 281] for the Landau gauge. The explicit results are shown in Appendix B

The calculation of the double triangle diagrams (d) of Figure 6.3 is fairly straightforward, all of the integrals can be rewritten in terms of products of one-loop functions. All of the Lorentz structures appear in the double triangle except for \mathcal{P}_6 , analogous to the triangle case. The explicit forms of form-factors corresponding to these structures is presented in Appendix B. Although in this calculation, the amplitude has been written using a different tensorial structure compared to ref.[245]. It was checked, using the relations between the two tensorial structures reported in section A.1 that the result obtained here is in agreement with the one presented in ref. [242].

6.3.3 Calculation of the p_T -expanded virtual corrections

The two-loop triangle diagrams can also be interpreted as an expansion in p_T , but this expansion terminates at $\mathcal{O}(p_T^2)$, rather than being an infinite series. Hence, in this section, we concentrate on the two-loop box diagrams p_T -expansion¹.

Like the two-loop triangle diagrams, the box diagrams amplitudes were generated and projected through the same pipeline. After the contraction of the epsilon tensors, the diagrams were expanded as described in subsection 6.1.1, keeping only $\mathcal{O}(p_T^4)$ terms. They were reduced to MIs using FIRE [290] and LiteRed [291]. The resulting MIs were identical to those for Higgs pair production [11]. Nearly all of them are expressed in terms of generalised harmonic polylogarithms, except for two elliptic integrals [292, 293]. The renormalisation and IR pole subtraction procedure was carried out as prescribed ???. As a control, the two-loop box diagrams are also computed in the HTL up to $\mathcal{O}(1/m_t^6)$. Since this expansion should be included within the p_T -expansion. We have retained the HTL analytic expression by further expanding the p_T -expanded amplitude in small \hat{s}/m_t^2 . Providing an additional cross-check for the validity of the p_T -expansion.

6.4 Results and conclusions

The virtual corrections to the ggF Zh production have been implemented in a FORTRAN code using `handyG` [294], for the evaluation of generalised harmonic polylogarithms and `Chaplin` [295] for the harmonic polylogarithms appearing in the triangle two-loop functions. On the other hand, the elliptic integrals are evaluated using the routines developed

¹The calculation of the box diagrams has been done by my collaborators, the co-authors of [247]

\hat{s}/m_t^2	\hat{t}/m_t^2	ref.[246]	$\mathcal{O}(p_T^6)$
1.707133657190554	-0.441203767016323	35.429092(6)	35.430479
3.876056604162662	-1.616287256345735	4339.045(1)	4340.754
4.130574250302561	-1.750372271104745	6912.361(3)	6915.797
4.130574250302561	-2.595461551488002	6981.09(2)	6984.20

Table 6.2. Comparison of $\mathcal{V}_{fin}4/(\alpha_s^2 \alpha^2)$ with the numerical results of ref.[246]. This plot has been published in [247].

in ref.[293]. Since the result is analytic, the code is significantly faster than the numerical evaluation of the two-loop amplitude [246], with evaluation time of ca. 0.5 min per one phase space point on a personal laptop.

In order to facilitate the comparison of these results with the ones presented in the literature, we define the finite part of the virtual corrections as in ref.[245]²

$$\begin{aligned} \mathcal{V}_{fin} = & \frac{G_F^2 m_Z^2}{16} \left(\frac{\alpha_s}{\pi} \right)^2 \left[\sum_i |\mathcal{A}_i^{(0)}|^2 \frac{C_A}{2} \left(\pi^2 - \log^2 \left(\frac{\mu_R^2}{\hat{s}} \right) \right) \right. \\ & \left. + 2 \sum_i \text{Re} \left[\mathcal{A}_i^{(0)} \left(\mathcal{A}_i^{(1)} \right)^* \right] \right] \end{aligned} \quad (6.36)$$

and in the numerical evaluation of eq.(6.36) is fixed $\mu_R = \sqrt{\hat{s}}$. The triangle and HTL box topologies were validated against the results of refs. [242, 245] finding perfect agreement at the form-factor level, i.e. $\mathcal{A}_i^{(1)}$.

The virtual part of the Partonic cross-section from the finite part of the virtual corrections in eq. (6.36) is defined by

$$\Delta\hat{\sigma}_{virt} = \int_{\hat{t}^-}^{\hat{t}^+} d\hat{t} \frac{\alpha_s}{16\pi^2} \frac{1}{\hat{s}^2} \mathcal{V}_{fin}. \quad (6.37)$$

This function is used to compare the p_T -expanded results with the other expansion methods. Starting with low M_{Zh} , the p_T -expanded is compared with the HTL \mathcal{V}_{fin} , finding an excellent numerical agreement. It is important to note that, at the same order in the expansion, the p_T -expanded terms are more accurate than the HTL ones, albeit computationally more demanding. Additional checks have been done using the numerical evaluation of the NLO amplitude by [246], where the authors have evaluated the exact two-loop MI's using `pySecDec` [296, 297]. Table 6.2 shows a comparison between the p_T -expanded $\mathcal{V}_{fin}4/(\frac{\alpha_s^0}{4\pi} \alpha^2)$ vs the exact numerical result of [246] for several phase space points. As can be seen from the table the relative difference between the two results is less than half a per-mille.

²The definition of the matrix elements here differs by a factor of $\frac{1}{\hat{s}}$ from ref.[245], cf. also section A.1.

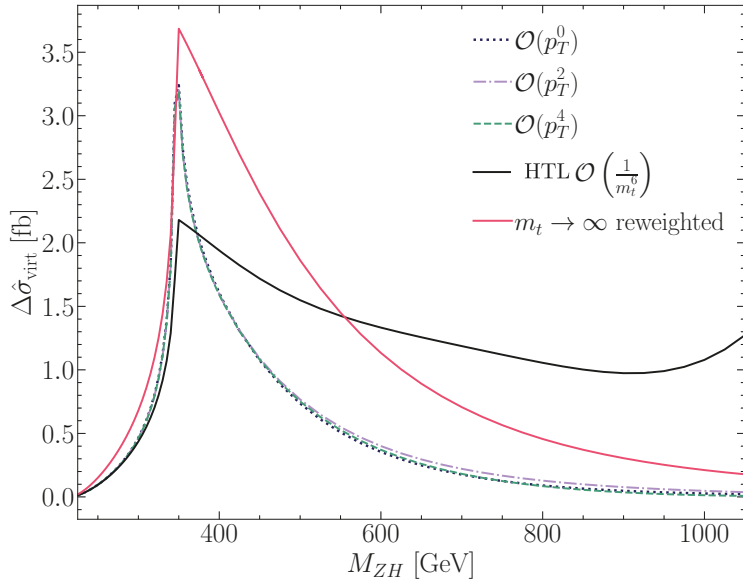


Figure 6.5. $\Delta\hat{\hat{\sigma}}_{\text{virt}}$ defined by eq.(6.37), shown as a function of M_{Zh} . The various orders of the p_T -expansion are plotted as dashed lines, while the black and red continuous lines stand for the HTL and reweighted $m_t \rightarrow \infty$ results, respectively. This plot has been published in [247].

In Figure 6.5, the dashed lines show the different orders of the expansion in p_T . For all parts of the matrix elements, the best results available, i.e. both $\mathcal{A}^{(0)}$ were used. The double-triangle topology is evaluated exactly, while for $\mathcal{A}^{(1)}$ we use the various orders in the p_T -expansion. For comparison, the results are shown where $\mathcal{A}^{(1)}$ is replaced by the one computed in HTL up to $\mathcal{O}(1/m_t^6)$ (full black line), which, is valid up to $M_{Zh} < 2m_t$. Within the validity of the HTL, the p_T -expanded results agree well with it. Furthermore, the results in the infinite top mass limit reweighted by the full amplitudes squared can be seen as the full red line in the plot, corresponding to the approach of ref.[240], keeping though the double triangle contribution in full top mass dependence. Differently from the HTL line, the $m_t \rightarrow \infty$ reweighted one shows a behaviour, for $M_{Zh} \gtrsim 400$ GeV, similar to the behaviour of the p_T lines. Still, the difference between the reweighted result and the p_T -expanded ones is significant. The p_T -expanded results show very good convergence. The zero-order in term of the p_T -expansion agrees exceptionally well with the higher orders, and all the three results are very close up to $M_{Zh} \sim 500$ GeV.

The calculation of the virtual two-loop corrections to the $gg \rightarrow Zh$ is carried out using exact results for the triangle and double-triangle topologies, while p_T -expansion method was applied for box one. The same MI's that were found for Higgs pair production [11] also appear in the Zh virtual corrections. Predominantly, these MI's are expressed in terms of generalised harmonic polylogarithms except two elliptic integrals. Using the LO calculation, we have shown the validity of the p_T -expansion covering the invariant mass interval $M_{Zh} \lesssim 750$ GeV, which covers $\sim 98\%$ of the total phase space for 13 – 14

TeV energies.

The p_T -expansion agrees within per mill level accuracy with the numerical results found in [246]. However, it allows for fast amplitude computation with circa one second per phase space point using a modern laptop with mid-range specifications. Furthermore, the integration over the \hat{t} variable in eq.(6.37) converges superbly. With the flexibility of these analytic results, an application to the beyond-the SMI is certainly possible.

Finally, it should be noted that this calculation complements nicely the results obtained in ref. [245] using a HE expansion, which according to the authors, provides precise results for $p_T \gtrsim 200$ GeV. The merging of the two analyses provided a result that covers the whole phase space, and can be easily implemented into a Monte Carlo code using the virtual correction results of this bridging procedure is published in [274].

7 Four top operators in Higgs production and decay

In chapter 4, the SMEFT has been portrayed as a pragmatic yet robust parametrisation of potential NP degrees of freedom for LHC searches, with the ansatz that these degrees of freedom have masses that are higher than the LHC reach. From the discussion and overview of Higgs-related SMEFT operators in that chapter, the operator \mathcal{O}_ϕ stood out as one of the weakly constrained among them. This is due to the current low experimental sensitivity on the Higgs self-couplings.

Though many of the top quark operators are strongly constrained from top quark production observables, some remain as weakly constrained as the trilinear Higgs self-coupling, particularly four-fermion operators involving the third generation quarks. They would be constrained directly from the production of four top quarks or $t\bar{t}b\bar{b}$ observation. However, the four top quark production process has a small cross-section at the LHC $\sim 12 \text{ fb}$ [298], which is more or less comparable to the Higgs pair production. Experimental searches for the production of four top quarks have been first done by CMS [299] combining different LHC runs, followed by ATLAS [300], the latter reporting a 4.3σ observation of this processes with a cross-section of 24^{+7}_{-6} fb . The same story can be told for the observation of $t\bar{t}b\bar{b}$ production, see [301, 302] for experimental searches and [303, 304] for SMEFT fits. It should be noted that for the production of four top quarks, or two top, two beauty quarks in SMEFT, that the contact terms do not interfere with the SM process and only appear proportional to $\mathcal{O}(1/\Lambda^4)$. This makes the SMEFT global analysis of these operators is highly dependent on the EFT truncation scheme used, i.e. whether to keep quadratic terms or not.

Intriguingly, these four-fermion operators enter in single Higgs processes at NLO similarly to the Higgs self-coupling. Since the four-fermions operators are weakly constrained, they should be included in fits that include Higgs data. In this chapter, I shall demonstrate a significant correlation between the Higgs self-coupling and the four-fermion operators.

The chapter is based on the paper [151] and structured as follows: in section 7.1 the complete NLO calculation of Higgs rates due to the four-fermion operators is shown. Afterwards, in section 7.2, a fit from single-Higgs data combining the Higgs trilinear coupling and the four-fermion operators is presented for both Run-II and HL-LHC,. More elaborate results for the HL-LHC is found in Appendix B. The results are further discussed in section 7.3.

7.1 Contribution of four-fermion operators to Higgs rates at NLO

We will consider the following dimension-six SMEFT operators:

Four-heavy-quark SMEFT operators modifying Higgs rates at NLO

Operators with homogenous chiral structure, i.e. (RR)(RR) or (LL)(LL)

$$\mathcal{O}_{tt}, \mathcal{O}_{bb}, \mathcal{O}_{tb}^{(1)}, \mathcal{O}_{tb}^{(8)}, \mathcal{O}_{QQ}^{(1)}, \mathcal{O}_{QQ}^{(8)}. \quad (7.1)$$

Operators with heterogeneous chiral structure, i.e. (LR)(LR) or (LL)(RR)

$$\mathcal{O}_{Qt}^{(1)}, \mathcal{O}_{Qt}^{(8)}, \mathcal{O}_{Qb}^{(1)}, \mathcal{O}_{Qb}^{(8)}, \mathcal{O}_{QtQb}^{(1)}, \mathcal{O}_{QtQb}^{(8)}. \quad (7.2)$$

The explicit definition of these operators can be found in [Table 4.1](#). Here, the notation is slightly modified from the standard Warsaw basis. The flavour indices were suppressed since only the the third generation is considered throughout this chapter. Adopting the same notation from previous chapters, Q denotes the (heavy) left-handed $SU(2)_L$ doublet quarks while t and b refer to the right-handed singlets. In studies involving SMEFT fits, such as [\[184\]](#) the $SU(3)_C$ singlet and octet left-handed operators $\mathcal{O}_{QQ}^{(1),SU(3)}$, $\mathcal{O}_{QQ}^{(8)}$ are used instead of the singlet and triplet of $SU(2)_L$ appearing in the standard Warsaw basis. The two conventions are related via the relations

$$\begin{aligned} C_{QQ}^{(1),SU(3)} &= 2C_{QQ}^{(1)} - \frac{2}{3}C_{QQ}^{(3)}, \\ C_{QQ}^{(8)} &= 8C_{QQ}^{(3)}. \end{aligned} \quad (7.3)$$

Additionally, all of these Wilson coefficients are assumed to be real.

We will consider operators that induce sizeable NLO corrections to Higgs processes. These operators turn out to be the ones that introduce loop corrections to the top- or beauty-quark Yukawa, their masses and finite corrections from top-quark loops. Such corrections will be proportional to the top mass. On the contrary, corrections from beauty-quark loops are highly suppressed by m_b . Also, operators with a chiral structure that does not enable them to enter the Yukawa RGE's will not be constrained from Higgs data as they would only contribute through small finite terms, as we shall see later. Hence, only four-top-quark and the $\mathcal{O}_{QtQb}^{(1),(8)}$ operators will be considered.

This section will demonstrate the calculation of NLO Higgs production and decay rates induced by the four heavy-quarks operators discussed above. The results were computed fully analytically and presented in this section for the production of Higgs via gluon fusion or Higgs decay to gluon, photons and beauty quarks. However, for the associated production of the Higgs with top pair $t\bar{t}h$, the corrections were computed numerically due to the length of the analytic expressions of the result.

7.1.1 Analytic calculations

The NLO corrections to gluon fusion, $h \rightarrow gg$, $h \rightarrow \gamma\gamma$ and $h \rightarrow b\bar{b}$ all come from the sub-diagrams listed in Table 7.1, with top loops entering in the mass renormalisation or top- or beauty-quark Yukawa vertex correction. In this table, $N_c = 3$ is the number of colours, and $c_F = (N_c^2 - 1)/(2N_c) = 4/3$ are the eigenvalues of the Casimir operator of $SU(3)_c$ in the fundamental representation. The effect of the beauty-quark loops coming

Diagram	colour factor		mass/coupling
	singlet	octet	
	$2N_c + 1$	c_F	$y_t m_b m_t^2$
	1	c_F	$y_t m_t^3$
	$2N_c + 1$	c_F	m_t^3
	1	c_F	m_t^3

Table 7.1. Sub-diagrams contributing to the NLO corrections of gluon fusion Higgs production and its decay to gluons, photons and beauty quarks.

from for $C_{QtQb}^{(1/8)}$ can be easily read from this table by exchanging $t \leftrightarrow b$. Although such corrections are significantly smaller than their counterparts coming from top-quark loops.

We see that these corrections correspond to the Wilson coefficients appearing in the RGE, and operators with (LL)(LL) or (RR(RR)) chiral structures do not contribute to these processes.

By considering the two-loop corrections to the ggF illustrated in Figure 7.1 we find that such correction contains the sub-diagrams shown in Table 7.1, except for diagram (e), which is found to be vanishing for on-shell gluons. Additionally, these diagrams indicated that the two-loop corrections would be reduced to products of two one-loop functions after the integral reduction.

Following the Feynman rules derived in ref. [305] for the four-fermion operators of interest here, the $gg \rightarrow h$ two-loop amplitude was calculated, then Dirac algebra and

further algebraic manipulations were preformed in Mathematica using **PackageX** [306]. Reduction of the resulting two-loop loop integrals to Master integrals has been preformed using **KIRA** [307]. The computation has been cross-checked independently by my collaborators, using a different pipeline: **FeynArts** [282], for amplitude generation then **FeynRules** [308] and **Fire** [309] for algebraic manipulation and loop-integral reduction.

The sub-diagrams appearing in the two-loop calculation corresponds to mass and vertex renormalisation, which require counter-terms for pole cancellation. A mixture of an on-shell (OS) and $\overline{\text{MS}}$ – schemes have been used for the mass and $hq\bar{q}$ coupling renormalisation, respectively. The renormalisation of SM quantities is done in the OS scheme, while the NP parameters are renormalised according to the $\overline{\text{MS}}$ scheme. This method of mixed-scheme renormalisation was proposed by [310].

The top/beauty mass renormalisation can be expressed as

$$m_{t/b}^{\text{OS}} = m_{t/b}^{(0)} - \delta m_{t/b}, \quad (7.4)$$

with the corresponding counter-terms

$$\delta m_t = \frac{1}{8\pi^2} \frac{C_{Qt}^{(1)} + c_F C_{Qt}^{(8)}}{\Lambda^2} m_t^3 \left[\frac{2}{\bar{\epsilon}} + 2 \log \left(\frac{\mu_R^2}{m_t^2} \right) + 1 \right] \quad (7.5)$$

$$- \frac{1}{16\pi^2} \frac{(2N_c + 1) C_{QtQb}^{(1)} + c_F C_{QtQb}^{(8)}}{\Lambda^2} \left[\frac{1}{\bar{\epsilon}} + \log \left(\frac{\mu_R^2}{m_b^2} \right) + 1 \right] m_b^3,$$

$$\delta m_b = - \frac{1}{16\pi^2} \frac{(2N_c + 1) C_{QtQb}^{(1)} + c_F C_{QtQb}^{(8)}}{\Lambda^2} \left[\frac{1}{\bar{\epsilon}} + \log \left(\frac{\mu_R^2}{m_t^2} \right) + 1 \right] m_t^3. \quad (7.6)$$

Here, we have $\bar{\epsilon}^{-1} = \epsilon^{-1} - \gamma_E + \log(4\pi)$, in dimensional regularisation in $d = 4 - 2\epsilon$ dimensions. It is possible to convert from OS to the $\overline{\text{MS}}$ – scheme for mass counter-terms via the following relations

$$\delta m_t^{\overline{\text{MS}}} = \frac{1}{8\pi^2} \frac{C_{Qt}^{(1)} + c_F C_{Qt}^{(8)}}{\Lambda^2} m_t^3 \frac{1}{\bar{\epsilon}} + \frac{1}{16\pi^2} \frac{(2N_c + 1) C_{QtQb}^{(1)} + c_F C_{QtQb}^{(8)}}{\Lambda^2} \frac{1}{\bar{\epsilon}} m_b^3, \quad (7.7)$$

$$\delta m_b^{\overline{\text{MS}}} = \frac{1}{16\pi^2} \frac{(2N_c + 1) C_{QtQb}^{(1)} + c_F C_{QtQb}^{(8)}}{\Lambda^2} \frac{1}{\bar{\epsilon}} m_t^3. \quad (7.8)$$

The effect of changing to the mass renormalisation scheme is small for the top quark but significant, up to 100% effect, for the beauty.

The top/beauty Higgs coupling in SMEFT, is written as

$$g_{ht\bar{t}/hb\bar{b}} = \frac{m_{t/b}}{v} - \frac{v^2}{\Lambda^2} \frac{C_{t\phi/b\phi}}{\sqrt{2}}. \quad (7.9)$$

Hence, a modification of the Higgs couplings to beauty and top quarks is generated by operator mixing, even if $C_{t\phi/b\phi}$ are set to zero at Λ . From this, the $\overline{\text{MS}}$ counter-term

should take the form

$$\delta g_{ht\bar{t}/hb\bar{b}} = \frac{m_{t/b}}{v} \delta m_{t/b} - \frac{v^2 \delta C_{t\phi/b\phi}}{\sqrt{2}}, \quad (7.10)$$

where $\delta C_{t\phi/b\phi}$ is directly read from the anomalous dimension, see ref. [179]

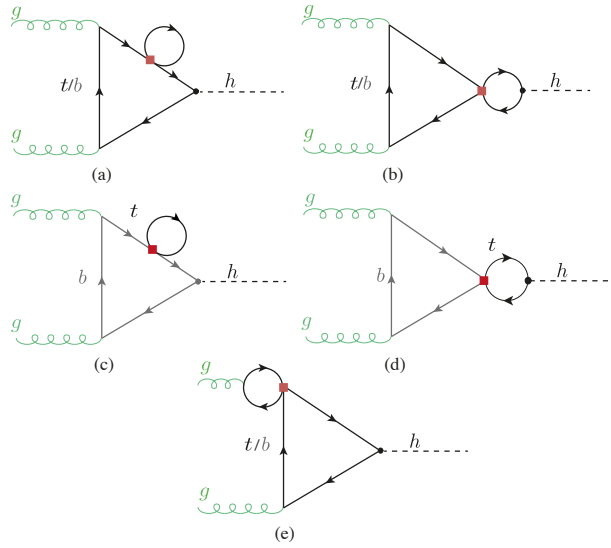


Figure 7.1. Example Feynman diagrams for the four-fermion-operator contributions to the Higgs production via gluon fusion. The red box indicates the four-fermion operator.

Correction to gluon fusion and $h \rightarrow gg$

The modification of the Higgs production via gluon fusion can be written as

$$\frac{\sigma_{ggF}}{\sigma_{ggF}^{\text{SM}}} = 1 + \frac{\sum_{i=t,b} 2\text{Re}(F_{\text{LO}}^i F_{\text{NLO}}^*)}{|F_{\text{LO}}^t + F_{\text{LO}}^b|^2}, \quad (7.11)$$

with

$$F_{\text{LO}}^i = -\frac{8m_i^2}{m_h^2} \left[1 - \frac{1}{4} \log^2(x_i) \left(1 - \frac{4m_i^2}{m_h^2} \right) \right], \quad (7.12)$$

and the NLO form-factors are given by

$$\begin{aligned}
 F_{\text{NLO}} = & \frac{1}{4\pi^2 \Lambda^2} (C_{Qt}^{(1)} + c_F C_{Qt}^{(8)}) F_{\text{LO}}^t \left[2m_t^2 + \frac{1}{4}(m_h^2 - 4m_t^2) \left(3 + 2\sqrt{1 - \frac{4m_t^2}{m_h^2}} \log(x_t) \right) \right. \\
 & \left. + \frac{1}{2}(m_h^2 - 4m_t^2) \log\left(\frac{\mu_R^2}{m_t^2}\right) \right] \\
 & + \frac{1}{32\pi^2 \Lambda^2} ((2N_c + 1) C_{QtQb}^{(1)} + c_F C_{QtQb}^{(8)}) \left[F_{\text{LO}}^b \frac{m_t}{m_b} \left(4m_t^2 - 2m_h^2 \right. \right. \\
 & \left. \left. - (m_h^2 - 4m_t^2) \sqrt{1 - \frac{4m_t^2}{m_h^2}} \log(x_t) - (m_h^2 - 4m_t^2) \log\left(\frac{\mu_R^2}{m_t^2}\right) \right) + (t \leftrightarrow b) \right]. \tag{7.13}
 \end{aligned}$$

Only top-quark loops contribute to the parts proportional to $C_{Qt}^{(1),(8)}$. The variable x_i for a loop particle with mass m_i is given by

$$x_i = \frac{-1 + \sqrt{1 - \frac{4m_i^2}{m_h^2}}}{1 + \sqrt{1 - \frac{4m_i^2}{m_h^2}}}. \tag{7.14}$$

Using the same amplitudes, the $h \rightarrow gg$ partial width modification can be written as

$$\frac{\Gamma_{h \rightarrow gg}}{\Gamma_{h \rightarrow gg}^{\text{SM}}} = 1 + \frac{\sum_{i=t,b} 2\text{Re}(F_{\text{LO}}^i F_{\text{NLO}}^*)}{|F_{\text{LO}}^t + F_{\text{LO}}^b|^2}. \tag{7.15}$$

Correction to Higgs decay to photons

Since the decay $h \rightarrow \gamma\gamma$ contains the same topologies as gluon fusion, it is possible to use the results from the above calculation in obtaining the NLO correction to the partial width for this decay

$$\frac{\Gamma_{h \rightarrow \gamma\gamma}}{\Gamma_{h \rightarrow \gamma\gamma}^{\text{SM}}} = 1 + \frac{2\text{Re}(F_{\text{LO},\gamma} F_{\text{NLO},\gamma}^*)}{|F_{\text{LO},\gamma}|^2}. \tag{7.16}$$

However, one should pay attention to the change in the prefactors, and the extra EW contributions for $h \rightarrow \gamma\gamma$

$$F_{\text{LO},\gamma} = N_C Q_t^2 F_{\text{LO}}^t + N_C Q_b^2 F_{\text{LO}}^b + F_{\text{LO}}^W + F_{\text{LO}}^G, \tag{7.17}$$

and $F_{\text{NLO},\gamma}$ is obtained from F_{NLO} by replacing the LO form-factor that appears inside of it by $F_{\text{LO}}^i \rightarrow N_c Q_i^2 F_{\text{LO}}^i$. The charges of the top and beauty quarks are $Q_t = 2/3$ and $Q_b = -1/3$, respectively.

The W -boson loops contribution is given by

$$F_{\text{LO}}^W = 2 \left(1 + 6 \frac{m_W^2}{m_h^2} \right) - 6 \frac{m_W^2}{m_h^2} \left(1 - 2 \frac{m_W^2}{m_h^2} \right) \log^2(x_W), \quad (7.18)$$

, and the Goldstone contribution

$$F_{\text{LO}}^G = 4 \frac{m_W^2}{m_h^2} \left(1 + \frac{m_W^2}{m_h^2} \log^2(x_W) \right). \quad (7.19)$$

These operators also affect the $h \rightarrow Z\gamma$ partial width. However, as in the diphoton case, the effect is expected to be small due to the dominance of the W -boson contributions. Furthermore, given the smallness of the $h \rightarrow Z\gamma$ branching ratio and the relatively low precision expected in probing this channel at the LHC, the effects of four-fermion interactions in the $h \rightarrow Z\gamma$ decay are neglected in this study.

Correction to Higgs decays to $b\bar{b}$

The dominant four-fermion contributions to decay channel $h \rightarrow b\bar{b}$ come from the operators $\mathcal{O}_{QtQb}^{(1),(8)}$; the corresponding diagram at NLO is shown in fig 7.2. Adopting the same renormalisation procedure as described earlier, we have the following expression for the correction to the $h \rightarrow b\bar{b}$ decay rate in the presence of $\mathcal{O}_{QtQb}^{(1),(8)}$

$$\begin{aligned} \frac{\Gamma_{h \rightarrow b\bar{b}}}{\Gamma_{h \rightarrow b\bar{b}}^{\text{SM}}} = & 1 + \frac{1}{16\pi^2} \frac{m_t}{m_b} (m_h^2 - 4m_t^2) \frac{(2N_c + 1)C_{QtQb}^{(1)} + c_F C_{QtQb}^{(8)}}{\Lambda^2} \\ & \times \left[2 + \sqrt{1 - \frac{4m_t^2}{m_h^2}} \log(x_t) - \log\left(\frac{m_t^2}{\mu_R^2}\right) \right]. \end{aligned} \quad (7.20)$$

This NLO correction carries an enhancement factor of m_t/m_b and is hence expected to be rather large.

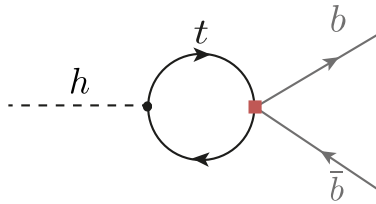


Figure 7.2. Feynman diagram contributing to the NLO $h \rightarrow b\bar{b}$ process.

The results of the NLO effects from the four-fermion operators reported above do not take into account the running of the Wilson coefficients. This would be based on assuming that these coefficients are defined at the process scale. Nevertheless, when we want

to compare different processes or assume that the four-fermion operators are defined at the UV scale Λ . One has to consider the running of these Wilson coefficients from Λ down to the process scale.

These running effects can be included via the RGE for the operators with Wilson coefficient $C_{t\phi}$ and $C_{b\phi}$ [177, 178], that leads approximatively to

$$C_{t\phi}(\mu_R) - C_{t\phi}(\Lambda) = \frac{1}{16\pi^2 v^2} \left[-2y_t(m_h^2 - 4m_t^2)(C_{Qt}^{(1)} + c_F C_{Qt}^{(8)}) \log\left(\frac{\mu_R^2}{\Lambda^2}\right) + \frac{y_b}{2}(m_h^2 - 4m_b^2) ((2N_c + 1)C_{QtQb}^{(1)} + c_F C_{QtQb}^{(8)}) \log\left(\frac{\mu_R^2}{\Lambda^2}\right) \right], \quad (7.21)$$

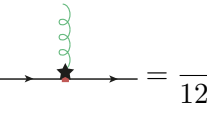
and

$$C_{b\phi}(\mu_R) - C_{b\phi}(\Lambda) = \frac{y_t}{32\pi^2 v^2} \left[(m_h^2 - 4m_t^2) ((2N_c + 1)C_{QtQb}^{(1)} + c_F C_{QtQb}^{(8)}) \log\left(\frac{\mu_R^2}{\Lambda^2}\right) \right], \quad (7.22)$$

where $y_{t/b} = \sqrt{2}m_{t/b}/v$. Note that the combinations of the Wilson coefficients appearing in (7.21) and (7.22) are the same as in F_{NLO} in (7.13). Effectively, it is possible to obtain the result under the assumption that the four-fermion operators are the only non-zero ones at the large scale by replacing in (7.13) $\mu_R \rightarrow \Lambda$. Here the op and beauty quark masses were renormalised the OS scheme. Including the leading logarithmic running of $C_{b\phi}$ of (7.22) from the high scale Λ to the electroweak scale is achieved by setting in (7.20) $\mu_R \rightarrow \Lambda$. The expression in (7.20) agrees with results obtained from the full calculation of the NLO effects in the dimension-six SMEFT, computed in ref. [311].

7.1.2 SMEFT-NLO calculation of $t\bar{t}h$

Unlike the previous processes, the associated production of the Higgs with top quark pair involves new topologies that are not limited to Yukawa vertex correction or mass renormalisation. At the LHC, there are two sub-processes responsible for the $t\bar{t}h$ production: gluon-initiated process that is depicted in Figure 7.3 and quark-initiated that is seen in Figure 7.4. The new *finite* topologies induced by the four-fermion operator correction are: triangle and box topologies, shown in diagrams (d) and (e) in Figure 7.3, as well as in the triangle topology shown in diagram (b) of Figure 7.4. Additionally, the $t\bar{t}g$ vertex correction in the quark-initiated process (diagram (c)) of Figure 7.4 is non-vanishing as the gluon is off-shell. This vertex correction has a UV pole that requires a counter-term for its cancellation



$$= \frac{ig_s}{12\pi^2 \Lambda^2} T_{ij}^A p_g^2 \gamma^\mu \left(C_{tt} P_R + (C_{QQ}^{(1)} + C_{QQ}^{(3)}) P_L + \frac{C_{Qt}^{(8)}}{4} \right) \left(\frac{1}{\epsilon} - 1 \right). \quad (7.23)$$

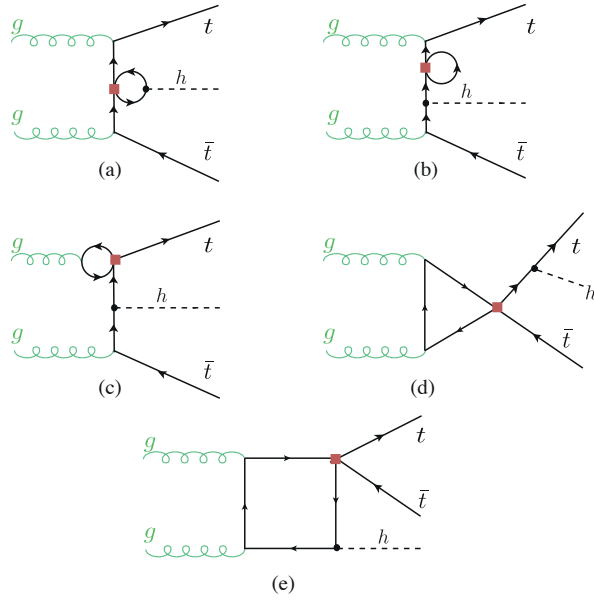


Figure 7.3. Feynman diagrams including the four-fermion loop contributions to the $gg \rightarrow t\bar{t}h$ subprocess.

Another difference between $t\bar{t}h$ and the other Higgs processes studied in this chapter is that this channel has a non-trivial colour structure. This manifests in the presence of multiple colour projectors, because the quark anti-quark triplets or the gluon pairs do not have to recombine to only a singlet state rather to both a singlet and an octet, according to the expansion of product $\mathbf{3} \otimes \overline{\mathbf{3}} \rightarrow \mathbf{1} + \mathbf{8}$. This breaks the degeneracy between the singlet and octet Wilson coefficients. Lastly, due to the new topologies and $t\bar{t}g$ vertex correction, operators with single chirality will contribute to NLO corrections, namely the operators \mathcal{O}_{tt} and $\mathcal{O}_{QQ}^{(1,3)}$.

All of the four-fermion operators are implemented in the loop-capable UFO model **SMEFTatNLO** [270] that is computed via **Madgraph_aMCNLO** [268] with some tweaking to remove the NLO QCD corrections. This is done via a user-defined loop filter function in Madgraph. The results were reproduced by an analytic computation based on the reduction of one-loop amplitudes via the method developed by G. Ossola, C.G. Papadopoulos and R. Pittau (OPP reduction) [312], implemented in the FORTRAN code **CutTools** [313]. This programme takes the full one-loop amplitude and then reduces it to terms with 1,2,3, and 4-point loop functions in four dimensions, keeping spurious terms from the ϵ part of the amplitude. To correct for such terms, one needs to compute the divergent UV counter-terms as well as finite rational terms, denoted by R_2 as in ref. [314].¹ The amplitudes were generated in the same way as for ggF. The UV and R_2 counter-terms, which need to be supplemented to **CutTools**, were computed

¹Another rational term R_1 appears due to a mismatch between the four and d dimensional amplitudes, but this is computed automatically in **CutTools**.

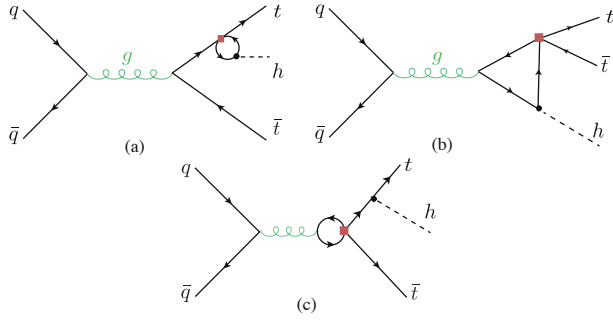


Figure 7.4. Feynman diagrams including the four-fermion loop contributions to the $q\bar{q} \rightarrow t\bar{t}h$ subprocess.

manually following the method detailed in [314]. For both codes, the NNPDF23 PDF set at NLO [315] was used.

The singlet and octet operators $\mathcal{O}_{QtQb}^{(1),(8)}$ contribute to $t\bar{t}h$ only via beauty-quark loops and, in principle, could be directly dismissed like the other beauty quark operators mentioned above. However, it is instructive to investigate their effect, albeit it is very small. Since the `SMEFTatNLO` model does not have these operators, it was needed to implement them manually in that model. This is simply done by including the vertices generated by these operators and their UV and R_2 counter-terms. The calculation of the NLO correction by these operators was done both in Madgraph using a modified UFO model and with the code based on `CutTools`. The effects were comparable to the leading log effects computed using `SMEFTsim` package [316] of $\sim 10^{-6}$. Hence confirming the expectation that beauty quark loops have a negligible effect.

To include the effects of Wilson coefficients' running, the relevant contribution for the gluon-initiated process is the same as the stated for the gluon fusion in (7.21). While for the quark-initiated process, one needs to consider the operator mixing in the running, particularly between operators that contain second and third-generation quarks mixed. These corrections can be obtained from the RGEs in refs. [177–179].

7.1.3 Results

The NLO effects generated by the SMEFT four-fermion operators of the third generation quarks on the Higgs rate have been extracted from the above computation using the formula

$$\delta R(C_i) = R/R^{\text{SM}} - 1, \quad (7.24)$$

here the rates could either be cross-section σ or partial width γ . The dependence of a given Higgs rate R on the Wilson coefficient C_i is denoted by $\delta R(C_i)$. Only contributions linear in the Wilson coefficients are considered. In order to isolate the finite terms from the ones coming from the RGE leading log approximation, the correction is further

expanded to finite $\delta R_{C_i}^{fin}$ and leading log terms $\delta R_{C_i}^{log}$ as follows

$$\delta R(C_i) = \frac{C_i}{\Lambda^2} \left(\delta R_{C_i}^{fin} + \delta R_{C_i}^{log} \log \left(\frac{\mu_R^2}{\Lambda^2} \right) \right). \quad (7.25)$$

Using this formula, one can obtain the correction at any NP scale Λ . Though, in the remainder of this chapter, this scale is set to 1 TeV. In Table 7.2, the finite and logarithmic corrections for the operators considered in this study are reported. Using this table in filling the formula (7.25) gives the correction to the Higgs rate in question. However, since some of the rates are Higgs partial widths, the Higgs total width Γ_h will be affected, and therefore, all Higgs rates are changed, as the branching fractions will carry the full width dependence on the Wilson coefficients. An important observation from Table 7.2 is that the finite terms, are either larger or at the same order than the leading-log ones, except for $h \rightarrow b\bar{b}$ corrections from $C_{QtQb}^{(1),(8)}$. This highlights the importance of the full NLO calculation for these corrections in constraining these four-fermion operators, in particular $\mathcal{O}_{Qt}^{(1),(8)}$.

As mentioned earlier, there is a degeneracy between the singlet and octet operators, seen clearly in the analytic result for gluon fusion and the Higgs decays considered. This degeneracy is though broken for $\mathcal{O}_{Qt}^{(1),(8)}$ due to $t\bar{t}h$. Since, the effect of $\mathcal{O}_{QtQb}^{(1),(8)}$ is negligible for this process, the independent degree of freedom for these operators' Wilson coefficients is the linear combination

$$C_{QtQb}^+ = (2N_c + 1)C_{QtQb}^{(1)} + c_F C_{QtQb}^{(8)}. \quad (7.26)$$

7.2 Fit to Higgs observables

Using the results from the NLO calculations discussed above and combining them with the calculations of NLO Higgs rates from the trilinear Higgs self-coupling λ_3 , performed in refs. [30–33, 35], the previous fits on λ_3 from single-Higgs observables can be extended with the inclusion of these four-fermion SMEFT Wilson coefficients. Hence, we revisit the sensitivity studies of single Higgs observables to the trilinear coupling λ_3 . Although combined fits from Higgs data, including λ_3 and SMEFT operators modifying Higgs rates at LO, have been preformed already, e.g. in ref. [188]. Such fits would not be sufficient to determine the actual sensitivity for λ_3 . In particular, if the SMEFT operators are weakly constrained and induce significant modifications to Higgs rates, which can be seen in Table 7.2. This chapter does not include a global SMEFT fit; instead merely motivates it by illustrating how the sensitivity for probing the Higgs-self coupling from single Higgs data gets mitigated when the four-fermion operators are included in the fit.

In the antecedent studies, the modification to Higgs self coupling was reported in terms of the κ -formalism, for the consistency of this analysis, the NLO corrections from the trilinear self-coupling will be converted to the SMEFT notation, in terms of the Wilson coefficient C_ϕ , for more details on the conversion between SMEFT and κ -formalism see subsection 4.2.2. In order to keep track of the SMEFT power-counting, the results of

Operator	Process	μ_R	$\delta R_{C_i}^{fin}$ [TeV 2]	$\delta R_{C_i}^{log}$ [TeV 2]
$\mathcal{O}_{Qt}^{(1)}$	ggF	$\frac{m_h}{2}$	$9.91 \cdot 10^{-3}$	$2.76 \cdot 10^{-3}$
	$h \rightarrow gg$	m_h	$6.08 \cdot 10^{-3}$	$2.76 \cdot 10^{-3}$
	$h \rightarrow \gamma\gamma$		$-1.76 \cdot 10^{-3}$	$-0.80 \cdot 10^{-3}$
	$t\bar{t}h$ 13 TeV	$m_t + \frac{m_h}{2}$	$-4.20 \cdot 10^{-1}$	$-2.78 \cdot 10^{-3}$
$\mathcal{O}_{Qt}^{(8)}$	$t\bar{t}h$ 14 TeV	$m_t + \frac{m_h}{2}$	$-4.30 \cdot 10^{-1}$	$-2.78 \cdot 10^{-3}$
	ggF	$\frac{m_h}{2}$	$1.32 \cdot 10^{-2}$	$3.68 \cdot 10^{-3}$
	$h \rightarrow gg$	m_h	$8.11 \cdot 10^{-3}$	$3.68 \cdot 10^{-3}$
	$h \rightarrow \gamma\gamma$		$-2.09 \cdot 10^{-3}$	$-1.07 \cdot 10^{-3}$
$\mathcal{O}_{QtQb}^{(1)}$	$t\bar{t}h$ 13 TeV	$m_t + \frac{m_h}{2}$	$6.81 \cdot 10^{-2}$	$-2.40 \cdot 10^{-3}$
	$t\bar{t}h$ 14 TeV	$m_t + \frac{m_h}{2}$	$7.29 \cdot 10^{-2}$	$-2.48 \cdot 10^{-3}$
	ggF	$\frac{m_h}{2}$	$2.84 \cdot 10^{-2}$	$9.21 \cdot 10^{-3}$
	$h \rightarrow gg$	m_h	$1.57 \cdot 10^{-2}$	$9.21 \cdot 10^{-3}$
$\mathcal{O}_{QtQb}^{(8)}$	$h \rightarrow \gamma\gamma$		$-1.30 \cdot 10^{-3}$	$-0.78 \cdot 10^{-3}$
	$h \rightarrow b\bar{b}$		$9.25 \cdot 10^{-2}$	$1.68 \cdot 10^{-1}$
	ggF	$\frac{m_h}{2}$	$5.41 \cdot 10^{-3}$	$1.76 \cdot 10^{-3}$
	$h \rightarrow gg$	m_h	$2.98 \cdot 10^{-3}$	$1.76 \cdot 10^{-3}$
$\mathcal{O}_{QQ}^{(1)}$	$h \rightarrow \gamma\gamma$		$-0.25 \cdot 10^{-3}$	$-0.15 \cdot 10^{-3}$
	$h \rightarrow b\bar{b}$		$1.76 \cdot 10^{-2}$	$3.20 \cdot 10^{-2}$
$\mathcal{O}_{QQ}^{(3)}$	$t\bar{t}h$ 13 TeV	$m_t + \frac{m_h}{2}$	$1.75 \cdot 10^{-3}$	$1.84 \cdot 10^{-3}$
	$t\bar{t}h$ 14 TeV	$m_t + \frac{m_h}{2}$	$1.65 \cdot 10^{-3}$	$1.76 \cdot 10^{-3}$
\mathcal{O}_{tt}	$t\bar{t}h$ 13 TeV	$m_t + \frac{m_h}{2}$	$4.60 \cdot 10^{-3}$	$1.82 \cdot 10^{-3}$
	$t\bar{t}h$ 14 TeV	$m_t + \frac{m_h}{2}$	$4.57 \cdot 10^{-3}$	$1.74 \cdot 10^{-3}$

Table 7.2. The NLO effects of the four heavy-quarks operators on the Higgs rates. The effects are separated into finite $\delta R_{C_i}^{fin}$ and leading log parts, in correspondence with (7.25). This table has been published in [151].

[31] are rewritten in terms of the SMEFT Wilson coefficient C_ϕ

$$\delta R_{\lambda_3} \equiv \frac{R_{\text{NLO}}(\lambda_3) - R_{\text{NLO}}(\lambda_3^{\text{SM}})}{R_{\text{LO}}} = -2 \frac{C_\phi v^4}{\Lambda^2 m_h^2} C_1 + \left(-4 \frac{C_\phi v^4}{\Lambda^2 m_h^2} + 4 \frac{C_\phi^2 v^8}{m_h^4 \Lambda^4} \right) C_2. \quad (7.27)$$

In (7.27), the coefficient C_1 corresponds to the contribution of the trilinear coupling to the single Higgs processes at one loop, adopting the same notation as [31]. The values of C_1 for the different processes of interest for this study are given in Table 7.3. The coefficient C_2 describes universal corrections and is given by

$$C_2 = \frac{\delta Z_h}{1 - \left(1 - \frac{2C_\phi v^4}{\Lambda^2 m_h^2} \right)^2 \delta Z_h}, \quad (7.28)$$

where the constant δZ_h is the SM contribution from the Higgs loops to the wave function renormalisation of the Higgs boson,

$$\delta Z_h = -\frac{9}{16} \frac{G_F m_h^2}{\sqrt{2}\pi^2} \left(\frac{2\pi}{3\sqrt{3}} - 1 \right). \quad (7.29)$$

The coefficient C_2 thus introduces additional $\mathcal{O}(1/\Lambda^4)$ (and higher order) terms in δR_{λ_3} . In ref. [31] considering the κ -formalism, the full expression of (7.28) is kept, while having two different descriptions: one in which δR_{λ_3} is expanded up to linear order in C_ϕ and an alternative scheme in which terms up to $\mathcal{O}(1/\Lambda^4)$ are also kept in the EFT expansion. Keeping the full expression in (7.28) and including terms up to $\mathcal{O}(1/\Lambda^4)$ in C_2 lead to nearly the same results as the simple $\mathcal{O}(1/\Lambda^4)$ fit.

Process	C_1	$\delta R_{C_\phi}^{fin}$
ggF/ $gg \rightarrow h$	$6.60 \cdot 10^{-3}$	$-3.10 \cdot 10^{-3}$
$t\bar{t}h$ 13 TeV	$3.51 \cdot 10^{-2}$	$-1.64 \cdot 10^{-2}$
$t\bar{t}h$ 14 TeV	$3.47 \cdot 10^{-2}$	$-1.62 \cdot 10^{-2}$
$h \rightarrow \gamma\gamma$	$4.90 \cdot 10^{-3}$	$-2.30 \cdot 10^{-3}$
$h \rightarrow b\bar{b}$	0.00	0.00
$h \rightarrow W^+W^-$	$7.30 \cdot 10^{-3}$	$-3.40 \cdot 10^{-3}$
$h \rightarrow ZZ$	$8.30 \cdot 10^{-3}$	$-3.90 \cdot 10^{-3}$
$pp \rightarrow Zh$ 13 TeV	$1.19 \cdot 10^{-2}$	$-5.60 \cdot 10^{-3}$
$pp \rightarrow Zh$ 14 TeV	$1.18 \cdot 10^{-2}$	$-5.50 \cdot 10^{-3}$
$pp \rightarrow W^\pm h$	$1.03 \cdot 10^{-2}$	$-4.80 \cdot 10^{-3}$
VBF	$6.50 \cdot 10^{-3}$	$-3.00 \cdot 10^{-3}$
$h \rightarrow 4\ell$	$8.20 \cdot 10^{-3}$	$-3.80 \cdot 10^{-3}$

Table 7.3. The NLO dependence of single Higgs rates on C_ϕ , these results were computed in [35]. The C_1 coefficients are to be used in eq. (7.27), while for a direct comparison with the effect of the four-fermion operators, we quote the translated effect $\delta R_{C_\phi}^{fin}$, which can be used directly in eq. (7.25). If the value of \sqrt{s} is not indicated the effect is the same for both 13 and 14 TeV. This table has been published in [151].

A Bayesian fit was preformed using Markov-chain Monte Carlo (MCMC) method. Using a flat prior $s \pi(C_i) = const.$ and a log likelihood of a Gaussian distribution

$$\log(L) = -\frac{1}{2} \left[(\vec{\mu}_{\text{Exp}} - \vec{\mu})^T \cdot \mathbf{V}^{-1} \cdot (\vec{\mu}_{\text{Exp}} - \vec{\mu}) \right]. \quad (7.30)$$

Constructed as follows:

Experimental inputs $\vec{\mu}_{\text{Exp}}$ The signal strengths from experimental measurements of single Higgs rates defined as

$$\mu_{\text{Exp}} \equiv \sigma_{\text{obs}} / \sigma_{\text{SM}}. \quad (7.31)$$

These measurements as taken from LHC Run II for centre-of-mass energy of

$\sqrt{s} = 13$ TeV and integrated luminosity of 139 fb^{-1} for ATLAS and 137 fb^{-1} for CMS. In addition to HL-LHC projections by CMS for $\sqrt{s} = 14$ TeV and integrated luminosity of 3000 fb^{-1} . Both of these inputs have been already discussed in chapter 3 and summarised in Table 3.1.

Theoretical predictions $\vec{\mu}$ The corresponding theoretical predictions for each of the experimental measurement /projections have been built using the modification to the cross-sections and branching ratios coming from the SMEFT four-fermion operators and C_ϕ . To keep with the power-counting, the signal strength is also expanded in powers of Λ , keeping only Λ^{-2} terms.

$$\mu(C_\phi, C_i) = \frac{\sigma_{\text{Prod}}(C_\phi, C_i) \times \text{BR}(C_\phi, C_i)}{\sigma_{\text{Prod,SM}} \times \text{BR}_{\text{SM}}} \approx 1 + \delta\sigma(C_\phi, C_i) + \delta\Gamma(C_\phi, C_i) - \delta\Gamma_h(C_\phi, C_i). \quad (7.32)$$

Uncertainties and correlations \mathbf{V} The variance matrix \mathbf{V} is build from thee experimental uncertainties found in Table 3.1. For Run-II data, only ATLAS collaboration reported the correlation amongst different channels of which only correlations $> 10\%$ are considered, while for the HL-LHC, the whole correlation matrix found on the webpage [317]. The HL-LHC projections for the S2 scenario explained in [235] were used. These assume the improvement on the systematics that is expected to be attained by the end of the HL-LHC physics programme, and that theory uncertainties are improved by a factor of two with respect to current values. Theoretical uncertainties were not considered in this fit.

The python package `pymc3` [318] was used to construct the posterior distribution. I have used the `Arviz` Bayesian analysis package [319] to extract the credible intervals (CIs) from the highest density posterior intervals (HDPI) of the posterior distributions, where the intervals covering 95% (68%) of the posterior distribution are considered the 95% (68%) CIs. In the Gaussian limit, these 95% (68%) CIs should be interpreted as equivalent to the 95% (68%) Frequentist confidence level (CL) two-sided bounds. `HEPfit` [320] code was used to validate the fits. Given that current bounds on these operators are rather weak, one may wonder about the uncertainty in these fits associated with the truncation of the EFT. Note that, since the four-quark operators only enter into the virtual corrections at NLO, Higgs production and decay contain only linear terms in $1/\Lambda^2$ in the corresponding Wilson coefficients, i.e. the quadratic terms coming from squaring the amplitudes are technically NNLO. Hence, the quadratic effects in the signal strengths coming from not linearising the corrections to the product $\sigma_{\text{Prod}} \times \text{BR}$. These effects have been investigated and found to have a negligible impact on the fit. The operators of single chirality \mathcal{O}_{tt} and $\mathcal{O}_{QQ}^{(1)/(3)}$ were not included in the fit, as their effect on Higgs rates is limited to small δR for $t\bar{t}h$. Thus, they cannot be contained simultaneously with C_ϕ using single Higgs data.

7.2.1 Fit results

In [Figure 7.5](#) and [Figure 7.6](#), I show the 68% and 95% CIs of the two-parameter posterior distributions and their marginalisation for the two-parameter fits involving C_ϕ and one of the four-heavy quark Wilson coefficients, evaluated at the scale $\Lambda = 1$ TeV for Run-II LHC measurements. Both linearised and quadratically truncated δR_{λ_3} fits are shown, and one can observe that the 95% CI bounds (shown on top of the panels) and correlations depend on the truncation.

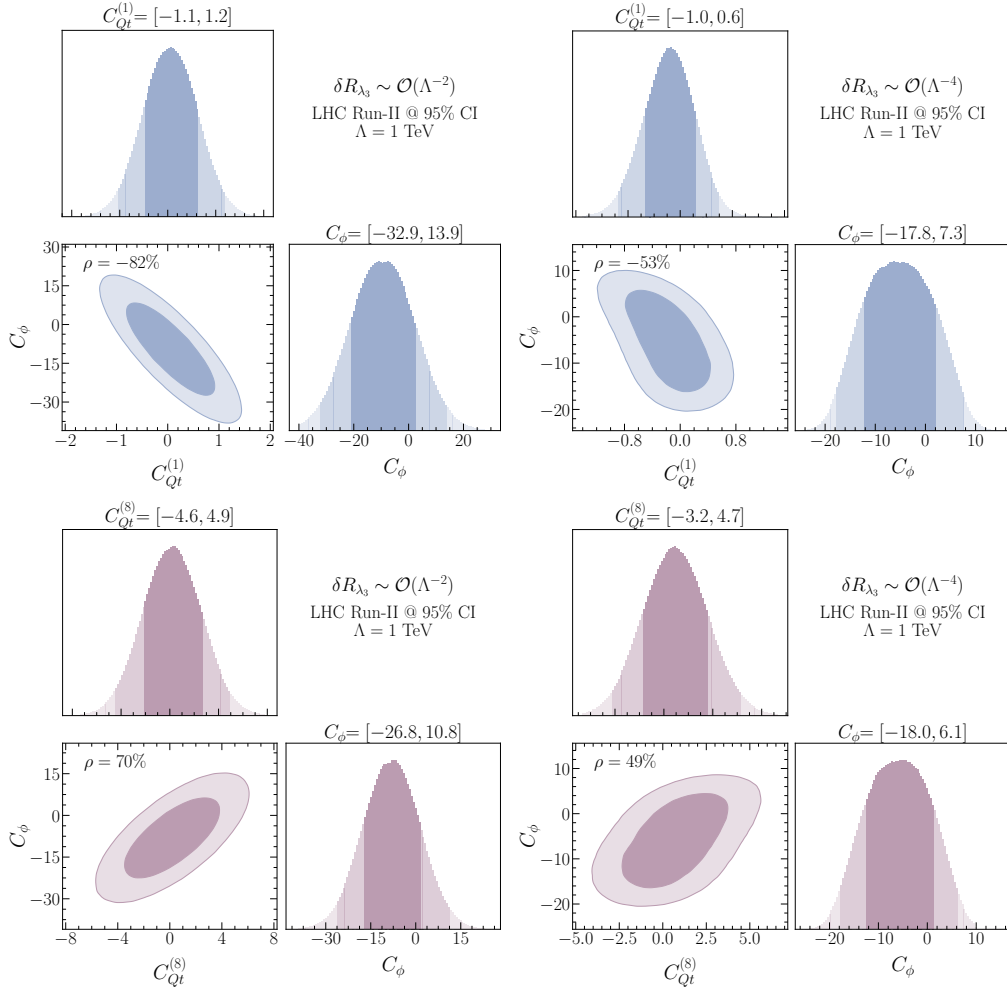


Figure 7.5. The posterior distributions of the Run-II data fits for C_ϕ with $C_{Qt}^{(1)}$ (up) and C_ϕ with $C_{Qt}^{(8)}$ (down). The 68% and 95% highest density posterior contours indicated. The limits shown on top of the plots indicate the 95% CIs. Plots on the left are made for the fully linearised δR_{λ_3} , while the ones on the right include the quadratic effects. This figure has been published in [\[151\]](#).

We observe that the four-fermion operators are strongly correlated with the Higgs self-

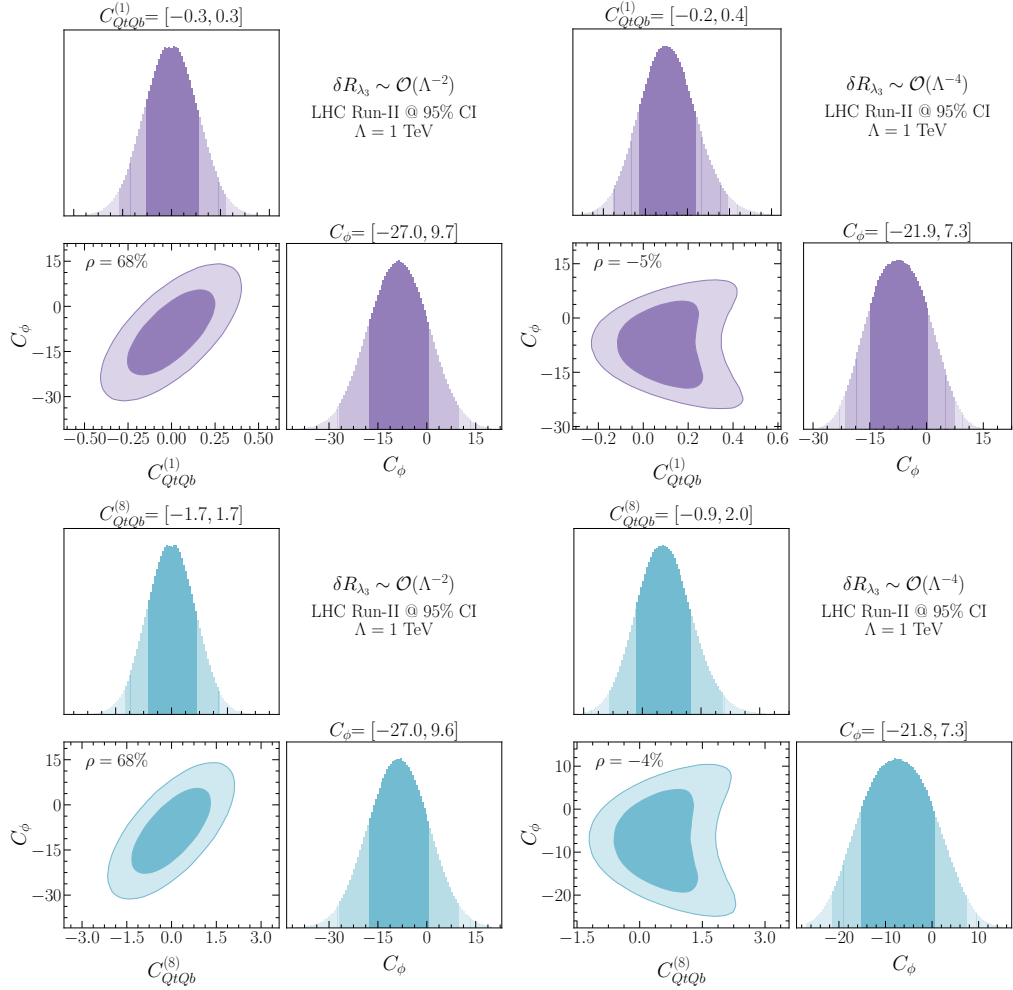


Figure 7.6. The posterior distributions of the Run-II data fits for C_ϕ with $C_{QtQb}^{(1)}$ (up) and C_ϕ with $C_{QtQb}^{(8)}$ (down). With the same annotations as in Figure 7.5. This figure has been published in [151].

coupling modifier \mathcal{O}_ϕ , in the linear fit, with Pearson's correlation of $\gtrsim 0.7$ and p -value $< 10^{-4}$. In the case of quadratic δR_{λ_3} fit, we observe diminished Pearson correlation, but in this scenario Pearson's correlation test is not particularly applicable, as we have non-linear relation between the variables.

The two-parameter fit results for the four-fermion Wilson coefficients are summarised in the forest plots in Figure 7.7, which is obtained by marginalising the posteriors distributions over C_ϕ . The finite effects were isolated by performing fits with δR^{fin} only. The finite effects are small for $O_{QtQb}^{(1)/(8)}$ but dominant for the four-top operators $O_{Qt}^{(1)/(8)}$; they are mainly coming from $t\bar{t}h$. The effect of EFT truncations of δR_{λ_3} can also be observed

as shifts in the mean values of the Wilson coefficients, but the 95% CIs themselves are not significantly affected. In these plots, the fit results from this study are also confronted with the limits obtained from fits to top-quark data [37, 184, 303, 304, 321, 322] and EWPO fits from [185]. When the Wilson coefficient running is taken into account, the 95% CI bounds obtained from Higgs data are consistently stronger than the ones from top data.

In Figure 7.8, the fit results for C_ϕ are shown after marginalising over the four-fermion Wilson coefficients in both EFT truncations schemes of δR_{λ_3} , as well as a single parameter fit for C_ϕ . These fits are compared also to the current 95 % CL bound on C_ϕ extracted from Higgs pair production search using the final state $b\bar{b}\gamma\gamma$ performed by ATLAS using Run-II data [323], which is translated from κ formalism.

The mean values and the 95% CIs change depending on the four-fermion Wilson coefficient that was paired with C_ϕ in the two-parameter fits. As expected, the single parameter fits for C_ϕ yield stronger bound on C_ϕ than the two-parameter fits, thus the inclusion of the four-fermion operators in single Higgs data dilutes C_ϕ bounds. Additionally, the truncation order of δR_{λ_3} appears to have a marked effect on the length of the CIs, with quadratic fits giving more stringent constraints on C_ϕ . Instead, for Higgs pair production it makes only a negligible effect if linear or up to quadratic terms in the EFT expansion are kept for the $C_\phi > 0$ bound, while the bound weakens at linear order in $1/\Lambda^2$ for $C_\phi < 0$ [324]. For instance, the quadratic single parameter fit for C_ϕ is comparable to the direct bound from Higgs pair production. However, this changes dramatically, when one includes the four-fermion operators in a combined fit, and the single-Higgs data constraints on C_ϕ become less significant compared to the direct hh bounds.

It should be noted that the strongest bond on the Higgs self-coupling currently comes from the perturbative unitarity bound of ref. [110].

One of the important aspects of multivariate studies is the correlation between the variables. Apart from the two-parameter fits discussed above, four-parameter fits are also considered. These fits include C_ϕ plus the three directions in the four heavy-quark operator parameter spaces that the Higgs rates are mostly sensitive too, i.e. neglecting $C_{QQ}^{(1),(3)}$ and C_{tt} , and trading $C_{QtQb}^{(1)}$ and $C_{QtQb}^{(8)}$ by C_{QtQb}^+ . When considering two- or four-parameter fits of C_ϕ and the four-heavy-quark Wilson coefficients, we observe non-trivial correlation patterns emerging amongst these coefficients. Figure 7.9 illustrates these correlation patterns for the four-parameter fit. We observe that the Wilson coefficients $C_{Qt}^{(1),(8)}$ are strongly correlated because, in analogy to $C_{QtQb}^{(1),(8)}$, they only appear in particular linear combination whenever correcting the Yukawa coupling. However, unlike $C_{QtQb}^{(1),(8)}$, they are not entirely degenerate because the main part of the NLO correction to $t\bar{t}h$ does not contain the aforementioned linear combination. The four-parameter fit also reveals that the Wilson coefficients $C_{Qt}^{(1),(8)}$ have a large correlation with C_{QtQb}^+ because all of the four Wilson coefficients appear in a linear combination in the NLO corrections except for $h \rightarrow b\bar{b}$ and $t\bar{t}h$. However, this correlation is not as strong due to the large NLO correction of the Higgs decay $h \rightarrow b\bar{b}$ from $C_{QtQb}^{(1),(8)}$. Moreover, the correlation between the four-heavy-quark Wilson coefficients and C_ϕ depends on the δR_{λ_3}

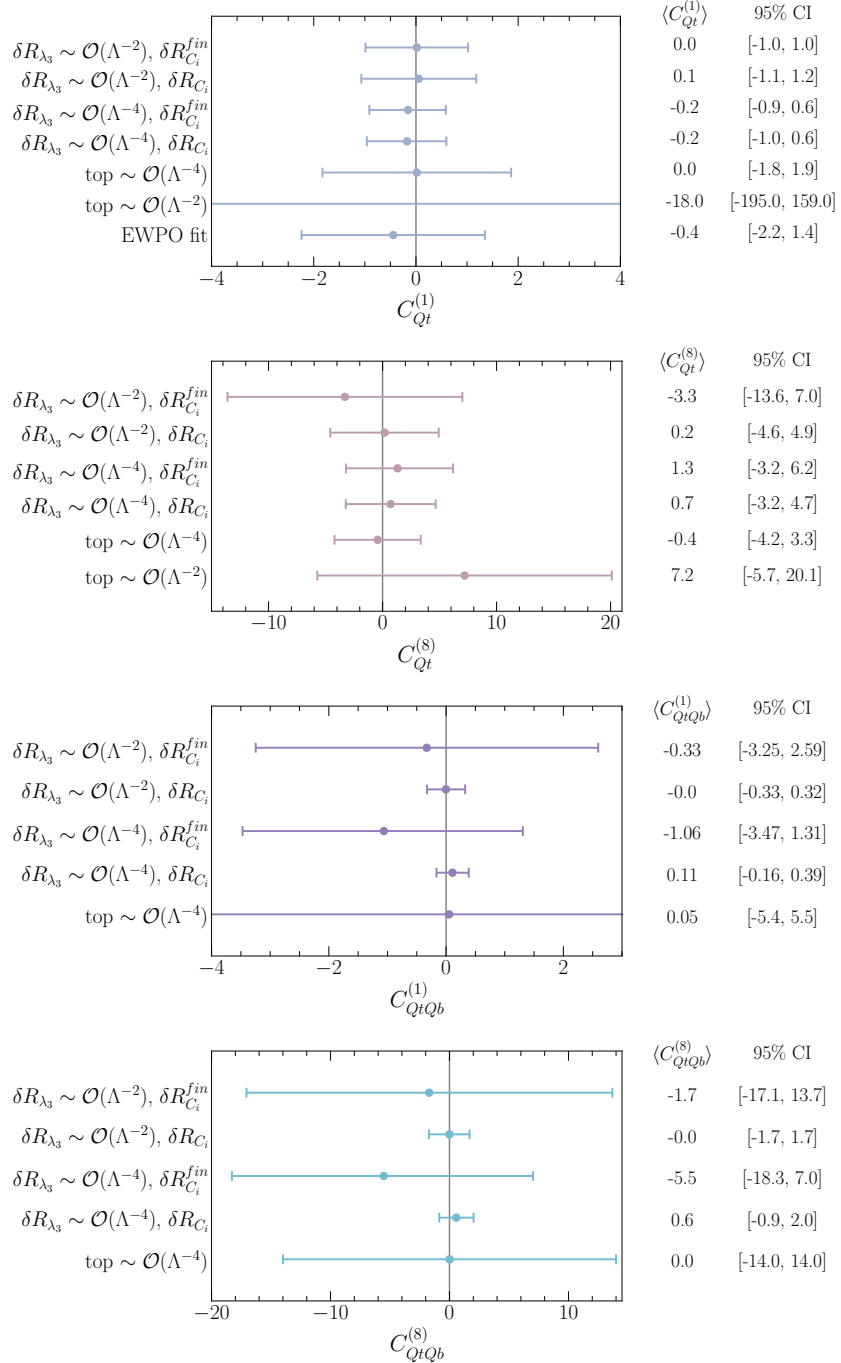


Figure 7.7. Forest plots illustrating the means and 95% CIs constraints on the four-heavy-quark Wilson coefficients C_i from Run-II data. These bounds are obtained from two-parameter fits including the aforementioned coefficients along with C_ϕ , then marginalising over the latter. The different fits with only the finite part of the NLO correction included vs the full results, as well as the EFT truncation scheme for the trilinear coupling, linear vs quadratic. Fits from top data [184] for $C_{Qt}^{(1),(8)}$ and [304] for $C_{QtQb}^{(1),(8)}$ as well as EWPO fits from [185] were included for comparison. This figure has been published in [151].

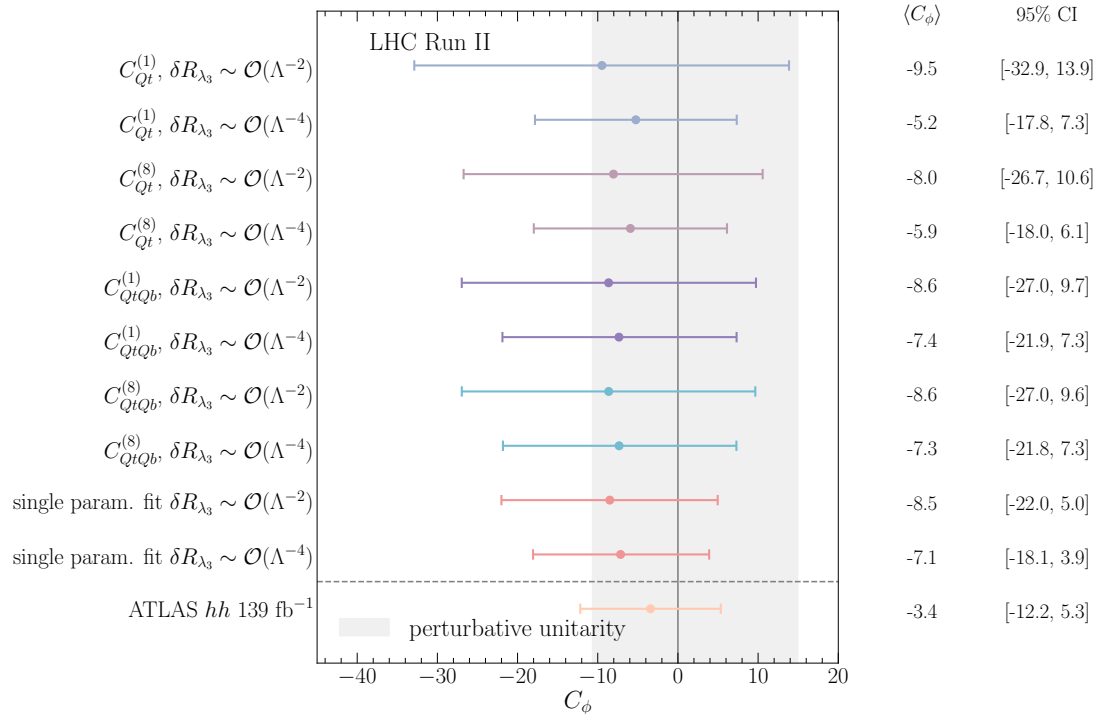


Figure 7.8. A forest plot illustrating the means and 95% CIs bounds for C_ϕ from the two-parameter fit, with the four-fermion operators marginalised. The fits results for C_ϕ from full Run-II Higgs data keeping terms up to $\mathcal{O}(1/\Lambda^2)$ or $\mathcal{O}(1/\Lambda^4)$ in δR_{λ_3} are shown. For comparison, also the 95% CI and means for the single parameter fit for C_ϕ with the same single Higgs data is shown as well as the bounds on C_ϕ from the 139 fb^{-1} search for Higgs pair production [323]. The horizontal grey band highlights the perturbative unitarity bound [110]. This figure has been published in [151].

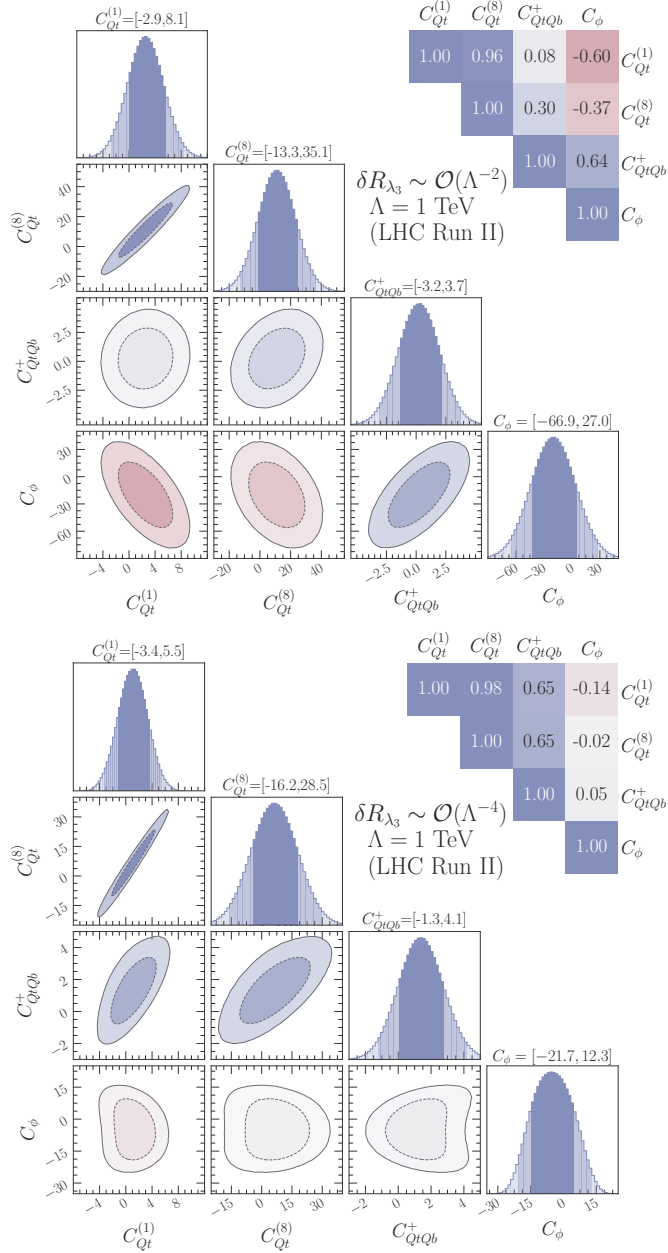


Figure 7.9. The marginalised 68% and 95% Highest density posterior contours for the four-parameter fits including the different four-quark Wilson coefficients and C_ϕ . The numbers above the plots show the 95% CI bounds while the correlations are given on the top-right side. The correlation between each pair of the Wilson coefficients is highlighted as a heatmap. The upper panel shows the fit including up to $\mathcal{O}(1/\Lambda^2)$ in δR_{λ_3} while the lower one shows the fit with including also $\mathcal{O}(1/\Lambda^4)$. This figure has been published in [151].

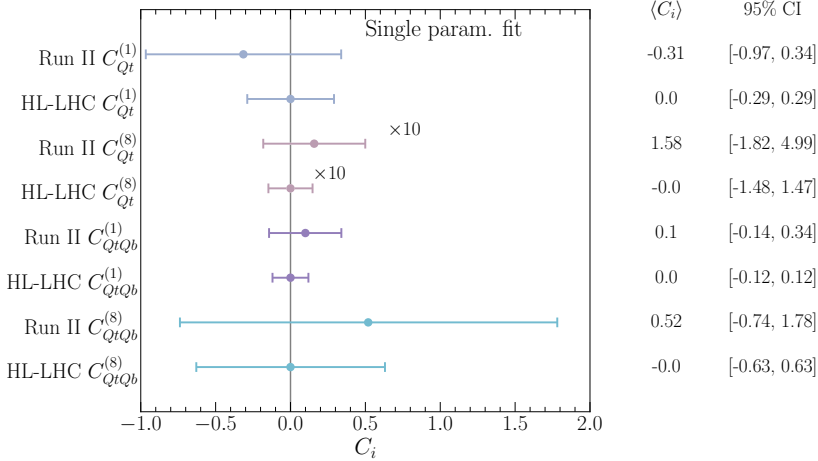


Figure 7.10. Results of single parameter fit showing the improvement in the constraining power of the HL-LHC over the current bounds from Run-2 data. This figure has been published in [151].

truncation.

7.2.2 Prospects for HL-LHC

Using the CMS Higgs signal strength projections for the HL-LHC in refs. [148, 317] for a centre-of-mass energy of $\sqrt{s} = 14$ TeV and integrated luminosity of 3 ab^{-1} , it is possible to repeat the fits done for Run-II. The projections for the S2 scenario explained in [235] were used. In Figure 7.10, I show the comparison between the fit results of Run-II data and the projections for the HL-LHC for single parameter fits. For the operators $\mathcal{O}_{Qt}^{(1),(8)}$ the constraining power of the HL-LHC is roughly a factor two better as the current bounds could be set from single Higgs data, while for the operators $\mathcal{O}_{QtQb}^{(1),(8)}$ the improvement is a little less prominent. In Figure 7.11, the limits on C_ϕ in a single parameter fit for Run-2 and the projections for the HL-LHC are shown. including δR_{λ_3} up to order $\mathcal{O}(1/\Lambda^2)$ or $\mathcal{O}(1/\Lambda^4)$. While for Run-II data, the inclusion of $\mathcal{O}(1/\Lambda^4)$ made a significant difference; this is less pronounced for the HL-LHC projections. These results are similar to the projections presented in a κ_λ fit in [325]. The results were also confronted with data from searches for Higgs pair production 139 fb^{-1} [323] and HL-LHC projections [326] on Higgs pair production, showing that Higgs pair production would still allow setting firmer limits on C_ϕ .

7.3 Conclusion

This chapter calculates the NLO corrections emanating from the SMEFT four-heavy-quark operators to single-Higgs rates. We have seen that both four-fermion operators' classes involving homogenous and heterogeneous chirality structures contribute to Higgs

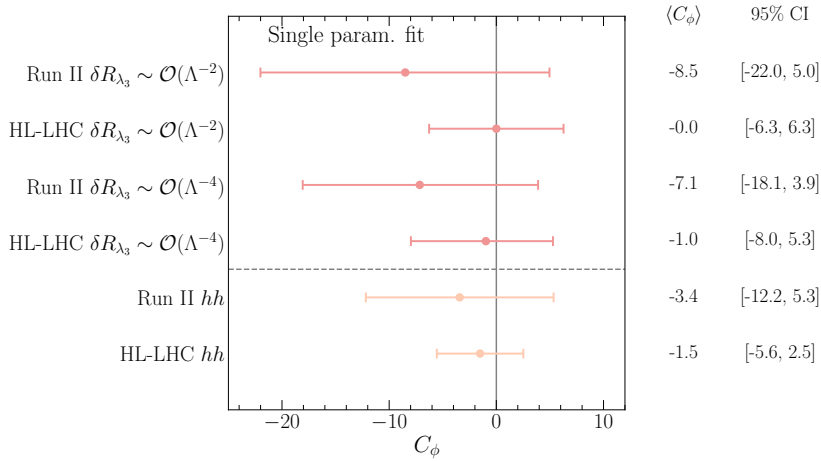


Figure 7.11. A forest plot illustrating the means and 95% CI's of the posteriors built from the C_ϕ in a single-parameter fit, showing also the differences in including terms of $\mathcal{O}(1/\Lambda^2)$ or up to $\mathcal{O}(1/\Lambda^4)$ in the definition of δR_{λ_3} . For comparison, also the limits and projections from searches for Higgs pair production are shown. This figure has been published in [151].

rates at NLO. Though, the operators with heterogeneous chirality structures have more sizeable effects as they would contribute to $h f \bar{f}$ vertex correction and quark mass renormalisation in SMEFT. Therefore, they appear in more channels compared to the operators baring homogenous chirality structures. The results of these calculations were utilised in fits on the Wilson coefficients associated with these operators using single-Higgs data. The operators with the same chirality structure are not constrained strongly by these fits, and hence their results were not included. This applies to the operators that contribute only via beauty-quark loops, like $\mathcal{O}_{Qb}^{(1),(8)}$.

Two processes stood out in this calculation in terms of their sensitivity to these operators. The first process is the decay of the Higgs to beauty quarks, which had a strong sensitivity to $\mathcal{O}_{QtQb}^{(1),(8)}$ operators. The second process is the associated production of the Higgs with top pair $t\bar{t}h$ having large finite corrections coming from $\mathcal{O}_{Qt}^{(1),(8)}$. Furthermore, these corrections depend on the colour factor and thus break the degeneracy between the singlet and octet operators.

Bayesian analysis combining the four-fermion operators with the SMEFT operator modifying the Higgs self-coupling C_ϕ has been performed and motivated by the fact that both operators are weakly constrained and only appear at NLO in single-Higgs rates. The fit results showed that the constraints on C_ϕ from single Higgs data would become significantly diluted compared to the fits performed with this operator alone, or even with ones that enter at LO [30–33, 35]. This is due to the strong correlation between C_ϕ and the four-fermion operators considered in this study. On the other hand, the fits yielded stronger bounds on the four-heavy-quark operators than those obtained from top-quark data [184, 304]. Comparable bounds can also be seen when EWPO data is considered

for their fit, cf. [185]. Similarly to single-Higgs processes, EWPO are modified by these operators at NLO, as well. Additionally, the authors of ref. [327] have shown that these operators could also be constrained from flavour observables involving $\Delta F = 2$, in particular $B_s - \bar{B}_s$ mixing. However, these bounds depend on the flavour ansatz of the NP and hence are not entirely model-independent.

The results of these calculations and consequent fits further emphasise the interconnectivity of SMEFT operators and experimental observables, which was discussed in ??.

Then remains the question: *How this interconnectivity would manifest in an NP model* ?. Remarkably, one might wonder if the strong correlation between these four-fermion operators and \mathcal{O}_ϕ could appear in a UV complete model. In fact, large effective couplings involving four top quarks are expected in many NP models, for example, partial compositeness [328]. These models would also generate sizeable modifications to the Higgs self-interaction. Similar effects could be obtained from models containing new scalars, such as an additional Higgs doublet $\varphi \sim (1, 2)_{\frac{1}{2}}$, or other scalars with non-singlet representation under $SU(3)_c$ like $(6, 1)_{\frac{1}{3}}$ and $(8, 2)_{\frac{1}{2}}$. For further details on these models and their matching, see [329]; for the NLO matching to SMEFT, see [330].

Part III

Higgs Pair Production

8 Overview of Higgs pair production at colliders

The determination of the shape of the Higgs potential is an essential part of the LHC physics programme. Unlike other Higgs measurements reviewed in this thesis, the light Yukawa and Higgs-self couplings are exceptionally hard to probe. This is evident from the conclusion of [chapter 7](#) for the case of trilinear Higgs coupling. We have seen that the effectiveness of using single-Higgs signals to probe the Higgs trilinear coupling is challenged by other weakly constrained operators also affecting these signals. Thus, Higgs pair production remains the only direct way to access this elusive interaction.

The production of Higgs in pairs has roughly 10^{-4} of the signal producing single Higgs at the LHC. Higgs pair production, with Higgs decays considered, has a cross-section of $\sim 1\text{fb}$, in the SM. This makes it inaccessible using Run-II or Run-III data but should be seen, in principle, using the total luminosity of the HL-LHC [[121](#), [235](#), [331](#)]. As for the quartic coupling, that requires NLO corrections to Higgs pair or triple Higgs production, both of which are beyond the sensitivity of the LHC [[332](#)]. The measurement potentials for the light Yukawa couplings shall be discussed in the next chapter. The main advantages for Higgs pair production in determining the Higgs trilinear self-coupling come from the dependence of the cross-section on λ_3 at the LO level, as well as the fact that the rest of SMEFT operators entering this process (see eq (4.11)) can be strongly constrained from other processes, breaking any potential correlations that might appear between them and the trilinear coupling using only di-Higgs data. However, the inclusion of light quark Yukawa couplings modifiers, e.g. $C_{u\phi}$ and $C_{d\phi}$, would complicate things, as we shall see in [chapter 9](#).

This chapter starts by reviewing the theoretical status of the dominant process for Higgs pair production, beginning with the gluon fusion in [section 8.1](#). Then, the other sub-dominant channels will be briefly reviewed in [section 8.2](#). Afterwards, I overview the experimental efforts in probing these rare yet fascinating processes in [section 8.3](#). Finally, I present in [section 8.4](#) a summary of the potential for Higgs production in probing Higgs elusive interactions.

8.1 Higgs pair production by gluon fusion

The dominant process for Higgs pair production at the LHC (and hadron colliders in general) is the gluon fusion channel via top quarks in the loops, while the beauty-quark loops contribute only to 1%, as shown in [Figure 8.1](#). This process is well-studied at leading order (LO) analytically [[333](#)–[336](#)]. The higher-order computations are significantly more

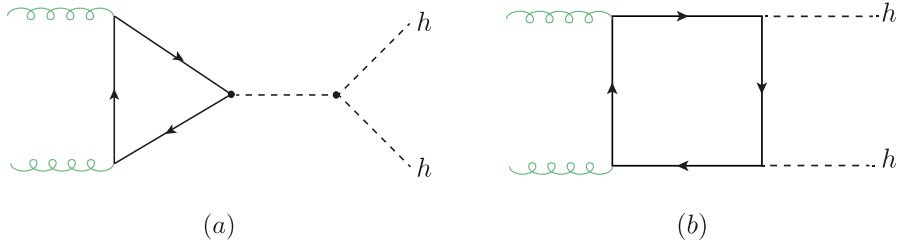


Figure 8.1. Feynman diagrams for the ggF process of Higgs pair production in the SM.

complicated to perform compared to the gluon fusion production of single-Higgs. This is because multi-scale amplitudes at two-loops (and more) cannot always be computed analytically using the current computational techniques. The first attempt to compute the NLO corrections to di-Higgs were via the HTL approximation [167, 240, 337] and implemented in HPAIR [336]. These corrections were large, with a K-factor of ~ 2 . This prompted more calculations with inclusion of top quark mass effects [218, 338–341], which improved the stability of the HTL expansion as well as corrected the cross-section by $\sim 10\%$. Later, the threshold resummation effects of the HTL have been included in [342]. This approach, however, is not sufficient to produce corrections to the differential cross-section, as the HTL fails for $m_{hh}^2/4m_t^2 \lesssim 1$. This particularly problematic for Higgs pair, as the peak of the cross-section is around $M_{hh} \approx 400\text{GeV}$, where this approximation fails. Using the numerical evaluation of the two-loop integrals, it is possible to obtain exact results with full top quark mass dependence, see refs. [343–345]. Nonetheless, this comes at the cost of computational power required to evaluate the cross-section. Hence, approximation methods were essential for obtaining more flexible results that can be used in simulations and BSM Higgs pair production. These approximations methods are analogous and sometimes connected to the ones used for Zh production that were discussed in chapter 6. This includes, small final particle transverse momentum [11], and high energy (HE) expansions [346]. In addition to a method developed in refs. [347, 348] that considers both \hat{s}, \hat{t} and m_t as large quantities while keeping the Higgs mass as a small one. This method has a wide coverage of the M_{hh} spectrum. The use of Padé approximants to improve the p_T -expanded amplitude coverage as well as to obtain a description for the three-loop (NNLO) form factors was demonstrated in [349]. The NNLO cross-section with top quark mass effects has been computed numerically in [350] and also at differential level [351], and analytically only in the HTL [352]. Also, NLO+NNL analytical results have been obtained by [353]. Parton shower matching for NLO Higgs pair production has been computed in [354, 355], which was essential for the POWHEG implementation for di-Higgs, with NLO corrections computed from a grid has been made available by [199, 355, 356]. Figure 8.2 shows the Higgs pair virtual partonic cross-section defined in eq.(6.37) vs the p_T and HE expansions bridged using Padé approximants [274]. The matching between the results across low and high energy intervals of m_{hh} shows the strength of the Padé approximants technique. This is the most recent analytic higher-order correction result for Higgs pair production.

The LO Higgs pair production with SMEFT operators is available in SMEFTatNLO model [270]

for MadGraph.

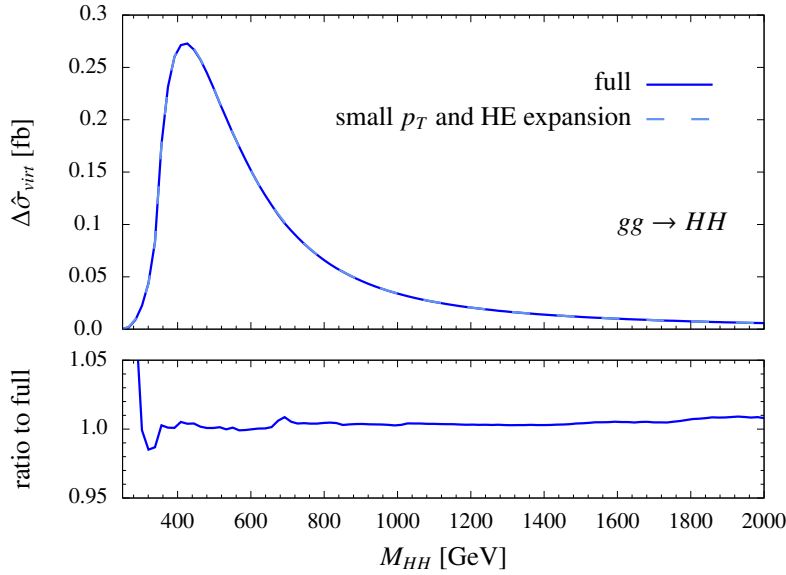


Figure 8.2. Combination of the HE and p_T expansions of the virtual two-loop NLO corrections using Padé approximants, confronted with the NLO results from a numerical grid. This plot is taken from [274].

Calculation of LO in addition to higher order corrections to Higgs pair production in EFT, MSSM and composite Higgs models can be found in [190, 196, 357–360].

The NNLO correction were used according to the Higgs cross-section working group recommended values [361, 362]:

$$K = \frac{\sigma_{NNLO}}{\sigma_{LO}}, \quad K_{14\text{TeV}} \approx 1.71. \quad (8.1)$$

8.1.1 Theoretical uncertainties

There are four main sources of the theoretical uncertainties for Higgs pair production:

1. Scale uncertainty: coming form the arbitrariness of scales choice.
2. PDF uncertainties: as a result of the uncertainty in the PDF fitting and modelling.
3. α_s running uncertainty: originating from the initial value (i.e. $\alpha_s(M_Z)$).
4. Top quark mass renormalisation scheme that involves m_t appearing in the loop propagators and in the top Yukawa.

The computation of the uncertainties is described in [363, 364]. for PDF and α_s uncertainties. In order to calculate the scale uncertainties, the cross-section was computed

	σ [fb]	Scale [fb]	PDF+ α_s [fb]	Total [fb]
SM HEFT (LO)	18.10	—	—	—
SM running mass (LO)	16.96	—	—	—
SM (LO)	21.45	$+4.29$ -3.43	± 1.46	$+4.53$ -3.73
SM (NLO) [368]	33.89	$+6.17$ -4.98	$+2.37$ -2.01	$+6.61$ -5.37
SM (NNLO) [350]	36.69	$+0.77$ -1.83	± 1.10	$+1.66$ -6.43 (incl. m_t uncertainty [365])

Table 8.1. Gluon fusion Higgs pair production cross-section at 14 TeV with theoretical uncertainties, the HTL is computed using HEFT, top running mass, LO, NLO and NNLO QCD corrections. The NLO and NNLO results are taken from the references cited in the table. The LO results are computed via a FORTRAN code.

with different μ_R and μ_F values ranging between:

$$\frac{M_{hh}}{4} \leq \mu_R/\mu_F \leq M_{hh} \quad (8.2)$$

As for the m_t renormalisation uncertainty, one uses the $\overline{\text{MS}}$ running of the top quark mass formula at N³LO [365]

$$\overline{m}_t(m_t^{pole}) = m_t^{pole} \left(1 + \frac{4}{3\pi} \alpha_s(m_t^{pole}) + 10.9 \frac{\alpha_s^2(m_t^{pole})}{\pi^2} + 107.11 \frac{\alpha_s^3(m_t^{pole})}{\pi^3} \right)^{-3}. \quad (8.3)$$

The total 14 TeV ggF hh , cross-section at different orders in computation with its uncertainties is shown in Table 8.1, which indicates that the uncertainties are dominated by the m_t renormalisation scheme of $\sim -18\%$ uncertainty in the lower envelope. This is a significant part of the uncertainty budget and needs to be resolved by including N³LO corrections to ggF hh . Such corrections are available hitherto only in the HTL [366, 367].

8.2 Other processes

Like single-Higgs production at hadron colliders, the production of Higgs pairs has the same subdominant channels VBF, di-Higgsstrahlung Vhh and associates production of Higgs pair with tops $t\bar{h}h/tjhh$. Their cross-sections and uncertainties at 14 TeV are shown in Table 8.2, while in Figure 8.3 their cross-sections as a function of the centre-of-mass energy \sqrt{s} is shown [325].

8.2.1 VBF hh

Vector boson fusion hh production has the second largest cross-section after ggF hh , which is calculated up to N³LO [368–370] inclusively and differentially at NNLO [371]. The dominant diagrams are analogous to the single Higgs VBF involving the W/Z

Process	Cross-section 14 TeV (fb)	Theo. accuracy	Theo. uncertainty (%)	Contribution (%)
1. ggF hh	36.690	NNLO QCD	12.3	90.1
2. VBF hh	2.050	N ³ LO QCD	2.1	5.0
3. Zhh	0.415	NNLO QCD	3.6	1.0
4. W ⁺ hh	0.369	NNLO QCD	2.1	0.9
5. W ⁻ hh	0.198	NNLO QCD	3.0	0.5
6. tt hh & tjh	0.986	NLO QCD	5.1	2.4

Table 8.2. Summary of the Higgs pair production processes at 14 TeV LHC.

bosons exchanged in the t -channel. The process has the same topology as the off shell single Higgs VBF, with the off-shell Higgs giving two final states ones via the trilinear self-coupling.

8.2.2 Di-Higgsstrahlung

The associated production of the Higgs pair with W and Z bosons has a small cross-section compared to ggF and VBF. This process is known up to NNLO QCD accuracy, including the gluon-fusion component in the full computation [372, 373].

8.2.3 Associated Higgs pair production with t -quarks

Sometimes called the di-Higgs bremsstrahlung off top quarks [325], this channel has a steeper dependence on \sqrt{s} than the single Higgs bremsstrahlung $t\bar{t}h$. One can see, for example, from Figure 8.3 that its cross-section becomes at roughly the same values as the VBF's at large \sqrt{s} . Only NLO computations for these channels have been carried out [374].

All three channels have a relatively small NLO correction compared to ggF, which ranges from 10-30%.

8.3 Experimental overview for Higgs pair production

The search for Higgs pair production can be divided into two categories, resonant and non-resonant production. The first searches for heavy resonances that decay into a Higgs pair, while the latter is concerned about the SM scenario or if the NP has a scale beyond the reach of the LHC, i.e. when the EFT limit is valid. In this review, I shall focus on the non-resonant searches, as these are the ones relevant to the focus of this thesis; for a detailed overview of the resonant searches, cf. [325].

Figure 8.4 shows the current experimental scopes for detecting non-resonant Higgs pair production by both ATLAS and CMS. The searches are summarised according to the final state:

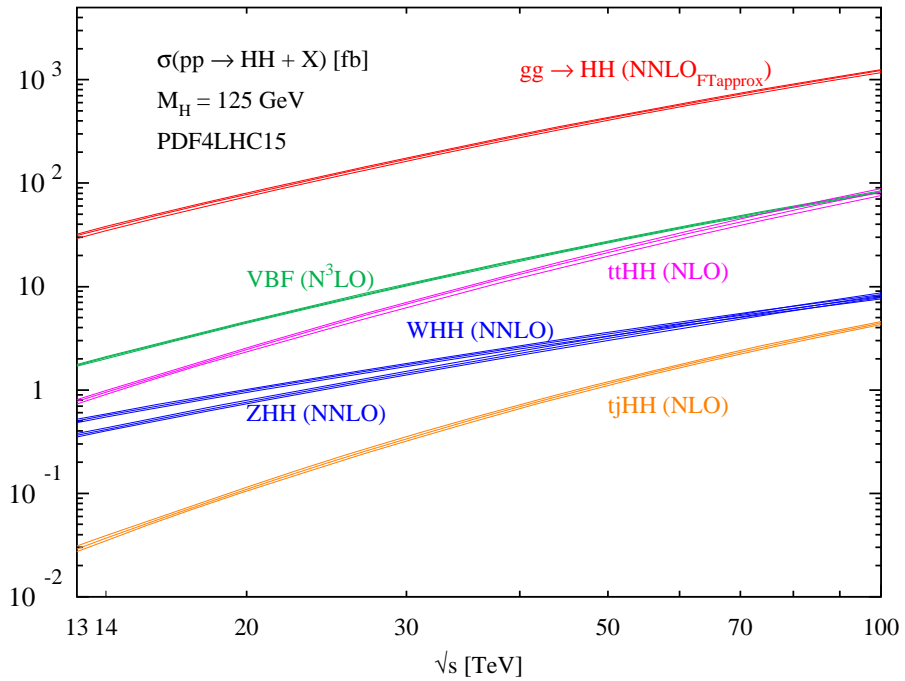


Figure 8.3. The cross-section of all Higgs pair production processes at the highest available perturbation order as a function of centre-of-mass energy \sqrt{s} . The bands show the uncertainties without the top quark mass renormalisation scheme. This plot is taken from [325].

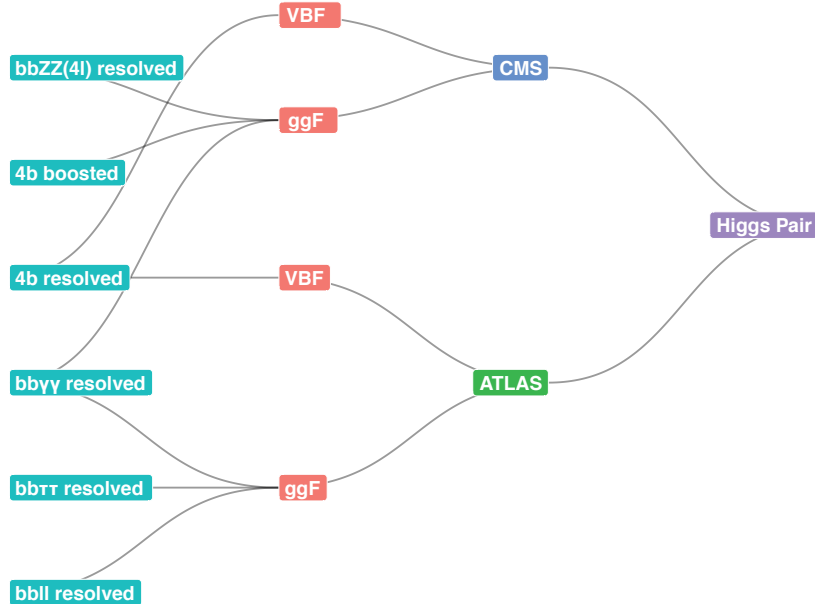


Figure 8.4. The non-resonant Higgs pair searches conducted by ATLAS and CMS using the full Run-II data.

$hh \rightarrow b\bar{b}b\bar{b}$

The final state $hh \rightarrow b\bar{b}b\bar{b}$ has the highest SM cross-section possible for the Higgs pair but is difficult to probe due to the large QCD background of four b-tagged jets in the final state. CMS [375] has used boosted decision trees (BDT) for studying this final state for ggF and VBF channels. This allowed for sensitivity on the trilinear and $hhVV$ couplings. Their analysis led to 95% CL bounds on $\kappa_\lambda \in [-2.3; 9.4]$ and $\kappa_{2V} \in [-0.1; 2.2]$. They have also performed a boosted analysis for the VBF channel by defining two large jets with a jet radius of $\Delta R = 0.8$. Despite their analysis not being sensitive to the trilinear self-coupling, it could probe both κ_V and κ_{2V} , which leads to the most stringent bound on the latter coupling modifier so far $\kappa_{2V} \in [0.6; 1.4]$. The $\kappa_{2V} = 0$ hypothesis is excluded with $p < 0.001$ [376]. On the other hand, ATLAS has performed only a resolved analysis for this final state and the VBF production channel [377]. Hence they were able to report bounds on $hhVV$ coupling $\kappa_{2V} \in [-0.43; 2.56]$.

 $hh \rightarrow b\bar{b}VV$

ATLAS has considered the gluon fusion final state $hh \rightarrow b\bar{b}\ell\ell$, with the leptons coming from WW/ZZ decays [378]. This state covers around 90% of the total $hh \rightarrow b\bar{b}VV$ signal. Their analysis was divided into two categories: same-flavour and different-flavour leptons. The observed signal strength was higher than the expected one. Hence, no bounds on the self-coupling could be extracted from this search. CMS has carried out a similar analysis but with a requirement to observe four leptons instead of two. That is, they have searched for the final state $hh \rightarrow b\bar{b}(ZZ^* \rightarrow 4\ell)$. The 95% CL upper limit on the signal strength was 30 times the SM one, with bounds on Higgs self-coupling of $\kappa_\lambda \in [-9; 14]$ [379].

 $hh \rightarrow b\bar{b}\tau\tau$

This channel has backgrounds coming from real τ 's, such as $t\bar{t}$ and Zj with heavy jets. In addition to fake τ 's coming from QCD multijet process. A neural network (NN) has been used by ATLAS [380] investigating this channel, using resolved b jets. The extracted bounds on the trilinear self-coupling are $\kappa_\lambda \in [-2.4; 9.2]$.

 $hh \rightarrow b\bar{b}\gamma\gamma$

This final state is the most promising for Higgs pair searches. Despite having a lower cross-section than the previous final states with BR of 0.27% in the SM, it has the highest selection efficiency. This is due to the low backgrounds and the ability to reconstruct the photons fully. The dominant non-reducible background is QCD/QED production of $b\bar{b}\gamma\gamma$, which has a cross-section of $\sim 13\text{fb}$ at the 14 TeV LHC, more details about the backgrounds of this final states are shown in Table 8.3.

Both ATLAS and CMS have published searches of this channel using BDT and NN analyses [323, 381]. With ATLAS reporting the strongest 95% CL bound on κ_λ thus far,

Channel	LO σ [fb]	NLO K -fact	6 ab^{-1} [#evt @ NLO]
$b\bar{b}h, y_b^2$	0.0648	1.5	583
$b\bar{b}h, y_b y_t$	-0.00829	1.9	-95
$b\bar{b}h, y_t^2$	0.123	2.5	1,840
Zh	0.0827	1.3	645
$\sum b\bar{b}h$	0.262	-	2,970
$b\bar{b}\gamma\gamma$	12.9	1.5	116,000
$t\bar{t}h$	1.156	1.2	6,938

Table 8.3. SM cross-section for the main background processes at 14 TeV with 6 ab^{-1} data at the HL-LHC. For $b\bar{b}h$ production, the Higgs boson is decayed to a pair of photons. The total production of Higgs associated with $b\bar{b}$ is denoted by $\sum b\bar{b}h$ and is the sum of the top four channels.

which was used in the comparisons in Figure 7.11. While CMS has reported bounds on both κ_λ and κ_{2V} : $\kappa_\lambda \in [-3.3; 8.5]$ and $\kappa_{2V} \in [-1.3; 3.5]$.

8.3.1 Prospects for the HL-LHC

The highlight of the HL-LHC programme is the detection of Higgs pair production. It is projected that the Higgs pair signal to be observed at $\sim 4 - 4.5\sigma$ level [325]. The use of machine learning techniques in the analysis of hh searches will be a key factor in the success of these searches [235]. In section 9.5, the interpretable machine learning technology will be exploited in improving the sensitivity for hh signals at the HL-LHC. With the main focus on the $b\bar{b}\gamma\gamma$ final state. As this channel has the highest potential for discovery of di-Higgs production [368, 382–387]. The projected constraints on κ_λ at the HL-LHC for combined ATLAS and CMS are $\kappa_\lambda \in [0.1, 2.3]$ [235, 325]

8.4 Summary

The Higgs pair production is a missing critical measurement of the SM; it is essential to determine the Higgs potential by directly constraining the Higgs trilinear self-coupling. Moreover, this channel is sensitive to non-linear couplings of the Higgs, like $hhVV$ and $hhf\bar{f}$. Due to the small cross-section of this channel, current searches obtain relatively weak bounds on κ_λ that are comparable with the perturbative unitarity bounds [110]. Nonetheless, the HL-LHC is expected to result in an observation or even discovery of this process, particularly with the help of advanced machine learning techniques.

The observation of Higgs pair production is expected to provide a direct measurement of one of the two “difficult” couplings in the SM Higgs sector, the trilinear Higgs self-coupling. However, as we shall explore in the upcoming chapter, it could also provide a window for observing the Higgs coupling to light quarks, the second challenging coupling class we discussed earlier.

9 Higgs pair as a probe for light Yukawa couplings

The vast hierarchy of quark (and lepton) masses that we have seen in section 2.3 is one of the most peculiar aspects of the SM. One might wonder whether the Braut-Englert-Higgs mechanism is responsible for the light quark mass generation or if other physics exists beyond the SM. In fact, one of S. Weinberg’s last papers addressed this question [388]. In this paper, Weinberg proposed that only the third generation fermions obtain their masses from Yukawa coupling, while the rest acquire theirs via loop-level interactions. Despite his models being only illustrative, his paper is a testament that even the pioneers of the SM theory still reflect upon this mystery.

The pragmatic approach to unravelling this puzzle directly measures the Higgs interaction with light fermions. Ideally, this would be via Higgs decay to first and second-generation fermions. This is feasible for the muon case [160, 161] and rather challenging for the charm quarks [162–164] and rather impossible with the current technologies for the electron [389], strange and first-generation quarks. Although, lepton colliders might have potential for *strange tagging* [390]. The difficulties here are twofold. First, the SM predicts that these couplings are extremely small, effectually making these decay channels vanish even at tens of ab^{-1} luminosity. Even if NP enhanced the Higgs coupling to these fermions, the resolution of the LHC would not be sufficient for reconstructing the Higgs from electron pairs, and it is not possible to distinguish up, down, or gluon jets at the LHC from the overwhelming QCD background. This means that the search for these couplings ought to take a non-trivial path. Enhancements of light quark Yukawa couplings would open the tree-level quark anti-quark annihilation Higgs production channel $q\bar{q}A$, which is enhanced by the presence of light quarks in the PDFs. Furthermore, it could break the degeneracy amongst the strange up and down quarks by having a *production tagging* coming from the different distributions of the PDFs amongst quark flavours [391]. For sufficiently large enhancement of the light quark Yukawa couplings, this channel would even become dominant over the loop-induced gluon fusion, as seen in Figure 9.2. Working strictly in the SMEFT paradigm, the $q\bar{q}A$ channel would contain a $hhq\bar{q}$ contact interaction illustrated in Figure 9.1; this interaction enhances the Higgs pair production more than the single Higgs $q\bar{q}A$, thus making Higgs pair production more sensitive to light quark Yukawa enhancement, as Figure 9.2 indicates.

Although the ggF Higgs pair production channel in SMEFT contains diagrams with contact $hhq\bar{q}$ interaction shown in Figure 9.3, the contribution of this diagram topology is suppressed by the kinematic mass of the quarks appearing inside the loops; hence the ggF channel is not affected by enhanced light quark Yukawa couplings in a relevant way.

This chapter aims to study the potential for Higgs pair production as a direct probe

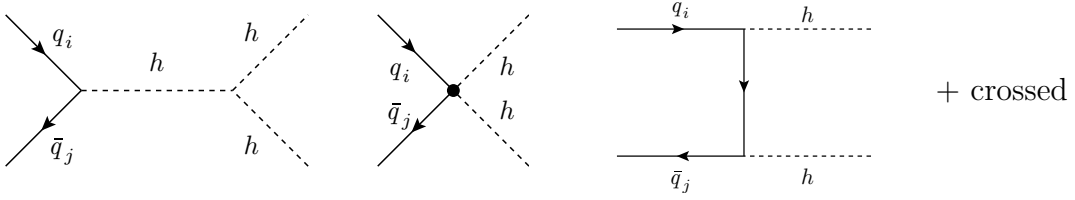


Figure 9.1. Feynman diagrams for the $q\bar{q}A$ Higgs pair production in the SMEFT paradigm. The middle diagram shows a contact $hhq\bar{q}$ interaction that significantly enhances this channel compared to its single Higgs counterpart.

channel for light quark Yukawa. Focusing on the first generation quarks. I will start by introducing the inclusion of light quark couplings to the Higgs in the SMEFT framework in section 9.1. Then the NLO QCD calculation of the $q\bar{q}A$ channel will be shown in section 9.2. section 9.4 will outline a cut-based analysis of the di-Higgs final state $b\bar{b}\gamma\gamma$ to estimate the sensitivity of this channel for the HL-LHC. Later, in section 9.5 an optimised approach for enhancing the sensitivity based on multi-variant analysis and interpretable machine learning will be showcased. The results of both analysis techniques will be discussed and compared in section 9.6 While in section 9.7 I will overview the other searches for light Yukawa couplings, comparing them to the Higgs pair production sensitivity. This chapter will be concluded in section 9.8.

The cut-based analysis has been published in [392], while the interpretable machine-learning one is an undergoing project with R. Gröber, C. Grojean, A. Paul, and Z. Qian, and expected to be published soon [324].

9.1 SMEFT and light Yukawa couplings

Explicitly writing the flavour indices ij of the SMEFT operators and lifting the condition of their flavour universality, we could get light quark -Higgs coupling enhancement from the operators

$$\Delta\mathcal{L}_y = \frac{\phi^\dagger\phi}{\Lambda^2} \left(C_{u\phi}^{ij} \overline{Q}_L^i \tilde{\phi} u_R^j + C_{d\phi}^{ij} \overline{Q}_L^i \phi d_R^j + h.c. \right), \quad (9.1)$$

The mass matrices of the up-and down-type quarks obtained from the Yukawa and the new SMEFT coupling are

$$M_{ij}^u = \frac{v}{\sqrt{2}} \left(y_{ij}^u - \frac{1}{2}(C_{u\phi})_{ij} \frac{v^2}{\Lambda^2} \right),$$

$$M_{ij}^d = \frac{v}{\sqrt{2}} \left(y_{ij}^d - \frac{1}{2}(C_{d\phi})_{ij} \frac{v^2}{\Lambda^2} \right), \quad (9.2)$$

where y_{ij}^q are the SM Yukawa matrix elements introduced in eq. (2.22). Since the quark masses are measured quantities, one would naturally rotate to the mass basis using bi-

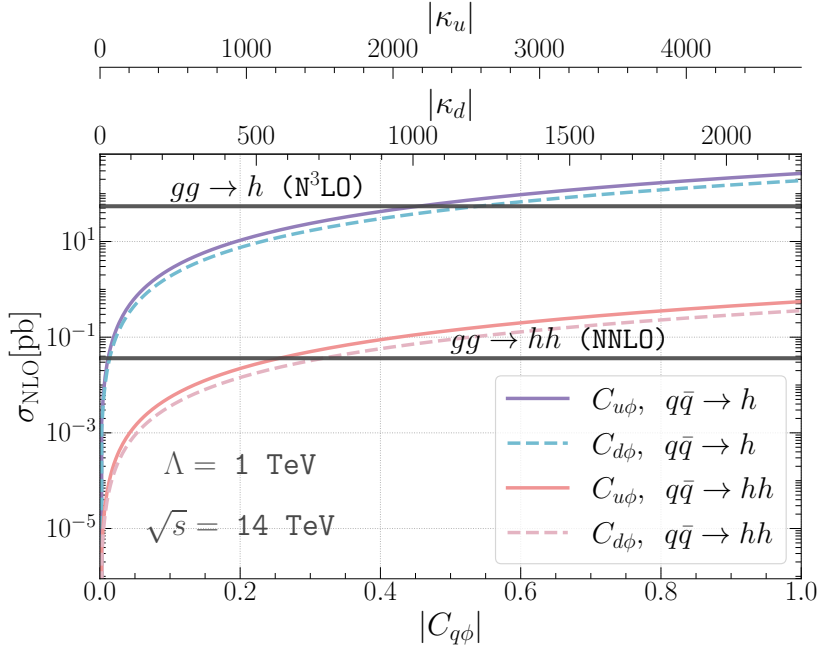


Figure 9.2. The production cross-section of single Higgs and di-Higgs at 14 TeV from the quark anti-quark annihilation $q\bar{q}A$ as a function of the Wilson coefficients $C_{u\phi}$ and $C_{d\phi}$ versus the SM gluon fusion cross-sections, the horizontal solid line for gluon fusion channels. One can observe that for values of $C_{u\phi} = 0.22$ (0.43) and $C_{d\phi} = 0.26$ (0.47) the $q\bar{q}A$ channel becomes the dominant di-Higgs (single Higgs) production channel. The NP scale is set to $\Lambda = 1$ TeV.

unitary transformation represented by the matrices $\mathcal{V}_q, \mathcal{U}_q$, like in the SM. The Wilson coefficients matrix elements in the flavour space in the mass basis can be written as

$$\tilde{C}_{q\phi}^{ij} = (\mathcal{V}_q)_{ni}^* C_{q\phi}^{nm} (\mathcal{U}_q)_{mj}, \quad \text{with} \quad q = u, d. \quad (9.3)$$

In order to match these Wilson coefficients to Higgs couplings to quarks, we use the Lagrangian operator describing these couplings

$$\mathcal{L} \supset g_{h\bar{q}_i q_j} \bar{q}_i q_j h + g_{h\bar{q}_i q_j} \bar{q}_i q_j h^2 \quad (9.4)$$

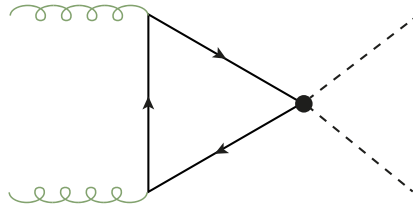


Figure 9.3. The new diagram for ggF emerging from the $hhq\bar{q}$ coupling appearing in SMEFT.

Then the matching results in identifying the SMEFT couplings of Higgs and quarks

$$g_{h\bar{q}_iq_j} := \frac{m_{q_i}}{v} \delta_{ij} - \frac{v^2}{\Lambda^2} \frac{\tilde{C}_{q\phi}^{ij}}{\sqrt{2}}, \quad g_{hh\bar{q}_iq_j} := -\frac{3}{2\sqrt{2}} \frac{v}{\Lambda^2} \tilde{C}_{q\phi}^{ij}. \quad (9.5)$$

We observe that, in the general case, we will be having non-diagonal couplings. However, such couplings are strongly constraint by flavour observables, particularly neutral meson mixing [393].

$$|\tilde{C}_{q\phi}^{12}| \lesssim 10^{-5} \Lambda^2/v^2 \quad |\tilde{C}_{d\phi}^{13/23}| \lesssim 10^{-4} \Lambda^2/v^2 \quad (9.6)$$

Due to these strong constraints, it is typical to consider SMEFT with minimal flavour violation (MFV) [394], in which the SM Yukawa matrices y_q^{ij} are the only spurions breaking the global $SU(3)_Q \otimes SU(3)_U \otimes SU(3)_D \rightarrow U^6(1)$ flavour symmetry. This implies that the Wilson coefficients matrices in the mass basis are simultaneously diagonalisable with the SM Yukawa matrices and inherit their hierarchy. Therefore, MFV is not a viable scheme for considering significant enhancements to the couplings for first and second generations while keeping the third generation couplings unchanged.

In order to bypass the constraints of MFV and also avoid flavour changing neutral currents (FCNC) that are prohibited by flavour observables, one needs to turn to flavour alignment [395, 396] or its generalisation aligned flavour violation (AFV) [397].

With flavour alignment, the NP flavour parameters (here the Wilson coefficients) are aligned with the SM Yukawa, such that both can be simultaneously diagonalised, thus preventing tree-level FCNCs. Contrary to MFV, the duress of making these new parameters proportional to the SM Yukawas is lifted. This would induce radiative FCNCs, as this formalism is unstable under quantum corrections [398–400]. This alignment breaking would not be seen in the SMEFT but rather when UV-complete models are considered. AFV resolves this instability by ensuring that any NP Spurion breaking the flavour symmetry will transform trivially under the quark phases transformations $U^6(1)$, keeping the CKM matrix the only flavour object that has non-trivial transformations. Thereby the CKM will have physical flavour changing currents as well as a \mathcal{CP} -violating phase. This constraint on the NP flavour spurions k_q , allows them to be written as a series in powers of the CKM matrix, known as the alignment expansion

$$k_u = K_{0,u} + K_{1,u} V_{CKM}^* K_{2,u} V_{CKM}^T K_{3,u} + \mathcal{O}(V_{CKM}^4) + \dots, \quad (9.7)$$

$$(k_d)^\dagger = K_{0,d} + K_{1,d} V_{CKM}^T K_{2,d} V_{CKM}^* K_{3,d} + \mathcal{O}(V_{CKM}^4) + \dots, \quad (9.8)$$

where $K_{i,u}$ and $K_{i,d}$ are complex 3×3 diagonal matrices invariant under flavour transformations. This formalism is stable under renormalisation group evolution as any linear combinations, or tensor products of the spurions will remain flavour aligned.

For simplicity, I shall only consider the first term in the alignment expansion, such that only diagonal $C_{q\phi}$ are investigated, as the other terms are already CKM-suppressed and not of particular phenomenological interest. With this in mind, and using the translation between SMEFT and κ -formalism discussed in subsection 4.2.2, it is possible to identify

the couplings in SMEFT with the κ 's

$$g_{h\bar{q}_iq_i} = \kappa_q g_{h\bar{q}_iq_i}^{\text{SM}}, \quad g_{hh\bar{q}_iq_i} = -\frac{3}{2} \frac{1-\kappa_q}{v} g_{h\bar{q}_iq_i}^{\text{SM}}, \quad (9.9)$$

in a slight abuse of language of the κ -formalism as the $hh\bar{q}\bar{q}$ coupling typically is not included in it.

Higgs pair production offers an extra advantage for probing light Yukawa interactions, as it is susceptible to the $hh\bar{q}\bar{q}$ interaction; one could also consider the non-linear HEFT by extending it to include Wilson coefficients c_q and c_{qq} for the first and second-generation quarks, in analogy to ones defined for the top quark in eq. (4.14) [401]. The analysis performed on these HEFT parameters is published in [392].

9.2 Higgs pair production and Higgs decays with modified light Yukawa couplings

As we have briefly discussed in the introduction, the gluon fusion channel of Higgs pair production is affected by enhanced light Yukawa couplings in two ways. First is the inclusion of light quark loops in the triangle and box diagrams. Second, the new diagrams introduced by the contact $hh\bar{q}\bar{q}$ coupling are shown in Figure 9.3. However, these effects are negligible due to the mass-suppression of these diagrams by the light quark appearing in the loops. Therefore, effectively, one could consider the ggF channel as purely derived by third-generation quarks and only affected by the trilinear coupling C_ϕ as far as this analysis is concerned.

9.2.1 Higgs pair production via quark anti-quark annihilation

Contrary to the ggF, the $q\bar{q}A$ channel does not exist in the SM, except for $b\bar{b} \rightarrow hh$, following the assumptions of 4(or 5)-flavour scheme, that the these quarks are massless. This channel contains four-diagrams shown in Figure 9.1, and its differential partonic cross-section is given by

$$\frac{d\hat{\sigma}_{q_i\bar{q}_j}}{d\hat{t}} = \frac{1}{16\pi} \frac{1}{12\hat{s}} \left[\left| 2g_{hhq_i\bar{q}_j} + \frac{g_{hhh} g_{hq_i\bar{q}_j}}{\hat{s} - m_h^2 - im_h\Gamma_h} \right|^2 + \mathcal{O}(g_{hq_i\bar{q}_j}^4) \right], \quad (9.10)$$

where the $\mathcal{O}(g_{hq_i\bar{q}_j}^4)$ terms stem from the \hat{t} and \hat{u} channel diagrams, and their contribution is typically only $\sim 0.1\%$ of the total cross-section. The hadronic cross section is then obtained by

$$\sigma_{\text{hadronic}} = \int_{\tau_0}^1 d\tau \int_{\hat{t}_-}^{\hat{t}_+} d\hat{t} \sum_{i,j} \frac{d\mathcal{L}^{q_i\bar{q}_j}}{d\tau} \frac{d\hat{\sigma}_{q_i\bar{q}_j}}{d\hat{t}}, \quad (9.11)$$

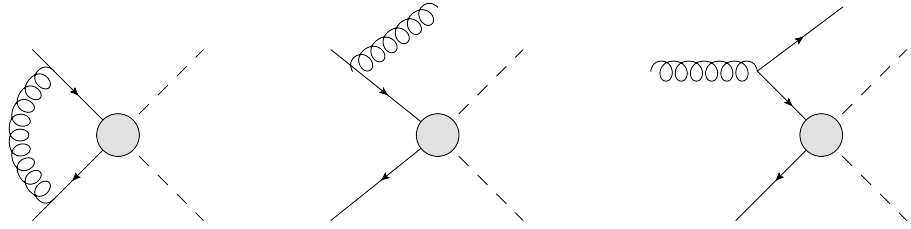


Figure 9.4. Generic form of the QCD corrections of order $\mathcal{O}(\alpha_s)$ to the $q\bar{q}A$ Higgs pair production.

with $\tau_0 = 4m_h^2/s$, $\hat{s} = \tau s$ and

$$\hat{t}_\pm = m_h^2 - \frac{\hat{s}(1 \mp \beta)}{2} \quad \text{and} \quad \beta = \sqrt{1 - \frac{4m_h^2}{\hat{s}}}. \quad (9.12)$$

The parton luminosity is given by

$$\frac{d\mathcal{L}^{q_i\bar{q}_j}}{d\tau} = \int_\tau^1 \frac{dx}{x} \left[f_{q_i}(x/\tau, \mu_F^2) f_{\bar{q}_j}(x, \mu_F^2) + f_{\bar{q}_j}(x/\tau, \mu_F^2) f_{q_i}(x, \mu_F^2) \right]. \quad (9.13)$$

All the kinematic masses were neglected, following the 5-flavour scheme of the PDF, while the coupling of the Higgs boson to the light quarks (for flavour diagonal couplings) is

$$g_{hq_i\bar{q}_j} = \frac{m_q^{\overline{MS}}(\mu_R)}{v} \kappa_q \delta_{ij}, \quad (9.14)$$

and analogously for the $g_{hhq_i\bar{q}_j}$ coupling. It is worth noting that there is no inconsistency with such an assumption since, in scenarios of modified Yukawa couplings, the masses of the quarks need not be generated by electroweak symmetry breaking.

NLO QCD correction

Since the ggF NLO QCD corrections are sizeable, it is reasonable to assume that the same would apply to the $q\bar{q}A$ counterpart. Computing the NLO QCD corrections to this channel is a relatively straightforward task. More simplifications can be made by neglecting the NLO corrections of the \hat{t} and \hat{u} channels because they are strongly suppressed. This enables us to adapt the NLO QCD corrections results from $b\bar{b} \rightarrow h$ in the 5-flavour scheme [402–404], also for $b\bar{b}hh$ [405, 406], to the s -channel and contract term $q\bar{q}A$ diagrams. This is achieved by some adjustments taking into account the modified LO cross-section and the different kinematics of the process. The Feynman diagrams at NLO QCD are shown in Figure 9.4. For convenience and to make our

adjustments explicit, we report here the formulae from [407]

$$\sigma(q\bar{q} \rightarrow h) = \sigma_{LO} + \Delta\sigma_{q\bar{q}} + \Delta\sigma_{qg} \quad (9.15a)$$

$$\Delta\sigma_{q\bar{q}} = \frac{\alpha_s(\mu_R)}{\pi} \int_{\tau_0}^1 d\tau \sum_q \frac{d\mathcal{L}^{q\bar{q}}}{d\tau} \int_{\tau}^1 dz \hat{\sigma}_{LO}(Q^2 = z\tau s) \omega_{q\bar{q}}(z) \quad (9.15b)$$

$$\Delta\sigma_{qg} = \frac{\alpha_s(\mu_R)}{\pi} \int_{\tau_0}^1 d\tau \sum_{q,\bar{q}} \frac{d\mathcal{L}^{qg}}{d\tau} \int_{\tau}^1 dz \hat{\sigma}_{LO}(Q^2 = z\tau s) \omega_{qg}(z) \quad (9.15c)$$

and

$$\hat{\sigma}_{LO}(Q^2) = \int_{\hat{t}_-}^{\hat{t}_+} \frac{d\hat{\sigma}_{q_i\bar{q}_j}}{d\hat{t}} \quad (9.16)$$

with $z = \tau_0/\tau$, $\sigma_{LO} = \sigma_{\text{hadronic}}$ of eq. (9.11), and the ω factors are given by

$$\begin{aligned} \omega_{q\bar{q}}(z) &= -P_{qq}(z) \ln \frac{\mu_F^2}{\tau s} + \frac{4}{3} \left\{ \left(2\zeta_2 - 1 + \frac{3}{2} \ln \frac{\mu_R^2}{M_{hh}^2} \right) \delta(1-z) \right. \\ &\quad \left. + (1+z^2) \left[2\mathcal{D}_1(z) - \frac{\ln z}{1-z} \right] + 1-z \right\}, \end{aligned} \quad (9.17a)$$

$$\omega_{qg}(z) = -\frac{1}{2} P_{qg}(z) \ln \left(\frac{\mu_F^2}{(1-z)^2 \tau s} \right) - \frac{1}{8} (1-z)(3-7z), \quad (9.17b)$$

with $\zeta_2 = \frac{\pi^2}{6}$. The Altarelli Parisi splitting functions $P_{qq}(z)$ and $P_{qg}(z)$ [408–410] are given by

$$P_{qq}(z) = \frac{4}{3} \left[2\mathcal{D}_0(z) - 1 - z + \frac{3}{2} \delta(1-z) \right], \quad (9.18a)$$

$$P_{qg} = \frac{1}{2} \left[z^2 + (1-z)^2 \right], \quad (9.18b)$$

and the “plus” distribution is

$$\mathcal{D}_n(z) := \left(\frac{\ln(1-z)^n}{1-z} \right)_+. \quad (9.19)$$

The renormalisation scale $\mu_R = M_{hh}$ and the factorisation scale $\mu_F = M_{hh}/4$, were chosen as central values.

The NLO $q\bar{q}A$ cross-section as well as the LO ggF were implemented in a private FORTRAN code utilising the VEGAS integration algorithm, and NNPDF30 parton distribution functions (PDF’s)[411] available through the LHAPDF-6 package [412]. For the one-loop integrals appearing in the form factors of the box and triangle diagrams, we have used the COLLIER library [413] to ensure numerical stability of the loop integral calculation

for massless quarks inside the loops¹. The resulting NLO K -factor was found to be

$$K_{NLO} = \frac{\sigma_{NLO}}{\sigma_{LO}} = 1.28 \pm 0.02, \quad (9.20)$$

with the error denoting the theoretical uncertainty. The K -factor does not depend on the scaling of the couplings nor the flavour of the initial $q\bar{q}$ since the LO cross-section factors out (except for the different integration in the real contributions).

The $q\bar{q}A$ channel will enhance the overall Higgs pair production cross-section. Still, if one considers the ggF as an SM background for the Yukawa enhancement “signal” $q\bar{q}A$ channel, it would be interesting to estimate qualitatively when this signal becomes dominant, further emphasising the sensitivity of Higgs pair to light Yukawa enhancements as Figure 9.2 demonstrates. The dominant term for $q\bar{q}A$ comes from the $hhq\bar{q}$ vertex diagram, such that the $q\bar{q}A$ cross-section behaves for large values of κ as (assuming that $\sigma_{SM}^{q\bar{q}A} \sim 0$)

$$(\sigma^{q\bar{q}A} - \sigma_{SM}^{q\bar{q}A}) \sim g_{hhq\bar{q}}^2 \sim v^{-4} m_q^2 \kappa_q^2. \quad (9.21)$$

The ggF cross-section instead gets contributions from light quark loops interfering with top quark loops in the triangle SM diagram, leading to scaling of

$$(\sigma^{ggF} - \sigma_{SM}^{ggF}) \sim \kappa_q \frac{m_q^2}{v^2 M_{hh}^2} \ln^2 \left(\frac{M_{hh}}{m_q} \right). \quad (9.22)$$

Taking the ratio we get

$$\frac{(\sigma^{q\bar{q}A} - \sigma_{SM}^{q\bar{q}A})}{(\sigma^{ggF} - \sigma_{SM}^{ggF})} \sim \frac{\kappa_q}{v^2 \left(\frac{\ln^2 \left(\frac{M_{hh}}{m_q} \right)}{M_{hh}^2} \right)}. \quad (9.23)$$

This ratio approaches one (neglecting effects from different PDFs) when

$$\kappa_q^{q\bar{q}A=ggF} \sim \frac{v^2 \ln^2 \left(\frac{M_{hh}}{m_q} \right)}{M_{hh}^2}. \quad (9.24)$$

Using this order of magnitude estimate, we see that the two cross sections are roughly equal if $\kappa_c^{q\bar{q}A=ggF} \sim 1$, $\kappa_s^{q\bar{q}A=ggF} \sim 10$ and $\kappa_u^{q\bar{q}A=ggF} \sim \kappa_d^{q\bar{q}A=ggF} \sim 10^3$. The actual values of $\kappa_q^{q\bar{q}A=ggF}$ for the first generation quarks can be read from fig. ???. It is interesting to point out to the pact that these κ_q values are not yet excluded.

9.2.2 Higgs decays

In the same way hh production acquires additional channels due to enhanced Yukawa couplings, also Higgs decays to light quarks will become significant compared to the SM

¹I have expanded the code to include other SMEFT operators, and it can be found in the GitHub repository https://github.com/aliasfar-lina/HH_XS_in_SMEFT

case with Higgs decays to first-generation BR'S being $< \mathcal{O}(10^{-9})$ [362]. In addition to the contribution of light quarks in the loop-level decays $h \rightarrow \gamma\gamma/Z\gamma$ and $h \rightarrow gg$, though this effect is small. Since the $h \rightarrow q\bar{q}$ decay are near impossible to detect with the current technologies, the effect of opening these decay channels is reduction in the branching ratios of the Higgs final states that are typically sought after, like $h \rightarrow b\bar{b}$ and $h \rightarrow \gamma\gamma$.

In order to compute the Higgs partial widths and branching ratios (BR) at higher orders in QCD, I have modified the FORTRAN programme **HDECAY** [414, 415] to include the light fermion decay channels and loops in the above-mentioned decays². The overall change of the Higgs total width is given by

$$\Gamma_H \approx \Gamma_{\text{SM}} + \sum_{q=c,s,u,d} \frac{g_{h\bar{q}_iq_i}^2}{(g_{h\bar{q}_iq_i}^{\text{SM}})^2} \Gamma_q, \quad (9.25)$$

where Γ_q can be obtained at NLO QCD from the modified **HDECAY** code. Detailed results for the Branching ratios for the final states of interest have been published in [392].

In order to have a preliminary estimate about the sensitivity of Higgs pair production to light Yukawa enhancements, it is important to consider both production and decay effects in terms of signal strength

$$\mu_i := \frac{\sigma \text{BR}_i}{\sigma^{\text{SM}} \text{BR}_i^{\text{SM}}}. \quad (9.26)$$

Comparing the production of single Higgs vs Higgs pair signal strengths, for any final state of interest, we could see in Figure 9.5 that for first-generation $C_{q\phi} \lesssim 0.8$ Higgs pair production has a higher signal strength than single-Higgs production despite having double the reduction in the signal strength from the decays of two Higgs bosons as opposed to a single one. In fact, and as we shall see in section 9.7, values of $C_{q\phi} > 0.4$ have been already excluded by multiple searches.

9.3 Event generation for the final state $hh \rightarrow b\bar{b}\gamma\gamma$

For this study, the final state $b\bar{b}\gamma\gamma$ is considered, as this channel has the most potential for Higgs pair searches [235]. It has the “clean” $h \rightarrow \gamma\gamma$ decay, but also the other Higgs decay to b -quark pair is a channel with a large branching ratio $\sim 58\%$ and b-tagging capabilities for ATLAS and CMS are continuously improving.

For the cut-based analysis, the FORTRAN codes used to compute the hh cross-section and decay have been interfaced with **Pythia** 6.4 [416], where the $q\bar{q}A$ process was generated at NLO and the ggF at NLO, then multiplied with the NLO K-factor. The generated events were written to a ROOT file via **RootTuple** tool [417] for further

²The modified **HDECAY** code can be found in the GitHub repository https://github.com/aliasfar-lina/hdecay_lightflavour

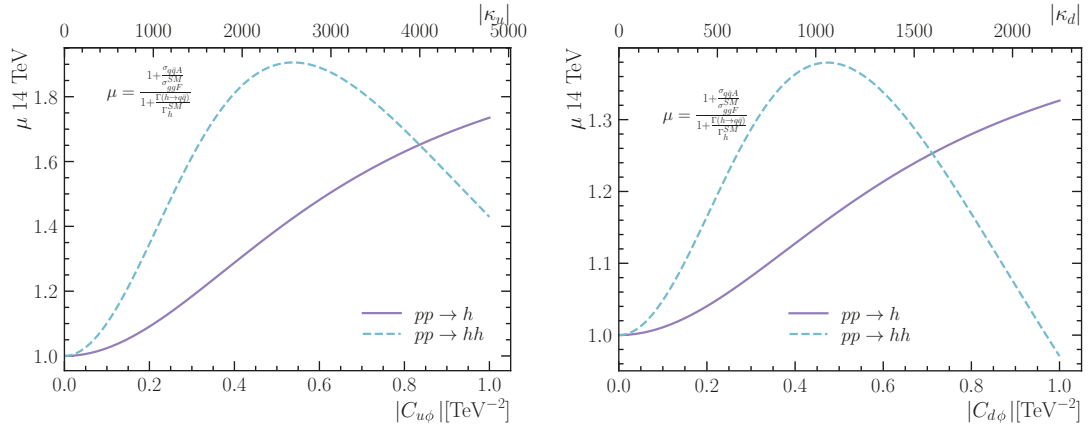


Figure 9.5. Signal strengths at 14 TeV LHC, of the single Higgs (purple solid line) vs. Higgs pair (blue dashed line) as functions of $C_{u\phi}$ (left) and $C_{d\phi}$ (right). Both plots show that for $C_{q\phi} \lesssim 0.8$ the signal strength of Higgs pair production is higher than the single Higgs one. This implies that Higgs pair production is more sensitive to enhancements of light quark Yukawa in SMEFT. This is independent of the final state (except for $h \rightarrow q\bar{q}$).

analysis.

The backgrounds were not simulated for this analysis; rather, the results from [382] were used because we have used the same cuts as this reference.

For the multivariate analysis based on interpretable BDT, the backgrounds and signal events needed to be generated. The backgrounds described in Table 8.3 were generated using `MadGraph_aMC@NLO` [268], then showered via `Pythia 8.3` [418] and a detector simulation is done using `Delphes 3` [419], the QED/QCD background $b\bar{b}\gamma\gamma$, Zh and $b\bar{b}h$ events were taken from the analysis data of ref. [40], while $t\bar{t}h$ events were generated specifically for this analysis. In order to obtain the NLO cross-section for these process, the events were multiplied by their respective K -factors that have been obtained from $t\bar{t}h$ [420], $b\bar{b}\gamma\gamma$ [421], Zh [422] and the remaining part of the $b\bar{b}h$ processes from [423].

The Higgs pair signals were generated in a slightly different pipeline. The ggF channel events were simulated first using `POWHEG` [199, 355, 356], which has been modified to separate the individual contributions from the box, triangle, and their interference individually. This is done to easily scale by κ_λ (or C_ϕ), as the box does not depend on it, while the triangle and the interference have quadratic and linear dependence, respectively. The $q\bar{q}A$ channel events were generated via `MadGraph_aMC@NLO` using a model created with `FeynRules` [308]. Samples for both up-and down-quark initiated $q\bar{q}A$ processes have been generated. Parton showering and fast detector simulation for both Higgs pair processes were run through the same pipeline as the backgrounds. This also goes for the scaling by the NLO of $q\bar{q}A$ and NNLO for ggF K -factors after the event generation. The Higgs bosons were decayed with the assumption of narrow width approximation, and the BR values were computed in the modified `HDECAY` code.

Channel	LO σ [fb]	K -fact.	Order	6 ab^{-1} [#evt @ order]
$hh_{\text{tri}}^{\text{ggF}}$	$7.288 \cdot 10^{-3}$	2.28		96
$hh_{\text{box}}^{\text{ggF}}$	0.054	1.98	NNLO	680
$hh_{\text{int}}^{\text{ggF}}$	-0.036	2.15		-460
$u\bar{u}\text{A}$ ($C_{d\phi} = 0.1$)	2.753	1.29	NLO	28
$d\bar{d}\text{A}$ ($C_{u\phi} = 0.1$)	4.270	1.30		43

Table 9.1. The LO cross-section for Higgs pair production processes (including the decay $hh \rightarrow b\bar{b}\gamma\gamma$) for 6 ab^{-1} 14 TeV HL-LHC.

To be inclusive and to explore the capabilities and importance of the full detector coverage, no generator-level cuts were applied on these processes except for the $b\bar{b}\gamma\gamma$ processes to avoid divergences. These minimal generator-level cuts for $b\bar{b}\gamma\gamma$ are

$$\begin{aligned} Xp_T^b &> 20 \text{ GeV}, \\ \text{generator level cuts: } &\eta_\gamma < 4.2, \Delta R_{b\gamma} > 0.2, \\ &100 < m_{\gamma\gamma} (\text{GeV}) < 150. \end{aligned} \quad (9.27)$$

Here Xp_T^b implies a minimum p_T cut for at least one b -jet. After the showering and detector simulation, further basic selection cuts were applied to select events with

$$\begin{aligned} \text{basic cuts: } &n_{\text{eff}}^{b\text{jet}} \geq 1, n_{\text{eff}}^{\gamma\text{jet}} \geq 2, \\ &p_T^{b\text{jet}} > 30 \text{ GeV}, p_T^{\gamma\text{jet}} > 5 \text{ GeV}, \\ &\eta_{b\text{jet},\gamma\text{jet}} < 4, 110 \text{ GeV} < m_{\gamma_1\gamma_2} < 140 \text{ GeV}, \end{aligned} \quad (9.28)$$

and $n_{\text{eff}}^{b/\gamma\text{jet}}$ representing the number of b/γ -jets that pass the basic selection. The cross-section, K -factors, number of events with 6 ab^{-1} luminosity at 14 TeV are given in Table 8.3 for the background and in Table 9.1 for the Higgs pair signals. Both analysis methods included sensitivity analysis for the HL-LHC, i.e. 14 TeV and 6 ab^{-1} ³ luminosity and projections for a future hadron circular collider (FCC-hh), with 100 TeV and the luminosity of 30 ab^{-1} have been made for the ML-based analysis. The results for the FCC can be found in the Appendix C.

9.4 Cut-based analysis

A cut and count analysis has been performed mainly as a “proof of concept” to demonstrate the sensitivity of Higgs pair production for probing light quark Yukawa couplings. The analysis used the same cuts and m_{hh} binning as ref. [382] such that their background events counts can be used.

³In the published cut-based analysis [392] 3 ab^{-1} luminosity for the HL-LHC were used. However, here I used 6 ab^{-1} when reporting fit results

9.4.1 Analysis strategy

The number of expected background N_b and signal N_s events needs to be estimated from simulated events to derive sensitivity bounds. Since N_b is taken from [382], the task is to estimate N_s for the $q\bar{q}A$ process as a function of $C_{q\phi}$, and to reproduce N_s of the ggF SM process published in the reference as a cross-check.

Since the cross-section, branching fraction and the integrated luminosity, it is only needed to estimate the selection efficiency ϵ_{SEL} from the applied cuts appearing in eq (3.1) to obtain the number of signal events.

The basic cuts of trigger-level selection are jets and photons with minimal p_T and maximal η .

$$p_T(\gamma/j) > 25 \text{ GeV}, \quad |\eta(\gamma/j)| < 2.5. \quad (9.29)$$

Additionally, a veto on the events with hard leptons is applied

$$p_T(\ell) > 20 \text{ GeV}, \quad |\eta(\ell)| < 2.5, \quad (9.30)$$

Jets were clustered using `fastjet` [424] with the anti-kt algorithm with a radius parameter of $R = 0.5$.

The b -tagging efficiency of $\epsilon_b = 0.7$, as well as the photon identification efficiency $\epsilon_\gamma = 0.8$ have been simulated in accordance with the ATLAS and CMS performance [425–427, 427, 428]. The selection cuts we used are the same ones as in [382], starting with the cuts of the transverse momentum p_T of the photons and b -tagged jets. The two hardest photons/ b -tagged jets, with transverse momentum $p_{T>}$, and the softer ones with $p_{T<}$ are selected to satisfy

$$p_{T>}^>(b/\gamma) > 50 \text{ GeV}, \quad \text{and} \quad p_{T<}^>(b/\gamma) > 30 \text{ GeV}. \quad (9.31)$$

In order to ensure well-separation of the photons and b -jets, we required the following cuts on the jet radius,

$$\Delta R(b, b) < 2, \quad \Delta R(\gamma, \gamma) < 2, \quad \Delta R(b, \gamma) > 1.5. \quad (9.32)$$

The mass windows used are about three times the photon resolution of ATLAS and CMS [427, 428], such wide windows were used in order to avoid significant signal loss.

$$105 \text{ GeV} < m_{b\bar{b}} < 145 \text{ GeV}, \quad 123 \text{ GeV} < m_{\gamma\gamma} < 130 \text{ GeV}. \quad (9.33)$$

The selection cuts are summarised in table Table 9.2 with their corresponding efficiency. The total selection efficiency for the ggF channel was found to be $\epsilon_{ggF} = 0.044$, consistent with the results of [382], while the $q\bar{q}A$ channel efficiency is slightly higher $\epsilon_{qq} = 0.05 \pm 0.001$ for the up and down quark initiated $q\bar{q}A$, results for second generation quarks can be found in [392].

cut	ϵ_{cut}	$\delta\epsilon_{\text{cut}}$
Trigger-level in eq. (9.29) and (9.30)	0.71	0.04
p_T cuts in eq. (9.31)	0.35	0.07
ΔR cuts in eq. (9.32)	0.69	0.21
total	0.11	0.06

Table 9.2. The cuts used in the analysis with their efficiency ϵ_{cut} and uncertainties on these efficiencies $\delta\epsilon_{\text{cut}} = \sqrt{\epsilon(1 - \epsilon)N}$, where N is the total number of events. The analysis was performed on 100K SM simulated events.

9.4.2 Statistical analysis

The likelihood ratio test statistic q_μ was used in order to estimate the HL-LHC sensitivity, and set projected limits on the SMEFT Wilson coefficients $C_{q\phi}$, with and without the modifier of the trilinear coupling C_ϕ .⁴ The likelihood function was constructed from the signal and background events in each bin of the m_{hh} distribution described in [382]

$$-\ln \mathcal{L}(\mu) = \sum_{i \in \text{bins}} (N_{bi} + \mu N_{si}) - n_i \ln(N_{bi} + \mu N_{si}), \quad (9.34)$$

with N_{bi} and N_{si} being the number of background and signal events in the i th m_{hh} distribution, respectively. In order to include the theoretical uncertainties on the expected number of signal events, the above likelihood was extended by a Gaussian distribution for N_{si} in which the mean equals to the central value of the bin values and standard deviation σ equals to its theoretical uncertainty. The signal strength μ was then estimated by minimising $-\ln \mathcal{L}(\mu)$ to obtain the estimator for $\hat{\mu}$ by injecting SM signal + background events n_i . The test statistic is then given by

$$q_\mu = 2(\ln \mathcal{L}(\mu) - \ln \mathcal{L}(\hat{\mu})), \quad (9.35)$$

following the procedure described in [429], and using the Python package `pyhf` [430, 431]. The expected 6 ab^{-1} HL-LHC sensitivity for the signal strength at 95% (68 %) CL is found to be $\mu = 1.5(1.1)$.

9.5 Optimised search for Higgs pair via Interpretable machine learning

When dealing with a multivariate problem, such as separating the Higgs pair signal from its backgrounds, using “simple” cuts is not the most efficient method for accomplishing this task. This is mainly because the various features used in the classification correlate with each other in multivariate analysis, and making simple cuts like in the previous

⁴ Additionally the HEFT parameters c_q and c_{qq} were studied, the results can be found in the published paper [392].

study will not capture this correlation. On the other hand, with a BDT classifier, it is possible to capture these correlations and introduce highly non-trivial cuts.

9.5.1 Constructing features

The simulated events of the signal and background described in the event selection section are required to contain at least two reconstructed photons and at a b -tagged jet. From these events, the following high-level features were constructed

- $p_T^{b_1}, p_T^{b_2}, p_T^{\gamma_1}, p_T^{\gamma\gamma},$
- $\eta_{b_{j1}}, \eta_{b_{j2}}, \eta_{\gamma_1}, \eta_{\gamma\gamma},$
- $n_{bjet}, n_{jet}, \Delta R_{\min}^{b\gamma}, \Delta\varphi_{\min}^{bb},$
- $m_{\gamma\gamma}, m_{bb}, m_{b_1 h}, m_{b\bar{b}h}, H_T.$

Here, $p_T^{b/\gamma_{1,2}}$ and $\eta^{b/\gamma_{1,2}}$ are the p_T and pseudorapidity for the tagged leading and sub-leading b/γ -jets (in our definition the subleading b -jet could be a null four-vector since we require one b -jet inclusive), n_{bj} is the number of tagged and passed b -jets. $\Delta R_{\min}^{b\gamma}$ and $\Delta\varphi_{\min}^{bb}$ are the minimum jet-distance and φ -angle between a tagged b -jet and a photon jet. The remaining variables are the invariant masses, and H_T is the scalar sum of the transverse mass of the system.

These features are the same as those studied in ref. [40] for $b\bar{b}h$. However, they are, by no means, unique. It is possible to run the analysis with another set of features and obtain the same results, as long as these features are independent and highly correlated. Figure 9.6 shows the distributions four most important features from this list, the $m_{\gamma\gamma}$ is very important in distinguishing the large $b\bar{b}\gamma\gamma$ background from the signal and $t\bar{t}h$ (or other background that contain $h \rightarrow \gamma\gamma$). While the rest, particularly H_T , distinguishes the different hh channels and also hh from other Higgs channels backgrounds.

9.5.2 Exploratory network analysis

The aim of this analysis is to explore how the kinematic variables constructed in the previous section are related to each other. Furthermore, we are interested in examining their variation across the channels. This can be achieved by calculating the intra-feature correlations stratified according to the signal types ($ggF, u\bar{u}A, d\bar{d}A$) or a background. Then draw them as network diagrams that can be seen in (a) of Figure 9.7. The Pearson's correlation networks show some differences amongst the different signal strata.⁵. These differences can be further investigated by a post-hoc hypothesis test, based on a linear mixed effects model for each pair of the features X_i, X_j stratified according to the processes ($ggF, u\bar{u}A, d\bar{d}A$ and background) S_k , given as follows

$$X_i = \beta_{ij} X_j + \beta_k S_k + \beta_0, \quad (9.36)$$

⁵For network plots of the backgrounds see [40].

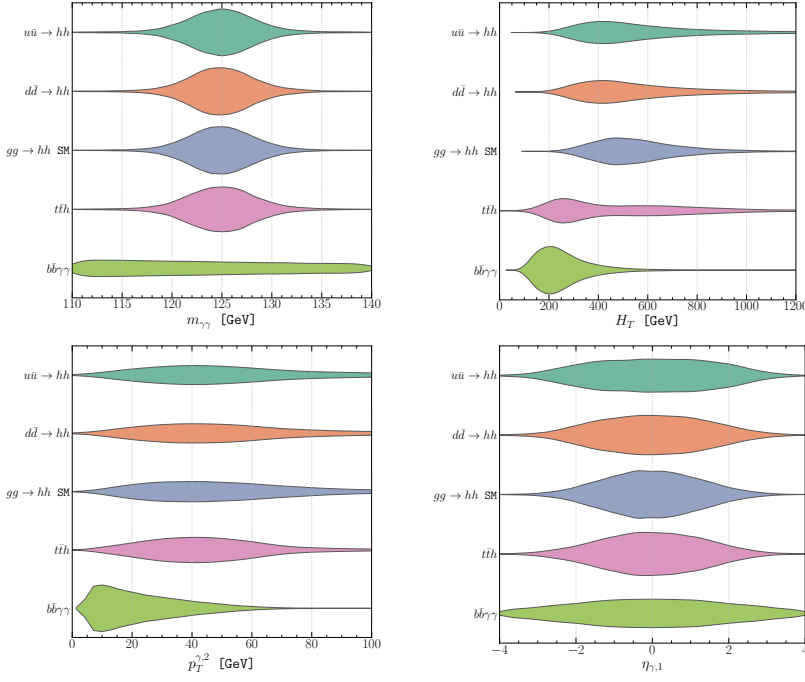


Figure 9.6. Violin plots showing the distributions of the most significant features used by the BDT classifier for the signal channels, and the two most significant backgrounds $b\bar{b}\gamma\gamma$.

where β_{ij} , β_k and β_0 are the constants for the fit. The hypothesis test is therefore preformed by taking the ratio of log likelihood for the linear model of eq. (9.36), defined as

$$t = \frac{\mathcal{L}(\beta_{ij}, \beta_k, \beta_0)}{\mathcal{L}(\beta_{ij}, \beta_k = 0, \beta_0)}. \quad (9.37)$$

This analysis of variation (ANOVA) yields a p -value for each feature pair, these p -values are false discovery rate (FDR) corrected, and the correlation difference amongst the strata is considered significant if the FDR-corrected p -values pass the threshold $p < 0.001$ or $p > 0.01$ when comparing $u\bar{u}A$ against $d\bar{d}A$.⁶ The result of these comparisons can be seen in sub-figures (b). We can see that many of the features do not have significant variation across the strata. This indicates that these features are not important in separating the signal from the background. The most significant variation is between the ggF (equivalently $q\bar{q}A$) and the background. While for the $q\bar{q}A$ channels, the correlation patterns are almost identical except for the correlation between the observables related to the PDFs, which is expected since the only kinematic difference between the up-and down-initiated $q\bar{q}A$ emerges from the PDFs of the up and down quarks.

⁶The threshold for this comparison is related due to the high degree of similarity between the two channels.

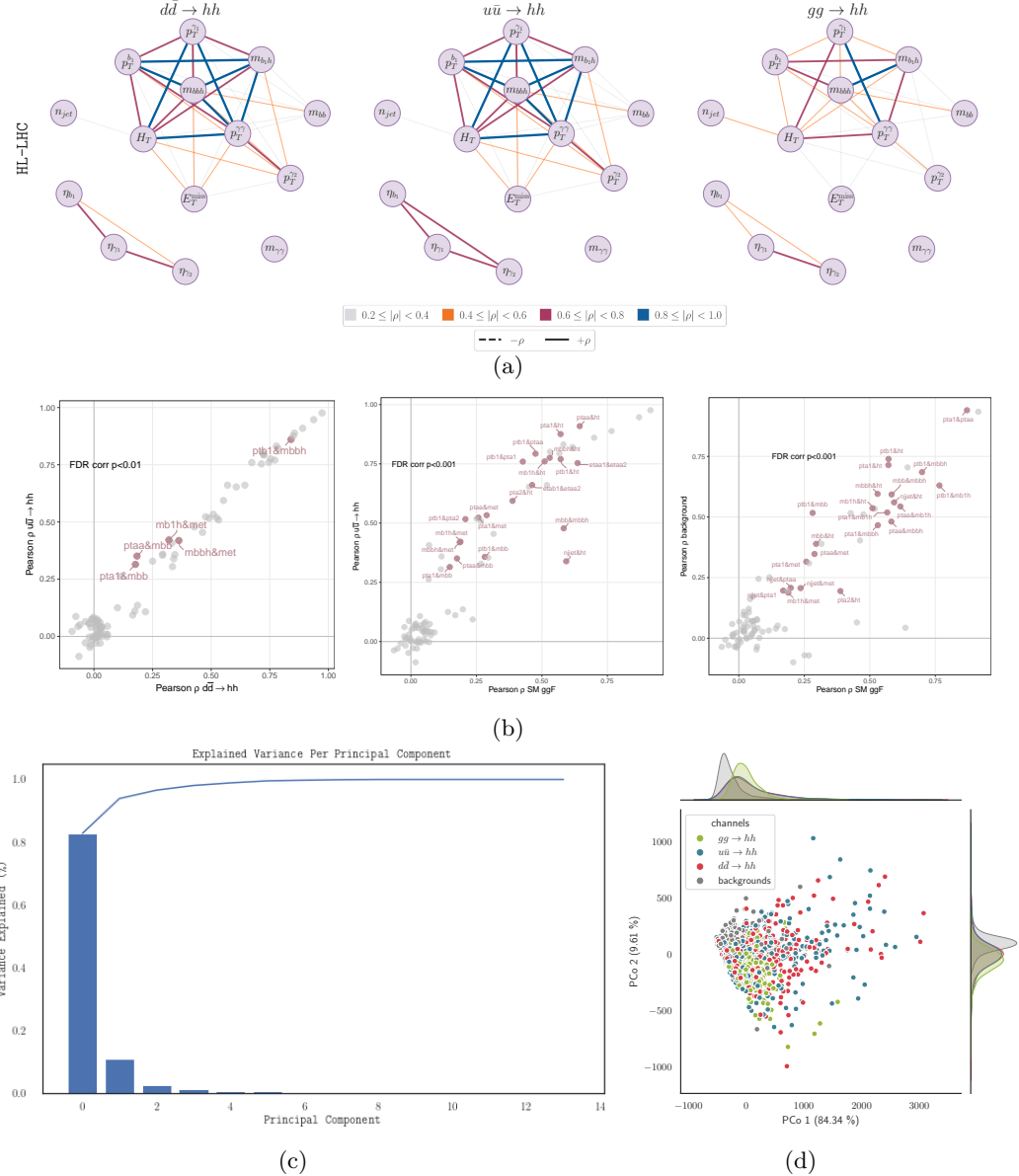


Figure 9.7. (a) Network diagrams of the signal channels of their Pearson correlation (ρ) between the features, showing slightly different patterns of correlation amongst these channels. (b) The same Pearson correlations of figure (a) plotted against each other for the different signals, with the colouring indicating whether the difference between the correlation passes the hypothesis testing (ANOVA) passes the threshold FDR-corrected p -value indicated at each figure. (c) Scree plot of the Principal-component clustering (PCo) of the the signal channels and the backgrounds, almost full variance coverage is obtained by the first four PCo's.(d) The clustering in the first two PCo's, one can see that even with unsupervised clustering the di-Higgs signals have a significantly different distribution than the background. However, it is hard to see a marked clustering for the different signal channels.

This network analysis gives some insight of the feature set at hand. When considering that many intra-feature correlations do not vary much across the channels as seen in (b) of Figure 9.7 and the features themselves cluster into four groups according to their correlations, it is tempting to further reduce the dimensionality of the feature space by performing an unsupervised clustering via Principle Component analysis (PCoA). Panel (c) in Figure 9.7 contains a scree plot showing that the variance explained by the first few PCo's is very high, thus reducing the dimensionality of our feature space significantly. When the first two PCo's are plotted in the panel (d) of Figure 9.7, the clustering of signal and the background channels can be seen. The distinction between the signals vs. backgrounds is visible, but less marked between the signal channel themselves, in particular $u\bar{u}A$ against $d\bar{d}A$. The first PCo contains, from highest weight to lowest, $m_{\gamma\gamma}$, H_T , n_{jet} , m_{bb} and $p_T^{\gamma 1}$. The rest of the features have a negligible weight. It is not surprising to see these features contribute the most in the clustering of events given how they are distributed as we have seen in Figure 9.6. In the next step of the analysis we will see them appear once more.

9.5.3 Classification analysis

The unsupervised clustering and network analysis merely offer a method to explore how the Higgs pair signal differs from the backgrounds. It is useful to reduce the dimensionality of the feature space and offer “hints” on which subset of features has the highest discriminant power. However, for analysis of the sensitivity and complete resolution of the signal against backgrounds, the gold standard is rule-based machine learning. BDTs and random forests in particle physics analysis have been explored since the early LHC era. Nowadays, it has become widespread, and its popularity becomes evident when one examines the literature review of this thesis. Many recent Higgs experimental analyses were performed using some rule-based ML algorithm.⁷

In this analysis, the EXtreme Gradient BDT (XGBoost), with its Python implementation [432], has been used as the classifier algorithm. The standard procedure for training and testing the classifier was followed, starting with the complete list of features listed in subsection 9.5.1 and then the most important features were shortlisted to improve the efficiency and performance of the classifier. This was possible due to the introduction of interpretability to the ML analysis, which provided variable importance measures by which features with a low importance index can be removed.

Interpretability is achieved by incorporating a mathematically robust measure from a game theory known as **Shapley values** [433]. This measure formulates an axiomatic prescription for fairly distributing the payoff of a game amongst the players in a n -player cooperative game. When applied to ML, Shapley values estimate the significance of the features used in the classification. The process naturally and mathematically lends itself to examining the correlations amongst the features used in the classification since all possible combinations of variables can be taken out of the game to check the

⁷Rule-based ML algorithms outperform deep neural networks (DNN) in terms of simplicity of implementation and computational requirements. In addition, rule-based algorithms, such as decision trees, are more transparent as far as the signal vs. background separation is concerned

Predicted no. of events at HL-LHC							
Actual no. of events	Channel	$hh_{\text{tri}}^{\text{ggF}}$	$hh_{\text{tri}}^{\text{ggF}}$	$hh_{\text{box}}^{\text{ggF}}$	$Q\bar{Q}h$	$b\bar{b}\gamma\gamma$	total
$hh_{\text{tri}}^{\text{ggF}}$		28	14	18	38	10	108
$hh_{\text{int}}^{\text{ggF}}$		89	80	129	178	41	517
$hh_{\text{box}}^{\text{ggF}}$		77	105	266	265	50	763
$Q\bar{Q}h$		177	98	191	5,457	1,835	7,758
$b\bar{b}\gamma\gamma$		1,743	845	1,074	30,849	287,280	321,791

Table 9.3. The confusion matrix output of the trained BDT five-channel classifier. The separation between the ggF topologies allows for setting constraints on C_ϕ . The events shown are for the HL-LHC at 14 TeV and integrated luminosity of 6ab^{-1} , assuming the SM signal.

outcome. Further information regarding the application of Shapley values in particle physics analysis can be found in refs. [40, 434, 435]. The same procedure described in [40] was followed for the Higgs pair production study. The importance of a variable in determining the outcome of classification will be quantified by the mean of the absolute Shapley value, $\overline{|S_v|}$, larger values signifying higher importance. The SHAP (Shapley Additive exPlanations) [436] package implemented in Python was used. This package computes the feature importance using Shapley values calculated exactly from tree-explainers [437, 438]. This analysis is to be published soon [324]

Classifier output

The trained BDT’s outputs are extracted in confusion matrices, with a number of events as entries. The diagonal elements of these matrices represent the true positive (TP) identification of the signal and true negative (TN) rejection of the background. In contrast, the upper triangular part represents the signal loss, or false-negative counts (FN). Finally, the lower triangular part shows the remaining background contamination of the signal, or the false-positive counts (FP). Using these counts, it is possible to estimate the accuracy score ACC of the classifiers

$$ACC = \frac{TP + TN}{TP + TN + FP + FN} \approx 0.7, \quad (9.38)$$

And the sensitivity $TP/P \approx 0.2$, which corresponds to the ϵ_{SEL} of the cut-based analysis. Here we see that the ML-based analysis yielded a four- to five-fold increase in ϵ_{SEL} compared to the cut and count method. Table 9.3 shows one of these matrices from the classification of the ggF SM signal separated into the topologies according to their dependence on C_ϕ . For up- and down-quark $q\bar{q}A$, the same matrices were constructed, and since the number of events for these processes scale with $C_{q\phi}^2$, it is only required to produce one matrix for each classification procedure, like the case of the ggF channel. For the fitting procedure, a Bayesian framework based on an MCMC method was used, analogous to the procedure described in section 7.2.

The full analysis code, including the BDT training and fits as well as the confusion ma-

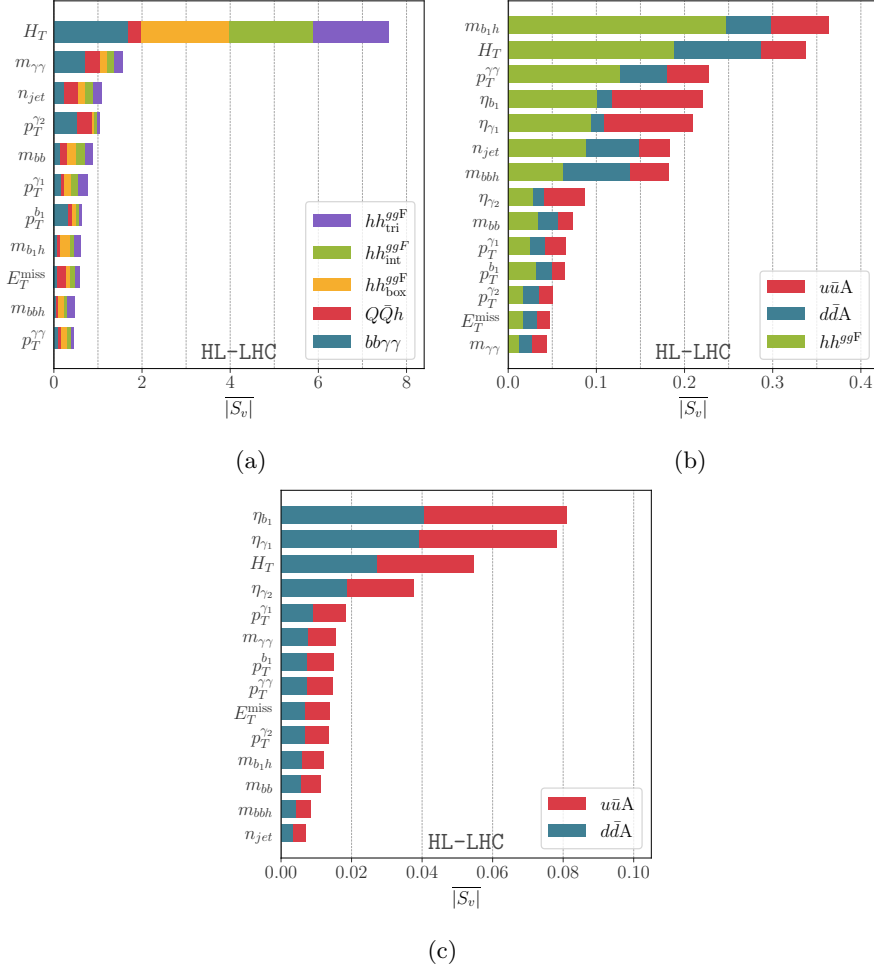


Figure 9.8. The feature importance output in terms of $|S_v|$. The higher the value of $|S_v|$, the more important the kinematic variable is in separating the different channels : (a) The hierarchy of variables important for the separation of hh_{tri}^{ggF} from hh_{int}^{ggF} events from hh_{box}^{ggF} , $Q\bar{Q}h$ and $b\bar{b}\gamma\gamma$ QCD-QED background (b) The hierarchy of variables important for the separation of hh^{ggF} , $u\bar{u}A$ and $d\bar{d}A$ events. (c) The hierarchy of variables important for the separation of $u\bar{u}A$ from $d\bar{d}A$ events.

trices for the classification procedures performed can be found in the **Github** repository: <https://github.com/talismanbrandi/IML-diHiggs.git>.

Feature importance and Shapley values

Another output of the interpretable BDT is the SHAP scores for the features used in the classification. The $|S_v|$ values are used to order the features used for the classification. The most important features in different classifiers used in this analysis is seen in Figure 9.8. Panel (a) shows the hierarchy of the features used for the separation of the SM ggF signal from the backgrounds, the same features that showed the most sig-

nificant change in the network analysis and unsupervised clustering appear in the top of the list. However, the BDT was able to distinguish between the different signals, a task the unsupervised clustering was unable to fulfil. Panel (b) shows the list of feature importance for the ggF vs $q\bar{q}A$ classification, while (c) demonstrates the full strength of the BDT in distinguishing $u\bar{u}A$ from $d\bar{d}A$ despite having very little variation of their kinematic distributions. As expected, $u\bar{u}A$ vs $d\bar{d}A$ classification, the features appeared on top of the list, are related to the different PDF's but their ranking was unintuitive because this classification is a genuine a multivariate problem, where the intra-variable correlations and differences have been fully extorted.

9.6 Fit results

The fit from the cut-bases analysis was originally made for 3 ab^{-1} and published in [392]. Still, for a better comparison with the optimised multivariate analysis, the fit for this thesis was carried out again for 6 ab^{-1} , and with SMEFT Wilson coefficient parametrisation, thus harmonising it with the results of the rest of the thesis. The fits were done in the $C_\phi - C_{q\phi}$ plane shown the top plots of Figure 9.9. As well as the $C_{u\phi} - C_{d\phi}$ one in the low panel of the same figure. We see that even with the traditional technique, two-parameter fits were possible. However, the bounds obtained on the trilinear self-coupling modifier are weaker than the projected bounds for the HL-LHC, made by ATLAS and CMS [148, 331, 439], which is expected due to the dilution of these bounds by adding Light Yukawa coupling modifiers and the loss of some signal due to the analysis technique. For the $C_{u\phi} - C_{d\phi}$ combined fit, no correlation between the two parameters is seen.

To demonstrate the power of multivariate (MV) analysis, we compare the fit results from single parameter fits of this analysis to the cut-and count technique (CC) for both up and down quark coupling modifiers at 68% CL/CI

$$\begin{aligned} C_{u\phi}^{MV}(\kappa_u^{MV}) &= [-0.09, 0.10] \quad ([-466, 454]), & C_{u\phi}^{CC}(\kappa_u^{CC}) &= [-0.18, 0.17] \quad ([-841, 820]), \\ C_{d\phi}^{MV}(\kappa_d^{MV}) &= [-0.16, 0.16] \quad ([-360, 360]), & C_{d\phi}^{CC}(\kappa_d^{CC}) &= [-0.18, 0.18] \quad ([-405, 405]). \end{aligned} \tag{9.39}$$

A significant improvement of the bounds from using MV analysis over CC one of two-fold for $C_{u\phi}$, but a mild one for $C_{d\phi}$ with $\mathcal{O}(10\%)$ improvement.

To compare the ML multivariate analysis used to other sensitivity projections, the projections on the trilinear coupling modifier C_ϕ are shown in Figure 9.10. These bounds are obtained by using a BDT classification showcased in Table 9.3, by showing the significance $\mathcal{Z} = \sqrt{q_\mu}$ functions for the linear, quadratic and combined dependence on C_ϕ . The constraints that we have obtained here are similar to or slightly better than the results quoted by the experimental sensitivity analysis quoted before. This was achieved by optimising the BDT by separating the signal and background channels, as well as

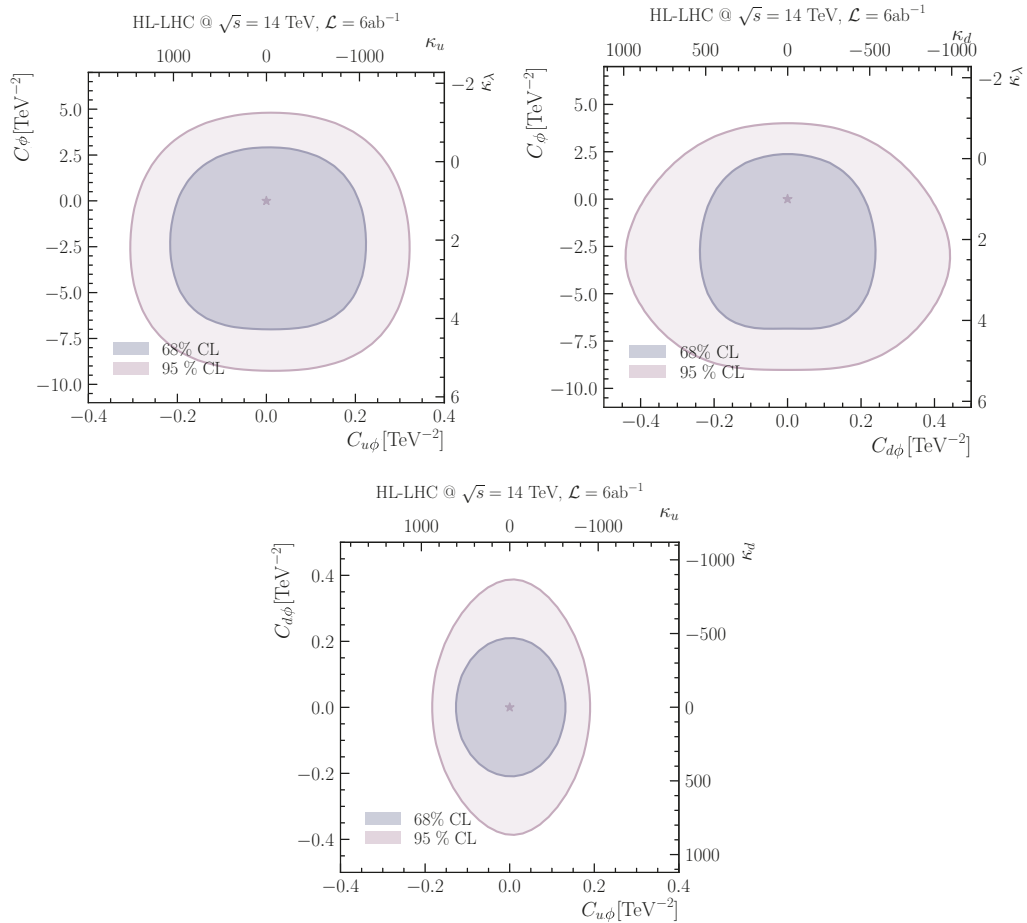


Figure 9.9. The 68% and 95% CL contours of the constraints on up and down Yukawa coupling modifiers as well as C_ϕ from two-parameter fits using the results of the cut-based analysis for the HL-LHC at 14 TeV and 6 ab^{-1} integrated luminosity.

the exclusion of less-important features. The projected 1σ bound on C_ϕ is $[-1.57, 1.00]$ at HL-LHC. Another advantage of the optimised multi-variate analysis is the ability to

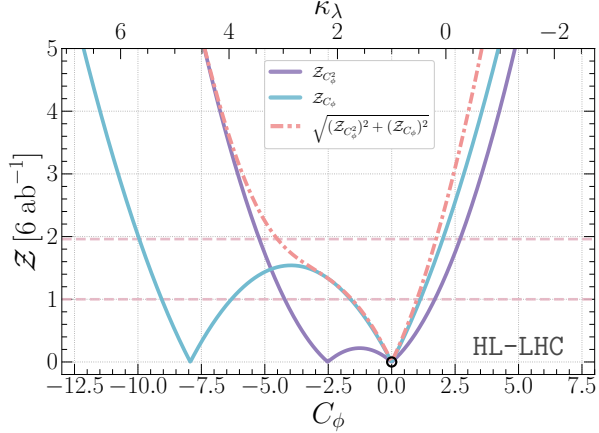


Figure 9.10. Bounds on C_ϕ (or κ_λ) at the HL-LHC from single parameter fit. The solid blue lines are the constraints from the $hh_{\text{int}}^{\text{ggF}}$ contribution, which scales linearly with the modified coupling. The solid purple line is from the $hh_{\text{tri}}^{\text{ggF}}$ contribution that scales quadratically with the modified coupling. The red dashed line is the combination of the quadratic and linear channels. The horizontal light red dashed lines mark the 68% and 95%CI's.

perform two-parameter fits in the same planes described above, shown in Figure 9.11 while maintaining the improvement over the cut-based one. Since the BDT training achieved sufficient accuracy for the seven-channel classifier, including up and down $q\bar{q}A$, the different ggF topologies and the backgrounds. It was possible to resolve all of the signal channels strata and their parametric dependence on the three Wilson coefficients $C_{u\phi}$, $C_{d\phi}$ and C_ϕ . A three-parameter fit is possible without degeneracies, as seen in Figure 9.12. However, the posterior distribution of the three-parameter fit shows no marked correlations amongst the Wilson coefficients. In both two- and three-parameter fits, a degeneracy in the $C_{d\phi}$ direction is observed at 99.7% CI. This is due to the reduction of the Higgs pair signal when the $h \rightarrow d\bar{d}$ decay channel is opened, particularly for high values of this Wilson coefficient as highlighted by Figure 9.5. When this analysis is applied for the strange quark, the overall effect of enhanced the strange quark is a reduction in the $b\bar{b}\gamma\gamma$ signal, making this Higgs pair final state insensitive to the strange Yukawa enhancements; more details on this were discussed in ref. [392]. Comparing with the constraints on C_ϕ from a single parameter fit in Figure 9.10, it can be seen from the two- and three-parameter fits in Figure 9.11 and Figure 9.12, respectively, that, the constraints on C_ϕ become diluted when the light-quark Yukawa coupling modifiers $C_{q\phi}$ are taken into an account. This effect is somewhat more prominent for $C_{d\phi}$ than for $C_{u\phi}$ and stems from the fact that away from $C_{u\phi,d\phi} = 0$ larger negative values of C_ϕ are allowed by the crescent shaped curves of the highest density posterior contours. The bounds on $C_{u\phi}$ and $C_{d\phi}$ from the fit with two-parameters including C_ϕ remain the same as the bounds on these Wilson coefficient from the single parameter $C_{u\phi,d\phi}$ fits. The fit

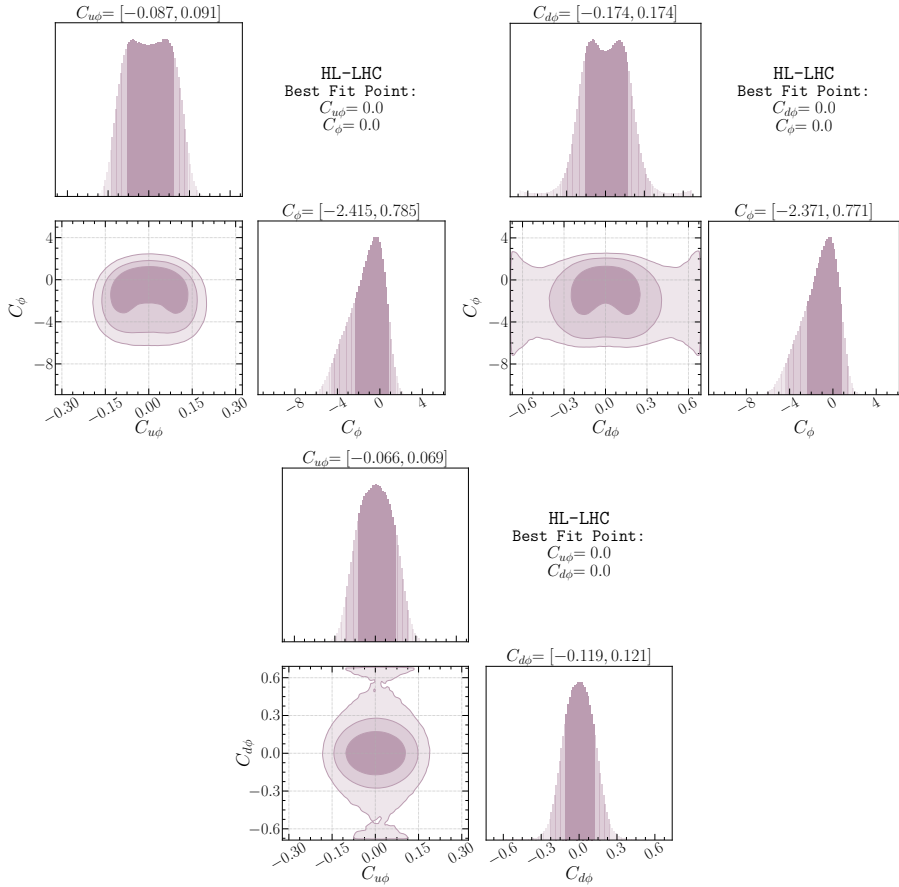


Figure 9.11. The 68%, 95% and 99.7% highest density posterior contours, for Bayesian fits preformed on pairs of Wilson coefficients for C_ϕ , $C_{u\phi}$ and $C_{d\phi}$ form the multi-variate analysis output. The quoted intervals on top of the panel correspond to the 68% CIs.

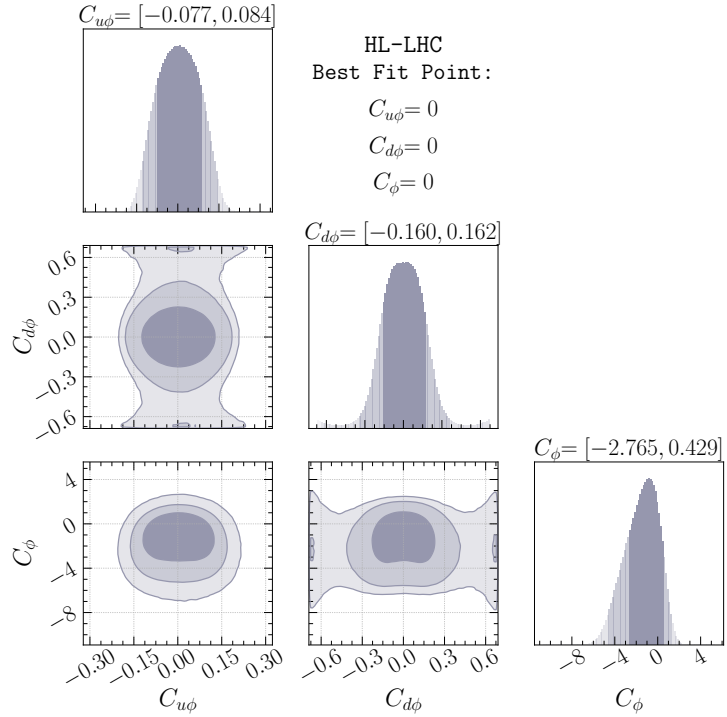


Figure 9.12. Three parameter Bayesian fits with $C_{u\phi}$, $C_{d\phi}$ and C_ϕ , the highest density posterior contours are the same as Figure 9.11.

results are summarised in Table 9.4.

9.7 Overview of Light Yukawa searches

Additional measurements of the light-quark Yukawa couplings might become relevant at HL-LHC or future hadron colliders like the FCC-hh, a careful study of which is beyond the scope of this thesis. Yet, we attempt to include a discussion here to provide a comparison with our study and to put it into proper context or to serve as a proposal for further studies. The channel $pp \rightarrow h + j$ has been suggested as a probe for charm Yukawa coupling [440] with charm-tagged jet having a potential bound of $\kappa_c \sim 1$ for the HL-LHC, depending on the charm-tagging scheme. This process could be used for the first and second generations' Yukawa couplings by looking at the shapes of kinematic distributions, the most important one being the p_T distribution [391, 441, 442]. The expected HL-LHC 95% CL bounds are $\kappa_c \in [-0.6, 3.0]$, $|\kappa_u| \lesssim 170$ and $|\kappa_d| \lesssim 990$. The use of the $h+j$ process along with other single Higgs processes have also been suggested as indirect probes for Higgs self coupling [29–33, 35], due to the contribution of the trilinear coupling to NLO electroweak corrections to these processes. In addition, experimental fits have been carried out for the trilinear coupling from single Higgs observables [189, 443].

Operators	$C_{u\phi}$	$C_{d\phi}$	C_ϕ		κ_u	κ_d	κ_λ
HL-LHC 14 TeV 6 ab^{-1} @ 68% CI							
\mathcal{O}_ϕ	—	—	[-1.57, 1.00]		—	—	[0.53, 1.73]
$\mathcal{O}_{u\phi}$	[-0.09, 0.10]	—	—		[-477, 431]	—	—
$\mathcal{O}_{d\phi}$	—	[-0.16, 0.16]	—		—	[-360, 360]	—
$\mathcal{O}_{u\phi}$ & \mathcal{O}_ϕ	[-0.087, 0.091]	—	[-2.42, 0.79]		[-434, 417]	—	[0.63, 2.13]
$\mathcal{O}_{d\phi}$ & \mathcal{O}_ϕ	—	[-0.17, 0.17]	[-2.73, 0.77]		—	[-381, 379]	[0.63, 2.27]
$\mathcal{O}_{u\phi}$ & $\mathcal{O}_{d\phi}$	[-0.065, 0.069]	[-0.12, 0.12]	—		[-331, 312]	[-268, 272]	—
All	[-0.077, 0.084]	[-0.160, 0.162]	[-2.77, 0.43]		[-400, 369]	[-362, 359]	[0.79, 2.30]

Table 9.4. Summary of the 68% projected bounds on $C_{u\phi}$, $C_{d\phi}$ and C_ϕ from single-, two- and three-parameter fits for HL-LHC with 6 ab^{-1} . The corresponding bounds on the rescaling of the effective couplings, κ_u , κ_d and κ_λ are presented on the right side of the table.

It seems that for the HL-LHC, an optimal bound for the trilinear coupling can be obtained by combining both the data from the single-Higgs process as well as Higgs pair production [188], with 68% CL bound on $\kappa_\lambda \in [0.1, 2.3]$, compared to the expected bound of $\kappa_\lambda \in [0.0, 2.5] \cup [4.9, 7.4]$ coming from using di-Higgs measurements alone. Moreover, single Higgs processes, namely Zh and $W^\pm h$ production, could also be useful in probing charm-Yukawa coupling utilising a mixture of b - and c -tagging schemes leveraging the mistagging probability of c -jets as b -jets in b -tagging working points, and vice-versa, to break the degeneracy in the signal strength [444]. This technique could probe $\kappa_c \sim 1$ in the FCC-hh. Of course, for the charm-Yukawa coupling, the constraints are set to improve significantly, as there has been a recent direct observation of $h \rightarrow c\bar{c}$ [162]. Therefore, from here on, we will mainly concentrate on the process with more potential for constraining Yukawa couplings of the first generation quarks.

Rare Higgs decays to mesons, $h \rightarrow M + V$, $M = \Upsilon, J/\Psi, \phi, \dots$, were also suggested as a probe for light-quark Yukawa couplings [445–447], and there have been experimental searches for these decays [162, 448] with bounds on the branching ratios, $\mathcal{B}(h \rightarrow X, \gamma)$, $X = \Upsilon, J/\Psi, \dots$ $\sim 10^{-4} - 10^{-6}$ at 95% CL. It was shown in Ref. [449], that the charge asymmetry of the process $pp \rightarrow hW^+$ vs $pp \rightarrow hW^-$ can be used as a probe for light-quark Yukawa couplings as well as to break the degeneracy amongst quark flavours. Moreover, the rare process $pp \rightarrow h\gamma$ is also a possible way to distinguish between enhancements of the up-and down-Yukawa couplings [450] where the authors have estimated the bounds on the up-Yukawa coupling of $\kappa_u \sim 2000$ at the HL-LHC. Despite some processes appearing more sensitive than others, one should think of these processes as complementary.

One of the main features of the effective couplings $hhq\bar{q}$ and $hhhq\bar{q}$ emerging from SMEFT operator $\mathcal{O}_{q\phi}$, or the EWChL for that matter, is that these couplings are either free from propagator suppression for $hhq\bar{q}$ or scale with energy for $hhhq\bar{q}$ while being safe from strong unitarity constraints. This feature gives processes with multiple Higgs and/or vector bosons $V = W^\pm, Z$ an advantage in constraining $\mathcal{O}_{q\phi}$. The latter constraints come from the longitudinal degrees of freedom of the gauge bosons, which can be understood from the Goldstone boson equivalence theorem. The use of the final state

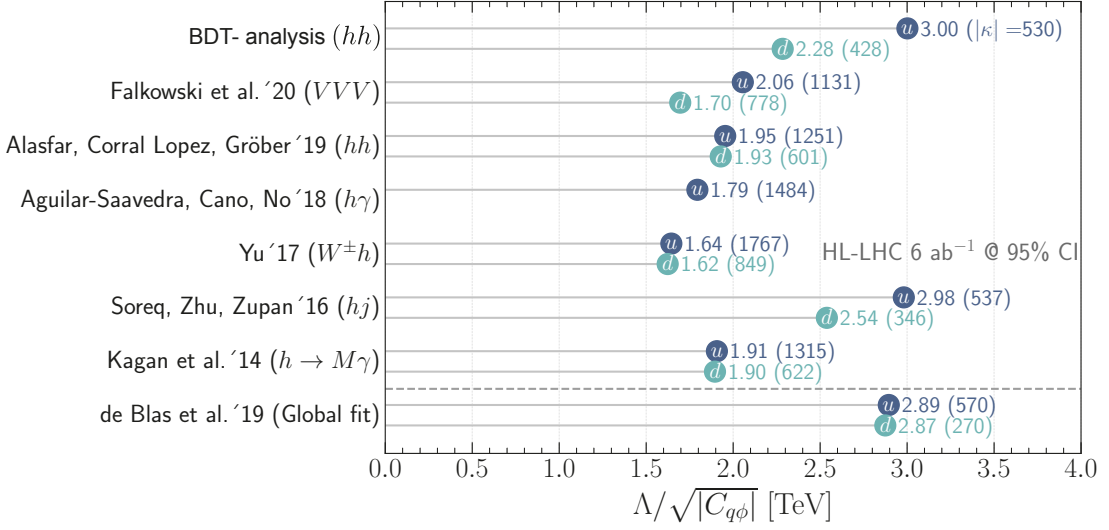


Figure 9.13. Summary of the 95% CI/CL sensitivity bounds on the SMEFT Wilson coefficients $C_{u\phi}$ (blue), and $C_{d\phi}$ (green). The bounds are interpreted in terms of the NP scale Λ that can be reached through the measurements of the Wilson coefficient at the HL-LHC at 6 ab^{-1} , the corresponding κ_q 's are shown inside the parentheses. Single parameter fit 95% CI bounds are used from this analysis for comparison with previous studies.

VV as a probe for $\mathcal{O}_{q\phi}$ is difficult due to the large SM background. However, the three-boson final state VVV gave strong projected bounds for light-quark Yukawa couplings for HL-LHC with 95% CL bounds on $\kappa_u \sim 1600$ and $\kappa_d \sim 1100$. A ten-fold improvement is expected at FCC-hh [451] with bounds of order $\kappa_d \sim 30$. Higgs pair production has a smaller SM background compared to VV production. Still, it has a significantly smaller cross-section, too, even when compared to VVV , as the latter process has already been observed at the LHC [452, 453].

On the contrary, Higgs pair production is inaccessible with the runs I-III of the LHC, but it is potentially accessible at the HL-LHC [454] having a $\sigma \cdot BR \sim 1 \text{ fb}^{-1}$. However, Higgs pair production, particularly the channel $h \rightarrow b\bar{b}\gamma\gamma$, is of significant interest as it has unique features. The first is the ability to simultaneously constrain the trilinear and light-quark Yukawa couplings, as we have already seen in the previous sections. Secondly, Higgs pair production could probe non-linear relations between Yukawa interaction and $hhq\bar{q}$ couplings [455]. Lastly, Higgs pair production is expected to be significantly enhanced in specific models involving modification of light-quark Yukawa couplings (cf. [456–458]). A numerical comparison of the strongest bounds from HL-LHC on the first-generation Yukawa couplings from the studies discussed above in Figure 9.13. In contrast to the global fit bounds that have been obtained with no invisible or untagged Higgs decays allowed [459]. For $C_{d\phi}$, the most stringent bound comes from the global fit and the $h + j$ channel as a model-independent bound, while this analysis provides the second most stringent model-independent bound. For $C_{u\phi}$, the BDT analysis presented here provided the most stringent constraint, while the bound from $h + j$

and the global analysis are comparable. The figure is interpreted in terms of the reach of NP scale Λ that can be achieved by measuring these Wilson coefficients. For future colliders, like the FCC-hh at 100 TeV, in addition to Higgs pair production, triple Higgs production might be an interesting channel for constraining the operators with Wilson coefficient $C_{u\phi}$ and $C_{d\phi}$ due to the energy increase of a Feynman diagram coupling the quarks to three Higgs bosons.

For future colliders, like the FCC-hh at 100 TeV, in addition to Higgs pair production, triple Higgs production might be an interesting channel for constraining the operators with Wilson coefficient $C_{u\phi}$ and $C_{d\phi}$ due to the energy increase of a Feynman diagram coupling the quarks to three Higgs bosons. In this case, a similar study to ours should be performed to see whether, also, in this case, it will be essential to do a combined fit on the light quark Yukawa couplings together with the trilinear and quartic Higgs self-couplings.⁸ Finally, it should be noted that there are also non-collider signatures for enhanced light-quark Yukawa couplings, manifesting in frequency shifts in atomic clocks from Higgs forces at the atomic level [461].

9.8 Discussion and conclusion

The chapter walked through the potential of Higgs pair production to glean information about the elusive Yukawa couplings of the first generation quarks from the final state $b\bar{b}\gamma\gamma$. This has been done in two different approaches: The first is the traditional cut and count method. Afterwards, significant improvement in the analysis was achieved using interpretable machine learning. To maintain harmony with other chapters of this thesis, the enhancements of light Yukawa couplings were parametrised within the SMEFT framework.

Despite the limitations of the cut-based analysis for the Higgs pair, it was still possible to estimate notable sensitivity for both up-and down-type Yukawa coupling to the Higgs boson, comparable with other channels and the model-dependent global fit. Superior estimated bounds, particularly for the up quark, emanated from fully exploiting the kinematical shapes and their correlations in a multivariate analysis. This was achieved by using a High-level kinematical distribution as a feature in a BDT classification. They were then interfacing it with an explainer based on Shapley's values.

The precedence of using an interpretable ML framework over DNNs stems from optimising the training procedure by employing physics-motivated dimensionality reduction by excluding less important features. Interpretable ML not only outperforms black-box models but also provides a physics understanding of the processes at hand, pointing to kinematic variables like H_T and $m_{\gamma\gamma}$ as being important variables that instrument this separation. Lastly, but most importantly, interpretable models provide higher confidence in the results of their classification or regression.

The use of a BDT classifier was not only beneficial for increasing the hh signal selection efficiency but also to classify the signal channels strata, such that it is possible

⁸In [460], it was shown that $\sim \mathcal{O}(1)$ bounds on the quartic Higgs self-coupling can be reached at the FCC-hh.

to parametrise it in terms of C_ϕ , $C_{u\phi}$ and $C_{d\phi}$. By decomposing the ggF channel into its sub-topologies depending on their C_ϕ parametrisation, where the box topologies do not depend on the trilinear coupling, the triangle scaling quadratically with C_ϕ and the interference between the two, which has a linear dependence on C_ϕ . The $q\bar{q}A$ is considered an NP channel exclusively. It scales quadratically with $C_{q\phi}$. The outcome of this technique is the ability to perform two and three-parameter fits, including all of the Wilson coefficients in question.

With the HL-LHC Higgs pair searches, it is expected to constrain the Higgs trilinear coupling to $\mathcal{O}(1)$ of the SM prediction. A result matched by other sensitivity analyses based on ML analysis done by experimentalists at the CMS and ATLAS [148, 331, 439]. This indicates the desideratum of Higgs pair production observation for understanding the Higgs potential. Despite light Yukawa modifiers like $C_{q\phi}$ being typically overlooked when studying Higgs pair production, this study showed that they could dilute the bounds on the trilinear Higgs coupling. Thus these coefficients need to be considered in any phenomenological studies of the Higgs pair. These Wilson coefficients are weakly bounded from other measurements, unlike other coefficients constrained from single-Higgs, EWPO or top data.

There exist a handful of potential UV-complete models in which both light Yukawa as well as the Higgs trilinear couplings are enhanced. For example, a model proposed in ref [456] based on vector-like quarks (VLQ) with AFV assumptions. The original assumption of this model is excluded, as the authors assumed an enhancement of all light quark-Higgs couplings to be equal to the beauty Yukawa. One could still get significant enhancement to light Yukawa fro VLQ masses of ~ 2 TeV, which is well above the current direct searches excluding VLQ of masses $M_{VLQ} < 1.6$ TeV [462, 463] for the hadronic final state, and $M_{VLQ} < 1.2$ TeV for the leptonic one [464]. Due to the AFV manifested in this model, the VLQ could be made not to couple to the third generation quarks and evade the tree-level EWPO bounds [38]. In addition, the trilinear Higgs coupling could be modified by the inclusion of an additional scalar singlet cf. [110, 465, 466]. Another example of models with enhanced light Yukawa is a two-Higgs-doublet model (2HDM) model proposed in refs. [458, 467]. This model has a special kind of AFV, known as spontaneous flavour violation (SFV). Enhancements to light Yukawa couplings come from the second Higgs Yukawa couplings, which are made diagonal in the flavour space K_q ($q = u, d$). SFV has the constraint that either the up-type or the down-type couplings can be enhanced, while the couplings of the other type maintain the SM hierarchy. The addition of the second doublet modifies the Higgs potential, and consequently, the Higgs self-coupling will be modified as well. Like any other 2HDM, the parameter space is rather large. The bounds on this model will depend on the region of its parameter space we are interested in. Figure 9.14 shows the bounds on this model for a point near the alignment limit. For a small mass of the “heavy” Higgs H and large Yukawa coupling K_d flavour bounds dominate, while for larger m_H , the dijet searches [468–470] would dominate due to the decay $H \rightarrow d\bar{d}$. On the contrary, the decay $H \rightarrow hh$ would become dominant from smaller values of K_d and larger H mass, but still $m_H < 2$ TeV. In this regime, resonant Higgs pair searches give string constraints for light Yukawa en-

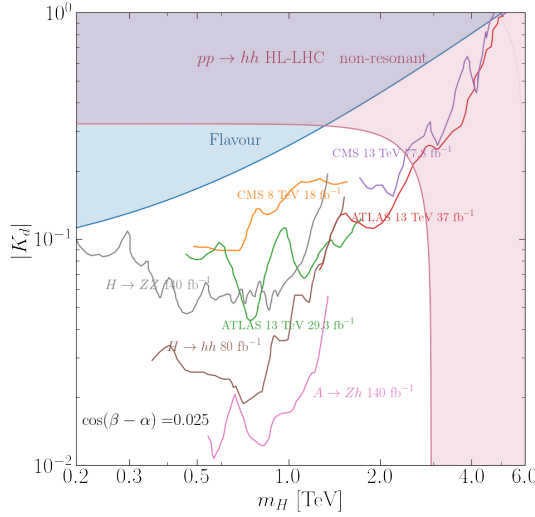


Figure 9.14. Example of constraints on the 2HDM with SFV presented in [458, 467] from flavour observables, LHC dijet, Zh, ZZ and resonant hh searches. The region shaded in Red is the bounds projected for the HL-LHC from the analysis presented in this chapter. This plot is based on the results quoted in ref. [458].

hancement [471, 472]. Similar light Yukawa bounds in this region of the parameter space could also be derived from Zh [473] and ZZ [474, 475] searches. Lastly, for $m_H > 2$ TeV, the non-resonant Higgs pair production will become the dominant bound on light Yukawa enhancement, coming from the analysis of this chapter.

Part IV

Flavour physics

10 Data-inspired models for $b \rightarrow s\ell\ell$ anomalies

Recent results from B -factories, including Belle and Babar, as well as the LHCb-experiment involving semileptonic decays of the beauty mesons B^0, B^\pm, B_s, \dots point to a marked deviation of $\sim 2.5\sigma$ from the SM prediction, particularly in the branching fractions ratios

$$R_{K^{(*)}} \equiv \frac{Br(B \rightarrow K^{(*)}\mu^+\mu^-)}{Br(B \rightarrow K^{(*)}e^+e^-)}, \quad (10.1)$$

in the high dilepton mass bins [41–45]¹. In addition to the results of angular analysis of the decay $B \rightarrow K^*\mu^+\mu^-$ [476, 477], particularly the observable P'_5 , showing similar deviation from the SM. The most recent measurement was published by LHCb [478] if the light cone sum rules for modelling the hadronic effects are considered, the deviation of the P'_5 observable would be comparable to or greater than the tension seen in $R_{K^{(*)}}$. Other observables derived from the branching fractions of semileptonic and full leptonic final states of B mesons decays, e.g. $B_s \rightarrow e^+e^-$, have shown deviations from the SM with the $2\sigma - 3\sigma$ range [46–49]. All of these observables have the FCNC transition $b \rightarrow s\ell\ell \ell = e, \mu$ in common, and are in conflict with the SM lepton universality of EW couplings. This tension could be translated into a strong case for the evidence of BSM physics with lepton flavour universality violation (LUV) [479–481].

When these aberrant results are added to the recent muon anomalous magnetic moment $g - 2$ measurement by Fermilab [482] or measurements of differential dilepton branching fractions of B -mesons, grounds for the muons being the source of LUV are established, i.e. the NP degrees of freedom contains muon-flavoured couplings. However, the hadronic contributions in the decay amplitudes and $g - 2$ corrections [483–487], that require non-perturbative QCD [488–491], make such conclusion debatable, see, e.g. [492, 493] and the most recent analysis, with the updated lepton flavour universality tests [494].

Another class of B decays involving the tree-level $b \rightarrow c\tau\nu_\tau$ transitions has shown similar tension with the SM [495–498]. Amongst other, the observable $R_{D^{(*)}} \equiv Br(B \rightarrow D^{(*)}\tau\nu)/Br(B \rightarrow D^{(*)}\ell\nu)$, originally found at Babar [499] and subsequently measured at Belle [500] and LHCb [501] has shown a $\sim 20\%$ deviation from the SM. All of the anomalous flavour observables as summarised in Figure 10.1 with their pull in σ 's shown in blue, compared the standard model predictions with their uncertainties in orange.

The simultaneous resolution for the anomalies emerging from $b \rightarrow s\ell\ell$ and the semileptonic $b \rightarrow c$ transitions, requires models with complicated flavour structure [50–59], as

¹The data from the most recent measurement of the R_{K^*} [45] has not been used in this work, as the fits shown in this chapter predates these results.

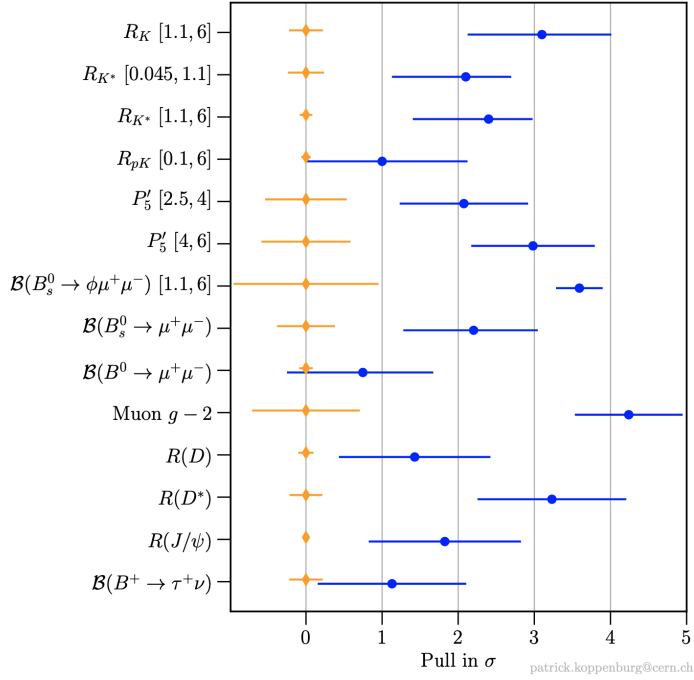


Figure 10.1. Forest plot summarising the flavour observables in tension with the SM predictions, the experimental pull in terms of standard deviations σ is shown in blue, while the SM prediction with the theoretical uncertainties is highlighted in orange. This figure is made by P. Koppenburg [502].

such models need to accommodate for similar deviations from the SM for both classes albeit these two transitions occur at different orders in the SM. Such models are often being at the edge of flavour physics constraints [327, 503] and collider bounds [504, 505]. On the other hand, most up-to-date measurements of $R_{D^{(*)}}$ from the Belle collaboration [506, 507] turns out to be in good agreement with the SM [508–511], thereby casting some doubt on the potential for NP lurking within $b \rightarrow c$ transitions. Furthermore, the ratios of branching fractions of decays involving the FCNC $b \rightarrow s\ell\ell$ transitions have a much lower dependence on the non-perturbative QCD effects, than $g - 2$, and differential distributions of semileptonic B -decays [512–515]. Therefore, the LUV information extracted from such “clean” observables have the highest potential for extracting LUV insights, see [516] for more details.

The $b \rightarrow s\ell\ell$ anomalies have been studied in a model-independent manner, in particular SMEFT framework in refs. [517–521] and more recently revisited in refs. [522–528]. Additionally, many UV-complete models were investigated, particularly leptoquarks (LQ), like in refs. [529–533]. Another class of models of special interest are Z' models, in which the B anomalies can be realised at the loop level. The simplest of these models has been proposed in ref. [534], extending the SM with a single new $U(1)$ gauge group, together with the presence of top- and muon-partners, resulting in a top-philic Z' boson capable of evading present collider constraints [535] and responsible for the required LUV sig-

natures. This model has the advantage of not introducing extra flavour spurions to the SM, i.e. similar to the MFV ansatz [394, 536, 537]. A more general set of models with the same features can be found in ref. [538] and subsequently elaborated upon in greater detail in the phenomenological study of ref. [539].

While evading flavour constraints, models with topophilic Z' are in strong tension with the Z -pole measurements [539, 540]. In fact, it has been shown in [522], that despite large hadronic uncertainties for the amplitude of the $B \rightarrow K^* \mu^+ \mu^-$ decay, a tension of at the 3σ level at least would persist between B data and EWPO for muonic LUV effects, and an even stronger tension would be found in the case of LUV scenarios involving electron couplings. This elucidates the interplay between B -physics and EWPO [522, 523, 531–533, 538, 541, 542].

This chapter aims to review a global fit, including both EWPO and flavour observables related to the B -anomalies. Then present, UV models that accommodate the resulting fit constraints are based on those present in the literature [534, 535, 538], that accommodate the resulting fit constraints investigated. This work is an extension of several studies done by some of my collaborators [489, 492, 520, 522, 543–545], and published in [546]. This chapter is organised as follows: in section 10.1, the SMEFT analysis of the flavour anomalies is presented; in ??, I discuss a viable Z' model in relation to our EFT results. After that, I present a possible alternative leptoquark scenarios in ???. Lastly, the conclusions are summarised in section 10.4.

10.1 Flavour anomalies in SMEFT

10.1.1 Theoretical preamble

Global fits from $b \rightarrow s \ell \ell$ anomalies show that if the NP degrees of freedom enter at tree-level, they would have an energy scale $\Lambda \sim 10$ TeV [517–521]. Highlighting that for LHC phenomenology, the use of SMEFT is justified. The operators of interest for the explanation of these B anomalies are [522, 523, 538]:

$$\mathcal{O}_{LQ^{(1)}}^{\ell\ell 23}, (\mathcal{O}_{LQ}^{(1,3)})^{\ell\ell 23}, \mathcal{O}_{Qe}^{23\ell\ell}, \mathcal{O}_{Ld}^{\ell\ell 23}, \mathcal{O}_{ed}^{\ell\ell 23}. \quad (10.2)$$

Following the same convention for the SM fields, in Table 2.1 and operator definitions in the Warsaw basis are presented in Table 4.1. Current data, taking non-perturbative QCD effects into account using light-cone sum rules, both left- and right-handed operators are permitted [522, 524–526]. Nevertheless, the statistical significance for the right-handed $b \rightarrow s$ interaction remains small, coming only from $R_{K^*}/R_K \neq 1$ [521, 522]. Hence, one can only consider the left-handed operators $(\mathcal{O}_{LQ}^{(1,3)})^{2223}$ and \mathcal{O}_{Qe}^{2322} for addressing the flavour anomalies. Additionally, when conservative hadronic uncertainties are considered [488–490], the preference of NP coupling to the muons exclusively becomes mitigated and the inclusion of electron interactions becomes viable as well [520]. From these considerations, we conclude that the operator $(\mathcal{O}_{LQ}^{(1,3)})^{\ell\ell 23}$ with either or both $\ell = e, \mu$ offers the minimal resolution of these anomalies within the SMEFT frame-

work [522].

Introducing these operators at tree-level will lead to flavour violation beyond the SM, as these operators are flavour spurions unrelated to the SM flavour violation. This can be avoided if they get generated at loop level from the RGE of operators involving the leptons and the Higgs [538]

$$(\mathcal{O}_{\phi L}^{(1,3)})^{\ell\ell}, \quad \mathcal{O}_{\phi e}^{\ell\ell}, \quad (10.3)$$

or alternatively, from the semileptonic four-fermion (SL-4F) operators with right-handed top-quark currents:

$$\mathcal{O}_{Lu}^{\ell\ell 33}, \quad \mathcal{O}_{eu}^{\ell\ell 33} \quad (10.4)$$

The leading log solution of the RGE for these operators [177, 178], with the matching conditions for the left-handed quark-current operators in eq. (10.2) at the EW scale $\mu_{\text{EW}} \sim v$ are:²

$$\begin{aligned} C_{LQ}^{(1)} \ell\ell 23 &= V_{ts}^* V_{tb} \left(\frac{y_t}{4\pi} \right)^2 \log \left(\frac{\Lambda}{\mu_{\text{EW}}} \right) \left(C_{Lu}^{\ell\ell 33} - C_{\phi L}^{(1)} \ell\ell \right), \\ C_{LQ}^{(3)} \ell\ell 23 &= V_{ts}^* V_{tb} \left(\frac{y_t}{4\pi} \right)^2 \log \left(\frac{\Lambda}{\mu_{\text{EW}}} \right) C_{\phi L}^{(3)} \ell\ell, \\ C_{Qe}^{23\ell\ell} &= V_{ts}^* V_{tb} \left(\frac{y_t}{4\pi} \right)^2 \log \left(\frac{\Lambda}{\mu_{\text{EW}}} \right) \left(C_{eu}^{\ell\ell 33} - C_{\phi e}^{\ell\ell} \right). \end{aligned} \quad (10.5)$$

In heavy quark physics, B decays are typically studied within the low energy weak effective theory [549–551], in which we have the vector and axial currents defined as

$$\begin{aligned} \mathcal{O}_{9V,\ell} &= \frac{\alpha_e}{8\pi} (\bar{s}\gamma_\mu(1-\gamma_5)b)(\bar{\ell}\gamma^\mu\ell), \\ \mathcal{O}_{10A,\ell} &= \frac{\alpha_e}{8\pi} (\bar{s}\gamma_\mu(1-\gamma_5)b)(\bar{\ell}\gamma^\mu\gamma_5\ell), \end{aligned} \quad (10.6)$$

and matched at the EW scale μ_{EW} with the SMEFT operators in eq. (10.3) - (10.4) follows:

$$\begin{aligned} C_{9,\ell}^{\text{NP}} &= \frac{\pi v^2}{\alpha\Lambda^2} \left(\frac{y_t}{4\pi} \right)^2 \log \left(\frac{\Lambda}{\mu_{\text{EW}}} \right) \left(C_{\phi L}^{(3)} \ell\ell - C_{\phi L}^{(1)} \ell\ell - C_{\phi e}^{\ell\ell} + C_{Lu}^{\ell\ell 33} + C_{eu}^{\ell\ell 33} \right), \\ C_{10,\ell}^{\text{NP}} &= \frac{\pi v^2}{\alpha\Lambda^2} \left(\frac{y_t}{4\pi} \right)^2 \log \left(\frac{\Lambda}{\mu_{\text{EW}}} \right) \left(C_{\phi L}^{(1)} \ell\ell - C_{\phi L}^{(1)} \ell\ell - C_{\phi e}^{\ell\ell} - sC_{Lu}^{\ell\ell 33} + C_{eu}^{\ell\ell 33} \right) \end{aligned} \quad (10.7)$$

The overall normalisation in the effective weak Hamiltonian follows the standard conventions adopted in refs. [489, 520, 522]. As anticipated, the set of operators of interest for the study of $R_{K^{(*)}}$ in eq. (10.5) is also sensitive to EWPO. The operators involving

²similar to the previous chapters, for one-loop effects, the NP scale is set to be $\Lambda = 1$ TeV. The renormalisation scale is set to $\mu_{\text{EW}} = m_t \simeq v/\sqrt{2}$ to minimise the matching-scale dependence with the inclusion of the NLO corrections [547, 548].

the Higgs field and lepton bilinears in the SMEFT induce tree-level modifications to EW-boson couplings. At the same time, modifications of the Z couplings to the leptons can also be induced via top quark loop contribution [84]. In the leading-log approximation and at the leading order in the top Yukawa coupling, LUV effects can be generated by:

$$\begin{aligned}\Delta g_{Z,L}^{\ell\ell}|_{\text{LUV}} &= -\frac{1}{2} \left(C_{\phi L}^{(1)\ell\ell} + C_{\phi L}^{(3)\ell\ell} \right) \frac{v^2}{\Lambda^2} - 3 \left(\frac{y_t v}{4\pi\Lambda} \right)^2 \log \left(\frac{\Lambda}{\mu_{\text{EW}}} \right) C_{Lu}^{\ell\ell 33}, \\ \Delta g_{Z,R}^{\ell\ell}|_{\text{LUV}} &= -\frac{1}{2} C_{\phi e}^{\ell\ell} \frac{v^2}{\Lambda^2} - 3 \left(\frac{y_t v}{4\pi\Lambda} \right)^2 \log \left(\frac{\Lambda}{\mu_{\text{EW}}} \right) C_{eu}^{\ell\ell 33},\end{aligned}\quad (10.8)$$

where $\Delta g_{Z,L(R)}^{\ell\ell} \equiv g_{Z,L(R)}^{\ell\ell} - g_{Z,L(R)}^{\ell\ell,\text{SM}}$ is the deviation with respect to the left-handed (right-handed) leptonic couplings to the Z boson in the SM theory. Since EW couplings to leptons have been precisely measured at LEP/SLC, they provide an important test threshold for lepton universality [85, 540].

These observations motivate a global SMEFT fit of the operators explaining the B -anomalies and their interplay with EWPO. Assuming that the LUV effects are generated by NP via radiative effects, matching what is seen in eq. (10.7). Consequently, the NP will contribute to EWPO at the tree level, whilst other SMEFT operators from the REG mixing are assumed to be small or constrained from other processes. For these assumptions to be fulfilled within SMEFT, the operators modifying the EW coupling of the quarks need to be included as well

$$\mathcal{O}_{\phi Q}^{(1)qq}, \mathcal{O}_{\phi Q}^{(3)qq}, \mathcal{O}_{\phi u}^{qq}, \mathcal{O}_{\phi d}^{qq}, \quad (10.9)$$

where $q = 1, 2, 3$ identifies quark generations. These operators are considered to be flavour aligned, in a similar fashion to $C_{q\phi}$ of the previous chapter; in particular, they are assumed to be aligned with the down-quark basis. This is needed to avoid pathological tree-level FCNC [327]. The same holds for the leptonic operators, aligned with the charged lepton mass bases.

The EWPO have a degeneracy between the first and second-generation quarks, particularly in the down-type quarks sector. Therefore, it is natural to impose a $U(2)^3$ symmetry between first and second generator quark operators, thus imposing $C_{\phi Q}^{(1,3)11} = C_{\phi Q}^{(1,3)22}$, $C_{\phi u}^{11} = C_{\phi u}^{22}$. This also helps to suppress large FCNC contributions from these operators. Additionally, the RGE boundary condition $C_{\phi u}^{33} = 0$ is assumed. This is motivated by the fact that this Wilson coefficient cannot be constrained by EWPO, as modifications to Z -coupling to right-handed top quarks cannot be probed by Z -pole measurements. Finally, for completeness, the four-lepton operator is also included in the fit:

$$O_{LL}^{1221} = (\bar{L}_1 \gamma^\mu L_2)(\bar{L}_2 \gamma_\mu L_1), \quad (10.10)$$

which contributes to the muon decay amplitude, and therefore alters the extraction of the value of the Fermi constant, G_F , which is one of the inputs of the SM EW sector.

The operators in eqs. (10.3), (10.9) and (10.10), with the assumptions mentioned before, saturate all the 17 degrees of freedom, i.e. combinations of operators, that can be constrained in a fit to EWPO in the dimension-six SMEFT framework while keeping flavour changing neutral currents in the light quark sector under control. Together with the 4 four-fermion operators from eq. (10.4), this completes a total of 21 operators, which is included in the fit setup described in the next section.

10.1.2 SMEFT fit

The global fit combining both flavour observables related to the $b \rightarrow s\ell\ell$ anomalies and EWPO is carried out in a Bayesian statistical framework. The experimental observables are modelled via state-of-the-art theoretical information already implemented and described in ref. [522] for flavour physics and EW and Higgs physics in ref. [82] and, more recently, in ref. [85]. EWPO are extended by flavour non-universal SMEFT contributions described in ref. [540, 552]. The statistical and physics frameworks are available within the publicly available `HEPfit` [320] package. An MCMC framework built using the Bayesian Analysis Toolkit [553]³

The experimental input used for the global is summarised in the following, which are also implemented in `HEPfitcode`:

- The set of EWPO including the Z -pole and W properties measurements from LEP and SLD, in addition to Tevatron and LHC measurements of EW bosons properties and rates [67, 69, 554–558]. The following EWPO used in the fit are

$$\begin{aligned} & M_H, m_t, \alpha_S(M_Z), \Delta\alpha_{\text{had}}^{(5)}(M_Z), \\ & M_Z, \Gamma_Z, R_{e,\mu,\tau}, \sigma_{\text{had}}, A_{FB}^{e,\mu,\tau}, A_{e,\mu,\tau}, A_{e,\tau}(P_\tau), R_{c,b}, A_{FB}^{c,b}, A_{s,c,b}, R_{u+c}, \\ & M_W, \Gamma_W, \text{BR}_{W \rightarrow e\nu, \mu\nu, \tau\nu}, \Gamma_{W \rightarrow cs}/\Gamma_{W \rightarrow ud+cs}, |V_{tb}|; \end{aligned}$$

- The angular distribution of the decay $B \rightarrow K^{(*)}\ell^+\ell^-$ including both the μ and e final states in the large $m_{\ell\ell}$ bins⁴. The data from ATLAS [559], Belle [514], CMS [560, 561] and LHCb [562, 563], in addition to the branching fractions from LHCb [564], the charged B^+ meson measured by LHCb [565], and the HFLAV average [566] for the branching fraction of the decay $B \rightarrow K^*\gamma$;
- The angular distribution of $B_s \rightarrow \phi\mu^+\mu^-$ [567] and the branching ratio of the decay $B_s \rightarrow \phi\gamma$ [568], measured by LHCb;
- The LUV ratios R_K [43] and R_{K^*} [42] from LHCb and Belle [44];
- Branching ratio of $B_{(s)} \rightarrow \mu^+\mu^-$ measured by LHCb [47], CMS [46], and ATLAS [48]; in addition to the upper bound on the decay $B_s \rightarrow e^+e^-$ reported by LHCb [49].

³`HEPfit` is developed by some of my collaborators, who have co-authored this work

⁴The measurements of $B \rightarrow K^{(*)}\ell^+\ell^-$ decays in the low di-lepton invariant mass region are plagued by large uncertainties for the J/ψ resonance, and thus not included in the fit.

Modelling the decays of hadrons involves factorisable (in terms of the decay constant) and non-factorisable non-perturbative QCD effects. The non-factorisable effects emerge from long-distance hadronic contributions to [483, 484, 488] QCD loops appearing in radiative corrections to these decays. In this analysis, the $B \rightarrow K^* \ell^+ \ell^-$ has two different scenarios to describe these hadronic effects, also discussed in other previous works of my collaborators [492, 520, 522, 543–545]. The first is a conservative approach (Phenomenological Data-Driven or PDD) as originally proposed in [489], and refined in ref. [492], whilst the second is a more optimistic one based on the results in [483] (Phenomenological Model Driven or PMD). The PDD scenario is based on a generic model of the hadronic effects, which is simultaneously fitted to $b \rightarrow s\ell\ell$ data alongside the NP effects. Contrary to the PDD approach, in the PMD scenario, the dispersion relations specified in [483] are used to constrain the hadronic contributions in the entire large-recoil region considered in the analysis. Ergo, PMD has smaller hadronic effects in the $B \rightarrow K^* \ell^+ \ell^-$ amplitudes [543]. The choice of the hadronic uncertainties model significantly affects the outcome of the fits to the B -decays observables [522].

In order to be as general as possible, the SMEFT global fit is done for four different scenarios, described as follows:

- **EW:** Using EWPO data only with the assumptions discussed in section 10.1. This fit includes the operators in eqs. (10.3), (10.9), and (10.10), giving a total of 17 Wilson coefficients.
- **EW (SL-4F Only):** This refers to a fit done with the Wilson coefficients of the SL-4F operators involving the right-handed top current, reported in eq. (10.4). This scenario assumes that BSM enters the modifications of the Z couplings to muons and electrons through top-quark loops only.
- **EW & Flavour:** Wilson coefficients of all the 21 operators given in eq. (10.3), (10.9), and eq. (10.10), together with eq. (10.4) are varied. All of the EW data and the flavour observables listed above are used. As explained above, this scenario comes in two varieties, PDD and PMD.
- **Flavour:** These fits exclusively include the Wilson coefficients of the *4 operators* (both electrons and muons) appearing in eq. (10.4), and are done including only flavour data, i.e. excluding EW measurements. Results are again distinguished for the PDD and PMD cases. This fit is typically done when flavour anomalies are discussed in the literature. Hence, it was included here to emphasise the importance of including EWPO.

10.1.3 Fit results

The fit was performed for each of the aforementioned scenarios, and the extracted average values of the Wilson coefficients and the corresponding 68% CI are summarised in Figure 10.2.

The EW only fits, involving 17 out of the total 21 Wilson coefficients are shown in orange. The EWPO fit shows good agreements with the SM within 2σ level. Additionally,

the Wilson coefficients involved in the fit seem to be highly correlated with the EWPO data as indicated by the correlation matrix in Figure 10.3.

The impact of these operators on the $b \rightarrow s\ell\ell$ observables are shown in Figure 10.4, where it collects the mean and standard deviation on the shift in the Z coupling to light leptons w.r.t the SM, it should be noted that these deviations of the Z couplings are related to the LUV ratios $R_{K^{(*)}}$ in the dilepton-mass range [1.0, 6.0] GeV² by:

$$\delta g_{Z,L(R)}^{ee(\mu\mu)} \equiv g_{Z,L(R)}^{ee(\mu\mu)} / g_{Z,L(R)}^{ee(\mu\mu),\text{SM}} - 1 , \quad \delta R_{K^{(*)}} \equiv R_{K^{(*)}} - R_{K^{(*)}}^{\text{SM}} , \quad (10.11)$$

which is tightly constraint by the EWPO data to per-mille level.

The other fit scenario only involves the **SL-4F** coefficients constraint from EWPO data, shown in yellow in Figure 10.2. Although EW data allows for more relaxed constraints on these operators, for example $\mathcal{O}_{Lu}^{\ell\ell 33}$ compared to the ones modifying Z couplings at tree-level e.g. $\mathcal{O}_{\phi L}$, the bounds remain compatible with the null (SM) Hypothesis and in about 3σ conflict with the experimental measurements on $R_{K^{(*)}}$ (indicated by the shaded red boxes in the right side of Figure 10.4).

We now move to the flavour data fits, with both ansätze for the hadronic contributions PDD highlighted in blue and PMD in pink. For this fit, deviations of the muonic C_{Lu}^{2233} show deviation from the SM hypothesis of 3σ for PDD and up to 6σ for the optimistic PMD scenario. The difference in the significance between the two cases stems from the interpretation of the angular analysis –namely the P'_5 observable– of the $B \rightarrow K^*\mu\mu$ decay. The PDD approach favours the fully left-handed NP coupling, i.e. $C_{9,\ell} = -C_{10,\ell}$, and allows for NP coupling to electrons, while the PMD exclusively predicts the muonic resolution [520, 522].

Flavour data seem to predict deviations in the Z coupling modifiers, implying a tension between the flavour fits and EWPO exacerbated by the PMD modelling of the long-distance QCD effects. This tension between B - anomalies and EW data reach $3(6)\sigma$ level for PDD(PMD). Of course, introducing a tree-level resolution of the $b \rightarrow s\ell\ell$ anomalies would decouple EW sensitive SMEFT operators from the four-fermion operators required for these anomalies. Still, it will not be compatible with the MFV ansatz. In fact, the size of flavour violation introduced by the tree-level resolution of the B anomalies brings any model with such structure to the brick of exclusion by other flavour observables [327, 503–505].

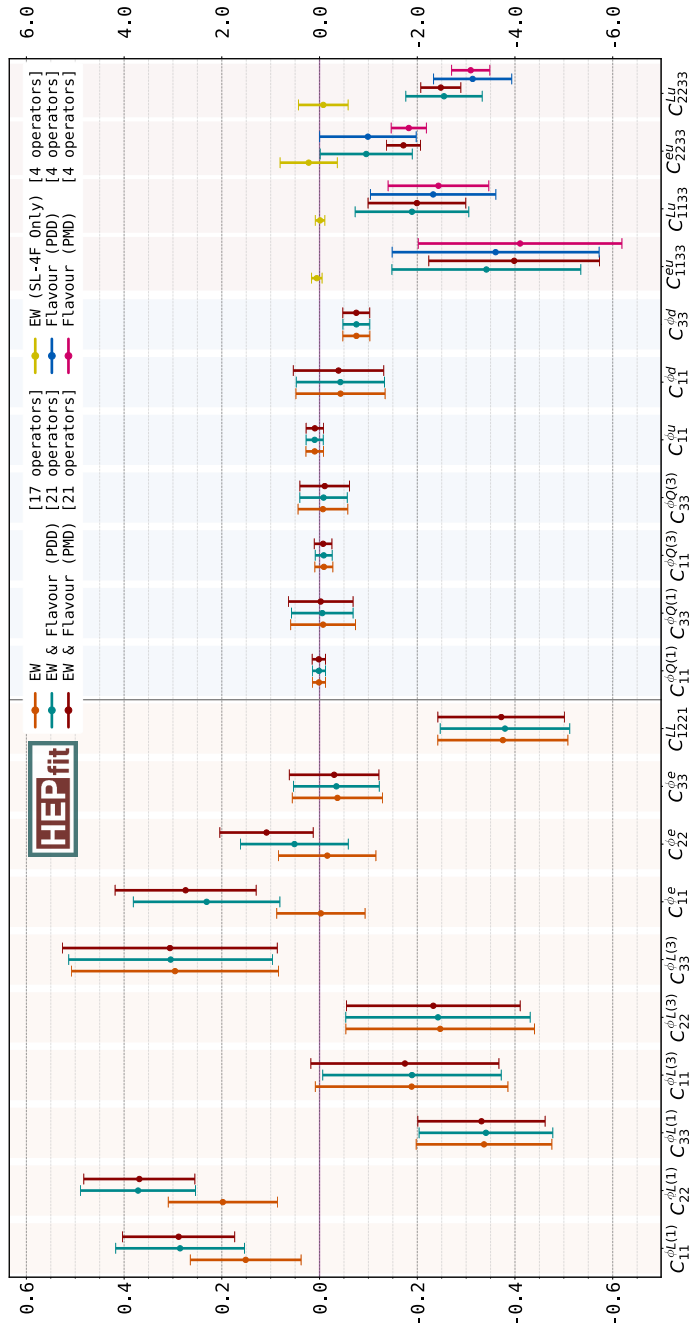


Figure 10.2. The marginalised fit results of the Wilson coefficients are considered in the scenarios detailed in subsection 10.1.2. The central points denote the mean of the marginalised posterior distribution, while the error bars are the 68% CI constraint of the Wilson coefficients. (Note the different scaling in the axes quantifying the size of the bounds presented in each half of the figure.) This figure is published in [546].

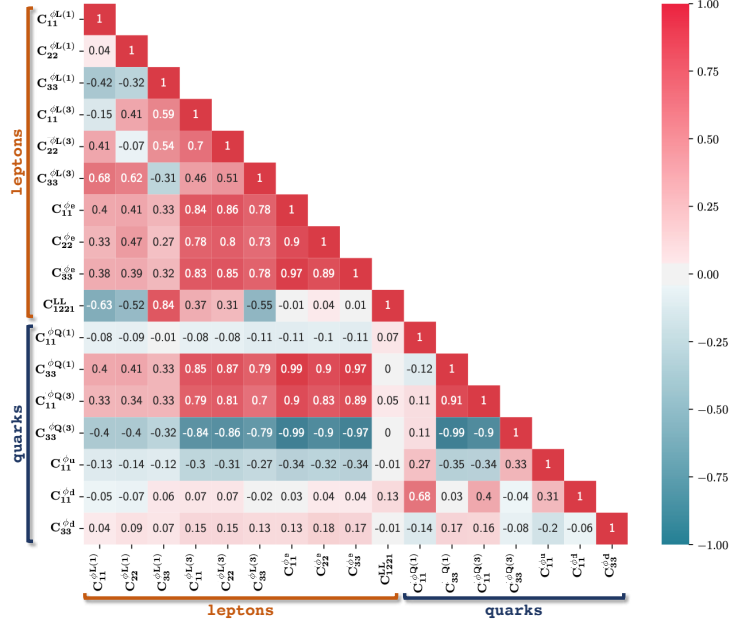


Figure 10.3. The correlation matrix resulting from the Bayesian fit of the Wilson coefficient of the operators listed in eqs. (10.3), (10.9), (10.10) in the EW scenario introduced in subsection 10.1.2. The two distinct groups of Wilson coefficients associated to leptonic and quark interactions are remarked as “leptons” and “quarks”, respectively. This figure is published in [546].

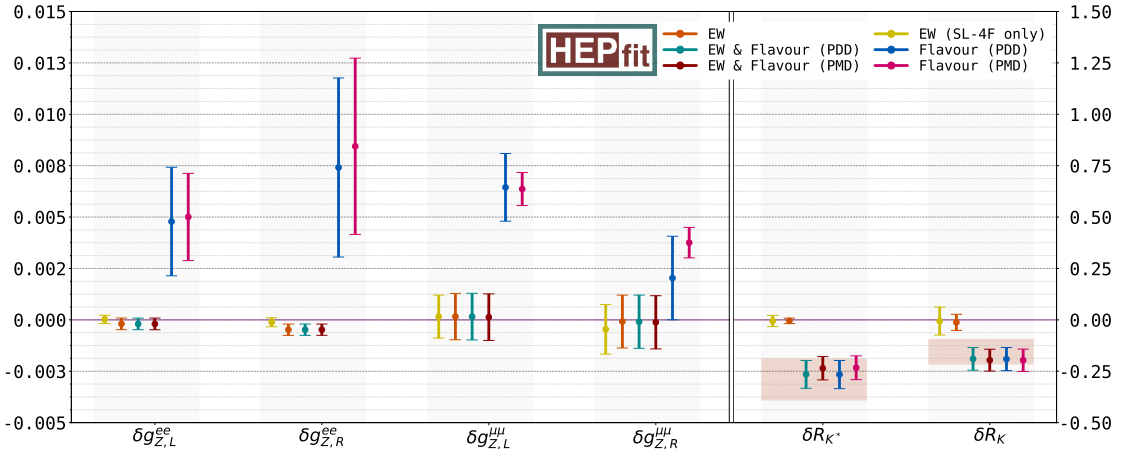


Figure 10.4. Fit results following the same convention as Figure 10.2 for the Z boson coupling modifiers for the muons and electrons, as well as the lepton universality violating ratios, see eq. (10.11), with the red boxes indicating the region selected by the experimental measurements of $R_{K,(K^*)}$. This figure is published in [546].

A global fit with the 21 coefficients, combining both flavour and EW data, is the way to reach a consensus between what is required by $b \rightarrow s\ell\ell$ observations resolution and EW precision tests. Similarly to the flavour scenario, the fits is preformed for PDD in

teal and PMD in red in Figure 10.2 and Figure 10.4. In these scenarios, the tension between EWPO and flavour data is lifted as the deviation from the SM Z -couplings remains within the EW data predictions. Also, the LUV generated by the Wilson coefficients matches the experimental observations. The resolution comes from deviation of $C_{\phi L(e)}^{\ell\ell}$ and the 4F operators $\mathcal{O}_{(L)eu}^{\ell\ell 33}$ from the SM hypothesis.

Another interesting observation from the global fit can be seen in the network graphs in [?], wherein the EW only fits the SL-4F Wilson coefficients are degenerate with the Higgs-lepton bilinear currents $C_{\phi L(e)}^{\ell\ell}$, having Pearson's correlation of $\rho \sim -1.0$. This degeneracy is broken once both EW and flavour data are taken into account, as seen in the lower panels of this figure. The breaking of the degeneracy is the reason for the observed shifts in the posterior distributions of $C_{\phi L(e)}^{\ell\ell}$ from the SM hypothesis.

It is not necessary to invoke all of the 21 SMEFT operators considered in the EW & Flavour scenario to have a resolution for the flavour anomalies and EWPO. A simpler picture using two or four operators satisfies the experimental need to explain LUV and respect EW measurements. This picture contain the fully left-handed operator, $\mathcal{O}_{LQ}^{\ell\ell 23}$ and $\mathcal{O}_{\phi L}^{(1)\ell\ell}$. The former operator would be generated at a loop-level by $\mathcal{O}_{Lu}^{\ell\ell 33}$, while the latter at the tree level. This minimalist SMEFT approach would then include only $\mathcal{O}_{\phi L}^{(1)\ell\ell}$ and $\mathcal{O}_{Lu}^{\ell\ell 33}$, and $\ell = \mu, e$. So the model could involve either muons, electrons or both of them.

In Figure 10.6, the EWPO (grey), flavour with PDD (orange) and combined (magenta) fits for this minimal SMEFT model. For the muonic (left) and electronic (right) solutions. We observe the tension between EWPO and $b \rightarrow s\ell\ell$ data if individual fits were performed, which is resolved in the combined fit. However, this induces a correlation between the four-fermion operator $\mathcal{O}_{Lu}^{\ell\ell 33}$ and the one involving the Higgs-doublet and lepton bilinears. This model also obeys MFV assumptions, protecting it from other flavour observables. However, as mentioned earlier, the B anomalies have to be explained at the one-loop level. Finally, note that the role played here by $\mathcal{O}_{Lu}^{\ell\ell 33}$ could be shared, in part, with $\mathcal{O}_{eu}^{\ell\ell 33}$, depending on how much departure is required from the fully left-handed solution to B anomalies. As already noted, this fact critically depends on the information stemming from the angular analysis of $B \rightarrow K^*\mu\mu$ [522]. On general grounds, to relieve the bounds from EWPO, the presence of $\mathcal{O}_{eu}^{\ell\ell 33}$ would also necessitate sizeable NP effects from $\mathcal{O}_{\phi e}^{\ell\ell}$, thus leaving us with a maximum of four needed operators to explain the flavour anomalies without being excluded by EWPO or including complex flavour structures.

10.2 Z' with vector-like partners

Exhilarated by the SMEFT fit and the consequent simplified model discussed in the previous section, we discuss some UV-complete models that explain the B -anomalies at the loop level; without adding extra flavour violation; and respect the EWPO bounds. The first model that satisfies these requirements is based on a Z' model published in ref. [534]. This model is a simple extension of the SM gauge group by an additional Abelian group $U(1)_X$ with a corresponding gauge boson X_μ identified as the Z' . All of

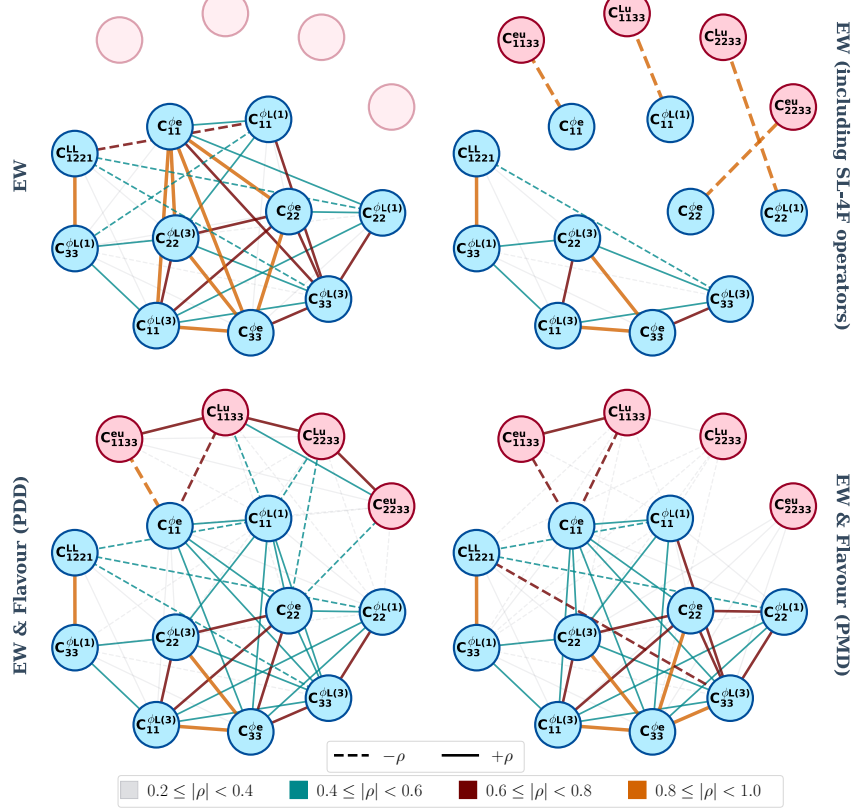


Figure 10.5. Network plot of the correlation between the Wilson coefficients considered in this study. The upper left panel shows the correlations from the **EW** fit, the upper right panel for the same fit but with the SL-4F Wilson coefficients included in the fit. The lower panel includes the flavour anomalies data in the **EW+Flavour** scenario, in which the degeneracy is broken. The lower left panel is for the PDD hadronic effects, while the lower right one is for the PMD case. This figure is published in [546].

the SM fields have no X charge. This gauge symmetry is spontaneously broken by a vev of an additional scalar singlet S , which gives a mass to the Z' boson $m_{Z'} = g_X \langle S \rangle$. A top-quark T , (VLQ) and a muonic partners M are added as well. These two fields mix with the top u_3 and muon L_2 via Yukawa interaction terms with the scalar field S . Kinematic mixing between the Z' and the SM Z boson and between the Higgs and the new scalar are assumed to be negligible. The new fields and their representation under the SM plus the new gauge group are summarised in Table 10.1.

This model is completely characterized by eight new parameters: the gauge coupling

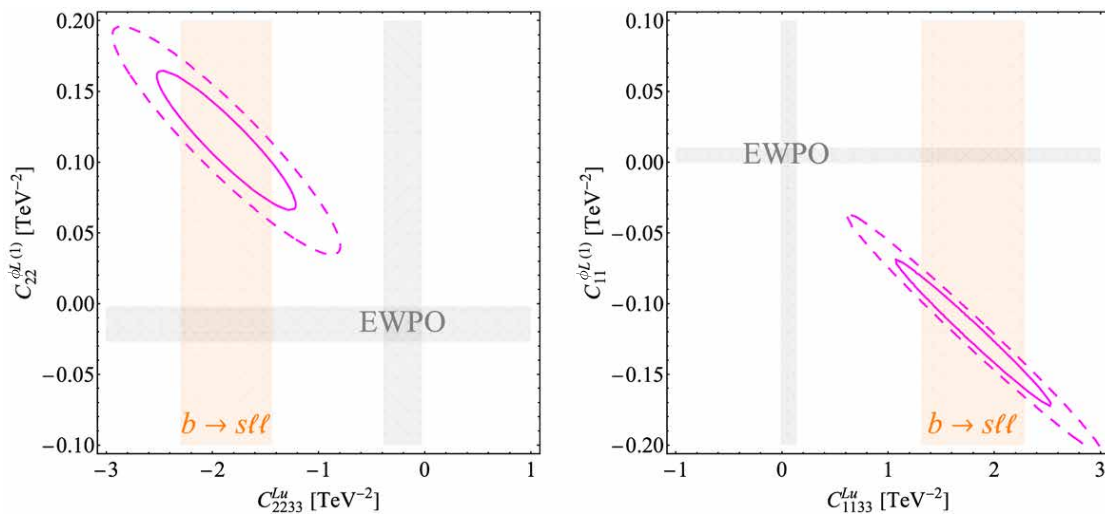


Figure 10.6. A minimal solution for the flavour anomalies within SMEFT while respecting EWPO. The left panel shows the four-fermion operators involving the muon, and on the right, the electronic solution is shown. EWPO fits are the grey regions, while the $b \rightarrow s\ell\ell$ measurements fits with PDD ansatz are highlighted by the orange bands. The combined fit's 1 and 2 σ contours are magenta coloured. This plot has been published in [546].

gx , the mass μ_S and quartic λ_S of the renormalizable potential of S , the new Yukawa couplings $Y_{T,M}$, here taken to be real, and the vector-like mass-term parameters $M_{T,M}$. In particular, the Lagrangian of the model contains the following terms:

$$\begin{aligned} \mathcal{L} = & M_T \bar{T}_R T_L + M_M \bar{M}_R M_L + Y_t \bar{u}_3 \tilde{\phi}^\dagger Q_3 \\ & + Y_T \bar{u}_3 T_L S + Y_\mu \bar{e}_2 \phi^\dagger L_2 + Y_M \bar{M}_R L_2 S + \text{h.c.} . \end{aligned} \quad (10.12)$$

From this Lagrangian, we can read off the mixing terms between the SM fields and

Particle/Field	$G_{\text{SM}} \otimes U(1)_X$	multiplicity
VL fermions		
T	$(\mathbf{3}, \mathbf{2})_{Y=\frac{1}{6}, X=-1}$	
M	$(\mathbf{1}, \mathbf{2})_{\frac{1}{2}, -1}$	
Gauge boson		
X_μ	$(\mathbf{1}, \mathbf{1})_{0,0}$	
Scalar		
S	$(\mathbf{1}, \mathbf{1})_{0,1}$	

Table 10.1. The added fields of this model and their representation under the SM gauge group and the new $U(1)_X$. Note that the new charge assignment here is not unique, and the model would produce the same phenomenology with different but consistent assignment.

vector-like (VL) partners.⁵ The spontaneous symmetry breaking of $U(1)_X$ is achieved in the way discussed at the beginning of this thesis in section 2.1 by a non-vanishing vev $\langle S \rangle^2 = -\mu_S^2/(2\lambda_S) \equiv \eta^2 \neq 0$, that implies the following fermionic mixing patterns:

$$\begin{aligned} \text{top sector: } & \left(\begin{array}{cc} \bar{u}_3 & \bar{T}_R \end{array} \right) \left(\begin{array}{cc} \frac{Y_t v}{\sqrt{2}} & \frac{Y_T \eta}{\sqrt{2}} \\ 0 & M_T \end{array} \right) \left(\begin{array}{c} U_3 \\ T_L \end{array} \right) + \text{h.c.} , \\ \text{muon sector: } & \left(\begin{array}{cc} \bar{e}_2 & \bar{M}_R \end{array} \right) \left(\begin{array}{cc} \frac{Y_\mu v}{\sqrt{2}} & 0 \\ \frac{Y_M \eta}{\sqrt{2}} & M_M \end{array} \right) \left(\begin{array}{c} E_2 \\ M_L \end{array} \right) + \text{h.c.} , \end{aligned} \quad (10.13)$$

where U_i (E_i) indicates the Q_i -component (L_i -component) with weak isospin $1/2$ ($-1/2$). Using the determinant and trace of the squared mass matrices, one can easily show that the eigenvalues $m_{t,T}$ and $m_{\mu,M}$ must satisfy [534]:

$$\begin{aligned} m_{t,\mu} m_{T,M} &= \frac{1}{\sqrt{2}} Y_{t,\mu} v M_{T,M} , \\ m_{t,\mu}^2 + m_{T,M}^2 &= M_{T,M}^2 + \frac{1}{2} (Y_{t,\mu} v)^2 + \frac{1}{2} (Y_{T,M} \eta)^2 , \end{aligned} \quad (10.14)$$

⁵Note that upon an opposite $U(1)_X$ charge assignment for the vector-like fermionic partners than the one implicitly assumed, one should replace in eq. (10.12) S with S^\dagger .

that in the decoupling limit clearly yield: $m_{t,\mu} \simeq Y_{t,\mu}v/\sqrt{2}$, $m_{\mathsf{T},\mathsf{M}} \simeq M_{\mathsf{T},\mathsf{M}}$. Defining for the top sector the rotation matrix from the interaction to the mass basis following the convention:

$$\begin{pmatrix} t_{R(L)} \\ \mathsf{T}'_{R(L)} \end{pmatrix} = \begin{pmatrix} \cos \theta_{R(L)}^t & -\sin \theta_{R(L)}^t \\ \sin \theta_{R(L)}^t & \cos \theta_{R(L)}^t \end{pmatrix} \begin{pmatrix} u_3(U_3) \\ \mathsf{T}_{R(L)} \end{pmatrix}, \quad (10.15)$$

and doing similarly for the muonic sector, the mixing angles between SM fields, t and μ , and their partner mass eigenstates, T' and M' , can be conveniently expressed in terms of the dimensionless ratios $\xi_{\mathsf{T},\mathsf{M}}$ and $\varepsilon_{t,\mu}$:

$$\begin{aligned} \tan 2\theta_R^t &= \frac{2\xi_{\mathsf{T}}}{\xi_{\mathsf{T}}^2 - \varepsilon_t^2 - 1}, \quad \tan 2\theta_L^t = \frac{2\varepsilon_t}{\xi_{\mathsf{T}}^2 - \varepsilon_t^2 + 1}, \text{ with } \varepsilon_t \equiv \frac{Y_t v}{Y_{\mathsf{T}} \eta}, \quad \xi_{\mathsf{T}} \equiv \frac{\sqrt{2} M_{\mathsf{T}}}{\eta Y_{\mathsf{T}}}; \\ \tan 2\theta_R^\mu &= \frac{2\varepsilon_\mu}{\xi_{\mathsf{M}}^2 - \varepsilon_\mu^2 + 1}, \quad \tan 2\theta_L^\mu = \frac{2\xi_{\mathsf{M}}}{\xi_{\mathsf{M}}^2 - \varepsilon_\mu^2 - 1}, \text{ with } \varepsilon_\mu \equiv \frac{Y_\mu v}{Y_{\mathsf{M}} \eta}, \quad \xi_{\mathsf{M}} \equiv \frac{\sqrt{2} M_{\mathsf{M}}}{\eta Y_{\mathsf{M}}}. \end{aligned} \quad (10.16)$$

In a perturbative expansion in $\varepsilon_{t,\mu}$, eq. (10.16) clearly shows that the mixing in the top sector proceeds mainly through $\tan \theta_R^t \simeq 1/\xi_{\mathsf{T}}$, while in the muonic sector one has $\tan \theta_L^\mu \simeq 1/\xi_{\mathsf{M}}$ and negligible $\tan \theta_R^\mu$.

Hence, for $\varepsilon_{t,\mu}/\xi_{\mathsf{T},\mathsf{M}} = Y_{t,\mu}v/\sqrt{2}M_{\mathsf{T},\mathsf{M}} < 1$, the leading couplings of the Z' boson to the SM fields correspond to right-handed top-quarks and to left-handed muons as well as neutrinos, these couplings are given by

$$g_{Z't_R} = g_X \sin^2 \theta_R^t = \frac{g_X}{1 + \xi_{\mathsf{T}}^2} + \mathcal{O}\left(\varepsilon_t^2/\xi_{\mathsf{T}}^2\right), \quad (10.17)$$

$$g_{Z'\mu_L(\nu)} = g_X \sin^2 \theta_L^\mu = \frac{g_X}{1 + \xi_{\mathsf{M}}^2} + \mathcal{O}\left(\varepsilon_\mu^2/\xi_{\mathsf{M}}^2\right), \quad (10.18)$$

with $g_{Z't_L(\mu_R)}$ contributing only at order $\varepsilon_{t(\mu)}^2/\xi_{\mathsf{T}(\mathsf{M})}^2$. The $b \rightarrow s\ell\ell$ anomalies can be

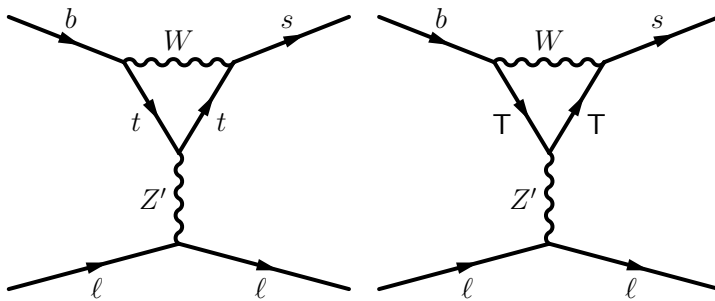


Figure 10.7. FCNC penguins with LUV emerging from the Z' model, explaining the $b \rightarrow s\ell\ell$ anomalies at loop-level. The penguin diagrams with the top-partners in the loop are the dominant ones.

explained in this model via penguin (also box) diagrams with LUV as shown in Figure 10.7. Since the Z' couples to the muons and not the electrons, LUV is generated at

loop-level.

10.2.1 SMEFT matching and constraints

Integrating out the Z' will generate the operator \mathcal{O}_{Lu}^{2233} with the matching condition:

$$C_{Lu}^{2233} = -\frac{g_{Z'} t_R g_{Z'} \mu_L}{m_{Z'}^2} \simeq -\frac{1}{(1 + \xi_T^2)(1 + \xi_M^2) \eta^2}, \quad (10.19)$$

Together with four-fermion operators built of t_R or μ_L, ν fields that can be potentially probed at collider and by experimental signatures like ν -trident production. From eq. (10.19) it is clear that in order to have $|C_{Lu}^{2233}| \sim 2 \text{ TeV}^{-2}$ as required by the fit in Figure 10.6, the SSB of the new gauge group needs to happen at a scale close to the EW, namely $\eta \lesssim \text{TeV}$;⁶ for $m_{Z'} \sim \text{TeV}$ this leads to a natural coupling $g_X \gtrsim 1$.

The main collider constraints come from the production of top pair $pp \rightarrow Z' \rightarrow t\bar{t}$, with the most stringent bounds at the time of conducting this work came from ATLAS [569]. In addition to the resonant di-muon searches [570]. In Figure 10.8 these searches are projected onto our model, with the choice of $\eta = 1 \text{ TeV}$ and other parameters chosen to be preferred by the B anomalies observables, we see that the constraints on this model are dominated by the resonant di-muon searches. The theoretical prediction of the resonant top pair and di-muon production via gluon fusion $gg \rightarrow Z' \rightarrow t\bar{t}/\mu\mu$ in this model has been calculated at NLO using the two-loop triangle calculations presented in chapter 6. Further emphasising the importance of calculating Higher-order corrections for the gluon fusion $gg \rightarrow Z^*$ for NP processes on top of Higgs measurements.

In Figure 10.9 collects the constraints on this model, starting with the 1σ region corresponding to the explanation of B anomalies via eq. (10.19) in the parameter space $\xi_{T,M}$, fixing the gauge coupling $g_X = m_{Z'}/\eta$ for a tentative Z' gauge boson at the TeV scale and the VEV of the new scalar field S set to $\eta = 250 \text{ GeV}$ and $\eta = 500 \text{ GeV}$ in the left and right panel, respectively. In the same plot, the collider searches are also presented, re-interpreted from the results presented in ref. [539]. The bounds from neutrino-trident production performed in [571] constrain small ξ_M , where the 95 %CL bounds are shown in the orange band of the plot. The top-philic Z' is predominantly produced at tree-level in association with top-pair, in the blue region we show the 95% high- p_T constraint stemming from the recasting of the $pp \rightarrow \mu^-\mu^+t\bar{t}$ search at ATLAS [570, 572]. The cyan contours are constraints coming from four-tops production analysis from CMS [573], see ref. [539] for more details. These constraints' prospects for the early runs of the HL-LHC at 300 fb^{-1} are also explored and indicated with the dashed lines. One can see that the model benchmark is shown in the right panel of Figure 10.9 old promising potential for discovery at the HL-LHC. Finally, in the same figure, fixing the partner Yukawa coupling to $\mathcal{O}(1)$ values as reported in the two panels, we mark in grey the region corresponding to the bound on the mass of the vector-like partner expected from collider, taken to be $m_T = 1.4 \text{ TeV}$ from the search at ATLAS in ref. [574], and $m_M = 0.8 \text{ TeV}$ from the CMS

⁶Note that even for masses as low as $\mu_S \sim \mathcal{O}(v)$, for $\eta \simeq v$ and $\lambda_S \sim \mathcal{O}(1)$, the interactions of S do not alter the phenomenology discussed here since the largest S -generated effects are still suppressed as $\mathcal{O}(\varepsilon_t^2/\xi_T^2)$.

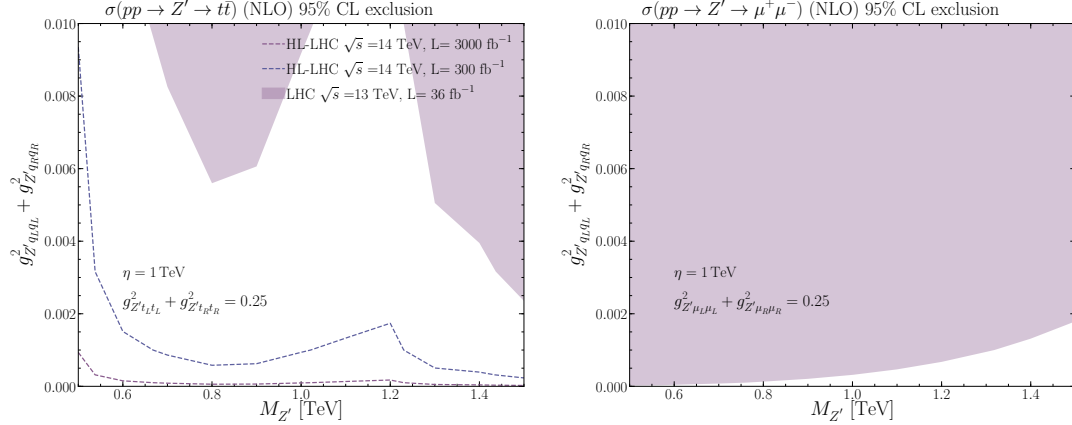


Figure 10.8. Direct searches for Z' using top pair production [569] and di-muon searches [569], the gluon fusion cross-sections for this model were calculated at NLO using the results of the two-loop triangle calculations of the process $gg \rightarrow Z^*$ preformed in chapter 6.

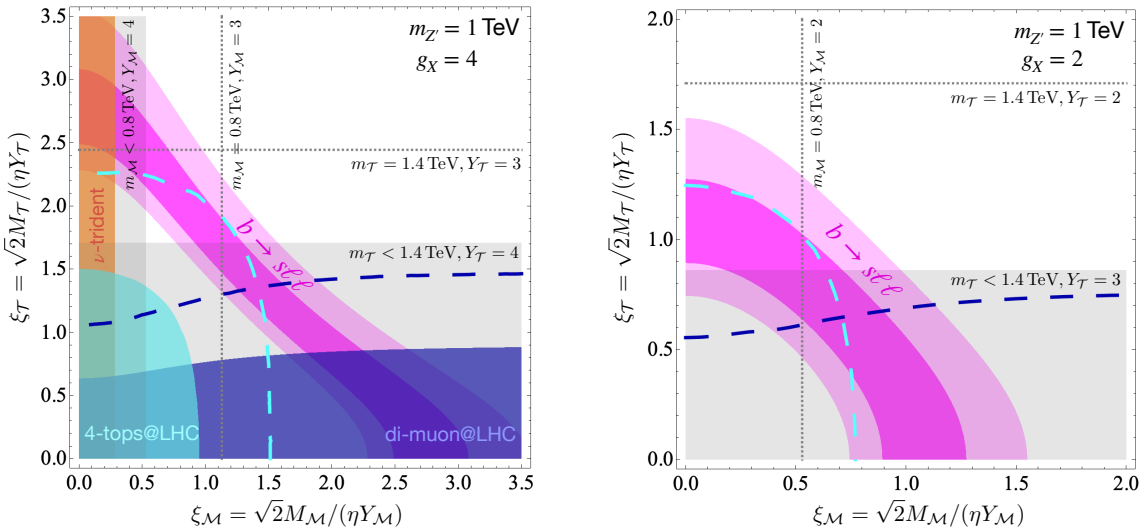


Figure 10.9. Collective of the constraints on the Z' model. the magenta regions show the 68% and 95% CL constraints from $b \rightarrow sll$ anomalies, while the rest are the collider searches re-interpreted from the ones in ref. [539]. The projections for the early HL-LHC (at 300 fb^{-1}) constraints are shown as dashed lines. Grey regions underlie the parameter space where the mass of the vector-like partner lies below current collider limits for a fixed Yukawa coupling as explicitly reported. At the same time, dashed lines show the corresponding shift of the limit due to a smaller value of the same type of Yukawa coupling. The left panel is for $\eta = m'_Z/4$ and the right panel is for $\eta = m'_Z/2$. This figure is published in [546].

analysis of ref. [575].

10.2.2 Expanding the model

For this model to survive EWPO constraints, it needs to induce $O_{\phi L}^{(1) 22}$ with the same correlation patterns observed in Figure 10.6. In principle, it is possible to achieve that by inducing tree-level $z - Z'$ mixing by charging S under $U_Y(1)$ in addition to $U_X(1)$, thereby inducing some misalignment in the weak hypercharge Y . However, this will create a tree-level (Drell Yan-like) resonant di-muon production enhancement, far beyond what is allowed by current collider searches [570]. Therefore, this mechanism is not possible. In order to accommodate for EW precision constraints, this model needs to be expanded further by including new VL leptonic states, like the ones discussed in refs. [576, 577]. These new degrees of freedom are interesting by their own merit, in particular with resolving the anomaly associated with $(g - 2)_\mu$ [482, 578], also for neutrino mass source and other interesting collider phenomenology [579, 580].

The simplest resolution can be accomplished by the inclusion of two new vector-like muonic partners: a singlet under $SU(2)_L$, S_Y , and a triplet of $SU(2)_L$, T_Y , where in both cases the subscript Y denotes the hypercharge of the fermion. Since they are VL fermions, they have a mass term, thus adding new parameters M_{S_Y, T_Y} . Their mixing with the SM leptons comes -like M- from Yukawa term, which for $Y = 0$ is given by

$$\mathcal{Y}_{S_0} \bar{S}_{0,R} \tilde{\phi}^\dagger L_2 + \mathcal{Y}_{T_0} \bar{T}_{0,R}^A \tau^A \tilde{\phi}^\dagger L_2 + \text{h.c.}, \quad (10.20)$$

Another possibility of interest may be the one of replacing in eq. (10.20) $\tilde{\phi}$ with the Higgs doublet, ϕ , and then the pair of vector-like partners with hypercharge $Y = 1$. The matching condition for these new fields produces the needed SMEFT operators, and the values and sign of the corresponding Wilson coefficients are given by the interplay between these fields [577, 578] of the form:

$$\begin{aligned} C_{\phi L}^{(1) 22} &= \frac{\mathcal{Y}_{S_0}^2}{4M_{S_0}^2} - \frac{\mathcal{Y}_{S_1}^2}{4M_{S_1}^2} + \frac{3\mathcal{Y}_{T_0}^2}{4M_{T_0}^2} - \frac{3\mathcal{Y}_{T_1}^2}{4M_{T_1}^2}, \\ C_{\phi L}^{(3) 22} &= -\frac{\mathcal{Y}_{S_0}^2}{4M_{S_0}^2} - \frac{\mathcal{Y}_{S_1}^2}{4M_{S_1}^2} + \frac{\mathcal{Y}_{T_0}^2}{4M_{T_0}^2} + \frac{\mathcal{Y}_{T_1}^2}{4M_{T_1}^2}. \end{aligned} \quad (10.21)$$

In order to obtain the needed value and sign of $C_{\phi L}^{(1) 22} \sim 0.1$ but also vanishing or negligible $C_{\phi L}^{(3) 22}$ some tuning between the singlet and the $Y = 0$ triplet is needed, although this tuning is stable under the RGE once generated at the NP scale.

Working under the PDD ansatz, it is possible to consider that the model would couple to the electron instead of the muon. Not much would change in terms of the particle content of this model, except for opposite charge assignment to get correct signs for the Wilson coefficients of O^{Lu} and $O_{\phi L}^{(1)}$ seen in the right panel off Figure 10.6, but making the electron and top partners having opposite X charges and then making the proper

adjustments to the Lagrangian. A final comment is needed for the electron scenario reported in the right panel of Figure 10.6, that involves opposite signs for the Wilson coefficients of O^{Lu} and $O_{\phi L}^{(1)}$ discussed so far. For the former, we note that the sign highlighted in the matching in eq. (10.19) follows from having assumed the same sign for the charge of the vector-like top and muon partners under $U(1)_X$. For what concerns the generation of $C_{\phi L}^{(1) \ 11} < 0$, according to eq. (10.21) one needs to correlate once again the contribution stemming from S_0 , or from S_1 , with the effect coming from a $SU(2)_L$ triplet, that now needs to be identified with T_1 , namely the triplet of hypercharge $Y = 1$.

10.3 Leptoquark scenarios

Leptoquark models are generically predicted in grand unified theories (GUTs) [581, 582]. They typically generate a baryon violating process that leads to proton decay, which is severely constrained. However, in light of the simplified SMEFT model discussed earlier Figure 10.6, it is possible to introduce leptoquarks (LQ) that couple non-universally to quark and lepton generations. These LQs are within reach of colliders and not pushed to the GUT scale like their flavour-universal counterparts. Actually, they are potential candidates for explaining the flavour anomalies [539, 583]. Such models typically involve a highly non-trivial flavour structure. For a comprehensive survey of LQ models, see for instance [329, 530, 584–586].

In this section, we limit ourselves to LQs that generate $C_{Lu}^{\ell\ell 33}$ and $C_{eu}^{\ell\ell 33}$, and introduce LUV in $b \rightarrow s\ell\ell$ transition at loop-level as shown in Figure 10.10. With that in mind, only a handful of LQs models remain; they are summarised in Table 10.2. From this

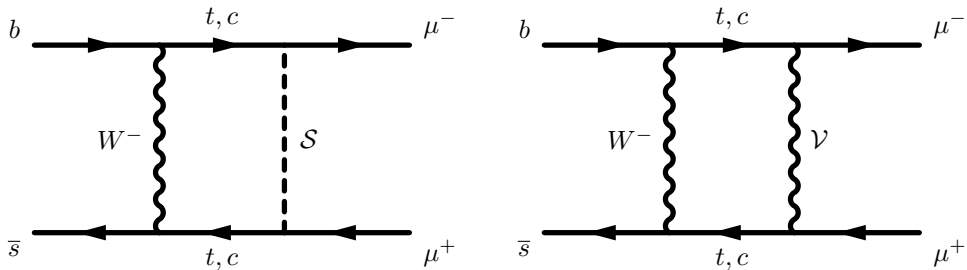


Figure 10.10. Box diagrams generated by scalar \mathcal{S} (left) and vector \mathcal{V} leptoquarks, of the $b \rightarrow s\ell\ell$ transition with LUV.

table, we can recognise the suitable models that explain the B anomalies at one loop as predicted in Figure 10.6. Unlike the Z' model, we have distinct cases for NP coupling to the electron or the muon. The case of the vector LQ $\mathcal{V}^\mu \sim (\bar{\mathbf{3}}, \mathbf{2}, -1/6)$ for LUV effects originating from electron couplings, and the scalar $\mathcal{S} \sim (\bar{\mathbf{3}}, \mathbf{2}, -7/6)$ for the ones associated to muons. The interaction terms of interest are:

$$\mathcal{L}_{\mathcal{V}\bar{f}f} = \tilde{\lambda}_{te} \bar{L}_1^c \gamma_\mu u_3 i\tau^2 \mathcal{V}^\mu + \text{h.c.} , \quad \mathcal{L}_{\mathcal{S}\bar{f}f} = \lambda_{t\mu} \bar{L}_2 u_3 \mathcal{S} + \text{h.c.}, \quad (10.22)$$

Vector LQ: \mathcal{V}^μ	$SU(3)_c \otimes SU(2)_L \otimes U(1)_Y$	Comments
$\bar{L}_\ell \gamma_\mu (\tau^A) Q_3 \mathcal{V}^{\mu(A)}$	$(\bar{\mathbf{3}}, \mathbf{1} \text{ or } \mathbf{3})_{-\frac{2}{3}}$	not of interest
$(\mathcal{V}^\mu)^\dagger \bar{e}_\ell^c \gamma_\mu Q_3$	$(\bar{\mathbf{3}}, \mathbf{2})_{\frac{5}{6}}$	not of interest
$\bar{L}_\ell^c \gamma_\mu u_3 i\tau^2 \mathcal{V}^\mu$	$(\bar{\mathbf{3}}, \mathbf{2})_{-\frac{1}{6}}$	generates $C_{\ell\ell 33}^{Lu} > 0$
$\bar{e}_\ell \gamma_\mu u_3 \mathcal{V}^\mu$	$(\bar{\mathbf{3}}, \mathbf{1})_{-\frac{5}{3}}$	generates $C_{\ell\ell 33}^{eu} < 0$
Scalar LQ: \mathcal{S}		
$\bar{L}_\ell (\tau^A) (i\tau^2) Q_3^c \mathcal{S}^{\dagger(A)}$	$(\bar{\mathbf{3}}, \mathbf{1} \text{ or } \mathbf{3}, 1/3)$	not of interest
$\bar{e}_\ell Q_3 i\tau^2 \mathcal{S}$	$(\bar{\mathbf{3}}, \mathbf{2})_{-\frac{7}{6}}$	not of interest
$\bar{L}_\ell u_3 \mathcal{S}$	$(\bar{\mathbf{3}}, \mathbf{2})_{-\frac{7}{6}}$	generates $C_{\ell\ell 33}^{Lu} < 0$
$\bar{e}_\ell^c u_3 \mathcal{S}$	$(\bar{\mathbf{3}}, \mathbf{1})_{\frac{1}{3}}$	generates $C_{\ell\ell 33}^{eu} > 0$

Table 10.2. Scalar and vector LQ interactions under scrutiny: LQs of interest for this analysis have to generate the dimension-six operators $O_{Lu,eu}^{\ell\ell 33}$. This table is published in [546].

When the LQs are integrated out, we arrive to the matching to SMEFT

$$C_{Lu}^{1133} = +\frac{|\tilde{\lambda}_{te}|^2}{M_{\mathcal{V}}^2} , \quad C_{Lu}^{2233} = -\frac{|\lambda_{t\mu}|^2}{2M_{\mathcal{S}}^2} . \quad (10.23)$$

The LQ models are simpler in terms of added fields and parameters than the Z' , this also reflects on their collider constraints. The scalar LQ with muonic coupling, has only one constraint coming from $pp \rightarrow t\bar{t}\mu\mu$, while the vector electro-phillic LQ has bounds from $t\bar{t}2\nu$ searches. These bounds are based on the dedicated collider study of ref. [587], and highlighted in orange in Figure 10.11, thy are also confronted with the $b \rightarrow s\ell\ell$ predictions shown as magenta regions. These leptoquarks can generate o $C_{\phi L}^{(1)} \ell\ell$ only at loop-level, see Figure 10.12, which is insufficient to fulfil the requirements of the flavour + EWPO fit Figure 10.6. Hence, the addition of the extra singlet and triplet leptonic partners discussed in the previous section is again needed to survive EWPO constraints.

10.4 Conclusion

This chapter addressed the $b \rightarrow s\ell\ell$ anomalies' resolution based on NP models that fall under the assumptions of MFV. Which required that LUV effects be generated at the loop level. Moreover, the interplay between EWPO and these anomalies was portrayed in Figure 10.2 and, supported with Figure 10.4.

The global SMEFT fit performed hints that a unifying solution for EWPO and LUV anomalies can be achieved by including the right operators. Furthermore, the picture can be simplified by only having a minimum of 2-4 SMEFT operators, portrayed in Fig-

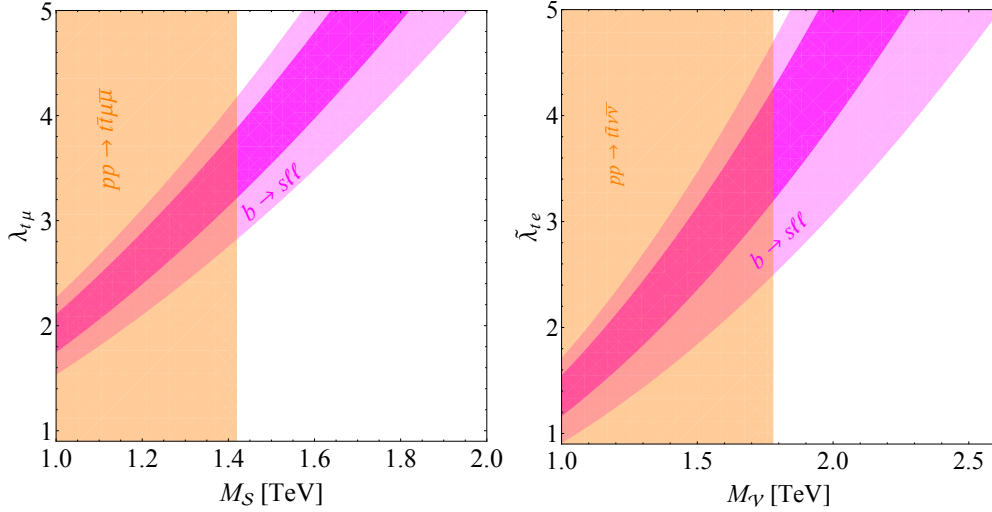


Figure 10.11. Constraints on the mass and LQ coupling with the muon for the scalar LQ model \mathcal{S} on the left panel; while on the right panel the vector electro-phillic LQ model parameters constraints are shown. The orange band shown the collider bounds based on comprehensive analysis found in ref. [587]. The magenta regions show the models phase space at 68% and 95% CL that explains the flavour anomalies at one-loop.

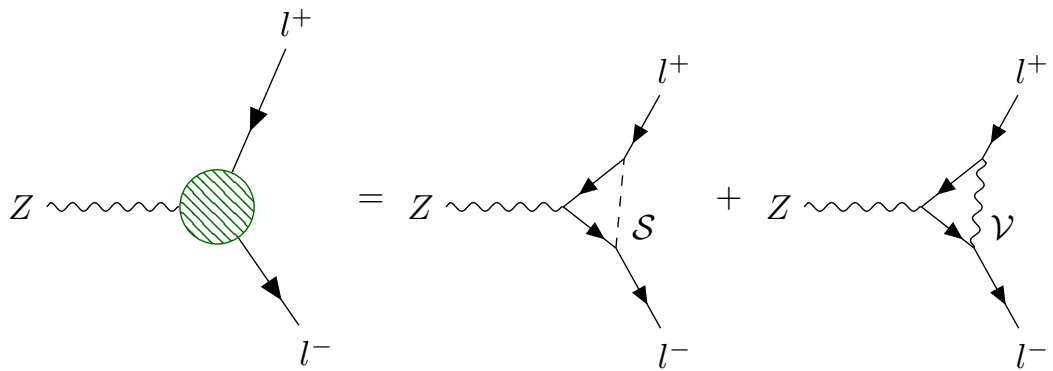


Figure 10.12. The leptoquarks considered can only generate $C_{\phi L}^{(1)} \ell\ell$ via loop matching.

ure 10.6. Like any multivariate analysis, the correlation amongst the coefficients played an essential role in finding the proper resolution of the EWPO and flavour observables conundrum.

Inspired by the simplified SMEFT model, we have discussed a top-philic Z' model with top and muon vector-like partners. Moreover, an alternative, simpler model based on leptoquarks can also produce the B anomalies at the loop level. Both models can be amended to include muonic or electronic solutions in the SMEFT simplified scenario. For the Z' model, the top and lepton partners need to have the same X charge for the muon case, while they need to carry an opposite one for the electronic NP coupling. The LQ models are different for the muonic and electronic; the former is compatible with scalar and the latter with vector LQs.

Both of these models required the inclusion of correlated pairs of vector-like leptons, a $SU(2)_L$ singlet and a triplet to realise the minimal EFT scenario depicted on Figure 10.6. We observe that the existence of these particles may be independently motivated by the heavy new dynamics underlying the origin of neutrino masses and/or by a tentative explanation of the $(g - 2)_\mu$ anomaly [482, 578].

Future measurements of B decays by the LHCb and Belle-II are expected to reach a precision regime in the upcoming years [516, 588]. These measurements, in addition to high-energy ones at linear colliders [459, 552] will reveal more about the nature of these anomalies and their connection with Higgs physics. This is already hinted at by the global fits done here with the current data predicting NP Higgs operators like $C_{\phi L/e}$. Understanding how observables from different sectors correlate is essential to understanding the nature of NP underlying these anomalies, amongst others.

11 Conclusion

Constraints on Higgs observables are deeply intertwined with top and flavour physics. This has been highlighted throughout the entirety of this thesis and the literature reviewed within.

The era of Higgs precision measurements is on the horizon, prompting the inclusion of Higher-order corrections to Higgs processes, which requires improved techniques for their calculation. An example of these techniques is the p_T expansion, first employed to obtain an analytic form for the Higgs pair virtual corrections [11]. This technique was used in chapter 6 for obtaining the QCD two-loop corrections of the gluon fusion component of Zh , which is the main source of this process’s theoretical uncertainty. The true power of this method is seen when combined with Padé approximants to bridge it with other expansions to obtain an analytic form for the virtual corrections covering the entire invariant mass spectrum [274].

The use of higher-order calculations in SMEFT opened the potential for probing the Higgs trilinear self-coupling [30–33, 35], and show connections between four-top operators and EWPO [185]. The nexus between the SMEFT four-heavy quark operators and the Higgs self-coupling is explored in chapter 7, via the inclusion of NLO SMEFT effects in single-Higgs rates.

Precision Higgs measurements will not be complete without observing Higgs pair production, the aspired jewel process of the HL-LHC, which carries the most potential for measuring the elusive Higgs self-coupling, consequently revealing the shape of the Higgs potential.

In chapter 9, we have demonstrated the potential of this process in constraining other “difficult” Higgs observable; its interaction with light quarks. Then, we treated Higgs pair production as a multivariate problem and employed aspects of Interpretable machine learning to increase the selection efficiency [40]. Using a BDT-classifier interfaced with Shapley values as an interpretability layer, we could constrain the trilinear coupling along with the up-and down-quark Yukawa coupling enhancements within SMEFT. The interpretability allowed for an optimised classifier and added physics understanding and confidence. The constraints projected for HL-LHC on up-quark Yukawa coupling enhancement obtained from this analysis are the most stringent amongst all other probes[391, 449–451], and even the global analysis [459].

The harmony amongst different observables within the SMEFT framework extends towards the newly-discovered flavour anomalies involving $b \rightarrow s\ell\ell$ transitions, which was explored in chapter 10. When these anomalies are confronted with EWPO, a marked tension of up to 6σ is observed between the data from B decays and EWPO, further highlighting the interplay between these anomalies and EWPO [522, 523, 531–533, 538, 541, 542].

This conundrum can be resolved by a global fit involving EW and flavour data. A minimalist SMEFT model, assuming no new flavour spurions are involved, would generate LUV at the loop level and involves operators from the top and Higgs sectors. We have later showcased UV-complete models ascertained from this fit to explain these flavour anomalies.

Appendices

A Details of Zh calculation

A.1 Orthogonal Projectors in $gg \rightarrow ZH$

In this appendix I present the explicit expressions of the projectors $\mathcal{P}_i^{\mu\nu\rho}$ appearing in eq.(6.2). The projectors are all normalized to 1. They are:

$$\mathcal{P}_1^{\mu\nu\rho} = \frac{m_Z}{\sqrt{2}s'p_T^2} \left[p_1^\nu \epsilon^{\mu\rho p_1 p_2} - p_2^\mu \epsilon^{\nu\rho p_1 p_2} + q_t^\mu \epsilon^{\nu\rho p_2 p_3} \right] \quad (\text{A.1})$$

$$+ q_u^\nu \epsilon^{\mu\rho p_1 p_3} + s' \epsilon^{\mu\nu\rho p_2} - s' \epsilon^{\mu\nu\rho p_1} \right], \quad (\text{A.2})$$

$$\mathcal{P}_2^{\mu\nu\rho} = \frac{1}{\sqrt{2}s'p_T} \left[q_u^\nu \epsilon^{\mu\rho p_1 p_3} + q_t^\mu \epsilon^{\nu\rho p_2 p_3} \right], \quad (\text{A.3})$$

$$\begin{aligned} \mathcal{P}_3^{\mu\nu\rho} = & \frac{\sqrt{3}}{2s'p_T} \left[s' \epsilon^{\mu\nu\rho p_1} + s' \epsilon^{\mu\nu\rho p_2} - p_1^\nu \epsilon^{\mu\rho p_1 p_2} - p_2^\mu \epsilon^{\nu\rho p_1 p_2} \right. \\ & + (q_u^\nu \epsilon^{\mu\rho p_1 p_3} - q_t^\mu \epsilon^{\nu\rho p_2 p_3}) \left(\frac{1}{3} + \frac{m_Z^2}{p_T^2} \right) \\ & \left. + \frac{m_Z^2}{p_T^2} (q_t^\mu \epsilon^{\nu\rho p_2 p_1} - q_u^\nu \epsilon^{\mu\rho p_1 p_2}) \right], \end{aligned} \quad (\text{A.4})$$

$$\mathcal{P}_4^{\mu\nu\rho} = \frac{m_Z}{\sqrt{2}s'p_T^2} \left[q_t^\mu (\epsilon^{\nu\rho p_2 p_1} - \epsilon^{\nu\rho p_2 p_3}) - q_u^\nu (\epsilon^{\mu\rho p_1 p_2} - \epsilon^{\mu\rho p_1 p_3}) \right], \quad (\text{A.5})$$

$$\mathcal{P}_5^{\mu\nu\rho} = \frac{1}{\sqrt{6}s'p_T} \left[q_t^\mu \epsilon^{\nu\rho p_2 p_3} - q_u^\nu \epsilon^{\mu\rho p_1 p_3} \right], \quad (\text{A.6})$$

$$\begin{aligned} \mathcal{P}_6^{\mu\nu\rho} = & \frac{1}{s'p_T} \left[g^{\mu\nu} \epsilon^{\rho p_1 p_2 p_3} + s' \epsilon^{\mu\nu\rho p_3} + p_1^\nu \epsilon^{\mu\rho p_2 p_3} - p_2^\mu \epsilon^{\nu\rho p_1 p_3} - \frac{s'}{2} \epsilon^{\mu\nu\rho p_2} \right. \\ & + \frac{1}{2} (p_1^\nu \epsilon^{\mu\rho p_1 p_2} + p_2^\mu \epsilon^{\nu\rho p_1 p_2} + q_u^\nu \epsilon^{\mu\rho p_1 p_3} - q_t^\mu \epsilon^{\nu\rho p_2 p_3} - s' \epsilon^{\mu\nu\rho p_1}) \\ & \left. + \frac{m_Z^2}{2p_T^2} (q_t^\mu \epsilon^{\nu\rho p_2 p_1} - q_u^\nu \epsilon^{\mu\rho p_1 p_2} + q_u^\nu \epsilon^{\mu\rho p_1 p_3} - q_t^\mu \epsilon^{\nu\rho p_2 p_3}) \right], \end{aligned} \quad (\text{A.7})$$

where we defined $q_t^\mu = (p_3^\mu - \frac{t'}{s'}p_2^\mu)$ and $q_u^\nu = (p_3^\nu - \frac{u'}{s'}p_1^\nu)$ and we used the shorthand notation $\epsilon^{\mu\nu\rho p_2} \equiv \epsilon^{\mu\nu\rho\sigma} p_2^\sigma$.

Using these projectors we obtained the relations between the form factors \mathcal{A}_i defined

in eq.(6.2) and those defined in section 2 of ref.[245]:

$$\mathcal{A}_1 = \frac{p_T^2}{2\sqrt{2}m_Z(p_T^2 + m_Z^2)} \left[(t' + u')F_{12}^+ - (t' - u')F_{12}^- \right], \quad (\text{A.8})$$

$$\begin{aligned} \mathcal{A}_2 &= -\frac{p_T}{2\sqrt{2}(p_T^2 + m_Z^2)} \left[(t' + u')F_{12}^+ - (t' - u')F_{12}^- \right. \\ &\quad \left. - \frac{p_T^2 + m_Z^2}{2s'} ((t' + u')F_3^+ - (t' - u')F_3^-) \right], \end{aligned} \quad (\text{A.9})$$

$$\begin{aligned} \mathcal{A}_3 &= \frac{p_T}{2\sqrt{3}(p_T^2 + m_Z^2)} \left[(t' + u')F_{12}^- - (t' - u')F_{12}^+ \right. \\ &\quad \left. + (p_T^2 + m_Z^2)(F_2^- + F_4) \right], \end{aligned} \quad (\text{A.10})$$

$$\begin{aligned} \mathcal{A}_4 &= -\frac{m_Z}{2\sqrt{2}(p_T^2 + m_Z^2)} \left[(t' + u')F_{12}^- - (t' - u')F_{12}^+ \right. \\ &\quad \left. + (p_T^2 + m_Z^2) \left((1 - \frac{p_T^2}{m_Z^2})F_2^- + 2F_4 \right) \right], \end{aligned} \quad (\text{A.11})$$

$$\begin{aligned} \mathcal{A}_5 &= \frac{p_T}{2\sqrt{6}(p_T^2 + m_Z^2)} \left[(t' + u')F_{12}^- - (t' - u')F_{12}^+ \right. \\ &\quad \left. + (p_T^2 + m_Z^2) \left(4(F_2^- + F_4) + \frac{3}{2s'} \left((t' + u')F_3^- - (t' - u')F_3^+ \right) \right) \right], \end{aligned} \quad (\text{A.12})$$

$$\mathcal{A}_6 = \frac{p_T}{2} F_4. \quad (\text{A.13})$$

A.2 Two-loop Results

The NLO amplitude can be written in terms of three contributions, namely the two-loop 1PI triangle, the two-loop 1PI box and the reducible double-triangle diagrams,

$$\mathcal{A}_i^{(1)} = \mathcal{A}_i^{(1,\Delta)} + \mathcal{A}_i^{(1,\square)} + \mathcal{A}_i^{(1,\bowtie)}. \quad (\text{A.14})$$

In this section, the exact analytic results for the triangle and double triangle topologies are presented.

The two-loop triangle results are

$$\mathcal{A}_1^{(1,\Delta)} = \frac{p_T^2 (\hat{s} - \Delta_m)}{4\sqrt{2}m_Z} \frac{\mathcal{K}_t^{(2l)}}{(p_T^2 + m_Z^2)}, \quad (\text{A.15})$$

$$\mathcal{A}_2^{(1,\Delta)} = -\frac{p_T (\hat{s} - \Delta_m)}{4\sqrt{2}} \frac{\mathcal{K}_t^{(2l)}}{(p_T^2 + m_Z^2)}, \quad (\text{A.16})$$

$$\mathcal{A}_3^{(1,\Delta)} = \frac{p_T (\hat{t} - \hat{u})}{4\sqrt{3}} \frac{\mathcal{K}_t^{(2l)}}{(p_T^2 + m_Z^2)}, \quad (\text{A.17})$$

$$\mathcal{A}_4^{(1,\Delta)} = -\frac{m_Z (\hat{t} - \hat{u})}{4\sqrt{2}} \frac{\mathcal{K}_t^{(2l)}}{(p_T^2 + m_Z^2)}, \quad (\text{A.18})$$

$$\mathcal{A}_5^{(1,\Delta)} = -\frac{p_T (\hat{t} - \hat{u})}{4\sqrt{6}} \frac{\mathcal{K}_t^{(2l)}}{(p_T^2 + m_Z^2)}, \quad (\text{A.19})$$

$$\mathcal{A}_6^{(1,\Delta)} = 0, \quad (\text{A.20})$$

where the $\mathcal{K}_t^{(2l)}$ function is defined in eq.(4.11) of ref.[281]. While the double-triangle for-factors are found to be.

$$\mathcal{A}_1^{(1,\bowtie)} = -\frac{m_t^2 p_T^2}{4\sqrt{2} m_Z (m_Z^2 + p_T^2)^2} \left[F_t(\hat{t}) (G_t(\hat{t}, \hat{u}) - G_b(\hat{t}, \hat{u})) + (\hat{t} \leftrightarrow \hat{u}) \right], \quad (\text{A.21})$$

$$\mathcal{A}_2^{(1,\bowtie)} = \frac{m_t^2 p_T}{4\sqrt{2} (m_Z^2 + p_T^2)^2} \left[F_t(\hat{t}) (G_t(\hat{t}, \hat{u}) - G_b(\hat{t}, \hat{u})) + (\hat{t} \leftrightarrow \hat{u}) \right], \quad (\text{A.22})$$

$$\mathcal{A}_3^{(1,\bowtie)} = \frac{m_t^2 p_T}{4\sqrt{3} \hat{s} (m_Z^2 + p_T^2)^2} \left[(m_h^2 - \hat{t}) F_t(\hat{t}) (G_t(\hat{t}, \hat{u}) - G_b(\hat{t}, \hat{u})) - (\hat{t} \leftrightarrow \hat{u}) \right], \quad (\text{A.23})$$

$$\begin{aligned} \mathcal{A}_4^{(1,\bowtie)} = & -\frac{m_t^2}{4\sqrt{2} m_Z \hat{s}^2 (m_Z^2 + p_T^2)^2} \left[(m_Z^2 (m_h^2 - \hat{t})^2 \right. \\ & \left. - \hat{t} (m_Z^2 - \hat{u})^2) F_t(\hat{t}) (G_t(\hat{t}, \hat{u}) - G_b(\hat{t}, \hat{u})) - (\hat{t} \leftrightarrow \hat{u}) \right], \end{aligned} \quad (\text{A.24})$$

$$\begin{aligned} \mathcal{A}_5^{(1,\bowtie)} = & -\frac{m_t^2 p_T}{4\sqrt{6} \hat{s} (m_Z^2 + p_T^2)^2} \left[(4m_Z^2 - \hat{s} - 4\hat{u}) F_t(\hat{t}) (G_t(\hat{t}, \hat{u}) - G_b(\hat{t}, \hat{u})) \right. \\ & \left. - (\hat{t} \leftrightarrow \hat{u}) \right], \end{aligned} \quad (\text{A.25})$$

$$\mathcal{A}_6^{(1,\bowtie)} = 0, \quad (\text{A.26})$$

where

$$\begin{aligned} F_t(\hat{t}) &= \frac{1}{(m_h^2 - \hat{t})^2} \left[2\hat{t} \left(B_0(\hat{t}, m_t^2, m_t^2) - B_0(m_h^2, m_t^2, m_t^2) \right) \right. \\ &\quad \left. + (m_h^2 - \hat{t}) \left((m_h^2 - 4m_t^2 - \hat{t}) C_0(0, m_h^2, \hat{t}, m_t^2, m_t^2, m_t^2) - 2 \right) \right], \end{aligned} \quad (\text{A.27})$$

$$\begin{aligned} G_x(\hat{t}, \hat{u}) &= (m_z^2 - \hat{u}) \left[m_z^2 \left(B_0(\hat{t}, m_x^2, m_x^2) - B_0(m_z^2, m_x^2, m_x^2) \right) \right. \\ &\quad \left. + (\hat{t} - m_z^2) \left(2m_x^2 C_0(0, \hat{t}, m_z^2, m_x^2, m_x^2, m_x^2) + 1 \right) \right]. \end{aligned} \quad (\text{A.28})$$

B Two-parameter fits of four-fermion operators and C_ϕ for HL-LHC

I present here in [Figure B.1](#) and [Figure B.2](#) the fit results for the SMEFT four heavy quark operators with the Higgs trilinear self-coupling modifier C_ϕ for the HL-LHC projections by CMS [148, 317] as an extension of the results presented in [chapter 7](#).

The expected constraints improve from the Run-II ones by a factor of

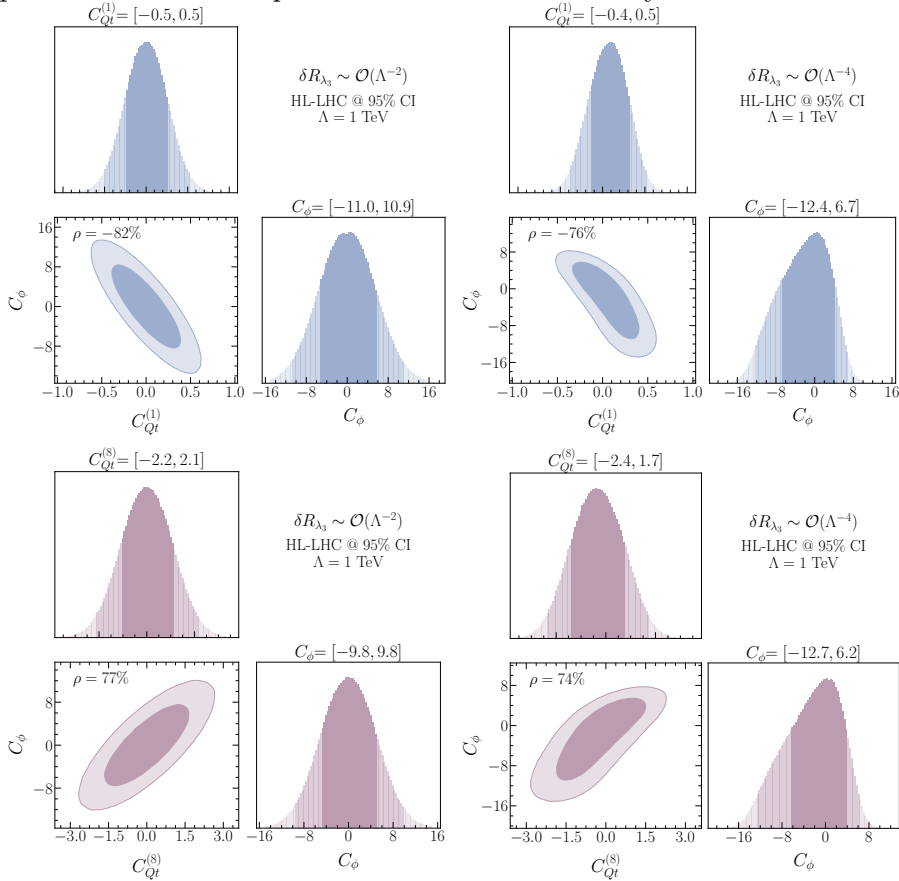


Figure B.1. The posterior distributions of the HL-LHC projections fits for C_ϕ with $C_{Qt}^{(1)}$ (up) and C_ϕ with $C_{Qt}^{(8)}$ (down). With 68% and 95% highest density posterior contours indicated. The limits shown on top of the plots indicate the 95% CI's. Plots on the left are made for the fully linearised δR_{λ_3} , while the ones on the right include the quadratic effects.

$$\sim \sqrt{\frac{\mathcal{L}_{\text{HL-LHC}}}{\mathcal{L}_{\text{Run-II}}}}, \quad (\text{B.1})$$

as expected, from statistical analysis. This comes from the adaptation of the S_2 uncertainties scheme.

The linear fits show similar correlation patterns to the ones from the Run-II in [Figure 7.5](#) and [Figure 7.6](#). However, the quadratic R_{λ_3} scheme shows strong correlation between C_ϕ and the four-heavy quark Wilson coefficients, while this is not seen in the Run-II fits. The implication of these correlations is worsened projected constraints on negative C_ϕ values in the two-parameter fits.

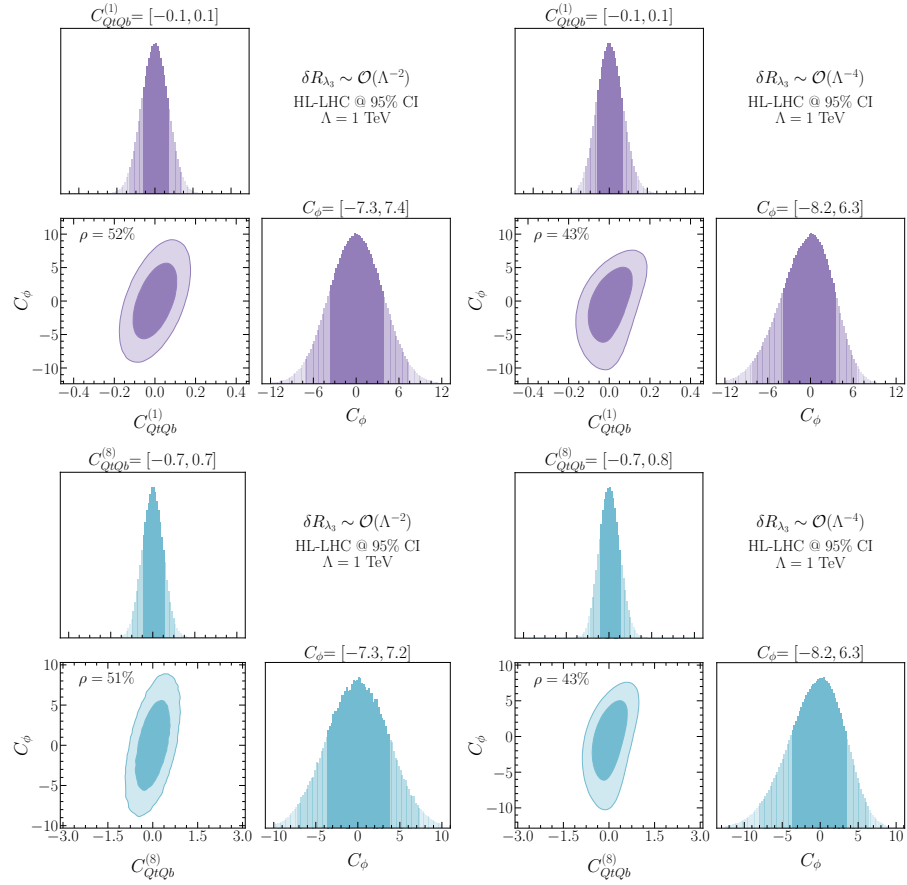


Figure B.2. The posterior distributions of the HL-LHC projections fits for C_ϕ with $C_{QtQb}^{(1)}$ (up) and C_ϕ with $C_{QtQb}^{(8)}$ (down). With the same annotations as in [Figure B.1](#).

C Prospects for Higgs pair production at the FCC

The analysis done in section 9.5 for Higgs pair at the HL-LHC can be repeated for the future hadron circular collider (FCC-hh), with centre-of-mass energy of 100 TeV and integrated luminosity of 30 ab^{-1} . The Higgs pair events and the backgrounds were generated in the same manner for the FCC-hh as for the HL-LHC. Moreover, the ML analysis and the consequent statistical framework were also identical to the ones done for the HL-LHC. With the caveat of using the 14 TeV K -factors for the 100 TeV cross-section scaling, as the 100 TeV K -factors were not available for all processes. I should note that we have explicitly checked that at least within the SM, for Higgs pair production via gluon fusion the difference is of $\mathcal{O}(1\%)$ [218] and hence small. An example output of the BDT-classifier for the FCC-hh is shown for the SM signal as a confusion matrix in Table C.1

Preforming a single-parameter fit on the light Yukawa modifiers, we see the projected bounds on these operators at FCC-hh are given by

$$\begin{aligned} C_{u\phi}^{MV}(\kappa_u^{MV}) &= [-0.012, 0.011] \quad ([-57.8, 54.7]), \\ C_{d\phi}^{MV}(\kappa_d^{MV}) &= [-0.012, 0.012] \quad ([-26.3, 28.4]). \end{aligned} \quad (\text{C.1})$$

These projected bounds for FCC-hh are an order of magnitude better than those for HL-LHC. In addition, the bounds on $C_{u\phi}$ and $C_{d\phi}$ are numerically the same displaying a much greater improvement in the bounds on $C_{d\phi}$ than on $C_{u\phi}$ at the higher energy collider. The results of the FCC-hh analysis are summarised in Table C.2

From this table, we observe that the constraints on the trilinear self-coupling reach the precision-level of $\sim 4\%$ at 68% CI. As for light Yukawa, the up-type will reach $\mathcal{O}(50)$

Predicted no. of events at FCC-hh							
Actual no. of events	Channel	$hh_{\text{tri}}^{\text{ggF}}$	$hh_{\text{tri}}^{\text{ggF}}$	$hh_{\text{box}}^{\text{ggF}}$	$Q\bar{Q}h$	$b\bar{b}\gamma\gamma$	total
	$hh_{\text{tri}}^{\text{ggF}}$	3,579	1,303	2,372	4,697	337	12,288
	$hh_{\text{int}}^{\text{ggF}}$	13,602	7,300	17,075	24,716	1523	64,216
	$hh_{\text{box}}^{\text{ggF}}$	14,534	11,416	35,988	415,26	1,996	105,460
	$Q\bar{Q}h$	29,611	12,355	23,279	1,238,266	214,564	1,518,075
	$b\bar{b}\gamma\gamma$	45,574	22,290	26,213	150,935	227,142	24,317,657
	Z_j	10.95	31.22	111.1	737.7	4,743	

Table C.1. The confusion matrix output of the trained BDT five-channel classifier for the FCC-hh analysis. This table is antireligious to for the HL-LHC ??

Operators	$C_{u\phi}$	$C_{d\phi}$	C_ϕ		κ_u	κ_d	κ_λ
\mathcal{O}_ϕ	—	—	[-0.066, 0.064]		—	—	[0.97, 1.03]
$\mathcal{O}_{u\phi}$	[-0.012, 0.011]	—	—		[-57.8, 54.7]	—	—
$\mathcal{O}_{d\phi}$	—	[-0.012, 0.011]	—		—	[-26.3, 28.4]	—
$\mathcal{O}_{u\phi} \& \mathcal{O}_\phi$	[-0.010, 0.011]	—	[-0.091, 0.042]		[-52, 49]	—	[0.98, 1.04]
$\mathcal{O}_{d\phi} \& \mathcal{O}_\phi$	—	[-0.010, 0.012]	[-0.092, 0.041]		—	[-24, 26]	[0.98, 1.04]
$\mathcal{O}_{u\phi} \& \mathcal{O}_{d\phi}$	[-0.008, 0.009]	[-0.008, 0.009]	—		[-42, 39]	[-19, 19]	—
All	[-0.009, 0.010]	[-0.009, 0.010]	[-0.105, 0.023]		[-47, 44]	[-21, 21]	[0.99, 1.05]

Table C.2. The 1σ bounds on $C_{u\phi}$, $C_{d\phi}$ and C_ϕ from one-, two- and three-parameter fits for FCC-hh with 30 ab^{-1} integrated luminosity.

times the SM value showing significant improvement over the HL-LHC, and $\mathcal{O}(20 - 30)$ for the down Yukawa. The posterior distributions for the two-parameter fits are shown in Figure C.1, while the three-parameter analysis in Figure C.2. These plots show more significant correlation patterns between $C : \phi$ and the light Yukawa modifiers compared to the HL-LHC fits in Figure 9.11 and Figure 9.12

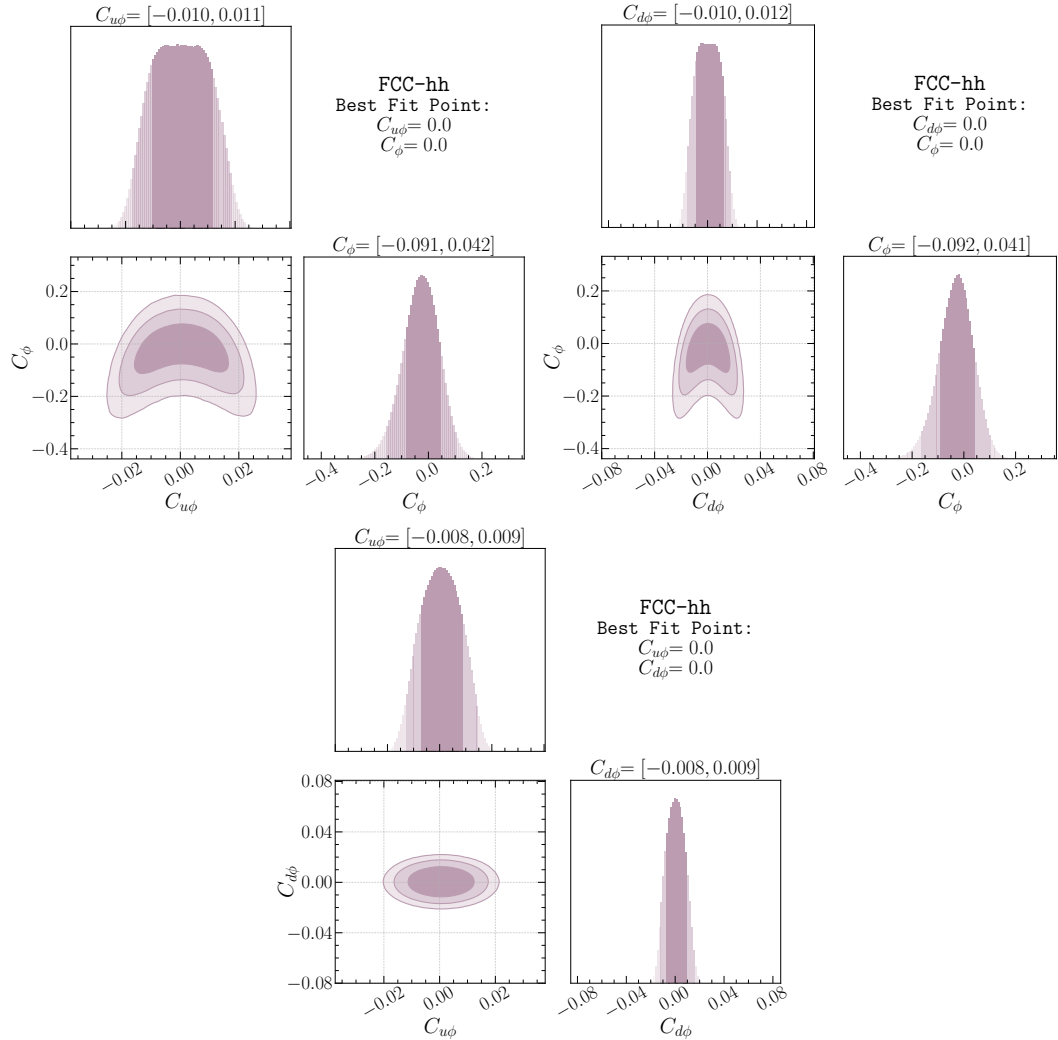


Figure C.1. Constraints on pairs of Wilson coefficients for C_ϕ , $C_{u\phi}$ and $C_{d\phi}$ for FCC-hh with 30 ab^{-1} integrated luminosity.

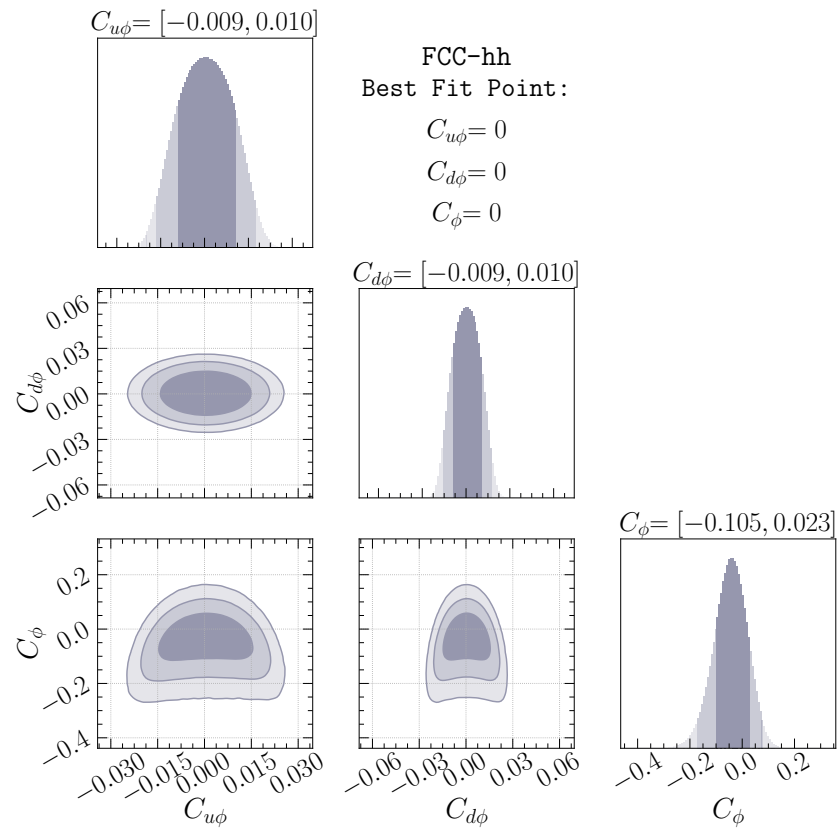


Figure C.2. Three parameter fits with $C_{u\phi}$, $C_{d\phi}$ and C_ϕ , using projection for the FCC-hh.

Bibliography

- [1] ATLAS Collaboration, G. Aad *et al.*, “Observation of a new particle in the search for the Standard Model Higgs boson with the ATLAS detector at the LHC,” *Phys. Lett. B* **716** (2012) 1–29, [arXiv:1207.7214 \[hep-ex\]](https://arxiv.org/abs/1207.7214).
- [2] CMS Collaboration, S. Chatrchyan *et al.*, “Observation of a New Boson at a Mass of 125 GeV with the CMS Experiment at the LHC,” *Phys. Lett. B* **716** (2012) 30–61, [arXiv:1207.7235 \[hep-ex\]](https://arxiv.org/abs/1207.7235).
- [3] A. Salam and J. C. Ward, “On a gauge theory of elementary interactions,” *Il Nuovo Cimento (1955-1965)* **19** no. 1, (1961) 165–170.
<https://doi.org/10.1007/BF02812723>.
- [4] A. Salam and J. C. Ward, “Weak and electromagnetic interactions,” *Il Nuovo Cimento (1955-1965)* **11** no. 4, (1959) 568–577.
<https://doi.org/10.1007/BF02726525>.
- [5] S. Weinberg, “A model of leptons,” *Phys. Rev. Lett.* **19** (Nov, 1967) 1264–1266.
<https://link.aps.org/doi/10.1103/PhysRevLett.19.1264>.
- [6] F. Englert and R. Brout, “Broken symmetry and the mass of gauge vector mesons,” *Phys. Rev. Lett.* **13** (Aug, 1964) 321–323.
<https://link.aps.org/doi/10.1103/PhysRevLett.13.321>.
- [7] P. W. Higgs, “Broken symmetries and the masses of gauge bosons,” *Phys. Rev. Lett.* **13** (Oct, 1964) 508–509.
<https://link.aps.org/doi/10.1103/PhysRevLett.13.508>.
- [8] P. Higgs, “Broken symmetries, massless particles and gauge fields,” *Physics Letters* **12** no. 2, (1964) 132–133.
<https://www.sciencedirect.com/science/article/pii/0031916364911369>.
- [9] G. S. Guralnik, C. R. Hagen, and T. W. B. Kibble, “Global conservation laws and massless particles,” *Phys. Rev. Lett.* **13** (Nov, 1964) 585–587.
<https://link.aps.org/doi/10.1103/PhysRevLett.13.585>.
- [10] G. S. Guralnik, “The History of the Guralnik, Hagen and Kibble development of the Theory of Spontaneous Symmetry Breaking and Gauge Particles,” *Int. J. Mod. Phys. A* **24** (2009) 2601–2627, [arXiv:0907.3466 \[physics.hist-ph\]](https://arxiv.org/abs/0907.3466).

- [11] R. Bonciani, G. Degrassi, P. P. Giardino, and R. Gröber, “Analytical Method for Next-to-Leading-Order QCD Corrections to Double-Higgs Production,” *Phys. Rev. Lett.* **121** no. 16, (2018) 162003, [arXiv:1806.11564 \[hep-ph\]](https://arxiv.org/abs/1806.11564).
- [12] **ATLAS Collaboration** Collaboration, “Search for direct pair production of sleptons and charginos decaying to two leptons and neutralinos with mass splittings near the W boson mass in $\sqrt{s} = 13$ TeV pp collisions with the ATLAS detector,” tech. rep., CERN, Geneva, Mar, 2022.
<http://cds.cern.ch/record/2805051>. All figures including auxiliary figures are available at
<https://atlas.web.cern.ch/Atlas/GROUPS/PHYSICS/CONFNOTES/ATLAS-CONF-2022-006>.
- [13] **ATLAS Collaboration** Collaboration, “Fiducial and differential measurements of W^+W^- production in decay topologies inspired by searches for electroweak supersymmetry in two-lepton final states,” tech. rep., CERN, Geneva, Mar, 2022.
<http://cds.cern.ch/record/2805215>. All figures including auxiliary figures are available at
<https://atlas.web.cern.ch/Atlas/GROUPS/PHYSICS/CONFNOTES/ATLAS-CONF-2022-011>.
- [14] **ATLAS Collaboration** Collaboration, “Search for dark matter produced in association with a single top quark and an energetic W boson in $\sqrt{s} = 13$ TeV (pp) collisions with the ATLAS detector,” tech. rep., CERN, Geneva, Mar, 2022.
<https://cds.cern.ch/record/2805216>. All figures including auxiliary figures are available at
<https://atlas.web.cern.ch/Atlas/GROUPS/PHYSICS/CONFNOTES/ATLAS-CONF-2022-012>.
- [15] **ATLAS Collaboration** Collaboration, “Search for doubly charged Higgs boson production in multi-lepton final states using 139 fb^{-1} of proton–proton collisions at $\sqrt{s} = 13$ TeV with the ATLAS detector,” tech. rep., CERN, Geneva, Mar, 2022. <https://cds.cern.ch/record/2805214>. All figures including auxiliary figures are available at
<https://atlas.web.cern.ch/Atlas/GROUPS/PHYSICS/CONFNOTES/ATLAS-CONF-2022-010>.
- [16] **ATLAS Collaboration** Collaboration, “Search for pair-produced scalar and vector leptoquarks decaying into third-generation quarks and first- or second-generation leptons in pp collisions with the ATLAS detector,” tech. rep., CERN, Geneva, Mar, 2022. <https://cds.cern.ch/record/2805213>. All figures including auxiliary figures are available at
<https://atlas.web.cern.ch/Atlas/GROUPS/PHYSICS/CONFNOTES/ATLAS-CONF-2022-009>.

- [17] **CMS Collaboration** Collaboration, “Search for heavy composite Majorana neutrino,” tech. rep., CERN, Geneva, 2022. <http://cds.cern.ch/record/2804305>.
- [18] **CMS Collaboration** Collaboration, “Search for paired dijet resonances,” tech. rep., CERN, Geneva, 2022. <http://cds.cern.ch/record/2803669>.
- [19] **CMS Collaboration** Collaboration, “Probing Majorana neutrinos and the Weinberg operator in the same-charge dimuon channel through vector boson fusion processes in proton-proton collisions at $\sqrt{s} = 13$ TeV ,” tech. rep., CERN, Geneva, 2022. <http://cds.cern.ch/record/2803671>.
- [20] **CMS Collaboration** Collaboration, “Search for Z' bosons decaying to pairs of heavy Majorana neutrinos in proton-proton collisions at $\sqrt{s} = 13$ TeV,” tech. rep., CERN, Geneva, 2022. <http://cds.cern.ch/record/2803617>.
- [21] **CMS Collaboration** Collaboration, “Search for long-lived particles decaying to a pair of muons in proton-proton collisions at $\sqrt{s} = 13$ TeV,” tech. rep., CERN, Geneva, 2022. <http://cds.cern.ch/record/2799212>.
- [22] **CMS** Collaboration, A. Tumasyan *et al.*, “Inclusive nonresonant multilepton probes of new phenomena at $\sqrt{s} = 13$ TeV,” [arXiv:2202.08676 \[hep-ex\]](https://arxiv.org/abs/2202.08676).
- [23] **CMS** Collaboration, A. Tumasyan *et al.*, “Search for new physics in the lepton plus missing transverse momentum final state in proton-proton collisions at $\sqrt{s} = 13$ TeV,” [arXiv:2202.06075 \[hep-ex\]](https://arxiv.org/abs/2202.06075).
- [24] G. F. Giudice, C. Grojean, A. Pomarol, and R. Rattazzi, “The Strongly-Interacting Light Higgs,” *JHEP* **06** (2007) 045, [arXiv:hep-ph/0703164](https://arxiv.org/abs/hep-ph/0703164).
- [25] B. Grzadkowski, M. Iskrzynski, M. Misiak, and J. Rosiek, “Dimension-Six Terms in the Standard Model Lagrangian,” *JHEP* **10** (2010) 085, [arXiv:1008.4884 \[hep-ph\]](https://arxiv.org/abs/1008.4884).
- [26] R. Contino, M. Ghezzi, C. Grojean, M. Muhlleitner, and M. Spira, “Effective Lagrangian for a light Higgs-like scalar,” *JHEP* **07** (2013) 035, [arXiv:1303.3876 \[hep-ph\]](https://arxiv.org/abs/1303.3876).
- [27] J. Elias-Miró, C. Grojean, R. S. Gupta, and D. Marzocca, “Scaling and tuning of EW and Higgs observables,” *JHEP* **05** (2014) 019, [arXiv:1312.2928 \[hep-ph\]](https://arxiv.org/abs/1312.2928).
- [28] R. S. Gupta, A. Pomarol, and F. Riva, “BSM Primary Effects,” *Phys. Rev. D* **91** no. 3, (2015) 035001, [arXiv:1405.0181 \[hep-ph\]](https://arxiv.org/abs/1405.0181).
- [29] M. McCullough, “An Indirect Model-Dependent Probe of the Higgs Self-Coupling,” *Phys. Rev. D* **90** no. 1, (2014) 015001, [arXiv:1312.3322 \[hep-ph\]](https://arxiv.org/abs/1312.3322). [Erratum: Phys.Rev.D 92, 039903 (2015)].

- [30] M. Gorbahn and U. Haisch, “Indirect probes of the trilinear Higgs coupling: $gg \rightarrow h$ and $h \rightarrow \gamma\gamma$,” *JHEP* **10** (2016) 094, [arXiv:1607.03773 \[hep-ph\]](https://arxiv.org/abs/1607.03773).
- [31] G. Degrassi, P. P. Giardino, F. Maltoni, and D. Pagani, “Probing the Higgs self coupling via single Higgs production at the LHC,” *JHEP* **12** (2016) 080, [arXiv:1607.04251 \[hep-ph\]](https://arxiv.org/abs/1607.04251).
- [32] W. Bizon, M. Gorbahn, U. Haisch, and G. Zanderighi, “Constraints on the trilinear Higgs coupling from vector boson fusion and associated Higgs production at the LHC,” *JHEP* **07** (2017) 083, [arXiv:1610.05771 \[hep-ph\]](https://arxiv.org/abs/1610.05771).
- [33] F. Maltoni, D. Pagani, A. Shivaji, and X. Zhao, “Trilinear Higgs coupling determination via single-Higgs differential measurements at the LHC,” *Eur. Phys. J. C* **77** no. 12, (2017) 887, [arXiv:1709.08649 \[hep-ph\]](https://arxiv.org/abs/1709.08649).
- [34] G. Degrassi and M. Vitti, “The effect of an anomalous Higgs trilinear self-coupling on the $h \rightarrow \gamma Z$ decay,” *Eur. Phys. J. C* **80** no. 4, (2020) 307, [arXiv:1912.06429 \[hep-ph\]](https://arxiv.org/abs/1912.06429).
- [35] G. Degrassi, B. Di Micco, P. P. Giardino, and E. Rossi, “Higgs boson self-coupling constraints from single Higgs, double Higgs and Electroweak measurements,” *Phys. Lett. B* **817** (2021) 136307, [arXiv:2102.07651 \[hep-ph\]](https://arxiv.org/abs/2102.07651).
- [36] U. Haisch and G. Koole, “Off-shell Higgs production at the LHC as a probe of the trilinear Higgs coupling,” [arXiv:2111.12589 \[hep-ph\]](https://arxiv.org/abs/2111.12589).
- [37] J. Ellis, M. Madigan, K. Mimasu, V. Sanz, and T. You, “Top, Higgs, Diboson and Electroweak Fit to the Standard Model Effective Field Theory,” *JHEP* **04** (2021) 279, [arXiv:2012.02779 \[hep-ph\]](https://arxiv.org/abs/2012.02779).
- [38] S. Dawson, S. Homiller, and S. D. Lane, “Putting SMEFT Fits to Work,” [arXiv:2007.01296 \[hep-ph\]](https://arxiv.org/abs/2007.01296).
- [39] **ATLAS Collaboration** Collaboration, C. Bernius, “HL-LHC prospects from ATLAS and CMS,” tech. rep., CERN, Geneva, Mar, 2019.
<https://cds.cern.ch/record/2666331>.
- [40] C. Grojean, A. Paul, and Z. Qian, “Resurrecting $b\bar{b}h$ with kinematic shapes,” *JHEP* **04** (2021) 139, [arXiv:2011.13945 \[hep-ph\]](https://arxiv.org/abs/2011.13945).
- [41] **LHCb** Collaboration, R. Aaij *et al.*, “Test of lepton universality using $B^+ \rightarrow K^+\ell^+\ell^-$ decays,” *Phys. Rev. Lett.* **113** (2014) 151601, [arXiv:1406.6482 \[hep-ex\]](https://arxiv.org/abs/1406.6482).
- [42] **LHCb** Collaboration, R. Aaij *et al.*, “Test of lepton universality with $B^0 \rightarrow K^{*0}\ell^+\ell^-$ decays,” *JHEP* **08** (2017) 055, [arXiv:1705.05802 \[hep-ex\]](https://arxiv.org/abs/1705.05802).

- [43] **LHCb** Collaboration, R. Aaij *et al.*, “Search for lepton-universality violation in $B^+ \rightarrow K^+ \ell^+ \ell^-$ decays,” *Phys. Rev. Lett.* **122** no. 19, (2019) 191801, [arXiv:1903.09252 \[hep-ex\]](https://arxiv.org/abs/1903.09252).
- [44] **Belle** Collaboration, A. Abdesselam *et al.*, “Test of lepton flavor universality in $B \rightarrow K^* \ell^+ \ell^-$ decays at Belle,” [arXiv:1904.02440 \[hep-ex\]](https://arxiv.org/abs/1904.02440).
- [45] **LHCb** Collaboration, R. Aaij *et al.*, “Test of lepton universality in beauty-quark decays,” [arXiv:2103.11769 \[hep-ex\]](https://arxiv.org/abs/2103.11769).
- [46] **CMS** Collaboration, S. Chatrchyan *et al.*, “Measurement of the $B_s^0 \rightarrow \mu^+ \mu^-$ Branching Fraction and Search for $B^0 \rightarrow \mu^+ \mu^-$ with the CMS Experiment,” *Phys. Rev. Lett.* **111** (2013) 101804, [arXiv:1307.5025 \[hep-ex\]](https://arxiv.org/abs/1307.5025).
- [47] **LHCb** Collaboration, R. Aaij *et al.*, “Measurement of the $B_s^0 \rightarrow \mu^+ \mu^-$ branching fraction and effective lifetime and search for $B^0 \rightarrow \mu^+ \mu^-$ decays,” *Phys. Rev. Lett.* **118** no. 19, (2017) 191801, [arXiv:1703.05747 \[hep-ex\]](https://arxiv.org/abs/1703.05747).
- [48] **ATLAS** Collaboration, M. Aaboud *et al.*, “Study of the rare decays of B_s^0 and B^0 mesons into muon pairs using data collected during 2015 and 2016 with the ATLAS detector,” *JHEP* **04** (2019) 098, [arXiv:1812.03017 \[hep-ex\]](https://arxiv.org/abs/1812.03017).
- [49] **LHCb** Collaboration, R. Aaij *et al.*, “Search for the rare decays $B_s^0 \rightarrow e^+ e^-$ and $B^0 \rightarrow e^+ e^-$,” *Phys. Rev. Lett.* **124** no. 21, (2020) 211802, [arXiv:2003.03999 \[hep-ex\]](https://arxiv.org/abs/2003.03999).
- [50] L. Di Luzio, A. Greljo, and M. Nardecchia, “Gauge leptoquark as the origin of B-physics anomalies,” *Phys. Rev. D* **96** no. 11, (2017) 115011, [arXiv:1708.08450 \[hep-ph\]](https://arxiv.org/abs/1708.08450).
- [51] L. Calibbi, A. Crivellin, and T. Li, “Model of vector leptoquarks in view of the B-physics anomalies,” *Phys. Rev. D* **98** no. 11, (2018) 115002, [arXiv:1709.00692 \[hep-ph\]](https://arxiv.org/abs/1709.00692).
- [52] M. Bordone, C. Cornella, J. Fuentes-Martin, and G. Isidori, “A three-site gauge model for flavor hierarchies and flavor anomalies,” *Phys. Lett. B* **779** (2018) 317–323, [arXiv:1712.01368 \[hep-ph\]](https://arxiv.org/abs/1712.01368).
- [53] R. Barbieri and A. Tesi, “ B -decay anomalies in Pati-Salam SU(4),” *Eur. Phys. J. C* **78** no. 3, (2018) 193, [arXiv:1712.06844 \[hep-ph\]](https://arxiv.org/abs/1712.06844).
- [54] N. Assad, B. Fornal, and B. Grinstein, “Baryon Number and Lepton Universality Violation in Leptoquark and Diquark Models,” *Phys. Lett. B* **777** (2018) 324–331, [arXiv:1708.06350 \[hep-ph\]](https://arxiv.org/abs/1708.06350).
- [55] J. Heeck and D. Teresi, “Pati-Salam explanations of the B-meson anomalies,” *JHEP* **12** (2018) 103, [arXiv:1808.07492 \[hep-ph\]](https://arxiv.org/abs/1808.07492).

- [56] B. Fornal, S. A. Gadam, and B. Grinstein, “Left-Right SU(4) Vector Leptoquark Model for Flavor Anomalies,” *Phys. Rev. D* **99** no. 5, (2019) 055025, [arXiv:1812.01603 \[hep-ph\]](https://arxiv.org/abs/1812.01603).
- [57] A. Crivellin, C. Greub, D. Müller, and F. Saturnino, “Importance of Loop Effects in Explaining the Accumulated Evidence for New Physics in B Decays with a Vector Leptoquark,” *Phys. Rev. Lett.* **122** no. 1, (2019) 011805, [arXiv:1807.02068 \[hep-ph\]](https://arxiv.org/abs/1807.02068).
- [58] A. Crivellin, D. Müller, and F. Saturnino, “Flavor Phenomenology of the Leptoquark Singlet-Triplet Model,” *JHEP* **06** (2020) 020, [arXiv:1912.04224 \[hep-ph\]](https://arxiv.org/abs/1912.04224).
- [59] M. Bordone, O. Catà, and T. Feldmann, “Effective Theory Approach to New Physics with Flavour: General Framework and a Leptoquark Example,” *JHEP* **01** (2020) 067, [arXiv:1910.02641 \[hep-ph\]](https://arxiv.org/abs/1910.02641).
- [60] R. A. Minlos, *Introduction to mathematical statistical physics*. No. 19. American Mathematical Soc., 2000.
- [61] M. Gell-Mann, “The eightfold way: A theory of strong interaction symmetry,” <https://www.osti.gov/biblio/4008239>.
- [62] C. N. Yang and R. L. Mills, “Conservation of isotopic spin and isotopic gauge invariance,” *Phys. Rev.* **96** (Oct, 1954) 191–195. <https://link.aps.org/doi/10.1103/PhysRev.96.191>.
- [63] **Particle Data Group** Collaboration, P. Zyla *et al.*, “Review of Particle Physics,” *PTEP* **2020** no. 8, (2020) 083C01.
- [64] D. S. Freed, “Lectures on topological quantum field theory,” 1993.
- [65] R. Dijkgraaf and E. Witten, “Topological gauge theories and group cohomology,” *Communications in Mathematical Physics* **129** no. 2, (1990) 393–429.
- [66] F. Capozzi, E. Lisi, A. Marrone, D. Montanino, and A. Palazzo, “Neutrino masses and mixings: Status of known and unknown 3ν parameters,” *Nucl. Phys. B* **908** (2016) 218–234, [arXiv:1601.07777 \[hep-ph\]](https://arxiv.org/abs/1601.07777).
- [67] **ALEPH, DELPHI, L3, OPAL, SLD, LEP Electroweak Working Group, SLD Electroweak Group, SLD Heavy Flavour Group** Collaboration, S. Schael *et al.*, “Precision electroweak measurements on the Z resonance,” *Phys. Rept.* **427** (2006) 257–454, [arXiv:hep-ex/0509008 \[hep-ex\]](https://arxiv.org/abs/hep-ex/0509008).
- [68] **SLD** Collaboration, K. Abe *et al.*, “First direct measurement of the parity violating coupling of the Z_0 to the s quark,” *Phys. Rev. Lett.* **85** (2000) 5059–5063, [arXiv:hep-ex/0006019](https://arxiv.org/abs/hep-ex/0006019).

- [69] **CDF, D0** Collaboration, T. E. W. Group, “2012 Update of the Combination of CDF and D0 Results for the Mass of the W Boson,” [arXiv:1204.0042 \[hep-ex\]](https://arxiv.org/abs/1204.0042).
- [70] **ALEPH, DELPHI, L3, OPAL, LEP Electroweak** Collaboration, S. Schael *et al.*, “Electroweak Measurements in Electron-Positron Collisions at W-Boson-Pair Energies at LEP,” *Phys. Rept.* **532** (2013) 119–244, [arXiv:1302.3415 \[hep-ex\]](https://arxiv.org/abs/1302.3415).
- [71] **DØ** Collaboration, V. M. Abazov *et al.*, “Measurement of $\sin^2 \theta_{\text{eff}}^\ell$ and Z-light quark couplings using the forward-backward charge asymmetry in $p\bar{p} \rightarrow Z/\gamma^* \rightarrow e^+e^-$ events with $\mathcal{L} = 5.0 \text{ fb}^{-1}$ at $\sqrt{s} = 1.96 \text{ TeV}$,” *Phys. Rev. D* **84** (2011) 012007, [arXiv:1104.4590 \[hep-ex\]](https://arxiv.org/abs/1104.4590).
- [72] **CMS** Collaboration, V. Khachatryan *et al.*, “Measurement of the t-channel single-top-quark production cross section and of the $|V_{tb}|$ CKM matrix element in pp collisions at $\sqrt{s} = 8 \text{ TeV}$,” *JHEP* **06** (2014) 090, [arXiv:1403.7366 \[hep-ex\]](https://arxiv.org/abs/1403.7366).
- [73] **ATLAS** Collaboration, M. Aaboud *et al.*, “Measurement of the W-boson mass in pp collisions at $\sqrt{s} = 7 \text{ TeV}$ with the ATLAS detector,” *Eur. Phys. J. C* **78** no. 2, (2018) 110, [arXiv:1701.07240 \[hep-ex\]](https://arxiv.org/abs/1701.07240). [Erratum: Eur.Phys.J.C 78, 898 (2018)].
- [74] Y. Nambu, “Quasi-particles and gauge invariance in the theory of superconductivity,” *Phys. Rev.* **117** (Feb, 1960) 648–663. <https://link.aps.org/doi/10.1103/PhysRev.117.648>.
- [75] J. Goldstone, “Field theories with superconductor solutions,” *Il Nuovo Cimento (1955-1965)* **19** no. 1, (1961) 154–164.
- [76] J. Goldstone, A. Salam, and S. Weinberg, “Broken symmetries,” *Phys. Rev.* **127** (Aug, 1962) 965–970. <https://link.aps.org/doi/10.1103/PhysRev.127.965>.
- [77] P. W. Anderson, “Plasmons, gauge invariance, and mass,” *Phys. Rev.* **130** (Apr, 1963) 439–442. <https://link.aps.org/doi/10.1103/PhysRev.130.439>.
- [78] J. Erler and M. Schott, “Electroweak Precision Tests of the Standard Model after the Discovery of the Higgs Boson,” *Prog. Part. Nucl. Phys.* **106** (2019) 68–119, [arXiv:1902.05142 \[hep-ph\]](https://arxiv.org/abs/1902.05142).
- [79] N. Cabibbo, “Unitary symmetry and leptonic decays,” *Phys. Rev. Lett.* **10** (Jun, 1963) 531–533. <https://link.aps.org/doi/10.1103/PhysRevLett.10.531>.
- [80] M. Kobayashi and T. Maskawa, “CP-Violation in the Renormalizable Theory of Weak Interaction,” *Progress of Theoretical Physics* **49** no. 2, (02, 1973) 652–657, <https://academic.oup.com/ptp/article-pdf/49/2/652/5257692/49-2-652.pdf>. <https://doi.org/10.1143/PTP.49.652>.

- [81] A. Falkowski, F. Riva, and A. Urbano, “Higgs at last,” *JHEP* **11** (2013) 111, [arXiv:1303.1812 \[hep-ph\]](https://arxiv.org/abs/1303.1812).
- [82] M. Ciuchini, E. Franco, S. Mishima, and L. Silvestrini, “Electroweak Precision Observables, New Physics and the Nature of a 126 GeV Higgs Boson,” *JHEP* **08** (2013) 106, [arXiv:1306.4644 \[hep-ph\]](https://arxiv.org/abs/1306.4644).
- [83] A. Falkowski and F. Riva, “Model-independent precision constraints on dimension-6 operators,” *JHEP* **02** (2015) 039, [arXiv:1411.0669 \[hep-ph\]](https://arxiv.org/abs/1411.0669).
- [84] J. de Blas, M. Chala, and J. Santiago, “Renormalization Group Constraints on New Top Interactions from Electroweak Precision Data,” *JHEP* **09** (2015) 189, [arXiv:1507.00757 \[hep-ph\]](https://arxiv.org/abs/1507.00757).
- [85] J. de Blas, M. Ciuchini, E. Franco, S. Mishima, M. Pierini, L. Reina, and L. Silvestrini, “Electroweak precision observables and Higgs-boson signal strengths in the Standard Model and beyond: present and future,” *JHEP* **12** (2016) 135, [arXiv:1608.01509 \[hep-ph\]](https://arxiv.org/abs/1608.01509).
- [86] J. de Blas, M. Ciuchini, E. Franco, S. Mishima, M. Pierini, L. Reina, and L. Silvestrini, “The Global Electroweak and Higgs Fits in the LHC era,” *PoS EPS-HEP2017* (2017) 467, [arXiv:1710.05402 \[hep-ph\]](https://arxiv.org/abs/1710.05402).
- [87] J. Haller, A. Hoecker, R. Kogler, K. Mönig, T. Peiffer, and J. Stelzer, “Update of the global electroweak fit and constraints on two-Higgs-doublet models,” *Eur. Phys. J. C* **78** no. 8, (2018) 675, [arXiv:1803.01853 \[hep-ph\]](https://arxiv.org/abs/1803.01853).
- [88] J. Ellis, C. W. Murphy, V. Sanz, and T. You, “Updated Global SMEFT Fit to Higgs, Diboson and Electroweak Data,” *JHEP* **06** (2018) 146, [arXiv:1803.03252 \[hep-ph\]](https://arxiv.org/abs/1803.03252).
- [89] R. E. Behrends, R. J. Finkelstein, and A. Sirlin, “Radiative corrections to decay processes,” *Phys. Rev.* **101** (Jan, 1956) 866–873.
<https://link.aps.org/doi/10.1103/PhysRev.101.866>.
- [90] T. Kinoshita and A. Sirlin, “Radiative corrections to fermi interactions,” *Phys. Rev.* **113** (Mar, 1959) 1652–1660.
<https://link.aps.org/doi/10.1103/PhysRev.113.1652>.
- [91] I. Mohammad and A. Donnachie, “Radiative Corrections to Radiative Muon Decay.”
- [92] T. van Ritbergen and R. G. Stuart, “Complete 2-loop quantum electrodynamic contributions to the muon lifetime in the fermi model,” *Phys. Rev. Lett.* **82** (Jan, 1999) 488–491. <https://link.aps.org/doi/10.1103/PhysRevLett.82.488>.
- [93] D. Ross and M. Veltman, “Neutral currents and the higgs mechanism,” *Nuclear Physics B* **95** no. 1, (1975) 135–147.
<https://www.sciencedirect.com/science/article/pii/055032137590485X>.

- [94] A. Djouadi, “The Anatomy of electro-weak symmetry breaking. I: The Higgs boson in the standard model,” *Phys. Rept.* **457** (2008) 1–216, [arXiv:hep-ph/0503172](https://arxiv.org/abs/hep-ph/0503172).
- [95] M. J. Dugan, H. Georgi, and D. B. Kaplan, “Anatomy of a composite higgs model,” *Nuclear Physics* **254** (1985) 299–326.
- [96] C. T. Hill and E. H. Simmons, “Strong Dynamics and Electroweak Symmetry Breaking,” *Phys. Rept.* **381** (2003) 235–402, [arXiv:hep-ph/0203079](https://arxiv.org/abs/hep-ph/0203079). [Erratum: Phys.Rept. 390, 553–554 (2004)].
- [97] M. Schwartz, *Quantum Field Theory and the Standard Model*. Quantum Field Theory and the Standard Model. Cambridge University Press, 2014.
<https://books.google.nl/books?id=HbdEAgAAQBAJ>.
- [98] M. Peskin and D. Schroeder, *An Introduction To Quantum Field Theory*. Frontiers in Physics. Avalon Publishing, 1995.
<https://books.google.de/books?id=EVeNNcslvXOC>.
- [99] M. Einhorn, D. Jones, and M. Veltman, “Heavy particles and the rho parameter in the standard model,” *Nuclear Physics B* **191** no. 1, (1981) 146–172.
<https://www.sciencedirect.com/science/article/pii/0550321381902923>.
- [100] W. J. Marciano and J. L. Rosner, “Atomic parity violation as a probe of new physics,” *Phys. Rev. Lett.* **65** (Dec, 1990) 2963–2966.
<https://link.aps.org/doi/10.1103/PhysRevLett.65.2963>.
- [101] M. E. Peskin and T. Takeuchi, “New constraint on a strongly interacting higgs sector,” *Phys. Rev. Lett.* **65** (Aug, 1990) 964–967.
<https://link.aps.org/doi/10.1103/PhysRevLett.65.964>.
- [102] D. C. Kennedy and P. Langacker, “Erratum: “precision electroweak experiments and heavy physics: A global analysis [phys. rev. lett. 65, 2967 (1990)],” *Phys. Rev. Lett.* **66** (Jan, 1991) 395–395.
<https://link.aps.org/doi/10.1103/PhysRevLett.66.395.2>.
- [103] M. E. Peskin and T. Takeuchi, “Estimation of oblique electroweak corrections,” 1991.
<https://www.sciencedirect.com/science/article/pii/0550321391906144>.
- [104] M. Golden and L. Randall, “Radiative corrections to electroweak parameters in technicolor theories,” *Nuclear Physics B* **361** no. 1, (1991) 3–23.
<https://www.sciencedirect.com/science/article/pii/0550321391906144>.
- [105] B. Holdom and J. Terning, “Large corrections to electroweak parameters in technicolor theories,” *Physics Letters B* **247** no. 1, (1990) 88–92.
<https://www.sciencedirect.com/science/article/pii/037026939091054F>.

- [106] G. Altarelli, R. Barbieri, and S. Jadach, “Toward a model-independent analysis of electroweak data,” *Nuclear Physics B* **369** no. 1, (1992) 3–32.
<https://www.sciencedirect.com/science/article/pii/055032139290376M>.
- [107] R. S. Chivukula, S. B. Selipsky, and E. H. Simmons, “Nonoblique effects in the $z\bar{b}b\bar{b}$ vertex from extended technicolor dynamics,” *Phys. Rev. Lett.* **69** (Jul, 1992) 575–577. <https://link.aps.org/doi/10.1103/PhysRevLett.69.575>.
- [108] E. H. Simmons, R. S. Chivukula, and J. Terning, “Testing extended technicolor with $R(b)$,” *Prog. Theor. Phys. Suppl.* **123** (1996) 87–96,
[arXiv:hep-ph/9509392](https://arxiv.org/abs/hep-ph/9509392).
- [109] G. Valencia and S. Willenbrock, “Goldstone-boson equivalence theorem and the higgs resonance,” *Phys. Rev. D* **42** (Aug, 1990) 853–859.
<https://link.aps.org/doi/10.1103/PhysRevD.42.853>.
- [110] L. Di Luzio, R. Gröber, and M. Spannowsky, “Maxi-sizing the trilinear Higgs self-coupling: how large could it be?,” *Eur. Phys. J. C* **77** no. 11, (2017) 788,
[arXiv:1704.02311 \[hep-ph\]](https://arxiv.org/abs/1704.02311).
- [111] M. Lindner, “Implications of Triviality for the Standard Model,” *Z. Phys. C* **31** (1986) 295.
- [112] M. Sher, “Electroweak Higgs Potentials and Vacuum Stability,” *Phys. Rept.* **179** (1989) 273–418.
- [113] J. A. Casas, J. R. Espinosa, and M. Quiros, “Standard model stability bounds for new physics within LHC reach,” *Phys. Lett. B* **382** (1996) 374–382,
[arXiv:hep-ph/9603227](https://arxiv.org/abs/hep-ph/9603227).
- [114] G. Isidori, G. Ridolfi, and A. Strumia, “On the metastability of the standard model vacuum,” *Nucl. Phys. B* **609** (2001) 387–409, [arXiv:hep-ph/0104016](https://arxiv.org/abs/hep-ph/0104016).
- [115] G. Degrassi, S. Di Vita, J. Elias-Miro, J. R. Espinosa, G. F. Giudice, G. Isidori, and A. Strumia, “Higgs mass and vacuum stability in the Standard Model at NNLO,” *JHEP* **08** (2012) 098, [arXiv:1205.6497 \[hep-ph\]](https://arxiv.org/abs/1205.6497).
- [116] J. Ellis, “Physics goals of the next century@ cern,” in *AIP Conference Proceedings*, vol. 542, pp. 267–292, American Institute of Physics. 2000.
- [117] “LHC-facts.” <http://www.lhc-facts.ch>.
- [118] “Weltmaschine- CERN und LHC.”
https://www.weltmaschine.de/cern_und_lhc/lhc/.
- [119] “LHC Design Report Vol.1: The LHC Main Ring.”
- [120] “LHC long term schedule .”
<https://lhc-commissioning.web.cern.ch/schedule/LHC-long-term.htm>.

- [121] “High-Luminosity Large Hadron Collider (HL-LHC) : Preliminary Design Report.”.
- [122] “LHC preformance tracking.” <https://bpt.web.cern.ch/lhc/>.
- [123] “Taking a look at the LHC.”
https://www.lhc-closer.de/taking_a_closer_look_at_lhc/0.luminosity.
- [124] “ATLAS Run 2 luminosity public results .” <https://twiki.cern.ch/twiki/bin/view/AtlasPublic/LuminosityPublicResults>.
- [125] “CMS luminosity public results .”
<https://twiki.cern.ch/twiki/bin/view/CMSPublic/LumiPublicResults>.
- [126] “ATLAS Run 2 luminosity public results .” <https://twiki.cern.ch/twiki/bin/view/AtlasPublic/LuminosityPublicResultsRun2>.
- [127] S. Fartoukh *et al.*, “LHC Configuration and Operational Scenario for Run 3,” tech. rep., CERN, Geneva, Nov, 2021. <https://cds.cern.ch/record/2790409>.
- [128] **CMS** Collaboration, A. M. Sirunyan *et al.*, “A measurement of the Higgs boson mass in the diphoton decay channel,” *Phys. Lett. B* **805** (2020) 135425, [arXiv:2002.06398 \[hep-ex\]](https://arxiv.org/abs/2002.06398).
- [129] **ATLAS** Collaboration, M. Aaboud *et al.*, “Measurement of the Higgs boson mass in the $H \rightarrow ZZ^* \rightarrow 4\ell$ and $H \rightarrow \gamma\gamma$ channels with $\sqrt{s} = 13$ TeV pp collisions using the ATLAS detector,” *Phys. Lett. B* **784** (2018) 345–366, [arXiv:1806.00242 \[hep-ex\]](https://arxiv.org/abs/1806.00242).
- [130] **ATLAS, CMS** Collaboration, G. Aad *et al.*, “Combined Measurement of the Higgs Boson Mass in pp Collisions at $\sqrt{s} = 7$ and 8 TeV with the ATLAS and CMS Experiments,” *Phys. Rev. Lett.* **114** (2015) 191803, [arXiv:1503.07589 \[hep-ex\]](https://arxiv.org/abs/1503.07589).
- [131] **CMS** Collaboration, A. M. Sirunyan *et al.*, “Measurements of properties of the Higgs boson decaying into the four-lepton final state in pp collisions at $\sqrt{s} = 13$ TeV,” *JHEP* **11** (2017) 047, [arXiv:1706.09936 \[hep-ex\]](https://arxiv.org/abs/1706.09936).
- [132] P. M. Aronow and B. T. Miller, *Foundations of Agnostic Statistics*. Cambridge University Press, 2019.
- [133] J. De Blas, G. Durieux, C. Grojean, J. Gu, and A. Paul, “On the future of Higgs, electroweak and diboson measurements at lepton colliders,” *JHEP* **12** (2019) 117, [arXiv:1907.04311 \[hep-ph\]](https://arxiv.org/abs/1907.04311).
- [134] S. Banerjee, R. S. Gupta, O. Ochoa-Valeriano, and M. Spannowsky, “High energy lepton colliders as the ultimate Higgs microscopes,” [arXiv:2109.14634 \[hep-ph\]](https://arxiv.org/abs/2109.14634).

- [135] **ATLAS** Collaboration, M. Aaboud *et al.*, “Constraints on off-shell Higgs boson production and the Higgs boson total width in $ZZ \rightarrow 4\ell$ and $ZZ \rightarrow 2\ell 2\nu$ final states with the ATLAS detector,” *Phys. Lett. B* **786** (2018) 223–244, [arXiv:1808.01191 \[hep-ex\]](https://arxiv.org/abs/1808.01191).
- [136] **CMS** Collaboration, A. M. Sirunyan *et al.*, “Measurements of the Higgs boson width and anomalous HVV couplings from on-shell and off-shell production in the four-lepton final state,” *Phys. Rev. D* **99** no. 11, (2019) 112003, [arXiv:1901.00174 \[hep-ex\]](https://arxiv.org/abs/1901.00174).
- [137] **ATLAS** Collaboration, G. Aad *et al.*, “Study of the spin and parity of the Higgs boson in diboson decays with the ATLAS detector,” *Eur. Phys. J. C* **75** no. 10, (2015) 476, [arXiv:1506.05669 \[hep-ex\]](https://arxiv.org/abs/1506.05669). [Erratum: Eur.Phys.J.C 76, 152 (2016)].
- [138] **CMS** Collaboration, V. Khachatryan *et al.*, “Constraints on the spin-parity and anomalous HVV couplings of the Higgs boson in proton collisions at 7 and 8 TeV,” *Phys. Rev. D* **92** no. 1, (2015) 012004, [arXiv:1411.3441 \[hep-ex\]](https://arxiv.org/abs/1411.3441).
- [139] **CMS** Collaboration, V. Khachatryan *et al.*, “Measurement of differential and integrated fiducial cross sections for Higgs boson production in the four-lepton decay channel in pp collisions at $\sqrt{s} = 7$ and 8 TeV,” *JHEP* **04** (2016) 005, [arXiv:1512.08377 \[hep-ex\]](https://arxiv.org/abs/1512.08377).
- [140] “Measurements of the total cross sections for Higgs boson production combining the $H \rightarrow \gamma\gamma$ and $H \rightarrow ZZ^* \rightarrow 4\ell$ decay channels at 7, 8 and 13 TeV center-of-mass energies with the ATLAS detector.”
- [141] **CMS** Collaboration, A. M. Sirunyan *et al.*, “Measurement and interpretation of differential cross sections for Higgs boson production at $\sqrt{s} = 13$ TeV,” *Phys. Lett. B* **792** (2019) 369–396, [arXiv:1812.06504 \[hep-ex\]](https://arxiv.org/abs/1812.06504).
- [142] **ATLAS** Collaboration, “Combined measurement of the total and differential cross sections in the $H \rightarrow \gamma\gamma$ and the $H \rightarrow ZZ^* \rightarrow 4\ell$ decay channels at $\sqrt{s} = 13$ TeV with the ATLAS detector.”
- [143] **ATLAS** Collaboration, “Measurements and interpretations of Higgs-boson fiducial cross sections in the diphoton decay channel using 139 fb^{-1} of pp collision data at $\sqrt{s} = 13$ TeV with the ATLAS detector.”
- [144] **CMS** Collaboration, “Measurements of properties of the Higgs boson in the four-lepton final state in proton-proton collisions at $\sqrt{s} = 13$ TeV.”
- [145] N. Berger *et al.*, “Simplified Template Cross Sections - Stage 1.1,” [arXiv:1906.02754 \[hep-ph\]](https://arxiv.org/abs/1906.02754).

- [146] **ATLAS** Collaboration, “A combination of measurements of Higgs boson production and decay using up to 139 fb^{-1} of proton–proton collision data at $\sqrt{s} = 13 \text{ TeV}$ collected with the ATLAS experiment,” Tech. Rep. ATLAS-CONF-2020-027, 2020.
- [147] **CMS** Collaboration, A. M. Sirunyan *et al.*, “Measurements of Higgs boson production cross sections and couplings in the diphoton decay channel at $\sqrt{s} = 13 \text{ TeV}$,” *JHEP* **07** (2021) 027, [arXiv:2103.06956 \[hep-ex\]](https://arxiv.org/abs/2103.06956).
- [148] **CMS Collaboration** Collaboration, “Sensitivity projections for Higgs boson properties measurements at the HL-LHC,” tech. rep., CERN, Geneva, 2018. <https://cds.cern.ch/record/2647699>.
- [149] **CMS** Collaboration, “Combined Higgs boson production and decay measurements with up to 137 fb^{-1} of proton-proton collision data at $\text{sqrt}s = 13 \text{ TeV}$,” Tech. Rep. CMS-PAS-HIG-19-005, 2020.
- [150] **CMS** Collaboration, “Measurement of Higgs boson production in association with a W or Z boson in the $H \rightarrow WW$ decay channel,” Tech. Rep. CMS-PAS-HIG-19-017, 2021.
- [151] L. Alasfar, J. de Blas, and R. Gröber, “Higgs probes of top quark contact interactions and their interplay with the Higgs self-coupling,” [arXiv:2202.02333 \[hep-ph\]](https://arxiv.org/abs/2202.02333).
- [152] **ATLAS** Collaboration, “Combined measurements of Higgs boson production and decay using up to 139 fb^{-1} of proton-proton collision data at $\sqrt{s} = 13 \text{ TeV}$ collected with the ATLAS experiment.”
- [153] H. Cooper, L. Hedges, and J. Valentine, *The handbook of research synthesis and meta-analysis 2nd edition*, pp. 1–615. Russell Sage Foundation, Dec., 2009.
- [154] **CMS** Collaboration, A. M. Sirunyan *et al.*, “Search for associated production of a Higgs boson and a single top quark in proton-proton collisions at $\sqrt{s} = 13 \text{ TeV}$,” *Phys. Rev. D* **99** no. 9, (2019) 092005, [arXiv:1811.09696 \[hep-ex\]](https://arxiv.org/abs/1811.09696).
- [155] **CMS** Collaboration, A. M. Sirunyan *et al.*, “Observation of Higgs boson decay to bottom quarks,” *Phys. Rev. Lett.* **121** no. 12, (2018) 121801, [arXiv:1808.08242 \[hep-ex\]](https://arxiv.org/abs/1808.08242).
- [156] **ATLAS** Collaboration, M. Aaboud *et al.*, “Observation of $H \rightarrow b\bar{b}$ decays and VH production with the ATLAS detector,” *Phys. Lett. B* **786** (2018) 59–86, [arXiv:1808.08238 \[hep-ex\]](https://arxiv.org/abs/1808.08238).
- [157] **ATLAS** Collaboration, M. Aaboud *et al.*, “Measurement of VH , $H \rightarrow b\bar{b}$ production as a function of the vector-boson transverse momentum in 13 TeV pp collisions with the ATLAS detector,” *JHEP* **05** (2019) 141, [arXiv:1903.04618 \[hep-ex\]](https://arxiv.org/abs/1903.04618).

- [158] **ATLAS** Collaboration, M. Aaboud *et al.*, “Cross-section measurements of the Higgs boson decaying into a pair of τ -leptons in proton-proton collisions at $\sqrt{s} = 13$ TeV with the ATLAS detector,” *Phys. Rev. D* **99** (2019) 072001, [arXiv:1811.08856 \[hep-ex\]](https://arxiv.org/abs/1811.08856).
- [159] **CMS** Collaboration, “Measurement of Higgs boson production and decay to the $\tau\tau$ final state.”
- [160] **ATLAS** Collaboration, G. Aad *et al.*, “A search for the dimuon decay of the Standard Model Higgs boson with the ATLAS detector,” *Phys. Lett. B* **812** (2021) 135980, [arXiv:2007.07830 \[hep-ex\]](https://arxiv.org/abs/2007.07830).
- [161] **CMS** Collaboration, A. M. Sirunyan *et al.*, “Evidence for Higgs boson decay to a pair of muons,” *JHEP* **01** (2021) 148, [arXiv:2009.04363 \[hep-ex\]](https://arxiv.org/abs/2009.04363).
- [162] **ATLAS** Collaboration, “Direct constraint on the Higgs-charm coupling from a search for Higgs boson decays to charm quarks with the ATLAS detector.”
- [163] **ATLAS** Collaboration, G. Aad *et al.*, “Direct constraint on the Higgs-charm coupling from a search for Higgs boson decays into charm quarks with the ATLAS detector,” [arXiv:2201.11428 \[hep-ex\]](https://arxiv.org/abs/2201.11428).
- [164] **CMS** Collaboration, A. M. Sirunyan *et al.*, “A search for the standard model Higgs boson decaying to charm quarks,” *JHEP* **03** (2020) 131, [arXiv:1912.01662 \[hep-ex\]](https://arxiv.org/abs/1912.01662).
- [165] **ATLAS** Collaboration, “Prospects for $H \rightarrow c\bar{c}$ using Charm Tagging with the ATLAS Experiment at the HL-LHC,” Tech. Rep. ATL-PHYS-PUB-2018-016, CERN, Geneva, Aug, 2018. <http://cds.cern.ch/record/2633635>.
- [166] **ATLAS** Collaboration, G. Aad *et al.*, “A search for the $Z\gamma$ decay mode of the Higgs boson in pp collisions at $\sqrt{s} = 13$ TeV with the ATLAS detector,” *Phys. Lett. B* **809** (2020) 135754, [arXiv:2005.05382 \[hep-ex\]](https://arxiv.org/abs/2005.05382).
- [167] S. Dawson, S. Dittmaier, and M. Spira, “Neutral Higgs boson pair production at hadron colliders: QCD corrections,” *Phys. Rev. D* **58** (1998) 115012, [arXiv:hep-ph/9805244](https://arxiv.org/abs/hep-ph/9805244).
- [168] A. Papaefstathiou and K. Sakurai, “Triple Higgs boson production at a 100 TeV proton-proton collider,” *JHEP* **02** (2016) 006, [arXiv:1508.06524 \[hep-ph\]](https://arxiv.org/abs/1508.06524).
- [169] S. Weinberg, “Phenomenological lagrangians,” *Physica A: Statistical Mechanics and its Applications* **96** no. 1, (1979) 327–340.
<https://www.sciencedirect.com/science/article/pii/0378437179902231>.
- [170] S. Weinberg, “Baryon- and lepton-nonconserving processes,” *Phys. Rev. Lett.* **43** (Nov, 1979) 1566–1570.
<https://link.aps.org/doi/10.1103/PhysRevLett.43.1566>.

- [171] L. Lehman, “Extending the Standard Model Effective Field Theory with the Complete Set of Dimension-7 Operators,” *Phys. Rev. D* **90** no. 12, (2014) 125023, [arXiv:1410.4193 \[hep-ph\]](https://arxiv.org/abs/1410.4193).
- [172] L. Lehman and A. Martin, “Low-derivative operators of the Standard Model effective field theory via Hilbert series methods,” *JHEP* **02** (2016) 081, [arXiv:1510.00372 \[hep-ph\]](https://arxiv.org/abs/1510.00372).
- [173] B. Henning, X. Lu, T. Melia, and H. Murayama, “2, 84, 30, 993, 560, 15456, 11962, 261485, ...: Higher dimension operators in the SM EFT,” *JHEP* **08** (2017) 016, [arXiv:1512.03433 \[hep-ph\]](https://arxiv.org/abs/1512.03433). [Erratum: JHEP 09, 019 (2019)].
- [174] J. A. Aguilar-Saavedra, “Effective four-fermion operators in top physics: A Roadmap,” *Nucl. Phys. B* **843** (2011) 638–672, [arXiv:1008.3562 \[hep-ph\]](https://arxiv.org/abs/1008.3562). [Erratum: Nucl.Phys.B 851, 443–444 (2011)].
- [175] W. Buchmüller and D. Wyler, “Effective lagrangian analysis of new interactions and flavour conservation,” *Nuclear Physics B* **268** no. 3, (1986) 621–653. <https://www.sciencedirect.com/science/article/pii/0550321386902622>.
- [176] K. Hagiwara, S. Ishihara, R. Szalapski, and D. Zeppenfeld, “Low-energy effects of new interactions in the electroweak boson sector,” *Phys. Rev. D* **48** (1993) 2182–2203.
- [177] E. E. Jenkins, A. V. Manohar, and M. Trott, “Renormalization Group Evolution of the Standard Model Dimension Six Operators I: Formalism and lambda Dependence,” *JHEP* **10** (2013) 087, [arXiv:1308.2627 \[hep-ph\]](https://arxiv.org/abs/1308.2627).
- [178] E. E. Jenkins, A. V. Manohar, and M. Trott, “Renormalization Group Evolution of the Standard Model Dimension Six Operators II: Yukawa Dependence,” *JHEP* **01** (2014) 035, [arXiv:1310.4838 \[hep-ph\]](https://arxiv.org/abs/1310.4838).
- [179] R. Alonso, E. E. Jenkins, A. V. Manohar, and M. Trott, “Renormalization Group Evolution of the Standard Model Dimension Six Operators III: Gauge Coupling Dependence and Phenomenology,” *JHEP* **04** (2014) 159, [arXiv:1312.2014 \[hep-ph\]](https://arxiv.org/abs/1312.2014).
- [180] M. Carena and H. Haber, “Higgs boson theory and phenomenology,” *Progress in Particle and Nuclear Physics* **50** no. 1, (2003) 63–152. <https://www.sciencedirect.com/science/article/pii/S0146641002001771>.
- [181] R. Contino, “The Higgs as a Composite Nambu-Goldstone Boson,” in *Theoretical Advanced Study Institute in Elementary Particle Physics: Physics of the Large and the Small*, pp. 235–306. 2011. [arXiv:1005.4269 \[hep-ph\]](https://arxiv.org/abs/1005.4269).
- [182] G. Panico and A. Wulzer, *The Composite Nambu-Goldstone Higgs*, vol. 913. Springer, 2016. [arXiv:1506.01961 \[hep-ph\]](https://arxiv.org/abs/1506.01961).

- [183] **ATLAS** Collaboration, “Methodology for EFT interpretation of Higgs boson Simplified Template Cross-section results in ATLAS,”.
- [184] **SMEFiT** Collaboration, J. J. Ethier, G. Magni, F. Maltoni, L. Mantani, E. R. Nocera, J. Rojo, E. Slade, E. Vryonidou, and C. Zhang, “Combined SMEFT interpretation of Higgs, diboson, and top quark data from the LHC,” *JHEP* **11** (2021) 089, [arXiv:2105.00006 \[hep-ph\]](https://arxiv.org/abs/2105.00006).
- [185] S. Dawson and P. P. Giardino, “Flavorful Electroweak Precision Observables in the Standard Model Effective Field Theory,” [arXiv:2201.09887 \[hep-ph\]](https://arxiv.org/abs/2201.09887).
- [186] G. Degrassi, P. Gambino, and P. P. Giardino, “The $m_W - m_Z$ interdependence in the Standard Model: a new scrutiny,” *JHEP* **05** (2015) 154, [arXiv:1411.7040 \[hep-ph\]](https://arxiv.org/abs/1411.7040).
- [187] G. D. Kribs, A. Maier, H. Rzehak, M. Spannowsky, and P. Waite, “Electroweak oblique parameters as a probe of the trilinear Higgs boson self-interaction,” *Phys. Rev. D* **95** no. 9, (2017) 093004, [arXiv:1702.07678 \[hep-ph\]](https://arxiv.org/abs/1702.07678).
- [188] S. Di Vita, C. Grojean, G. Panico, M. Riembau, and T. Vantalon, “A global view on the Higgs self-coupling,” *JHEP* **09** (2017) 069, [arXiv:1704.01953 \[hep-ph\]](https://arxiv.org/abs/1704.01953).
- [189] **ATLAS** Collaboration, “Constraints on the Higgs boson self-coupling from the combination of single-Higgs and double-Higgs production analyses performed with the ATLAS experiment,” Tech. Rep. ATLAS-CONF-2019-049, 2019.
- [190] R. Grober, M. Mühlleitner, and M. Spira, “Higgs Pair Production at NLO QCD for CP-violating Higgs Sectors,” *Nucl. Phys. B* **925** (2017) 1–27, [arXiv:1705.05314 \[hep-ph\]](https://arxiv.org/abs/1705.05314).
- [191] J. Gasser and H. Leutwyler, “Chiral perturbation theory to one loop,” *Annals of Physics* **158** no. 1, (1984) 142–210.
<https://www.sciencedirect.com/science/article/pii/0003491684902422>.
- [192] J. Gasser and H. Leutwyler, “Chiral perturbation theory: Expansions in the mass of the strange quark,” *Nuclear Physics B* **250** no. 1, (1985) 465–516.
<https://www.sciencedirect.com/science/article/pii/0550321385904924>.
- [193] G. Buchalla, O. Catà, and C. Krause, “Complete Electroweak Chiral Lagrangian with a Light Higgs at NLO,” *Nucl. Phys. B* **880** (2014) 552–573, [arXiv:1307.5017 \[hep-ph\]](https://arxiv.org/abs/1307.5017). [Erratum: Nucl.Phys.B 913, 475–478 (2016)].
- [194] G. Buchalla, O. Cata, A. Celis, and C. Krause, “Note on Anomalous Higgs-Boson Couplings in Effective Field Theory,” *Phys. Lett. B* **750** (2015) 298–301, [arXiv:1504.01707 \[hep-ph\]](https://arxiv.org/abs/1504.01707).
- [195] **LHC Higgs Cross Section Working Group** Collaboration, D. de Florian *et al.*, “Handbook of LHC Higgs Cross Sections: 4. Deciphering the Nature of the Higgs Sector,” [arXiv:1610.07922 \[hep-ph\]](https://arxiv.org/abs/1610.07922).

- [196] G. Buchalla, M. Capozi, A. Celis, G. Heinrich, and L. Scyboz, “Higgs boson pair production in non-linear Effective Field Theory with full m_t -dependence at NLO QCD,” *JHEP* **09** (2018) 057, [arXiv:1806.05162 \[hep-ph\]](https://arxiv.org/abs/1806.05162).
- [197] M. Capozi and G. Heinrich, “Exploring anomalous couplings in Higgs boson pair production through shape analysis,” *JHEP* **03** (2020) 091, [arXiv:1908.08923 \[hep-ph\]](https://arxiv.org/abs/1908.08923).
- [198] D. de Florian, I. Fabre, G. Heinrich, J. Mazzitelli, and L. Scyboz, “Anomalous couplings in Higgs-boson pair production at approximate NNLO QCD,” [arXiv:2106.14050 \[hep-ph\]](https://arxiv.org/abs/2106.14050).
- [199] G. Heinrich, S. P. Jones, M. Kerner, and L. Scyboz, “A non-linear EFT description of $gg \rightarrow HH$ at NLO interfaced to POWHEG,” *JHEP* **10** (2020) 021, [arXiv:2006.16877 \[hep-ph\]](https://arxiv.org/abs/2006.16877).
- [200] K. Agashe, R. Contino, and A. Pomarol, “The minimal composite higgs model,” *Nuclear Physics B* **719** no. 1, (2005) 165–187.
<https://www.sciencedirect.com/science/article/pii/S0550321305003445>.
- [201] W. D. Goldberger, B. Grinstein, and W. Skiba, “Distinguishing the higgs boson from the dilaton at the large hadron collider,” *Phys. Rev. Lett.* **100** (Mar, 2008) 111802. <https://link.aps.org/doi/10.1103/PhysRevLett.100.111802>.
- [202] K. Habaa, S. Matsuzaki, and K. Yamawaki, “Holographic Techni-dilaton, or Conformal Higgs,” in *International Workshop on Strong Coupling Gauge Theories in LHC Era: SCGT 09*, pp. 401–403. 2011. [arXiv:1003.2841 \[hep-ph\]](https://arxiv.org/abs/1003.2841).
- [203] A. Delgado, K. Lane, and A. Martin, “A Light Scalar in Low-Scale Technicolor,” *Phys. Lett. B* **696** (2011) 482–486, [arXiv:1011.0745 \[hep-ph\]](https://arxiv.org/abs/1011.0745).
- [204] J. Galloway, M. A. Luty, Y. Tsai, and Y. Zhao, “Induced Electroweak Symmetry Breaking and Supersymmetric Naturalness,” *Phys. Rev. D* **89** no. 7, (2014) 075003, [arXiv:1306.6354 \[hep-ph\]](https://arxiv.org/abs/1306.6354).
- [205] S. Chang, J. Galloway, M. Luty, E. Salvioni, and Y. Tsai, “Phenomenology of Induced Electroweak Symmetry Breaking,” *JHEP* **03** (2015) 017, [arXiv:1411.6023 \[hep-ph\]](https://arxiv.org/abs/1411.6023).
- [206] C. Hartmann and M. Trott, “Higgs Decay to Two Photons at One Loop in the Standard Model Effective Field Theory,” *Phys. Rev. Lett.* **115** no. 19, (2015) 191801, [arXiv:1507.03568 \[hep-ph\]](https://arxiv.org/abs/1507.03568).
- [207] A. Falkowski, B. Fuks, K. Mawatari, K. Mimasu, F. Riva, and V. Sanz, “Rosetta: an operator basis translator for Standard Model effective field theory,” *Eur. Phys. J. C* **75** no. 12, (2015) 583, [arXiv:1508.05895 \[hep-ph\]](https://arxiv.org/abs/1508.05895).

- [208] M. Gonzalez-Alonso, A. Greljo, G. Isidori, and D. Marzocca, “Pseudo-observables in Higgs decays,” *Eur. Phys. J. C* **75** (2015) 128, [arXiv:1412.6038 \[hep-ph\]](#).
- [209] S. Di Vita, G. Durieux, C. Grojean, J. Gu, Z. Liu, G. Panico, M. Riembau, and T. Vantalon, “A global view on the Higgs self-coupling at lepton colliders,” *JHEP* **02** (2018) 178, [arXiv:1711.03978 \[hep-ph\]](#).
- [210] M. Bonetti, K. Melnikov, and L. Tancredi, “Higher order corrections to mixed QCD-EW contributions to Higgs boson production in gluon fusion,” *Phys. Rev. D* **97** no. 5, (2018) 056017, [arXiv:1801.10403 \[hep-ph\]](#). [Erratum: *Phys. Rev. D* 97, 099906 (2018)].
- [211] X. Chen, T. Gehrmann, E. W. N. Glover, A. Huss, B. Mistlberger, and A. Pelloni, “Fully Differential Higgs Boson Production to Third Order in QCD,” *Phys. Rev. Lett.* **127** no. 7, (2021) 072002, [arXiv:2102.07607 \[hep-ph\]](#).
- [212] G. Billis, B. Dehnadi, M. A. Ebert, J. K. L. Michel, and F. J. Tackmann, “Higgs pT Spectrum and Total Cross Section with Fiducial Cuts at Third Resummed and Fixed Order in QCD,” *Phys. Rev. Lett.* **127** no. 7, (2021) 072001, [arXiv:2102.08039 \[hep-ph\]](#).
- [213] M. Bonetti, K. Melnikov, and L. Tancredi, “Three-loop mixed QCD-electroweak corrections to Higgs boson gluon fusion,” *Phys. Rev. D* **97** no. 3, (2018) 034004, [arXiv:1711.11113 \[hep-ph\]](#).
- [214] M. Bonetti, E. Panzer, V. A. Smirnov, and L. Tancredi, “Two-loop mixed QCD-EW corrections to $gg \rightarrow Hg$,” *JHEP* **11** (2020) 045, [arXiv:2007.09813 \[hep-ph\]](#).
- [215] M. Bechetti, R. Bonciani, V. Del Duca, V. Hirschi, F. Moriello, and A. Schweitzer, “Next-to-leading order corrections to light-quark mixed QCD-EW contributions to Higgs boson production,” *Phys. Rev. D* **103** no. 5, (2021) 054037, [arXiv:2010.09451 \[hep-ph\]](#).
- [216] M. L. Czakon and M. Niggetiedt, “Exact quark-mass dependence of the Higgs-gluon form factor at three loops in QCD,” *JHEP* **05** (2020) 149, [arXiv:2001.03008 \[hep-ph\]](#).
- [217] M. Czakon, R. V. Harlander, J. Klappert, and M. Niggetiedt, “Exact Top-Quark Mass Dependence in Hadronic Higgs Production,” *Phys. Rev. Lett.* **127** no. 16, (2021) 162002, [arXiv:2105.04436 \[hep-ph\]](#).
- [218] F. Maltoni, E. Vryonidou, and M. Zaro, “Top-quark mass effects in double and triple Higgs production in gluon-gluon fusion at NLO,” *JHEP* **11** (2014) 079, [arXiv:1408.6542 \[hep-ph\]](#).

- [219] K. Kudashkin, K. Melnikov, and C. Wever, “Two-loop amplitudes for processes $gg \rightarrow Hg$, $qg \rightarrow Hq$ and $q\bar{q} \rightarrow Hg$ at large Higgs transverse momentum,” *JHEP* **02** (2018) 135, [arXiv:1712.06549 \[hep-ph\]](https://arxiv.org/abs/1712.06549).
- [220] J. M. Lindert, K. Kudashkin, K. Melnikov, and C. Wever, “Higgs bosons with large transverse momentum at the LHC,” *Phys. Lett. B* **782** (2018) 210–214, [arXiv:1801.08226 \[hep-ph\]](https://arxiv.org/abs/1801.08226).
- [221] S. P. Jones, M. Kerner, and G. Luisoni, “Next-to-leading-order qcd corrections to higgs boson plus jet production with full top-quark mass dependence,” *Phys. Rev. Lett.* **120** (Apr, 2018) 162001.
<https://link.aps.org/doi/10.1103/PhysRevLett.120.162001>.
- [222] V. Hankele, G. Klämke, D. Zeppenfeld, and T. Figy, “Anomalous higgs boson couplings in vector boson fusion at the cern lhc,” *Physical Review D* **74** no. 9, (2006) 095001.
- [223] T. Han, G. Valencia, and S. Willenbrock, “Structure function approach to vector boson scattering in p p collisions,” *Phys. Rev. Lett.* **69** (1992) 3274–3277, [arXiv:hep-ph/9206246](https://arxiv.org/abs/hep-ph/9206246).
- [224] T. Figy, C. Oleari, and D. Zeppenfeld, “Next-to-leading order jet distributions for Higgs boson production via weak boson fusion,” *Phys. Rev. D* **68** (2003) 073005, [arXiv:hep-ph/0306109](https://arxiv.org/abs/hep-ph/0306109).
- [225] E. L. Berger and J. M. Campbell, “Higgs boson production in weak boson fusion at next-to-leading order,” *Phys. Rev. D* **70** (2004) 073011, [arXiv:hep-ph/0403194](https://arxiv.org/abs/hep-ph/0403194).
- [226] M. Gomez-Bock, M. Mondragon, M. Muhlleitner, M. Spira, and P. M. Zerwas, “Concepts of Electroweak Symmetry Breaking and Higgs Physics,” in *4th CERN-CLAF School of High-Energy Physics*, pp. 177–238. 12, 2007. [arXiv:0712.2419 \[hep-ph\]](https://arxiv.org/abs/0712.2419).
- [227] P. Bolzoni, F. Maltoni, S.-O. Moch, and M. Zaro, “Higgs production via vector-boson fusion at NNLO in QCD,” *Phys. Rev. Lett.* **105** (2010) 011801, [arXiv:1003.4451 \[hep-ph\]](https://arxiv.org/abs/1003.4451).
- [228] A. Denner, S. Dittmaier, S. Kallweit, and A. Mück, “HAWK 2.0: A Monte Carlo program for Higgs production in vector-boson fusion and Higgs strahlung at hadron colliders,” *Comput. Phys. Commun.* **195** (2015) 161–171, [arXiv:1412.5390 \[hep-ph\]](https://arxiv.org/abs/1412.5390).
- [229] M. Ciccolini, A. Denner, and S. Dittmaier, “Strong and electroweak corrections to the production of Higgs + 2jets via weak interactions at the LHC,” *Phys. Rev. Lett.* **99** (2007) 161803, [arXiv:0707.0381 \[hep-ph\]](https://arxiv.org/abs/0707.0381).

Bibliography

- [230] A. Denner, S. Dittmaier, S. Kallweit, and A. Muck, “Electroweak corrections to Higgs-strahlung off W/Z bosons at the Tevatron and the LHC with HAWK,” *JHEP* **03** (2012) 075, [arXiv:1112.5142 \[hep-ph\]](https://arxiv.org/abs/1112.5142).
- [231] A. Denner, S. Dittmaier, and J.-N. Lang, “Renormalization of mixing angles,” *JHEP* **11** (2018) 104, [arXiv:1808.03466 \[hep-ph\]](https://arxiv.org/abs/1808.03466).
- [232] T. Han and S. Willenbrock, “QCD correction to the $p\ p \rightarrow W\ H$ and $Z\ H$ total cross-sections,” *Phys. Lett. B* **273** (1991) 167–172.
- [233] O. Brein, A. Djouadi, and R. Harlander, “NNLO QCD corrections to the Higgs-strahlung processes at hadron colliders,” *Phys. Lett. B* **579** (2004) 149–156, [arXiv:hep-ph/0307206](https://arxiv.org/abs/hep-ph/0307206).
- [234] S. Amoroso *et al.*, “Les Houches 2019: Physics at TeV Colliders: Standard Model Working Group Report,” in *11th Les Houches Workshop on Physics at TeV Colliders: PhysTeV Les Houches*. 3, 2020. [arXiv:2003.01700 \[hep-ph\]](https://arxiv.org/abs/2003.01700).
- [235] M. Cepeda *et al.*, “Report from Working Group 2: Higgs Physics at the HL-LHC and HE-LHC,” *CERN Yellow Rep. Monogr.* **7** (2019) 221–584, [arXiv:1902.00134 \[hep-ph\]](https://arxiv.org/abs/1902.00134).
- [236] C. Englert, M. McCullough, and M. Spannowsky, “Gluon-initiated associated production boosts Higgs physics,” *Phys. Rev. D* **89** no. 1, (2014) 013013, [arXiv:1310.4828 \[hep-ph\]](https://arxiv.org/abs/1310.4828).
- [237] C. Englert, R. Rosenfeld, M. Spannowsky, and A. Tonero, “New physics and signal-background interference in associated $pp \rightarrow HZ$ production,” *EPL* **114** no. 3, (2016) 31001, [arXiv:1603.05304 \[hep-ph\]](https://arxiv.org/abs/1603.05304).
- [238] B. A. Kniehl, “Associated Production of Higgs and Z Bosons From Gluon Fusion in Hadron Collisions,” *Phys. Rev. D* **42** (1990) 2253–2258.
- [239] D. A. Dicus and C. Kao, “Higgs Boson - Z^0 Production From Gluon Fusion,” *Phys. Rev. D* **38** (1988) 1008. [Erratum: Phys.Rev.D 42, 2412 (1990)].
- [240] L. Altenkamp, S. Dittmaier, R. V. Harlander, H. Rzehak, and T. J. Zirke, “Gluon-induced Higgs-strahlung at next-to-leading order QCD,” *JHEP* **02** (2013) 078, [arXiv:1211.5015 \[hep-ph\]](https://arxiv.org/abs/1211.5015).
- [241] R. V. Harlander, A. Kulesza, V. Theeuwes, and T. Zirke, “Soft gluon resummation for gluon-induced Higgs Strahlung,” *JHEP* **11** (2014) 082, [arXiv:1410.0217 \[hep-ph\]](https://arxiv.org/abs/1410.0217).
- [242] A. Hasselhuhn, T. Luthe, and M. Steinhauser, “On top quark mass effects to $gg \rightarrow ZH$ at NLO,” *JHEP* **01** (2017) 073, [arXiv:1611.05881 \[hep-ph\]](https://arxiv.org/abs/1611.05881).

- [243] R. Harlander, J. Klappert, C. Pandini, and A. Papaefstathiou, “Exploiting the WH/ZH symmetry in the search for New Physics,” *Eur. Phys. J. C* **78** no. 9, (2018) 760, [arXiv:1804.02299 \[hep-ph\]](https://arxiv.org/abs/1804.02299).
- [244] B. Hespel, F. Maltoni, and E. Vryonidou, “Higgs and Z boson associated production via gluon fusion in the SM and the 2HDM,” *JHEP* **06** (2015) 065, [arXiv:1503.01656 \[hep-ph\]](https://arxiv.org/abs/1503.01656).
- [245] J. Davies, G. Mishima, and M. Steinhauser, “Virtual corrections to $gg \rightarrow ZH$ in the high-energy and large- m_t limits,” [arXiv:2011.12314 \[hep-ph\]](https://arxiv.org/abs/2011.12314).
- [246] L. Chen, G. Heinrich, S. P. Jones, M. Kerner, J. Klappert, and J. Schlenk, “ZH production in gluon fusion: two-loop amplitudes with full top quark mass dependence,” [arXiv:2011.12325 \[hep-ph\]](https://arxiv.org/abs/2011.12325).
- [247] L. Alasfar, G. Degrassi, P. P. Giardino, R. Gröber, and M. Vitti, “Virtual corrections to $gg \rightarrow ZH$ via a transverse momentum expansion,” *JHEP* **05** (2021) 168, [arXiv:2103.06225 \[hep-ph\]](https://arxiv.org/abs/2103.06225).
- [248] A. Broggio, A. Ferroglio, R. Frederix, D. Pagani, B. D. Pecjak, and I. Tsinikos, “Top-quark pair hadroproduction in association with a heavy boson at NLO+NNLL including EW corrections,” *JHEP* **08** (2019) 039, [arXiv:1907.04343 \[hep-ph\]](https://arxiv.org/abs/1907.04343).
- [249] A. Kulesza, L. Motyka, D. Schwartländer, T. Stebel, and V. Theeuwes, “Associated top quark pair production with a heavy boson: differential cross sections at NLO+NNLL accuracy,” *Eur. Phys. J. C* **80** no. 5, (2020) 428, [arXiv:2001.03031 \[hep-ph\]](https://arxiv.org/abs/2001.03031).
- [250] G. Bevilacqua, H.-Y. Bi, H. B. Hartanto, M. Kraus, and M. Worek, “The simplest of them all: $t\bar{t}W^\pm$ at NLO accuracy in QCD,” *JHEP* **08** (2020) 043, [arXiv:2005.09427 \[hep-ph\]](https://arxiv.org/abs/2005.09427).
- [251] A. Denner and G. Pelliccioli, “NLO QCD corrections to off-shell $t\bar{t}W^+$ production at the LHC,” *JHEP* **11** (2020) 069, [arXiv:2007.12089 \[hep-ph\]](https://arxiv.org/abs/2007.12089).
- [252] G. Bevilacqua, H.-Y. Bi, H. B. Hartanto, M. Kraus, J. Nasufi, and M. Worek, “NLO QCD corrections to off-shell $t\bar{t}W^\pm$ production at the LHC: correlations and asymmetries,” *Eur. Phys. J. C* **81** no. 7, (2021) 675, [arXiv:2012.01363 \[hep-ph\]](https://arxiv.org/abs/2012.01363).
- [253] A. Denner and G. Pelliccioli, “Combined NLO EW and QCD corrections to off-shell $t\bar{t}W$ production at the LHC,” *Eur. Phys. J. C* **81** no. 4, (2021) 354, [arXiv:2102.03246 \[hep-ph\]](https://arxiv.org/abs/2102.03246).
- [254] F. F. Cordero, M. Kraus, and L. Reina, “Top-quark pair production in association with a W^\pm gauge boson in the POWHEG-BOX,” *Phys. Rev. D* **103** no. 9, (2021) 094014, [arXiv:2101.11808 \[hep-ph\]](https://arxiv.org/abs/2101.11808).

- [255] G. Bevilacqua, H. Y. Bi, F. Febres Cordero, H. B. Hartanto, M. Kraus, J. Nasufi, L. Reina, and M. Worek, “Modeling uncertainties of $t\bar{t}W^\pm$ multilepton signatures,” *Phys. Rev. D* **105** no. 1, (2022) 014018, [arXiv:2109.15181 \[hep-ph\]](https://arxiv.org/abs/2109.15181).
- [256] A. Denner, J.-N. Lang, and M. Pellen, “Full NLO QCD corrections to off-shell $t\bar{t}\text{--}bb^-$ production,” *Phys. Rev. D* **104** no. 5, (2021) 056018, [arXiv:2008.00918 \[hep-ph\]](https://arxiv.org/abs/2008.00918).
- [257] G. Bevilacqua, H.-Y. Bi, H. B. Hartanto, M. Kraus, M. Lupattelli, and M. Worek, “ $t\bar{t}b\bar{b}$ at the LHC: on the size of corrections and b-jet definitions,” *JHEP* **08** (2021) 008, [arXiv:2105.08404 \[hep-ph\]](https://arxiv.org/abs/2105.08404).
- [258] A. Denner, J.-N. Lang, M. Pellen, and S. Uccirati, “NLO QCD + electroweak predictions for off-shell ttH production at the LHC,” in *12th International Workshop on Top Quark Physics*. 12, 2019. [arXiv:1912.08493 \[hep-ph\]](https://arxiv.org/abs/1912.08493).
- [259] F. Maltoni, E. Vryonidou, and C. Zhang, “Higgs production in association with a top-antitop pair in the Standard Model Effective Field Theory at NLO in QCD,” *JHEP* **10** (2016) 123, [arXiv:1607.05330 \[hep-ph\]](https://arxiv.org/abs/1607.05330).
- [260] F. Dulat, A. Lazopoulos, and B. Mistlberger, “iHixs 2 — Inclusive Higgs cross sections,” *Comput. Phys. Commun.* **233** (2018) 243–260, [arXiv:1802.00827 \[hep-ph\]](https://arxiv.org/abs/1802.00827).
- [261] S. Alioli, P. Nason, C. Oleari, and E. Re, “NLO Higgs boson production via gluon fusion matched with shower in POWHEG,” *JHEP* **04** (2009) 002, [arXiv:0812.0578 \[hep-ph\]](https://arxiv.org/abs/0812.0578).
- [262] P. Nason and C. Oleari, “NLO Higgs boson production via vector-boson fusion matched with shower in POWHEG,” *JHEP* **02** (2010) 037, [arXiv:0911.5299 \[hep-ph\]](https://arxiv.org/abs/0911.5299).
- [263] E. Bagnaschi, G. Degrassi, P. Slavich, and A. Vicini, “Higgs production via gluon fusion in the POWHEG approach in the SM and in the MSSM,” *JHEP* **02** (2012) 088, [arXiv:1111.2854 \[hep-ph\]](https://arxiv.org/abs/1111.2854).
- [264] J. M. Campbell, R. K. Ellis, R. Frederix, P. Nason, C. Oleari, and C. Williams, “NLO Higgs Boson Production Plus One and Two Jets Using the POWHEG BOX, MadGraph4 and MCFM,” *JHEP* **07** (2012) 092, [arXiv:1202.5475 \[hep-ph\]](https://arxiv.org/abs/1202.5475).
- [265] G. Luisoni, P. Nason, C. Oleari, and F. Tramontano, “ $HW^\pm/\text{HZ} + 0$ and 1 jet at NLO with the POWHEG BOX interfaced to GoSam and their merging within MiNLO,” *JHEP* **10** (2013) 083, [arXiv:1306.2542 \[hep-ph\]](https://arxiv.org/abs/1306.2542).

- [266] B. Jäger, F. Schissler, and D. Zeppenfeld, “Parton-shower effects on Higgs boson production via vector-boson fusion in association with three jets,” *JHEP* **07** (2014) 125, [arXiv:1405.6950 \[hep-ph\]](https://arxiv.org/abs/1405.6950).
- [267] H. B. Hartanto, B. Jager, L. Reina, and D. Wackerlo, “Higgs boson production in association with top quarks in the POWHEG BOX,” *Phys. Rev. D* **91** no. 9, (2015) 094003, [arXiv:1501.04498 \[hep-ph\]](https://arxiv.org/abs/1501.04498).
- [268] J. Alwall, R. Frederix, S. Frixione, V. Hirschi, F. Maltoni, O. Mattelaer, H. S. Shao, T. Stelzer, P. Torrielli, and M. Zaro, “The automated computation of tree-level and next-to-leading order differential cross sections, and their matching to parton shower simulations,” *JHEP* **07** (2014) 079, [arXiv:1405.0301 \[hep-ph\]](https://arxiv.org/abs/1405.0301).
- [269] “Higgs corss-sections working group.” <https://twiki.cern.ch/twiki/bin/view/LHCPhysics/LHCHWG?redirectedfrom=LHCPhysics.LHCHXSWG>.
- [270] C. Degrande, G. Durieux, F. Maltoni, K. Mimasu, E. Vryonidou, and C. Zhang, “Automated one-loop computations in the standard model effective field theory,” *Phys. Rev. D* **103** no. 9, (2021) 096024, [arXiv:2008.11743 \[hep-ph\]](https://arxiv.org/abs/2008.11743).
- [271] ATLAS Collaboration, M. Aaboud *et al.*, “Observation of $H \rightarrow b\bar{b}$ decays and VH production with the ATLAS detector,” *Phys. Lett. B* **786** (2018) 59–86, [arXiv:1808.08238 \[hep-ex\]](https://arxiv.org/abs/1808.08238).
- [272] CMS Collaboration, A. M. Sirunyan *et al.*, “Observation of Higgs boson decay to bottom quarks,” *Phys. Rev. Lett.* **121** no. 12, (2018) 121801, [arXiv:1808.08242 \[hep-ex\]](https://arxiv.org/abs/1808.08242).
- [273] R. V. Harlander, S. Liebler, and T. Zirke, “Higgs Strahlung at the Large Hadron Collider in the 2-Higgs-Doublet Model,” *JHEP* **02** (2014) 023, [arXiv:1307.8122 \[hep-ph\]](https://arxiv.org/abs/1307.8122).
- [274] L. Bellafronte, G. Degrassi, P. P. Giardino, R. Gröber, and M. Vitti, “Gluon Fusion Production at NLO: Merging the Transverse Momentum and the High-Energy Expansions,” [arXiv:2202.12157 \[hep-ph\]](https://arxiv.org/abs/2202.12157).
- [275] W. H. Furry, “A symmetry theorem in the positron theory,” *Phys. Rev.* **51** (Jan, 1937) 125–129. <https://link.aps.org/doi/10.1103/PhysRev.51.125>.
- [276] L. D. Landau, “On the angular momentum of a system of two photons,” *Dokl. Akad. Nauk SSSR* **60** no. 2, (1948) 207–209.
- [277] C.-N. Yang, “Selection Rules for the Dematerialization of a Particle Into Two Photons,” *Phys. Rev.* **77** (1950) 242–245.
- [278] G. Passarino and M. J. G. Veltman, “One Loop corrections for e^+e^- annihilation into $\mu^+\mu^-$ in the Weinberg Model,” *Nucl. Phys.* **B160** (1979) 151.

- [279] S. Larin, “The Renormalization of the axial anomaly in dimensional regularization,” *Phys. Lett. B* **303** (1993) 113–118, [arXiv:hep-ph/9302240](#).
- [280] M. Spira, A. Djouadi, D. Graudenz, and P. M. Zerwas, “Higgs boson production at the LHC,” *Nucl. Phys. B* **453** (1995) 17–82, [arXiv:hep-ph/9504378](#).
- [281] U. Aglietti, R. Bonciani, G. Degrassi, and A. Vicini, “Analytic Results for Virtual QCD Corrections to Higgs Production and Decay,” *JHEP* **01** (2007) 021, [arXiv:hep-ph/0611266](#).
- [282] T. Hahn, “Generating Feynman diagrams and amplitudes with FeynArts 3,” *Comput. Phys. Commun.* **140** (2001) 418–431, [arXiv:hep-ph/0012260](#).
- [283] R. Mertig, M. Bohm, and A. Denner, “FEYN CALC: Computer algebraic calculation of Feynman amplitudes,” *Comput. Phys. Commun.* **64** (1991) 345–359.
- [284] V. Shtabovenko, R. Mertig, and F. Orellana, “New Developments in FeynCalc 9.0,” *Comput. Phys. Commun.* **207** (2016) 432–444, [arXiv:1601.01167 \[hep-ph\]](#).
- [285] H. H. Patel, “Package-X 2.0: A Mathematica package for the analytic calculation of one-loop integrals,” *Comput. Phys. Commun.* **218** (2017) 66–70, [arXiv:1612.00009 \[hep-ph\]](#).
- [286] P. Maierhöfer, J. Usovitsch, and P. Uwer, “Kira—A Feynman integral reduction program,” *Comput. Phys. Commun.* **230** (2018) 99–112, [arXiv:1705.05610 \[hep-ph\]](#).
- [287] R. Bonciani, P. Mastrolia, and E. Remiddi, “Master integrals for the two loop QCD virtual corrections to the forward backward asymmetry,” *Nucl. Phys. B* **690** (2004) 138–176, [arXiv:hep-ph/0311145](#).
- [288] S. Borowka and G. Heinrich, “Massive non-planar two-loop four-point integrals with SecDec 2.1,” *Comput. Phys. Commun.* **184** (2013) 2552–2561, [arXiv:1303.1157 \[hep-ph\]](#).
- [289] S. Borowka, G. Heinrich, S. P. Jones, M. Kerner, J. Schlenk, and T. Zirke, “SecDec-3.0: numerical evaluation of multi-scale integrals beyond one loop,” *Comput. Phys. Commun.* **196** (2015) 470–491, [arXiv:1502.06595 \[hep-ph\]](#).
- [290] A. V. Smirnov, “FIRE5: a C++ implementation of Feynman Integral REduction,” *Comput. Phys. Commun.* **189** (2015) 182–191, [arXiv:1408.2372 \[hep-ph\]](#).
- [291] R. N. Lee, “LiteRed 1.4: a powerful tool for reduction of multiloop integrals,” *J. Phys. Conf. Ser.* **523** (2014) 012059, [arXiv:1310.1145 \[hep-ph\]](#).

- [292] A. von Manteuffel and L. Tancredi, “A non-planar two-loop three-point function beyond multiple polylogarithms,” *JHEP* **06** (2017) 127, [arXiv:1701.05905 \[hep-ph\]](#).
- [293] R. Bonciani, G. Degrassi, P. P. Giardino, and R. Gröber, “A Numerical Routine for the Crossed Vertex Diagram with a Massive-Particle Loop,” *Comput. Phys. Commun.* **241** (2019) 122–131, [arXiv:1812.02698 \[hep-ph\]](#).
- [294] L. Naterop, A. Signer, and Y. Ulrich, “handyG —Rapid numerical evaluation of generalised polylogarithms in Fortran,” *Comput. Phys. Commun.* **253** (2020) 107165, [arXiv:1909.01656 \[hep-ph\]](#).
- [295] S. Buehler and C. Duhr, “CHAPLIN - Complex Harmonic Polylogarithms in Fortran,” *Comput. Phys. Commun.* **185** (2014) 2703–2713, [arXiv:1106.5739 \[hep-ph\]](#).
- [296] S. Borowka, G. Heinrich, S. Jahn, S. P. Jones, M. Kerner, J. Schlenk, and T. Zirke, “pySecDec: a toolbox for the numerical evaluation of multi-scale integrals,” *Comput. Phys. Commun.* **222** (2018) 313–326, [arXiv:1703.09692 \[hep-ph\]](#).
- [297] S. Borowka, G. Heinrich, S. Jahn, S. P. Jones, M. Kerner, and J. Schlenk, “A GPU compatible quasi-Monte Carlo integrator interfaced to pySecDec,” *Comput. Phys. Commun.* **240** (2019) 120–137, [arXiv:1811.11720 \[physics.comp-ph\]](#).
- [298] R. Frederix, D. Pagani, and M. Zaro, “Large NLO corrections in $t\bar{t}W^\pm$ and $t\bar{t}t\bar{t}$ hadroproduction from supposedly subleading EW contributions,” *JHEP* **02** (2018) 031, [arXiv:1711.02116 \[hep-ph\]](#).
- [299] CMS Collaboration, A. M. Sirunyan *et al.*, “Search for the production of four top quarks in the single-lepton and opposite-sign dilepton final states in proton-proton collisions at $\sqrt{s} = 13$ TeV,” *JHEP* **11** (2019) 082, [arXiv:1906.02805 \[hep-ex\]](#).
- [300] ATLAS Collaboration, G. Aad *et al.*, “Evidence for $t\bar{t}t\bar{t}$ production in the multilepton final state in proton–proton collisions at $\sqrt{s} = 13$ TeV with the ATLAS detector,” *Eur. Phys. J. C* **80** no. 11, (2020) 1085, [arXiv:2007.14858 \[hep-ex\]](#).
- [301] CMS Collaboration, A. M. Sirunyan *et al.*, “Measurement of the cross section for $t\bar{t}$ production with additional jets and b jets in pp collisions at $\sqrt{s} = 13$ TeV,” *JHEP* **07** (2020) 125, [arXiv:2003.06467 \[hep-ex\]](#).
- [302] ATLAS Collaboration, “Measurements of fiducial and differential cross-sections of $t\bar{t}$ production with additional heavy-flavour jets in proton-proton collisions at $\sqrt{s} = 13$ TeV with the ATLAS detector,” Tech. Rep. ATLAS-CONF-2018-029, 2018.

- [303] J. D'Hondt, A. Mariotti, K. Mimasu, S. Moortgat, and C. Zhang, “Learning to pinpoint effective operators at the LHC: a study of the $t\bar{t}b\bar{b}$ signature,” *JHEP* **11** (2018) 131, [arXiv:1807.02130 \[hep-ph\]](https://arxiv.org/abs/1807.02130).
- [304] N. P. Hartland, F. Maltoni, E. R. Nocera, J. Rojo, E. Slade, E. Vryonidou, and C. Zhang, “A Monte Carlo global analysis of the Standard Model Effective Field Theory: the top quark sector,” *JHEP* **04** (2019) 100, [arXiv:1901.05965 \[hep-ph\]](https://arxiv.org/abs/1901.05965).
- [305] A. Dedes, W. Materkowska, M. Paraskevas, J. Rosiek, and K. Suxho, “Feynman rules for the Standard Model Effective Field Theory in R_ξ -gauges,” *JHEP* **06** (2017) 143, [arXiv:1704.03888 \[hep-ph\]](https://arxiv.org/abs/1704.03888).
- [306] H. Patel, “Package-X: A Mathematica package for the analytic calculation of one-loop integrals,” *Comput. Phys. Commun.* **197** (2015) 276–290, [arXiv:1503.01469 \[hep-ph\]](https://arxiv.org/abs/1503.01469).
- [307] P. Maierhöfer, J. Usovitsch, and P. Uwer, “Kira—A Feynman integral reduction program,” *Comput. Phys. Commun.* **230** (2018) 99–112, [arXiv:1705.05610 \[hep-ph\]](https://arxiv.org/abs/1705.05610).
- [308] A. Alloul, N. D. Christensen, C. Degrande, C. Duhr, and B. Fuks, “FeynRules 2.0 - A complete toolbox for tree-level phenomenology,” *Comput. Phys. Commun.* **185** (2014) 2250–2300, [arXiv:1310.1921 \[hep-ph\]](https://arxiv.org/abs/1310.1921).
- [309] A. Smirnov, “Algorithm FIRE – Feynman Integral REduction,” *JHEP* **10** (2008) 107, [arXiv:0807.3243 \[hep-ph\]](https://arxiv.org/abs/0807.3243).
- [310] S. Dawson and P. P. Giardino, “Higgs decays to ZZ and $Z\gamma$ in the standard model effective field theory: An NLO analysis,” *Phys. Rev. D* **97** no. 9, (2018) 093003, [arXiv:1801.01136 \[hep-ph\]](https://arxiv.org/abs/1801.01136).
- [311] R. Gauld, B. D. Pecjak, and D. J. Scott, “One-loop corrections to $h \rightarrow b\bar{b}$ and $h \rightarrow \tau\bar{\tau}$ decays in the Standard Model Dimension-6 EFT: four-fermion operators and the large- m_t limit,” *JHEP* **05** (2016) 080, [arXiv:1512.02508 \[hep-ph\]](https://arxiv.org/abs/1512.02508).
- [312] G. Ossola, C. G. Papadopoulos, and R. Pittau, “Reducing full one-loop amplitudes to scalar integrals at the integrand level,” *Nucl. Phys. B* **763** (2007) 147–169, [arXiv:hep-ph/0609007](https://arxiv.org/abs/hep-ph/0609007).
- [313] G. Ossola, C. G. Papadopoulos, and R. Pittau, “CutTools: A Program implementing the OPP reduction method to compute one-loop amplitudes,” *JHEP* **03** (2008) 042, [arXiv:0711.3596 \[hep-ph\]](https://arxiv.org/abs/0711.3596).
- [314] G. Ossola, C. G. Papadopoulos, and R. Pittau, “On the Rational Terms of the one-loop amplitudes,” *JHEP* **05** (2008) 004, [arXiv:0802.1876 \[hep-ph\]](https://arxiv.org/abs/0802.1876).

- [315] R. D. Ball *et al.*, “Parton distributions with LHC data,” *Nucl. Phys. B* **867** (2013) 244–289, [arXiv:1207.1303 \[hep-ph\]](https://arxiv.org/abs/1207.1303).
- [316] I. Brivio, Y. Jiang, and M. Trott, “The SMEFTsim package, theory and tools,” *JHEP* **12** (2017) 070, [arXiv:1709.06492 \[hep-ph\]](https://arxiv.org/abs/1709.06492).
- [317] “Guidelines for extrapolation of cms and atlas lhc/hl-lhc couplings projections to he-lhc.” <https://twiki.cern.ch/twiki/bin/view/LHCPhysics/GuidelinesCouplingProjections2018#Details%20of%20the%20CMS%20projections>.
- [318] J. Salvatier, T. V. Wiecki, and C. Fonnesbeck, “Probabilistic programming in python using PyMC3,” *PeerJ Computer Science* **2** (Apr, 2016) e55. <https://doi.org/10.7717/peerj-cs.55>.
- [319] R. Kumar, C. Carroll, A. Hartikainen, and O. Martin, “Arviz a unified library for exploratory analysis of bayesian models in python,” *Journal of Open Source Software* **4** no. 33, (2019) 1143. <https://doi.org/10.21105/joss.01143>.
- [320] J. de Blas *et al.*, “HEPfit: a Code for the Combination of Indirect and Direct Constraints on High Energy Physics Models,” *Eur. Phys. J. C* **80** no. 5, (2020) 456, [arXiv:1910.14012 \[hep-ph\]](https://arxiv.org/abs/1910.14012).
- [321] I. Brivio, S. Bruggisser, F. Maltoni, R. Moutafis, T. Plehn, E. Vryonidou, S. Westhoff, and C. Zhang, “O new physics, where art thou? A global search in the top sector,” *JHEP* **02** (2020) 131, [arXiv:1910.03606 \[hep-ph\]](https://arxiv.org/abs/1910.03606).
- [322] C. Zhang, “Constraining $qqt\bar{t}$ operators from four-top production: a case for enhanced EFT sensitivity,” *Chin. Phys. C* **42** no. 2, (2018) 023104, [arXiv:1708.05928 \[hep-ph\]](https://arxiv.org/abs/1708.05928).
- [323] **ATLAS** Collaboration, “Search for Higgs boson pair production in the two bottom quarks plus two photons final state in pp collisions at $\sqrt{s} = 13$ TeV with the ATLAS detector,” Tech. Rep. ATLAS-CONF-2021-016, 2021.
- [324] L. Alasfar, R. Gröber, C. Grojean, A. Paul, and Z. Qian, “Machine learning augmented probes of light-quark Yukawa and trilinear couplings from Higgs pair production,” *In preparation* (2021) .
- [325] J. Alison *et al.*, “Higgs boson potential at colliders: Status and perspectives,” *Rev. Phys.* **5** (2020) 100045, [arXiv:1910.00012 \[hep-ph\]](https://arxiv.org/abs/1910.00012).
- [326] **CMS** Collaboration, “Prospects for HH measurements at the HL-LHC,” *CMS-PAS-FTR-18-019* (2018) .
- [327] L. Silvestrini and M. Valli, “Model-independent Bounds on the Standard Model Effective Theory from Flavour Physics,” *Phys. Lett. B* **799** (2019) 135062, [arXiv:1812.10913 \[hep-ph\]](https://arxiv.org/abs/1812.10913).

- [328] G. Banelli, E. Salvioni, J. Serra, T. Theil, and A. Weiler, “The Present and Future of Four Top Operators,” *JHEP* **02** (2021) 043, [arXiv:2010.05915 \[hep-ph\]](https://arxiv.org/abs/2010.05915).
- [329] J. de Blas, J. C. Criado, M. Perez-Victoria, and J. Santiago, “Effective description of general extensions of the Standard Model: the complete tree-level dictionary,” *JHEP* **03** (2018) 109, [arXiv:1711.10391 \[hep-ph\]](https://arxiv.org/abs/1711.10391).
- [330] Anisha, S. D. Bakshi, S. Banerjee, A. Biekötter, J. Chakrabortty, S. K. Patra, and M. Spannowsky, “Effective limits on single scalar extensions in the light of recent LHC data,” [arXiv:2111.05876 \[hep-ph\]](https://arxiv.org/abs/2111.05876).
- [331] **ATLAS Collaboration** Collaboration, “Measurement prospects of the pair production and self-coupling of the Higgs boson with the ATLAS experiment at the HL-LHC,”.
- [332] T. Plehn and M. Rauch, “The quartic higgs coupling at hadron colliders,” *Phys. Rev.* **D72** (2005) 053008, [arXiv:hep-ph/0507321 \[hep-ph\]](https://arxiv.org/abs/hep-ph/0507321).
- [333] O. Eboli, G. Marques, S. Novaes, and A. Natale, “Twin higgs-boson production,” *Physics Letters B* **197** no. 1, (1987) 269–272.
- [334] E. Glover and J. van der Bij, “Higgs boson pair production via gluon fusion,” *Nuclear Physics B* **309** no. 2, (1988) 282–294.
- [335] D. A. Dicus, C. Kao, and S. S. D. Willenbrock, “Higgs Boson Pair Production From Gluon Fusion,” *Phys. Lett.* **B203** (1988) 457–461.
- [336] T. Plehn, M. Spira, and P. M. Zerwas, “Pair production of neutral Higgs particles in gluon-gluon collisions,” *Nucl. Phys.* **B479** (1996) 46–64, [arXiv:hep-ph/9603205 \[hep-ph\]](https://arxiv.org/abs/hep-ph/9603205). [Erratum: Nucl. Phys.B531,655(1998)].
- [337] J. Grigo, K. Melnikov, and M. Steinhauser, “Virtual corrections to Higgs boson pair production in the large top quark mass limit,” *Nucl. Phys.* **B888** (2014) 17–29, [arXiv:1408.2422 \[hep-ph\]](https://arxiv.org/abs/1408.2422).
- [338] D. de Florian and J. Mazzitelli, “Two-loop virtual corrections to Higgs pair production,” *Phys. Lett. B* **724** (2013) 306–309, [arXiv:1305.5206 \[hep-ph\]](https://arxiv.org/abs/1305.5206).
- [339] J. Grigo, J. Hoff, K. Melnikov, and M. Steinhauser, “On the Higgs boson pair production at the LHC,” *Nucl. Phys.* **B875** (2013) 1–17, [arXiv:1305.7340 \[hep-ph\]](https://arxiv.org/abs/1305.7340).
- [340] J. Grigo, J. Hoff, and M. Steinhauser, “Higgs boson pair production: top quark mass effects at NLO and NNLO,” *Nucl. Phys. B* **900** (2015) 412–430, [arXiv:1508.00909 \[hep-ph\]](https://arxiv.org/abs/1508.00909).

- [341] G. Degrassi, P. P. Giardino, and R. Gröber, “On the two-loop virtual QCD corrections to Higgs boson pair production in the Standard Model,” *Eur. Phys. J. C* **76** no. 7, (2016) 411, [arXiv:1603.00385 \[hep-ph\]](#).
- [342] D. Y. Shao, C. S. Li, H. T. Li, and J. Wang, “Threshold resummation effects in Higgs boson pair production at the LHC,” *JHEP* **07** (2013) 169, [arXiv:1301.1245 \[hep-ph\]](#).
- [343] S. Borowka, N. Greiner, G. Heinrich, S. P. Jones, M. Kerner, J. Schlenk, and T. Zirke, “Full top quark mass dependence in Higgs boson pair production at NLO,” *JHEP* **10** (2016) 107, [arXiv:1608.04798 \[hep-ph\]](#).
- [344] S. Borowka, N. Greiner, G. Heinrich, S. P. Jones, M. Kerner, J. Schlenk, U. Schubert, and T. Zirke, “Higgs Boson Pair Production in Gluon Fusion at Next-to-Leading Order with Full Top-Quark Mass Dependence,” *Phys. Rev. Lett.* **117** no. 1, (2016) 012001, [arXiv:1604.06447 \[hep-ph\]](#). [Erratum: *Phys. Rev. Lett.* 117,no.7,079901(2016)].
- [345] J. Baglio, F. Campanario, S. Glaus, M. Mühlleitner, M. Spira, and J. Streicher, “Gluon fusion into Higgs pairs at NLO QCD and the top mass scheme,” *Eur. Phys. J. C* **79** no. 6, (2019) 459, [arXiv:1811.05692 \[hep-ph\]](#).
- [346] J. Davies, G. Mishima, M. Steinhauser, and D. Wellmann, “Double-Higgs boson production in the high-energy limit: planar master integrals,” *JHEP* **03** (2018) 048, [arXiv:1801.09696 \[hep-ph\]](#).
- [347] X. Xu and L. L. Yang, “Towards a new approximation for pair-production and associated-production of the Higgs boson,” *JHEP* **01** (2019) 211, [arXiv:1810.12002 \[hep-ph\]](#).
- [348] G. Wang, Y. Wang, X. Xu, Y. Xu, and L. L. Yang, “Efficient computation of two-loop amplitudes for Higgs boson pair production,” *Phys. Rev. D* **104** no. 5, (2021) L051901, [arXiv:2010.15649 \[hep-ph\]](#).
- [349] J. Davies, R. Gröber, A. Maier, T. Rauh, and M. Steinhauser, “Top quark mass dependence of the Higgs boson-gluon form factor at three loops,” *Phys. Rev. D* **100** no. 3, (2019) 034017, [arXiv:1906.00982 \[hep-ph\]](#).
- [350] M. Grazzini, G. Heinrich, S. Jones, S. Kallweit, M. Kerner, J. M. Lindert, and J. Mazzitelli, “Higgs boson pair production at NNLO with top quark mass effects,” *JHEP* **05** (2018) 059, [arXiv:1803.02463 \[hep-ph\]](#).
- [351] D. de Florian, M. Grazzini, C. Hanga, S. Kallweit, J. M. Lindert, P. Maierhöfer, J. Mazzitelli, and D. Rathlev, “Differential Higgs Boson Pair Production at Next-to-Next-to-Leading Order in QCD,” *JHEP* **09** (2016) 151, [arXiv:1606.09519 \[hep-ph\]](#).

- [352] D. de Florian and J. Mazzitelli, “Higgs Boson Pair Production at Next-to-Next-to-Leading Order in QCD,” *Phys. Rev. Lett.* **111** (2013) 201801, [arXiv:1309.6594 \[hep-ph\]](https://arxiv.org/abs/1309.6594).
- [353] D. de Florian and J. Mazzitelli, “Higgs pair production at next-to-next-to-leading logarithmic accuracy at the LHC,” *JHEP* **09** (2015) 053, [arXiv:1505.07122 \[hep-ph\]](https://arxiv.org/abs/1505.07122).
- [354] S. Jones and S. Kuttimalai, “Parton Shower and NLO-Matching uncertainties in Higgs Boson Pair Production,” *JHEP* **02** (2018) 176, [arXiv:1711.03319 \[hep-ph\]](https://arxiv.org/abs/1711.03319).
- [355] G. Heinrich, S. P. Jones, M. Kerner, G. Luisoni, and L. Scyboz, “Probing the trilinear Higgs boson coupling in di-Higgs production at NLO QCD including parton shower effects,” *JHEP* **06** (2019) 066, [arXiv:1903.08137 \[hep-ph\]](https://arxiv.org/abs/1903.08137).
- [356] G. Heinrich, S. P. Jones, M. Kerner, G. Luisoni, and E. Vryonidou, “NLO predictions for Higgs boson pair production with full top quark mass dependence matched to parton showers,” *JHEP* **08** (2017) 088, [arXiv:1703.09252 \[hep-ph\]](https://arxiv.org/abs/1703.09252).
- [357] R. Gröber and M. Mühlleitner, “Composite Higgs Boson Pair Production at the LHC,” *JHEP* **06** (2011) 020, [arXiv:1012.1562 \[hep-ph\]](https://arxiv.org/abs/1012.1562).
- [358] R. Gröber, *Aspects of Higgs Physics and New Physics at the LHC*. PhD thesis, Karlsruhe U., 2014.
- [359] R. Grober, M. Muhlleitner, M. Spira, and J. Streicher, “NLO QCD Corrections to Higgs Pair Production including Dimension-6 Operators,” *JHEP* **09** (2015) 092, [arXiv:1504.06577 \[hep-ph\]](https://arxiv.org/abs/1504.06577).
- [360] D. de Florian, I. Fabre, and J. Mazzitelli, “Higgs boson pair production at NNLO in QCD including dimension 6 operators,” *JHEP* **10** (2017) 215, [arXiv:1704.05700 \[hep-ph\]](https://arxiv.org/abs/1704.05700).
- [361] S. Dittmaier *et al.*, “Handbook of LHC Higgs Cross Sections: 2. Differential Distributions,” [arXiv:1201.3084 \[hep-ph\]](https://arxiv.org/abs/1201.3084).
- [362] **LHC Higgs Cross Section Working Group** Collaboration, D. de Florian *et al.*, “Handbook of LHC Higgs Cross Sections: 4. Deciphering the Nature of the Higgs Sector,” [arXiv:1610.07922 \[hep-ph\]](https://arxiv.org/abs/1610.07922).
- [363] A. D. Martin, W. J. Stirling, R. S. Thorne, and G. Watt, “Uncertainties on alpha(S) in global PDF analyses and implications for predicted hadronic cross sections,” *Eur. Phys. J.* **C64** (2009) 653–680, [arXiv:0905.3531 \[hep-ph\]](https://arxiv.org/abs/0905.3531).
- [364] F. Demartin, S. Forte, E. Mariani, J. Rojo, and A. Vicini, “The impact of PDF and alphas uncertainties on Higgs Production in gluon fusion at hadron colliders,” *Phys. Rev.* **D82** (2010) 014002, [arXiv:1004.0962 \[hep-ph\]](https://arxiv.org/abs/1004.0962).

- [365] J. Baglio, F. Campanario, S. Glaus, M. Mühlleitner, J. Ronca, and M. Spira, “ $gg \rightarrow HH$: Combined uncertainties,” *Phys. Rev. D* **103** no. 5, (2021) 056002, [arXiv:2008.11626 \[hep-ph\]](https://arxiv.org/abs/2008.11626).
- [366] L.-B. Chen, H. T. Li, H.-S. Shao, and J. Wang, “Higgs boson pair production via gluon fusion at N³LO in QCD,” *Phys. Lett. B* **803** (2020) 135292, [arXiv:1909.06808 \[hep-ph\]](https://arxiv.org/abs/1909.06808).
- [367] L.-B. Chen, H. T. Li, H.-S. Shao, and J. Wang, “The gluon-fusion production of Higgs boson pair: N³LO QCD corrections and top-quark mass effects,” *JHEP* **03** (2020) 072, [arXiv:1912.13001 \[hep-ph\]](https://arxiv.org/abs/1912.13001).
- [368] J. Baglio, A. Djouadi, R. Gröber, M. M. Mühlleitner, J. Quevillon, and M. Spira, “The measurement of the Higgs self-coupling at the LHC: theoretical status,” *JHEP* **04** (2013) 151, [arXiv:1212.5581 \[hep-ph\]](https://arxiv.org/abs/1212.5581).
- [369] L.-S. Ling, R.-Y. Zhang, W.-G. Ma, L. Guo, W.-H. Li, and X.-Z. Li, “NNLO QCD corrections to Higgs pair production via vector boson fusion at hadron colliders,” *Phys. Rev. D* **89** no. 7, (2014) 073001, [arXiv:1401.7754 \[hep-ph\]](https://arxiv.org/abs/1401.7754).
- [370] F. A. Dreyer and A. Karlberg, “Vector-Boson Fusion Higgs Pair Production at N³LO,” *Phys. Rev. D* **98** no. 11, (2018) 114016, [arXiv:1811.07906 \[hep-ph\]](https://arxiv.org/abs/1811.07906).
- [371] F. A. Dreyer and A. Karlberg, “Fully differential Vector-Boson Fusion Higgs Pair Production at Next-to-Next-to-Leading Order,” *Phys. Rev. D* **99** no. 7, (2019) 074028, [arXiv:1811.07918 \[hep-ph\]](https://arxiv.org/abs/1811.07918).
- [372] H. T. Li and J. Wang, “Fully Differential Higgs Pair Production in Association With a W Boson at Next-to-Next-to-Leading Order in QCD,” *Phys. Lett. B* **765** (2017) 265–271, [arXiv:1607.06382 \[hep-ph\]](https://arxiv.org/abs/1607.06382).
- [373] H. T. Li, C. S. Li, and J. Wang, “Fully differential Higgs boson pair production in association with a Z boson at next-to-next-to-leading order in QCD,” *Phys. Rev. D* **97** no. 7, (2018) 074026, [arXiv:1710.02464 \[hep-ph\]](https://arxiv.org/abs/1710.02464).
- [374] R. Frederix, S. Frixione, V. Hirschi, F. Maltoni, O. Mattelaer, P. Torrielli, E. Vryonidou, and M. Zaro, “Higgs pair production at the LHC with NLO and parton-shower effects,” *Phys. Lett. B* **732** (2014) 142–149, [arXiv:1401.7340 \[hep-ph\]](https://arxiv.org/abs/1401.7340).
- [375] **CMS Collaboration** Collaboration, “Search for Higgs boson pair production in the four b quark final state,” tech. rep., CERN, Geneva, 2021.
<https://cds.cern.ch/record/2771912>.
- [376] **CMS Collaboration** Collaboration, “Search for Higgs boson pair production via vector boson fusion with highly Lorentz-boosted Higgs bosons in the four b quark final state at $\sqrt{s} = 13$ TeV,” tech. rep., CERN, Geneva, 2021.
[http://cds.cern.ch/record/2776802](https://cds.cern.ch/record/2776802).

- [377] **ATLAS** Collaboration, G. Aad *et al.*, “Search for the $HH \rightarrow b\bar{b}b\bar{b}$ process via vector-boson fusion production using proton-proton collisions at $\sqrt{s} = 13$ TeV with the ATLAS detector,” *JHEP* **07** (2020) 108, [arXiv:2001.05178 \[hep-ex\]](https://arxiv.org/abs/2001.05178). [Erratum: JHEP 01, 145 (2021), Erratum: JHEP 05, 207 (2021)].
- [378] **ATLAS** Collaboration, G. Aad *et al.*, “Search for non-resonant Higgs boson pair production in the $b\bar{b}\ell\nu\ell\nu$ final state with the ATLAS detector in pp collisions at $\sqrt{s} = 13$ TeV,” *Phys. Lett. B* **801** (2020) 135145, [arXiv:1908.06765 \[hep-ex\]](https://arxiv.org/abs/1908.06765).
- [379] **CMS Collaboration** Collaboration, “Search for nonresonant Higgs boson pair production in the 4 leptons plus 2 b jets final state in proton-proton collisions at $\sqrt{s} = 13$ TeV,” tech. rep., CERN, Geneva, 2020.
<https://cds.cern.ch/record/2725691>.
- [380] **ATLAS Collaboration** Collaboration, “Combination of searches for non-resonant and resonant Higgs boson pair production in the $b\bar{b}\gamma\gamma$, $b\bar{b}\tau^+\tau^-$ and $b\bar{b}b\bar{b}$ decay channels using pp collisions at $\sqrt{s} = 13$ TeV with the ATLAS detector,” tech. rep., CERN, Geneva, Oct, 2021.
<https://cds.cern.ch/record/2786865>. All figures including auxiliary figures are available at
<https://atlas.web.cern.ch/Atlas/GROUPS/PHYSICS/CONFNOTES/ATLAS-CONF-2021-052>.
- [381] **CMS** Collaboration, A. M. Sirunyan *et al.*, “Search for nonresonant Higgs boson pair production in final states with two bottom quarks and two photons in proton-proton collisions at $\sqrt{s} = 13$ TeV,” *JHEP* **03** (2021) 257, [arXiv:2011.12373 \[hep-ex\]](https://arxiv.org/abs/2011.12373).
- [382] A. Azatov, R. Contino, G. Panico, and M. Son, “Effective field theory analysis of double Higgs boson production via gluon fusion,” *Phys. Rev.* **D92** no. 3, (2015) 035001, [arXiv:1502.00539 \[hep-ph\]](https://arxiv.org/abs/1502.00539).
- [383] U. Baur, T. Plehn, and D. L. Rainwater, “Probing the Higgs selfcoupling at hadron colliders using rare decays,” *Phys. Rev.* **D69** (2004) 053004, [arXiv:hep-ph/0310056 \[hep-ph\]](https://arxiv.org/abs/hep-ph/0310056).
- [384] F. Kling, T. Plehn, and P. Schichtel, “Maximizing the significance in Higgs boson pair analyses,” *Phys. Rev.* **D95** no. 3, (2017) 035026, [arXiv:1607.07441 \[hep-ph\]](https://arxiv.org/abs/1607.07441).
- [385] V. Barger, L. L. Everett, C. B. Jackson, and G. Shaughnessy, “Higgs-Pair Production and Measurement of the Triscalar Coupling at LHC(8,14),” *Phys. Lett.* **B728** (2014) 433–436, [arXiv:1311.2931 \[hep-ph\]](https://arxiv.org/abs/1311.2931).
- [386] A. Adhikary, S. Banerjee, R. K. Barman, B. Bhattacherjee, and S. Niyogi, “Revisiting the non-resonant Higgs pair production at the HL-LHC,” *JHEP* **07** (2018) 116, [arXiv:1712.05346 \[hep-ph\]](https://arxiv.org/abs/1712.05346).

- [387] A. Alves, T. Ghosh, and K. Sinha, “Can We Discover Double Higgs Production at the LHC?,” *Phys. Rev. D* **96** no. 3, (2017) 035022, [arXiv:1704.07395 \[hep-ph\]](#).
- [388] S. Weinberg, “Models of Lepton and Quark Masses,” *Phys. Rev. D* **101** no. 3, (2020) 035020, [arXiv:2001.06582 \[hep-th\]](#).
- [389] CMS Collaboration, V. Khachatryan *et al.*, “Search for a standard model-like Higgs boson in the $\mu^+\mu^-$ and e^+e^- decay channels at the LHC,” *Phys. Lett. B* **744** (2015) 184–207, [arXiv:1410.6679 \[hep-ex\]](#).
- [390] Y. Nakai, D. Shih, and S. Thomas, “Strange Jet Tagging,” [arXiv:2003.09517 \[hep-ph\]](#).
- [391] Y. Soreq, H. X. Zhu, and J. Zupan, “Light quark Yukawa couplings from Higgs kinematics,” *JHEP* **12** (2016) 045, [arXiv:1606.09621 \[hep-ph\]](#).
- [392] L. Alasfar, R. Corral Lopez, and R. Gröber, “Probing Higgs couplings to light quarks via Higgs pair production,” *JHEP* **11** (2019) 088, [arXiv:1909.05279 \[hep-ph\]](#).
- [393] G. Blankenburg, J. Ellis, and G. Isidori, “Flavour-Changing Decays of a 125 GeV Higgs-like Particle,” *Phys. Lett. B* **712** (2012) 386–390, [arXiv:1202.5704 \[hep-ph\]](#).
- [394] G. D’Ambrosio, G. F. Giudice, G. Isidori, and A. Strumia, “Minimal flavor violation: An Effective field theory approach,” *Nucl. Phys. B* **645** (2002) 155–187, [arXiv:hep-ph/0207036 \[hep-ph\]](#).
- [395] A. Pich and P. Tuzon, “Yukawa Alignment in the Two-Higgs-Doublet Model,” *Phys. Rev. D* **80** (2009) 091702, [arXiv:0908.1554 \[hep-ph\]](#).
- [396] A. Pich, “Flavour constraints on multi-Higgs-doublet models: Yukawa alignment,” *Nucl. Phys. B Proc. Suppl.* **209** (2010) 182–187, [arXiv:1010.5217 \[hep-ph\]](#).
- [397] D. Egana-Ugrinovic, S. Homiller, and P. Meade, “Aligned and Spontaneous Flavor Violation,” *Phys. Rev. Lett.* **123** no. 3, (2019) 031802, [arXiv:1811.00017 \[hep-ph\]](#).
- [398] P. M. Ferreira, L. Lavoura, and J. P. Silva, “Renormalization-group constraints on Yukawa alignment in multi-Higgs-doublet models,” *Phys. Lett. B* **688** (2010) 341–344, [arXiv:1001.2561 \[hep-ph\]](#).
- [399] M. Jung, A. Pich, and P. Tuzon, “Charged-Higgs phenomenology in the Aligned two-Higgs-doublet model,” *JHEP* **11** (2010) 003, [arXiv:1006.0470 \[hep-ph\]](#).
- [400] F. J. Botella, G. C. Branco, A. M. Coutinho, M. N. Rebelo, and J. I. Silva-Marcos, “Natural Quasi-Alignment with two Higgs Doublets and RGE Stability,” *Eur. Phys. J. C* **75** (2015) 286, [arXiv:1501.07435 \[hep-ph\]](#).

- [401] R. Contino, C. Grojean, M. Moretti, F. Piccinini, and R. Rattazzi, “Strong Double Higgs Production at the LHC,” *JHEP* **05** (2010) 089, [arXiv:1002.1011 \[hep-ph\]](https://arxiv.org/abs/1002.1011).
- [402] D. Dicus, T. Stelzer, Z. Sullivan, and S. Willenbrock, “Higgs boson production in association with bottom quarks at next-to-leading order,” *Phys. Rev.* **D59** (1999) 094016, [arXiv:hep-ph/9811492 \[hep-ph\]](https://arxiv.org/abs/hep-ph/9811492).
- [403] C. Balazs, H.-J. He, and C. P. Yuan, “QCD corrections to scalar production via heavy quark fusion at hadron colliders,” *Phys. Rev.* **D60** (1999) 114001, [arXiv:hep-ph/9812263 \[hep-ph\]](https://arxiv.org/abs/hep-ph/9812263).
- [404] R. V. Harlander and W. B. Kilgore, “Higgs boson production in bottom quark fusion at next-to-next-to leading order,” *Phys. Rev.* **D68** (2003) 013001, [arXiv:hep-ph/0304035 \[hep-ph\]](https://arxiv.org/abs/hep-ph/0304035).
- [405] S. Dawson, C. Kao, Y. Wang, and P. Williams, “QCD Corrections to Higgs Pair Production in Bottom Quark Fusion,” *Phys. Rev.* **D75** (2007) 013007, [arXiv:hep-ph/0610284 \[hep-ph\]](https://arxiv.org/abs/hep-ph/0610284).
- [406] A. H. Ajjath, P. Banerjee, A. Chakraborty, P. K. Dhani, P. Mukherjee, N. Rana, and V. Ravindran, “Higgs pair production from bottom quark annihilation to NNLO in QCD,” *JHEP* **05** (2019) 030, [arXiv:1811.01853 \[hep-ph\]](https://arxiv.org/abs/1811.01853).
- [407] M. Spira, “Higgs Boson Production and Decay at Hadron Colliders,” *Prog. Part. Nucl. Phys.* **95** (2017) 98–159, [arXiv:1612.07651 \[hep-ph\]](https://arxiv.org/abs/1612.07651).
- [408] V. N. Gribov and L. N. Lipatov, “Deep inelastic e p scattering in perturbation theory,” *Sov. J. Nucl. Phys.* **15** (1972) 438–450. [Yad. Fiz.15,781(1972)].
- [409] G. Altarelli and G. Parisi, “Asymptotic Freedom in Parton Language,” *Nucl. Phys.* **B126** (1977) 298–318.
- [410] Y. L. Dokshitzer, “Calculation of the Structure Functions for Deep Inelastic Scattering and e+ e- Annihilation by Perturbation Theory in Quantum Chromodynamics.,” *Sov. Phys. JETP* **46** (1977) 641–653. [Zh. Eksp. Teor. Fiz.73,1216(1977)].
- [411] **NNPDF** Collaboration, R. D. Ball *et al.*, “Parton distributions from high-precision collider data,” *Eur. Phys. J.* **C77** no. 10, (2017) 663, [arXiv:1706.00428 \[hep-ph\]](https://arxiv.org/abs/1706.00428).
- [412] A. Buckley, J. Ferrando, S. Lloyd, K. Nordström, B. Page, M. Rüfenacht, M. Schönherr, and G. Watt, “LHAPDF6: parton density access in the LHC precision era,” *Eur. Phys. J.* **C75** (2015) 132, [arXiv:1412.7420 \[hep-ph\]](https://arxiv.org/abs/1412.7420).
- [413] A. Denner, S. Dittmaier, and L. Hofer, “COLLIER - A fortran-library for one-loop integrals,” *PoS* **LL2014** (2014) 071, [arXiv:1407.0087 \[hep-ph\]](https://arxiv.org/abs/1407.0087).

- [414] A. Djouadi, J. Kalinowski, and M. Spira, “HDECAY: A Program for Higgs boson decays in the standard model and its supersymmetric extension,” *Comput. Phys. Commun.* **108** (1998) 56–74, [arXiv:hep-ph/9704448 \[hep-ph\]](https://arxiv.org/abs/hep-ph/9704448).
- [415] A. Djouadi, J. Kalinowski, M. Muehlleitner, and M. Spira, “HDECAY: Twenty₊₊ years after,” *Comput. Phys. Commun.* **238** (2019) 214–231, [arXiv:1801.09506 \[hep-ph\]](https://arxiv.org/abs/1801.09506).
- [416] T. Sjostrand, S. Mrenna, and P. Z. Skands, “PYTHIA 6.4 Physics and Manual,” *JHEP* **05** (2006) 026, [arXiv:hep-ph/0603175 \[hep-ph\]](https://arxiv.org/abs/hep-ph/0603175).
- [417] D. C. Hall, “RootTuple: A library enabling ROOT n-tuple output from FORTRAN HEP programs,” <http://roottuple.hepforge.org>.
- [418] T. Sjöstrand, S. Ask, J. R. Christiansen, R. Corke, N. Desai, P. Ilten, S. Mrenna, S. Prestel, C. O. Rasmussen, and P. Z. Skands, “An introduction to PYTHIA 8.2,” *Comput. Phys. Commun.* **191** (2015) 159–177, [arXiv:1410.3012 \[hep-ph\]](https://arxiv.org/abs/1410.3012).
- [419] **DELPHES 3** Collaboration, J. de Favereau, C. Delaere, P. Demin, A. Giammanco, V. Lemaître, A. Mertens, and M. Selvaggi, “DELPHES 3, A modular framework for fast simulation of a generic collider experiment,” *JHEP* **02** (2014) 057, [arXiv:1307.6346 \[hep-ex\]](https://arxiv.org/abs/1307.6346).
- [420] W. Beenakker, S. Dittmaier, M. Kramer, B. Plumper, M. Spira, and P. M. Zerwas, “Higgs radiation off top quarks at the Tevatron and the LHC,” *Phys. Rev. Lett.* **87** (2001) 201805, [arXiv:hep-ph/0107081](https://arxiv.org/abs/hep-ph/0107081).
- [421] D. Fäh and N. Greiner, “Diphoton production in association with two bottom jets,” *Eur. Phys. J. C* **77** no. 11, (2017) 750, [arXiv:1706.08309 \[hep-ph\]](https://arxiv.org/abs/1706.08309).
- [422] F. Campanario, R. Roth, and D. Zeppenfeld, “QCD radiation in WH and WZ production and anomalous coupling measurements,” *Phys. Rev. D* **91** (2015) 054039, [arXiv:1410.4840 \[hep-ph\]](https://arxiv.org/abs/1410.4840).
- [423] S. Dawson, C. Jackson, L. Reina, and D. Wackerlo, “Higgs production in association with bottom quarks at hadron colliders,” *Mod. Phys. Lett. A* **21** (2006) 89–110, [arXiv:hep-ph/0508293](https://arxiv.org/abs/hep-ph/0508293).
- [424] M. Cacciari, G. P. Salam, and G. Soyez, “FastJet User Manual,” *Eur. Phys. J. C* **72** (2012) 1896, [arXiv:1111.6097 \[hep-ph\]](https://arxiv.org/abs/1111.6097).
- [425] CMS Collaboration, S. Chatrchyan *et al.*, “Inclusive b -jet production in pp collisions at $\sqrt{s} = 7$ TeV,” *JHEP* **04** (2012) 084, [arXiv:1202.4617 \[hep-ex\]](https://arxiv.org/abs/1202.4617).
- [426] CMS Collaboration, “Performance of b tagging at $\text{sqrt}(s)=8$ TeV in multijet, $t\bar{t}$ bar and boosted topology events,” Tech. Rep. CMS-PAS-BTV-13-001, CERN, Geneva, 2013. <https://cds.cern.ch/record/1581306>.

- [427] **ATLAS** Collaboration, “Performance assumptions based on full simulation for an upgraded ATLAS detector at a High-Luminosity LHC,” Tech. Rep. ATL-PHYS-PUB-2013-009, CERN, Geneva, 2013.
<http://cds.cern.ch/record/1604420>.
- [428] **CMS** Collaboration, “Photon ID performance with 19.6 fb^{-1} of data collected at $\sqrt{s} = 8 \text{ TeV}$ with the CMS detector,” Tech. Rep. CMS-DP-2013-010, CERN, Geneva, 2013. <http://cds.cern.ch/record/1542855>.
- [429] G. Cowan, K. Cranmer, E. Gross, and O. Vitells, “Asymptotic formulae for likelihood-based tests of new physics,” *Eur. Phys. J.* **C71** (2011) 1554, [arXiv:1007.1727 \[physics.data-an\]](https://arxiv.org/abs/1007.1727). [Erratum: Eur. Phys. J.C73,2501(2013)].
- [430] L. Heinrich, M. Feickert, and G. Stark, “pyhf: v0.6.3.”
<https://doi.org/10.5281/zenodo.1169739>.
<https://github.com/scikit-hep/pyhf/releases/tag/v0.6.3>.
- [431] L. Heinrich, M. Feickert, G. Stark, and K. Cranmer, “pyhf: pure-python implementation of histfactory statistical models,” *Journal of Open Source Software* **6** no. 58, (2021) 2823. <https://doi.org/10.21105/joss.02823>.
- [432] T. Chen and C. Guestrin, “**XGBoost: A Scalable Tree Boosting System**,” in *Proceedings of the 22nd ACM SIGKDD International Conference on Knowledge Discovery and Data Mining*, KDD ’16, p. 785–794. Association for Computing Machinery, New York, NY, USA, 2016.
<https://dl.acm.org/doi/10.1145/2939672.2939785>.
- [433] L. S. Shapley, “Notes on the n-Person Game-II: The Value of an n-Person Game,” *Rand Corporation* (1951).
https://www.rand.org/pubs/research_memoranda/RM0670.html.
- [434] D. Alvestad, N. Fomin, J. Kersten, S. Maeland, and I. Strümke, “Beyond Cuts in Small Signal Scenarios - Enhanced Sneutrino Detectability Using Machine Learning,” [arXiv:2108.03125 \[hep-ph\]](https://arxiv.org/abs/2108.03125).
- [435] A. S. Cornell, W. Doorsamy, B. Fuks, G. Harmsen, and L. Mason, “Boosted decision trees in the era of new physics: a muon analysis case study,” [arXiv:2109.11815 \[hep-ph\]](https://arxiv.org/abs/2109.11815).
- [436] S. M. Lundberg and S.-I. Lee, “A unified approach to interpreting model predictions,” in *Advances in Neural Information Processing Systems*, I. Guyon, U. V. Luxburg, S. Bengio, H. Wallach, R. Fergus, S. Vishwanathan, and R. Garnett, eds., vol. 30, pp. 4765–4774. Curran Associates, Inc., 2017. [1705.07874. https://proceedings.neurips.cc/paper/2017/file/1705.07874.pdf](https://proceedings.neurips.cc/paper/2017/file/1705.07874.pdf).

- [437] S. M. Lundberg, G. G. Erion, and S.-I. Lee, “Consistent Individualized Feature Attribution for Tree Ensembles,” *arXiv e-prints* (Feb., 2018) , [arXiv:1802.03888 \[cs.LG\]](https://arxiv.org/abs/1802.03888).
- [438] S. M. Lundberg, G. Erion, H. Chen, A. DeGrave, J. M. Prutkin, B. Nair, R. Katz, J. Himmelfarb, N. Bansal, and S.-I. Lee, “From local explanations to global understanding with explainable AI for trees,” *Nature Machine Intelligence* **2** no. 1, (2020) 56–67. <https://www.nature.com/articles/s42256-019-0138-9>.
- [439] **ATLAS** Collaboration, “Measurement prospects of the pair production and self-coupling of the Higgs boson with the ATLAS experiment at the HL-LHC,”.
- [440] I. Brivio, F. Goertz, and G. Isidori, “Probing the Charm Quark Yukawa Coupling in Higgs+Charm Production,” *Phys. Rev. Lett.* **115** no. 21, (2015) 211801, [arXiv:1507.02916 \[hep-ph\]](https://arxiv.org/abs/1507.02916).
- [441] F. Bishara, U. Haisch, P. F. Monni, and E. Re, “Constraining Light-Quark Yukawa Couplings from Higgs Distributions,” *Phys. Rev. Lett.* **118** no. 12, (2017) 121801, [arXiv:1606.09253 \[hep-ph\]](https://arxiv.org/abs/1606.09253).
- [442] G. Bonner and H. E. Logan, “Constraining the Higgs couplings to up and down quarks using production kinematics at the CERN Large Hadron Collider,” [arXiv:1608.04376 \[hep-ph\]](https://arxiv.org/abs/1608.04376).
- [443] **CMS** Collaboration, “Constraints on the Higgs boson self-coupling from ttH+tH, H to gamma gamma differential measurements at the HL-LHC,” Tech. Rep. CMS-PAS-FTR-18-020, 2018.
- [444] G. Perez, Y. Soreq, E. Stamou, and K. Tobioka, “Prospects for measuring the Higgs boson coupling to light quarks,” *Phys. Rev.* **D93** no. 1, (2016) 013001, [arXiv:1505.06689 \[hep-ph\]](https://arxiv.org/abs/1505.06689).
- [445] G. T. Bodwin, F. Petriello, S. Stoynev, and M. Velasco, “Higgs boson decays to quarkonia and the $H\bar{c}c$ coupling,” *Phys. Rev.* **D88** no. 5, (2013) 053003, [arXiv:1306.5770 \[hep-ph\]](https://arxiv.org/abs/1306.5770).
- [446] A. L. Kagan, G. Perez, F. Petriello, Y. Soreq, S. Stoynev, and J. Zupan, “Exclusive Window onto Higgs Yukawa Couplings,” *Phys. Rev. Lett.* **114** no. 10, (2015) 101802, [arXiv:1406.1722 \[hep-ph\]](https://arxiv.org/abs/1406.1722).
- [447] M. König and M. Neubert, “Exclusive Radiative Higgs Decays as Probes of Light-Quark Yukawa Couplings,” *JHEP* **08** (2015) 012, [arXiv:1505.03870 \[hep-ph\]](https://arxiv.org/abs/1505.03870).
- [448] **CMS** Collaboration, A. M. Sirunyan *et al.*, “Search for rare decays of Z and Higgs bosons to J/ψ and a photon in proton-proton collisions at $\sqrt{s} = 13$ TeV,” *Eur. Phys. J. C* **79** no. 2, (2019) 94, [arXiv:1810.10056 \[hep-ex\]](https://arxiv.org/abs/1810.10056).

- [449] F. Yu, “Light Quark Yukawa Couplings and the $W^\pm h$ Charge Asymmetry,” *Nucl. Part. Phys. Proc.* **285-286** (2017) 123–125.
- [450] J. A. Aguilar-Saavedra, J. M. Cano, and J. M. No, “More light on Higgs flavor at the LHC: Higgs boson couplings to light quarks through $h + \gamma$ production,” *Phys. Rev. D* **103** no. 9, (2021) 095023, [arXiv:2008.12538 \[hep-ph\]](https://arxiv.org/abs/2008.12538).
- [451] A. Falkowski, S. Ganguly, P. Gras, J. M. No, K. Tobioka, N. Vignaroli, and T. You, “Light quark Yukawas in triboson final states,” *JHEP* **04** (2021) 023, [arXiv:2011.09551 \[hep-ph\]](https://arxiv.org/abs/2011.09551).
- [452] **ATLAS** Collaboration, A. Sciandra, “Measurement of Triboson Production and aQGCs with the ATLAS detector,”
- [453] **CMS** Collaboration, “Observation of heavy triboson production in leptonic final states in proton-proton collisions at $\sqrt{s} = 13$ TeV,”
- [454] T. Binoth, S. Karg, N. Kauer, and R. Ruckl, “Multi-Higgs boson production in the Standard Model and beyond,” *Phys. Rev. D* **74** (2006) 113008, [arXiv:hep-ph/0608057 \[hep-ph\]](https://arxiv.org/abs/hep-ph/0608057).
- [455] R. Contino, M. Ghezzi, M. Moretti, G. Panico, F. Piccinini, and A. Wulzer, “Anomalous Couplings in Double Higgs Production,” *JHEP* **08** (2012) 154, [arXiv:1205.5444 \[hep-ph\]](https://arxiv.org/abs/1205.5444).
- [456] S. Bar-Shalom and A. Soni, “Universally enhanced light-quarks Yukawa couplings paradigm,” *Phys. Rev. D* **98** no. 5, (2018) 055001, [arXiv:1804.02400 \[hep-ph\]](https://arxiv.org/abs/1804.02400).
- [457] M. Bauer, M. Carena, and A. Carmona, “Higgs Pair Production as a Signal of Enhanced Yukawa Couplings,” *Phys. Rev. Lett.* **121** no. 2, (2018) 021801, [arXiv:1801.00363 \[hep-ph\]](https://arxiv.org/abs/1801.00363).
- [458] D. Egana-Ugrinovic, S. Homiller, and P. Meade, “Multi-Higgs Production Probes Higgs Flavor,” *Phys. Rev. D* **103** (2021) 115005, [arXiv:2101.04119 \[hep-ph\]](https://arxiv.org/abs/2101.04119).
- [459] J. De Blas *et al.*, “Higgs Boson Studies at Future Particle Colliders,” [arXiv:1905.03764 \[hep-ph\]](https://arxiv.org/abs/1905.03764).
- [460] A. Papaefstathiou and K. Sakurai, “Triple Higgs boson production at a 100 TeV proton-proton collider,” *JHEP* **02** (Aug, 2015) 006. 10 p, [arXiv:1508.06524](https://arxiv.org/abs/1508.06524). <https://cds.cern.ch/record/2047255>. Corrected version of Figure 6.
- [461] C. Delaunay, R. Ozeri, G. Perez, and Y. Soreq, “Probing Atomic Higgs-like Forces at the Precision Frontier,” *Phys. Rev. D* **96** no. 9, (2017) 093001, [arXiv:1601.05087 \[hep-ph\]](https://arxiv.org/abs/1601.05087).
- [462] **ATLAS** Collaboration Collaboration, M. Unal, “Searches for vector-like quarks with the ATLAS Detector.”. [http://cds.cern.ch/record/2777832](https://cds.cern.ch/record/2777832).

- [463] **CMS** Collaboration, A. M. Sirunyan *et al.*, “Search for pair production of vectorlike quarks in the fully hadronic final state,” *Phys. Rev. D* **100** no. 7, (2019) 072001, [arXiv:1906.11903 \[hep-ex\]](https://arxiv.org/abs/1906.11903).
- [464] **CMS** Collaboration, A. M. Sirunyan *et al.*, “Search for vector-like quarks in events with two oppositely charged leptons and jets in proton-proton collisions at $\sqrt{s} = 13$ TeV,” *Eur. Phys. J. C* **79** no. 4, (2019) 364, [arXiv:1812.09768 \[hep-ex\]](https://arxiv.org/abs/1812.09768).
- [465] A. Falkowski and R. Rattazzi, “Which EFT,” [arXiv:1902.05936 \[hep-ph\]](https://arxiv.org/abs/1902.05936).
- [466] S. Chang and M. A. Luty, “The Higgs Trilinear Coupling and the Scale of New Physics,” *JHEP* **03** (2020) 140, [arXiv:1902.05556 \[hep-ph\]](https://arxiv.org/abs/1902.05556).
- [467] D. Egana-Ugrinovic, S. Homiller, and P. R. Meade, “Higgs bosons with large couplings to light quarks,” [arXiv:1908.11376 \[hep-ph\]](https://arxiv.org/abs/1908.11376).
- [468] **ATLAS** Collaboration, M. Aaboud *et al.*, “Search for low-mass resonances decaying into two jets and produced in association with a photon using pp collisions at $\sqrt{s} = 13$ TeV with the ATLAS detector,” *Phys. Lett. B* **795** (2019) 56–75, [arXiv:1901.10917 \[hep-ex\]](https://arxiv.org/abs/1901.10917).
- [469] **ATLAS** Collaboration, G. Aad *et al.*, “Search for new resonances in mass distributions of jet pairs using 139 fb^{-1} of pp collisions at $\sqrt{s} = 13$ TeV with the ATLAS detector,” *JHEP* **03** (2020) 145, [arXiv:1910.08447 \[hep-ex\]](https://arxiv.org/abs/1910.08447).
- [470] **CMS** Collaboration, A. M. Sirunyan *et al.*, “Search for high mass dijet resonances with a new background prediction method in proton-proton collisions at $\sqrt{s} = 13$ TeV,” *JHEP* **05** (2020) 033, [arXiv:1911.03947 \[hep-ex\]](https://arxiv.org/abs/1911.03947).
- [471] **CMS** Collaboration, A. M. Sirunyan *et al.*, “Combination of searches for Higgs boson pair production in proton-proton collisions at $\sqrt{s} = 13$ TeV,” *Phys. Rev. Lett.* **122** no. 12, (2019) 121803, [arXiv:1811.09689 \[hep-ex\]](https://arxiv.org/abs/1811.09689).
- [472] **ATLAS** Collaboration, G. Aad *et al.*, “Combination of searches for Higgs boson pairs in pp collisions at $\sqrt{s} = 13$ TeV with the ATLAS detector,” [arXiv:1906.02025 \[hep-ex\]](https://arxiv.org/abs/1906.02025).
- [473] **ATLAS** Collaboration, “Search for heavy resonances decaying into a Z boson and a Higgs boson in final states with leptons and b -jets in 139 fb^{-1} of pp collisions at $\sqrt{s} = 13\text{TeV}$ with the ATLAS detector,”
- [474] **ATLAS** Collaboration, G. Aad *et al.*, “Search for heavy resonances decaying into a pair of Z bosons in the $\ell^+\ell^-\ell'^+\ell'^-$ and $\ell^+\ell^-\nu\bar{\nu}$ final states using 139 fb^{-1} of proton-proton collisions at $\sqrt{s} = 13$ TeV with the ATLAS detector,” [arXiv:2009.14791 \[hep-ex\]](https://arxiv.org/abs/2009.14791).

- [475] **CMS** Collaboration, A. M. Sirunyan *et al.*, “Search for a new scalar resonance decaying to a pair of Z bosons in proton-proton collisions at $\sqrt{s} = 13$ TeV,” *JHEP* **06** (2018) 127, [arXiv:1804.01939 \[hep-ex\]](#). [Erratum: JHEP 03, 128 (2019)].
- [476] S. Descotes-Genon, J. Matias, and J. Virto, “Understanding the $B \rightarrow K^* \mu^+ \mu^-$ Anomaly,” *Phys. Rev.* **D88** (2013) 074002, [arXiv:1307.5683 \[hep-ph\]](#).
- [477] S. Descotes-Genon, L. Hofer, J. Matias, and J. Virto, “Global analysis of $b \rightarrow s\ell\ell$ anomalies,” *JHEP* **06** (2016) 092, [arXiv:1510.04239 \[hep-ph\]](#).
- [478] **LHCb** Collaboration, R. Aaij *et al.*, “Measurement of CP -Averaged Observables in the $B^0 \rightarrow K^{*0} \mu^+ \mu^-$ Decay,” *Phys. Rev. Lett.* **125** no. 1, (2020) 011802, [arXiv:2003.04831 \[hep-ex\]](#).
- [479] G. Hiller and M. Schmaltz, “ R_K and future $b \rightarrow s\ell\ell$ physics beyond the standard model opportunities,” *Phys. Rev.* **D90** (2014) 054014, [arXiv:1408.1627 \[hep-ph\]](#).
- [480] G. Hiller and M. Schmaltz, “Diagnosing lepton-nonuniversality in $b \rightarrow s\ell\ell$,” *JHEP* **02** (2015) 055, [arXiv:1411.4773 \[hep-ph\]](#).
- [481] M. Bordone, G. Isidori, and A. Pattori, “On the Standard Model predictions for R_K and R_{K^*} ,” *Eur. Phys. J. C* **76** no. 8, (2016) 440, [arXiv:1605.07633 \[hep-ph\]](#).
- [482] **Muon g-2** Collaboration, B. Abi *et al.*, “Measurement of the Positive Muon Anomalous Magnetic Moment to 0.46 ppm,” *Phys. Rev. Lett.* **126** no. 14, (2021) 141801, [arXiv:2104.03281 \[hep-ex\]](#).
- [483] A. Khodjamirian, T. Mannel, A. A. Pivovarov, and Y. M. Wang, “Charm-loop effect in $B \rightarrow K^{(*)} \ell^+ \ell^-$ and $B \rightarrow K^* \gamma$,” *JHEP* **09** (2010) 089, [arXiv:1006.4945 \[hep-ph\]](#).
- [484] J. Lyon and R. Zwicky, “Resonances gone topsy turvy - the charm of QCD or new physics in $b \rightarrow s\ell^+ \ell^-$?,” [arXiv:1406.0566 \[hep-ph\]](#).
- [485] V. Chobanova, T. Hurth, F. Mahmoudi, D. Martinez Santos, and S. Neshatpour, “Large hadronic power corrections or new physics in the rare decay $B \rightarrow K^* \mu^+ \mu^-$,” *JHEP* **07** (2017) 025, [arXiv:1702.02234 \[hep-ph\]](#).
- [486] T. Blake, U. Egede, P. Owen, K. A. Petridis, and G. Pomery, “An empirical model to determine the hadronic resonance contributions to $\bar{B}^0 \rightarrow \bar{K}^{*0} \mu^+ \mu^-$ transitions,” *Eur. Phys. J. C* **78** no. 6, (2018) 453, [arXiv:1709.03921 \[hep-ph\]](#).
- [487] C. Bobeth, M. Chrzaszcz, D. van Dyk, and J. Virto, “Long-distance effects in $B \rightarrow K^* \ell\ell$ from analyticity,” *Eur. Phys. J. C* **78** no. 6, (2018) 451, [arXiv:1707.07305 \[hep-ph\]](#).

- [488] S. Jäger and J. Martin Camalich, “Reassessing the discovery potential of the $B \rightarrow K^* \ell^+ \ell^-$ decays in the large-recoil region: SM challenges and BSM opportunities,” *Phys. Rev. D* **93** no. 1, (2016) 014028, [arXiv:1412.3183 \[hep-ph\]](#).
- [489] M. Ciuchini, M. Fedele, E. Franco, S. Mishima, A. Paul, L. Silvestrini, and M. Valli, “ $B \rightarrow K^* \ell^+ \ell^-$ decays at large recoil in the Standard Model: a theoretical reappraisal,” *JHEP* **06** (2016) 116, [arXiv:1512.07157 \[hep-ph\]](#).
- [490] A. Arbey, T. Hurth, F. Mahmoudi, and S. Neshatpour, “Hadronic and New Physics Contributions to $b \rightarrow s$ Transitions,” *Phys. Rev. D* **98** no. 9, (2018) 095027, [arXiv:1806.02791 \[hep-ph\]](#).
- [491] M. Chrzaszcz, A. Mauri, N. Serra, R. Silva Coutinho, and D. van Dyk, “Prospects for disentangling long- and short-distance effects in the decays $B \rightarrow K^* \mu^+ \mu^-$,” *JHEP* **10** (2019) 236, [arXiv:1805.06378 \[hep-ph\]](#).
- [492] M. Ciuchini, A. M. Coutinho, M. Fedele, E. Franco, A. Paul, L. Silvestrini, and M. Valli, “Hadronic uncertainties in semileptonic $B \rightarrow K^* \mu^+ \mu^-$ decays,” *PoS BEAUTY2018* (2018) 044, [arXiv:1809.03789 \[hep-ph\]](#).
- [493] T. Hurth, F. Mahmoudi, and S. Neshatpour, “On the new LHCb angular analysis of $B \rightarrow K^* \mu^+ \mu^-$: Hadronic effects or New Physics?,” [arXiv:2006.04213 \[hep-ph\]](#).
- [494] M. Ciuchini, M. Fedele, E. Franco, A. Paul, L. Silvestrini, and M. Valli, “New Physics without bias: Charming Penguins and Lepton Universality Violation in $b \rightarrow sl^+ \ell^-$ decays,” [arXiv:2110.10126 \[hep-ph\]](#).
- [495] A. Azatov, D. Bardhan, D. Ghosh, F. Sgarlata, and E. Venturini, “Anatomy of $b \rightarrow c\tau\nu$ anomalies,” *JHEP* **11** (2018) 187, [arXiv:1805.03209 \[hep-ph\]](#).
- [496] A. K. Alok, D. Kumar, S. Kumbhakar, and S. Uma Sankar, “Solutions to R_D - R_{D^*} in light of Belle 2019 data,” *Nucl. Phys. B* **953** (2020) 114957, [arXiv:1903.10486 \[hep-ph\]](#).
- [497] C. Murgui, A. Peñuelas, M. Jung, and A. Pich, “Global fit to $b \rightarrow c\tau\nu$ transitions,” *JHEP* **09** (2019) 103, [arXiv:1904.09311 \[hep-ph\]](#).
- [498] R.-X. Shi, L.-S. Geng, B. Grinstein, S. Jäger, and J. Martin Camalich, “Revisiting the new-physics interpretation of the $b \rightarrow c\tau\nu$ data,” *JHEP* **12** (2019) 065, [arXiv:1905.08498 \[hep-ph\]](#).
- [499] **BaBar** Collaboration, J. Lees *et al.*, “Measurement of an Excess of $\overline{B} \rightarrow D^{(*)}\tau^-\bar{\nu}_\tau$ Decays and Implications for Charged Higgs Bosons,” *Phys. Rev. D* **88** no. 7, (2013) 072012, [arXiv:1303.0571 \[hep-ex\]](#).

- [500] **Belle** Collaboration, M. Huschle *et al.*, “Measurement of the branching ratio of $\overline{B} \rightarrow D^{(*)}\tau^-\bar{\nu}_\tau$ relative to $\overline{B} \rightarrow D^{(*)}\ell^-\bar{\nu}_\ell$ decays with hadronic tagging at Belle,” *Phys. Rev. D* **92** no. 7, (2015) 072014, [arXiv:1507.03233 \[hep-ex\]](https://arxiv.org/abs/1507.03233).
- [501] **LHCb** Collaboration, R. Aaij *et al.*, “Measurement of the ratio of the $B^0 \rightarrow D^{*-}\tau^+\nu_\tau$ and $B^0 \rightarrow D^{*-}\mu^+\nu_\mu$ branching fractions using three-prong τ -lepton decays,” *Phys. Rev. Lett.* **120** no. 17, (2018) 171802, [arXiv:1708.08856 \[hep-ex\]](https://arxiv.org/abs/1708.08856).
- [502] P. Koppenburg, “Penguin B decays. Seminario de physica, USACH,.” <http://cds.cern.ch/record/2767155>.
- [503] **UTfit** Collaboration, M. Bona *et al.*, “Model-independent constraints on $\Delta F = 2$ operators and the scale of new physics,” *JHEP* **03** (2008) 049, [arXiv:0707.0636 \[hep-ph\]](https://arxiv.org/abs/0707.0636).
- [504] A. Greljo and D. Marzocca, “High- p_T dilepton tails and flavor physics,” *Eur. Phys. J.* **C77** no. 8, (2017) 548, [arXiv:1704.09015 \[hep-ph\]](https://arxiv.org/abs/1704.09015).
- [505] M. J. Baker, J. Fuentes-Martín, G. Isidori, and M. König, “High- p_T signatures in vector-leptoquark models,” *Eur. Phys. J.* **C79** no. 4, (2019) 334, [arXiv:1901.10480 \[hep-ph\]](https://arxiv.org/abs/1901.10480).
- [506] **Belle** Collaboration, S. Hirose *et al.*, “Measurement of the τ lepton polarization and $R(D^*)$ in the decay $\overline{B} \rightarrow D^*\tau^-\bar{\nu}_\tau$,” *Phys. Rev. Lett.* **118** no. 21, (2017) 211801, [arXiv:1612.00529 \[hep-ex\]](https://arxiv.org/abs/1612.00529).
- [507] **Belle** Collaboration, A. Abdesselam *et al.*, “Measurement of $\mathcal{R}(D)$ and $\mathcal{R}(D^*)$ with a semileptonic tagging method,” [arXiv:1904.08794 \[hep-ex\]](https://arxiv.org/abs/1904.08794).
- [508] D. Bigi and P. Gambino, “Revisiting $B \rightarrow D\ell\nu$,” *Phys. Rev. D* **94** no. 9, (2016) 094008, [arXiv:1606.08030 \[hep-ph\]](https://arxiv.org/abs/1606.08030).
- [509] F. U. Bernlochner, Z. Ligeti, M. Papucci, and D. J. Robinson, “Combined analysis of semileptonic B decays to D and D^* : $R(D^{(*)})$, $|V_{cb}|$, and new physics,” *Phys. Rev. D* **95** no. 11, (2017) 115008, [arXiv:1703.05330 \[hep-ph\]](https://arxiv.org/abs/1703.05330). [Erratum: *Phys. Rev. D* 97, 059902 (2018)].
- [510] D. Bigi, P. Gambino, and S. Schacht, “ $R(D^*)$, $|V_{cb}|$, and the Heavy Quark Symmetry relations between form factors,” *JHEP* **11** (2017) 061, [arXiv:1707.09509 \[hep-ph\]](https://arxiv.org/abs/1707.09509).
- [511] S. Jaiswal, S. Nandi, and S. K. Patra, “Extraction of $|V_{cb}|$ from $B \rightarrow D^{(*)}\ell\nu_\ell$ and the Standard Model predictions of $R(D^{(*)})$,” *JHEP* **12** (2017) 060, [arXiv:1707.09977 \[hep-ph\]](https://arxiv.org/abs/1707.09977).
- [512] B. Capdevila, S. Descotes-Genon, J. Matias, and J. Virto, “Assessing lepton-flavour non-universality from $B \rightarrow K^*\ell\ell$ angular analyses,” *JHEP* **10** (2016) 075, [arXiv:1605.03156 \[hep-ph\]](https://arxiv.org/abs/1605.03156).

- [513] N. Serra, R. Silva Coutinho, and D. van Dyk, “Measuring the breaking of lepton flavor universality in $B \rightarrow K^* \ell^+ \ell^-$,” *Phys. Rev. D* **95** no. 3, (2017) 035029, [arXiv:1610.08761 \[hep-ph\]](#).
- [514] **Belle** Collaboration, S. Wehle *et al.*, “Lepton-Flavor-Dependent Angular Analysis of $B \rightarrow K^* \ell^+ \ell^-$,” *Phys. Rev. Lett.* **118** no. 11, (2017) 111801, [arXiv:1612.05014 \[hep-ex\]](#).
- [515] M. Algueró, B. Capdevila, S. Descotes-Genon, P. Masjuan, and J. Matias, “What R_K and Q_5 can tell us about New Physics in $b \rightarrow s\ell\ell$ transitions?,” *JHEP* **07** (2019) 096, [arXiv:1902.04900 \[hep-ph\]](#).
- [516] **Belle-II** Collaboration, W. Altmannshofer *et al.*, “The Belle II Physics Book,” *PTEP* **2019** no. 12, (2019) 123C01, [arXiv:1808.10567 \[hep-ex\]](#). [Erratum: PTEP 2020, 029201 (2020)].
- [517] G. D’Amico, M. Nardecchia, P. Panci, F. Sannino, A. Strumia, R. Torre, and A. Urbano, “Flavour anomalies after the R_{K^*} measurement,” *JHEP* **09** (2017) 010, [arXiv:1704.05438 \[hep-ph\]](#).
- [518] L.-S. Geng, B. Grinstein, S. Jäger, J. Martin Camalich, X.-L. Ren, and R.-X. Shi, “Towards the discovery of new physics with lepton-universality ratios of $b \rightarrow s\ell\ell$ decays,” *Phys. Rev. D* **96** no. 9, (2017) 093006, [arXiv:1704.05446 \[hep-ph\]](#).
- [519] B. Capdevila, A. Crivellin, S. Descotes-Genon, J. Matias, and J. Virto, “Patterns of New Physics in $b \rightarrow s\ell^+\ell^-$ transitions in the light of recent data,” *JHEP* **01** (2018) 093, [arXiv:1704.05340 \[hep-ph\]](#).
- [520] M. Ciuchini, A. M. Coutinho, M. Fedele, E. Franco, A. Paul, L. Silvestrini, and M. Valli, “On Flavourful Easter eggs for New Physics hunger and Lepton Flavour Universality violation,” *Eur. Phys. J.* **C77** no. 10, (2017) 688, [arXiv:1704.05447 \[hep-ph\]](#).
- [521] G. Hiller and I. Nisandzic, “ R_K and R_{K^*} beyond the standard model,” *Phys. Rev. D* **96** no. 3, (2017) 035003, [arXiv:1704.05444 \[hep-ph\]](#).
- [522] M. Ciuchini, A. M. Coutinho, M. Fedele, E. Franco, A. Paul, L. Silvestrini, and M. Valli, “New Physics in $b \rightarrow s\ell^+\ell^-$ confronts new data on Lepton Universality,” *Eur. Phys. J.* **C79** no. 8, (2019) 719, [arXiv:1903.09632 \[hep-ph\]](#).
- [523] J. Aebischer, W. Altmannshofer, D. Guadagnoli, M. Reboud, P. Stangl, and D. M. Straub, “B-decay discrepancies after Moriond 2019,” *Eur. Phys. J.* **C80** no. 3, (2020) 252, [arXiv:1903.10434 \[hep-ph\]](#).
- [524] A. K. Alok, A. Dighe, S. Gangal, and D. Kumar, “Continuing search for new physics in $b \rightarrow s\mu\mu$ decays: two operators at a time,” *JHEP* **06** (2019) 089, [arXiv:1903.09617 \[hep-ph\]](#).

- [525] M. Algueró, B. Capdevila, A. Crivellin, S. Descotes-Genon, P. Masjuan, J. Matias, M. Novoa, and J. Virto, “Emerging patterns of New Physics with and without Lepton Flavour Universal contributions,” *Eur. Phys. J. C* **79** no. 8, (2019) 714, [arXiv:1903.09578 \[hep-ph\]](https://arxiv.org/abs/1903.09578).
- [526] K. Kowalska, D. Kumar, and E. M. Sessolo, “Implications for new physics in $b \rightarrow s\mu\mu$ transitions after recent measurements by Belle and LHCb,” *Eur. Phys. J. C* **79** no. 10, (2019) 840, [arXiv:1903.10932 \[hep-ph\]](https://arxiv.org/abs/1903.10932).
- [527] A. Arbey, T. Hurth, F. Mahmoudi, D. M. Santos, and S. Neshatpour, “Update on the $b \rightarrow s$ anomalies,” *Phys. Rev. D* **100** no. 1, (2019) 015045, [arXiv:1904.08399 \[hep-ph\]](https://arxiv.org/abs/1904.08399).
- [528] A. Datta, J. Kumar, and D. London, “The B anomalies and new physics in $b \rightarrow se^+e^-$,” *Phys. Lett. B* **797** (2019) 134858, [arXiv:1903.10086 \[hep-ph\]](https://arxiv.org/abs/1903.10086).
- [529] L. Calibbi, A. Crivellin, and T. Ota, “Effective Field Theory Approach to $b \rightarrow s\ell\ell^{(\prime)}$, $B \rightarrow K^{(*)}\nu\bar{\nu}$ and $B \rightarrow D^{(*)}\tau\nu$ with Third Generation Couplings,” *Phys. Rev. Lett.* **115** (2015) 181801, [arXiv:1506.02661 \[hep-ph\]](https://arxiv.org/abs/1506.02661).
- [530] I. Doršner, S. Fajfer, A. Greljo, J. Kamenik, and N. Košnik, “Physics of leptoquarks in precision experiments and at particle colliders,” *Phys. Rept.* **641** (2016) 1–68, [arXiv:1603.04993 \[hep-ph\]](https://arxiv.org/abs/1603.04993).
- [531] D. Buttazzo, A. Greljo, G. Isidori, and D. Marzocca, “B-physics anomalies: a guide to combined explanations,” *JHEP* **11** (2017) 044, [arXiv:1706.07808 \[hep-ph\]](https://arxiv.org/abs/1706.07808).
- [532] J. Kumar, D. London, and R. Watanabe, “Combined Explanations of the $b \rightarrow s\mu^+\mu^-$ and $b \rightarrow c\tau^-\bar{\nu}$ Anomalies: a General Model Analysis,” *Phys. Rev. D* **99** no. 1, (2019) 015007, [arXiv:1806.07403 \[hep-ph\]](https://arxiv.org/abs/1806.07403).
- [533] C. Cornella, J. Fuentes-Martin, and G. Isidori, “Revisiting the vector leptoquark explanation of the B-physics anomalies,” *JHEP* **07** (2019) 168, [arXiv:1903.11517 \[hep-ph\]](https://arxiv.org/abs/1903.11517).
- [534] J. F. Kamenik, Y. Soreq, and J. Zupan, “Lepton flavor universality violation without new sources of quark flavor violation,” *Phys. Rev. D* **97** no. 3, (2018) 035002, [arXiv:1704.06005 \[hep-ph\]](https://arxiv.org/abs/1704.06005).
- [535] P. J. Fox, I. Low, and Y. Zhang, “Top-philic Z' forces at the LHC,” *JHEP* **03** (2018) 074, [arXiv:1801.03505 \[hep-ph\]](https://arxiv.org/abs/1801.03505).
- [536] A. Buras, P. Gambino, M. Gorbahn, S. Jager, and L. Silvestrini, “Universal unitarity triangle and physics beyond the standard model,” *Phys. Lett. B* **500** (2001) 161–167, [arXiv:hep-ph/0007085](https://arxiv.org/abs/hep-ph/0007085).

- [537] A. L. Kagan, G. Perez, T. Volansky, and J. Zupan, “General Minimal Flavor Violation,” *Phys. Rev. D* **80** (2009) 076002, [arXiv:0903.1794 \[hep-ph\]](#).
- [538] A. Celis, J. Fuentes-Martin, A. Vicente, and J. Virto, “Gauge-invariant implications of the LHCb measurements on lepton-flavor nonuniversality,” *Phys. Rev. D* **96** no. 3, (2017) 035026, [arXiv:1704.05672 \[hep-ph\]](#).
- [539] J. E. Camargo-Molina, A. Celis, and D. A. Faroughy, “Anomalies in Bottom from new physics in Top,” *Phys. Lett. B* **784** (2018) 284–293, [arXiv:1805.04917 \[hep-ph\]](#).
- [540] A. Efrati, A. Falkowski, and Y. Soreq, “Electroweak constraints on flavorful effective theories,” *JHEP* **07** (2015) 018, [arXiv:1503.07872 \[hep-ph\]](#).
- [541] B. Bhattacharya, A. Datta, D. London, and S. Shivashankara, “Simultaneous Explanation of the R_K and $R(D^{(*)})$ Puzzles,” *Phys. Lett. B* **742** (2015) 370–374, [arXiv:1412.7164 \[hep-ph\]](#).
- [542] F. Feruglio, P. Paradisi, and A. Pattori, “Revisiting Lepton Flavor Universality in B Decays,” *Phys. Rev. Lett.* **118** no. 1, (2017) 011801, [arXiv:1606.00524 \[hep-ph\]](#).
- [543] M. Ciuchini, M. Fedele, E. Franco, S. Mishima, A. Paul, L. Silvestrini, and M. Valli, “ $B \rightarrow K^* \ell^+ \ell^-$ in the Standard Model: Elaborations and Interpretations,” *PoS ICHEP2016* (2016) 584, [arXiv:1611.04338 \[hep-ph\]](#).
- [544] M. Ciuchini, M. Fedele, E. Franco, S. Mishima, A. Paul, L. Silvestrini, and M. Valli, “Knowns and Unknowns in the Predictions for $B \rightarrow K^* \mu^+ \mu^-$,” *Nucl. Part. Phys. Proc.* **285-286** (2017) 45–49.
- [545] M. Ciuchini, A. M. Coutinho, M. Fedele, E. Franco, A. Paul, L. Silvestrini, and M. Valli, “On hadronic uncertainties polluting the New Physics hunt in $b \rightarrow s$ transitions,” *Nucl. Part. Phys. Proc.* **303-305** (2018) 8–13.
- [546] L. Alasfar, A. Azatov, J. de Blas, A. Paul, and M. Valli, “ B anomalies under the lens of electroweak precision,” *JHEP* **12** (2020) 016, [arXiv:2007.04400 \[hep-ph\]](#).
- [547] J. Aebischer, A. Crivellin, M. Fael, and C. Greub, “Matching of gauge invariant dimension-six operators for $b \rightarrow s$ and $b \rightarrow c$ transitions,” *JHEP* **05** (2016) 037, [arXiv:1512.02830 \[hep-ph\]](#).
- [548] C. Bobeth, A. J. Buras, A. Celis, and M. Jung, “Yukawa enhancement of Z -mediated new physics in $\Delta S = 2$ and $\Delta B = 2$ processes,” *JHEP* **07** (2017) 124, [arXiv:1703.04753 \[hep-ph\]](#).
- [549] G. Buchalla, A. J. Buras, and M. E. Lautenbacher, “Weak decays beyond leading logarithms,” *Rev. Mod. Phys.* **68** (1996) 1125–1144, [arXiv:hep-ph/9512380](#).

- [550] A. J. Buras, “Weak Hamiltonian, CP violation and rare decays,” in *Les Houches Summer School in Theoretical Physics, Session 68: Probing the Standard Model of Particle Interactions*, pp. 281–539. 6, 1998. [arXiv:hep-ph/9806471](https://arxiv.org/abs/hep-ph/9806471).
- [551] L. Silvestrini, “Effective Theories for Quark Flavour Physics,” in *Les Houches summer school: EFT in Particle Physics and Cosmology*. 5, 2019. [arXiv:1905.00798 \[hep-ph\]](https://arxiv.org/abs/1905.00798).
- [552] J. de Blas, G. Durieux, C. Grojean, J. Gu, and A. Paul, “On the future of Higgs, electroweak and diboson measurements at lepton colliders,” *JHEP* **12** (2019) 117, [arXiv:1907.04311 \[hep-ph\]](https://arxiv.org/abs/1907.04311).
- [553] A. Caldwell, D. Kollár, and K. Kröninger, “BAT - The Bayesian analysis toolkit,” *Computer Physics Communications* **180** no. 11, (Nov., 2009) 2197–2209, [arXiv:0808.2552 \[physics.data-an\]](https://arxiv.org/abs/0808.2552).
- [554] **SLD** Collaboration, K. Abe *et al.*, “First direct measurement of the parity violating coupling of the Z0 to the s quark,” *Phys. Rev. Lett.* **85** (2000) 5059–5063, [arXiv:hep-ex/0006019 \[hep-ex\]](https://arxiv.org/abs/hep-ex/0006019).
- [555] **ALEPH, DELPHI, L3, OPAL, LEP Electroweak** Collaboration, S. Schael *et al.*, “Electroweak Measurements in Electron-Positron Collisions at W-Boson-Pair Energies at LEP,” *Phys. Rept.* **532** (2013) 119–244, [arXiv:1302.3415 \[hep-ex\]](https://arxiv.org/abs/1302.3415).
- [556] **ATLAS** Collaboration, M. Aaboud *et al.*, “Measurement of the W -boson mass in pp collisions at $\sqrt{s} = 7$ TeV with the ATLAS detector,” *Eur. Phys. J. C* **78** no. 2, (2018) 110, [arXiv:1701.07240 \[hep-ex\]](https://arxiv.org/abs/1701.07240). [Erratum: Eur.Phys.J.C 78, 898 (2018)].
- [557] **CMS** Collaboration, V. Khachatryan *et al.*, “Measurement of the t-channel single-top-quark production cross section and of the $|V_{tb}|$ CKM matrix element in pp collisions at $\sqrt{s}= 8$ TeV,” *JHEP* **06** (2014) 090, [arXiv:1403.7366 \[hep-ex\]](https://arxiv.org/abs/1403.7366).
- [558] **D0** Collaboration, V. Abazov *et al.*, “Measurement of $\sin^2 \theta_{\text{eff}}^\ell$ and Z -light quark couplings using the forward-backward charge asymmetry in $p\bar{p} \rightarrow Z/\gamma^* \rightarrow e^+e^-$ events with $\mathcal{L} = 5.0 \text{ fb}^{-1}$ at $\sqrt{s} = 1.96 \text{ TeV}$,” *Phys. Rev. D* **84** (2011) 012007, [arXiv:1104.4590 \[hep-ex\]](https://arxiv.org/abs/1104.4590).
- [559] **ATLAS** Collaboration, M. Aaboud *et al.*, “Angular analysis of $B_d^0 \rightarrow K^* \mu^+ \mu^-$ decays in pp collisions at $\sqrt{s} = 8$ TeV with the ATLAS detector,” *JHEP* **10** (2018) 047, [arXiv:1805.04000 \[hep-ex\]](https://arxiv.org/abs/1805.04000).
- [560] **CMS** Collaboration, V. Khachatryan *et al.*, “Angular analysis of the decay $B^0 \rightarrow K^{*0} \mu^+ \mu^-$ from pp collisions at $\sqrt{s} = 8$ TeV,” *Phys. Lett. B* **753** (2016) 424–448, [arXiv:1507.08126 \[hep-ex\]](https://arxiv.org/abs/1507.08126).

- [561] **CMS** Collaboration, A. M. Sirunyan *et al.*, “Measurement of angular parameters from the decay $B^0 \rightarrow K^{*0}\mu^+\mu^-$ in proton-proton collisions at $\sqrt{s} = 8$ TeV,” *Phys. Lett. B* **781** (2018) 517–541, [arXiv:1710.02846 \[hep-ex\]](https://arxiv.org/abs/1710.02846).
- [562] **LHCb** Collaboration, R. Aaij *et al.*, “Angular analysis of the $B^0 \rightarrow K^{*0}e^+e^-$ decay in the low- q^2 region,” *JHEP* **04** (2015) 064, [arXiv:1501.03038 \[hep-ex\]](https://arxiv.org/abs/1501.03038).
- [563] **LHCb** Collaboration, R. Aaij *et al.*, “Measurement of CP -averaged observables in the $B^0 \rightarrow K^{*0}\mu^+\mu^-$ decay,” [arXiv:2003.04831 \[hep-ex\]](https://arxiv.org/abs/2003.04831).
- [564] **LHCb** Collaboration, R. Aaij *et al.*, “Measurements of the S-wave fraction in $B^0 \rightarrow K^+\pi^-\mu^+\mu^-$ decays and the $B^0 \rightarrow K^*(892)^0\mu^+\mu^-$ differential branching fraction,” *JHEP* **11** (2016) 047, [arXiv:1606.04731 \[hep-ex\]](https://arxiv.org/abs/1606.04731). [Erratum: JHEP04,142(2017)].
- [565] **LHCb** Collaboration, R. Aaij *et al.*, “Differential branching fractions and isospin asymmetries of $B \rightarrow K^{(*)}\mu^+\mu^-$ decays,” *JHEP* **06** (2014) 133, [arXiv:1403.8044 \[hep-ex\]](https://arxiv.org/abs/1403.8044).
- [566] **HFLAV** Collaboration, Y. S. Amhis *et al.*, “Averages of b -hadron, c -hadron, and τ -lepton properties as of 2018,” [arXiv:1909.12524 \[hep-ex\]](https://arxiv.org/abs/1909.12524).
- [567] **LHCb** Collaboration, R. Aaij *et al.*, “Angular analysis and differential branching fraction of the decay $B_s^0 \rightarrow \phi\mu^+\mu^-$,” *JHEP* **09** (2015) 179, [arXiv:1506.08777 \[hep-ex\]](https://arxiv.org/abs/1506.08777).
- [568] **LHCb** Collaboration, R. Aaij *et al.*, “Measurement of the ratio of branching fractions $BR(B_0 \rightarrow K^{*0}\gamma)/BR(B_{s0} \rightarrow \phi\gamma)$ and the direct CP asymmetry in $B_0 \rightarrow K^{*0}\gamma$,” *Nucl. Phys. B* **867** (2013) 1–18, [arXiv:1209.0313 \[hep-ex\]](https://arxiv.org/abs/1209.0313).
- [569] **ATLAS** Collaboration, M. Aaboud *et al.*, “Search for heavy particles decaying into a top-quark pair in the fully hadronic final state in pp collisions at $\sqrt{s} = 13$ TeV with the ATLAS detector,” *Phys. Rev. D* **99** no. 9, (2019) 092004, [arXiv:1902.10077 \[hep-ex\]](https://arxiv.org/abs/1902.10077).
- [570] **ATLAS Collaboration** Collaboration, “Search for high-mass dilepton resonances using 139 fb^{-1} of pp collision data collected at $\sqrt{s} = 13$ TeV with the ATLAS detector,” tech. rep., CERN, Geneva, Feb, 2019.
<https://cds.cern.ch/record/2663393>. All figures including auxiliary figures are available at
<https://atlas.web.cern.ch/Atlas/GROUPS/PHYSICS/CONFNOTES/ATLAS-CONF-2019-001>.
- [571] **CCFR** Collaboration, S. Mishra *et al.*, “Neutrino tridents and WZ interference,” *Phys. Rev. Lett.* **66** (1991) 3117–3120.

- [572] **ATLAS** Collaboration, M. Aaboud *et al.*, “Search for new high-mass phenomena in the dilepton final state using 36 fb^{-1} of proton-proton collision data at $\sqrt{s} = 13 \text{ TeV}$ with the ATLAS detector,” *JHEP* **10** (2017) 182, [arXiv:1707.02424 \[hep-ex\]](https://arxiv.org/abs/1707.02424).
- [573] **CMS** Collaboration, A. M. Sirunyan *et al.*, “Search for standard model production of four top quarks with same-sign and multilepton final states in proton–proton collisions at $\sqrt{s} = 13 \text{ TeV}$,” *Eur. Phys. J. C* **78** no. 2, (2018) 140, [arXiv:1710.10614 \[hep-ex\]](https://arxiv.org/abs/1710.10614).
- [574] **ATLAS** Collaboration, M. Aaboud *et al.*, “Search for pair production of heavy vector-like quarks decaying into high- p_T gy bosons and top quarks in the lepton-plus-jets final state in pp collisions at $\sqrt{s} = 13 \text{ TeV}$ with the ATLAS detector,” *JHEP* **08** (2018) 048, [arXiv:1806.01762 \[hep-ex\]](https://arxiv.org/abs/1806.01762).
- [575] **CMS** Collaboration, A. M. Sirunyan *et al.*, “Search for vector-like leptons in multilepton final states in proton-proton collisions at $\sqrt{s} = 13 \text{ TeV}$,” *Phys. Rev. D* **100** no. 5, (2019) 052003, [arXiv:1905.10853 \[hep-ex\]](https://arxiv.org/abs/1905.10853).
- [576] S. D. Thomas and J. D. Wells, “Phenomenology of Massive Vectorlike Doublet Leptons,” *Phys. Rev. Lett.* **81** (1998) 34–37, [arXiv:hep-ph/9804359](https://arxiv.org/abs/hep-ph/9804359).
- [577] F. del Aguila, J. de Blas, and M. Perez-Victoria, “Effects of new leptons in Electroweak Precision Data,” *Phys. Rev. D* **78** (2008) 013010, [arXiv:0803.4008 \[hep-ph\]](https://arxiv.org/abs/0803.4008).
- [578] K. Kannike, M. Raidal, D. M. Straub, and A. Strumia, “Anthropic solution to the magnetic muon anomaly: the charged see-saw,” *JHEP* **02** (2012) 106, [arXiv:1111.2551 \[hep-ph\]](https://arxiv.org/abs/1111.2551). [Erratum: JHEP10,136(2012)].
- [579] N. Kumar and S. P. Martin, “Vectorlike Leptons at the Large Hadron Collider,” *Phys. Rev. D* **92** no. 11, (2015) 115018, [arXiv:1510.03456 \[hep-ph\]](https://arxiv.org/abs/1510.03456).
- [580] P. N. Bhattacharya and S. P. Martin, “Prospects for vectorlike leptons at future proton-proton colliders,” *Phys. Rev. D* **100** no. 1, (2019) 015033, [arXiv:1905.00498 \[hep-ph\]](https://arxiv.org/abs/1905.00498).
- [581] J. C. Pati and A. Salam, “Lepton Number as the Fourth Color,” *Phys. Rev. D* **10** (1974) 275–289. [Erratum: Phys.Rev.D 11, 703–703 (1975)].
- [582] H. Georgi and S. L. Glashow, “Unity of all elementary-particle forces,” *Phys. Rev. Lett.* **32** (Feb, 1974) 438–441.
<https://link.aps.org/doi/10.1103/PhysRevLett.32.438>.
- [583] R. Coy, M. Frigerio, F. Mescia, and O. Sumensari, “New physics in $b \rightarrow s\ell\ell$ transitions at one loop,” *Eur. Phys. J. C* **80** no. 1, (2020) 52, [arXiv:1909.08567 \[hep-ph\]](https://arxiv.org/abs/1909.08567).

- [584] W. Buchmuller, R. Ruckl, and D. Wyler, “Leptoquarks in Lepton - Quark Collisions,” *Phys. Lett. B* **191** (1987) 442–448. [Erratum: Phys.Lett.B 448, 320–320 (1999)].
- [585] F. del Aguila, J. de Blas, and M. Perez-Victoria, “Electroweak Limits on General New Vector Bosons,” *JHEP* **09** (2010) 033, [arXiv:1005.3998 \[hep-ph\]](#).
- [586] R. Alonso, B. Grinstein, and J. Martin Camalich, “Lepton universality violation and lepton flavor conservation in B -meson decays,” *JHEP* **10** (2015) 184, [arXiv:1505.05164 \[hep-ph\]](#).
- [587] A. Angelescu, D. Bećirević, D. Faroughy, and O. Sumensari, “Closing the window on single leptoquark solutions to the B -physics anomalies,” *JHEP* **10** (2018) 183, [arXiv:1808.08179 \[hep-ph\]](#).
- [588] **LHCb** Collaboration, R. Aaij *et al.*, “Physics case for an LHCb Upgrade II - Opportunities in flavour physics, and beyond, in the HL-LHC era,” [arXiv:1808.08865 \[hep-ex\]](#).